Evolution of Degenerate Oxygen-Neon Cores

Entwicklung Entarteter Sauerstoff-Neon-Kerne

Zur Erlangung des Grades eines Doktors der Naturwissenschaften (Dr. rer. nat.)
genehmigte Dissertation von M.Sc. Heiko Möller, geb. in Wiesbaden
Tag der Einreichung: 6.2.2017, Tag der Prüfung: 24.4.2017
Darmstadt 2017 — D 17

1. Gutachten: Prof. Dr. Gabriel Martínez-Pinedo
2. Gutachten: Prof. Dr. Karlheinz Langanke

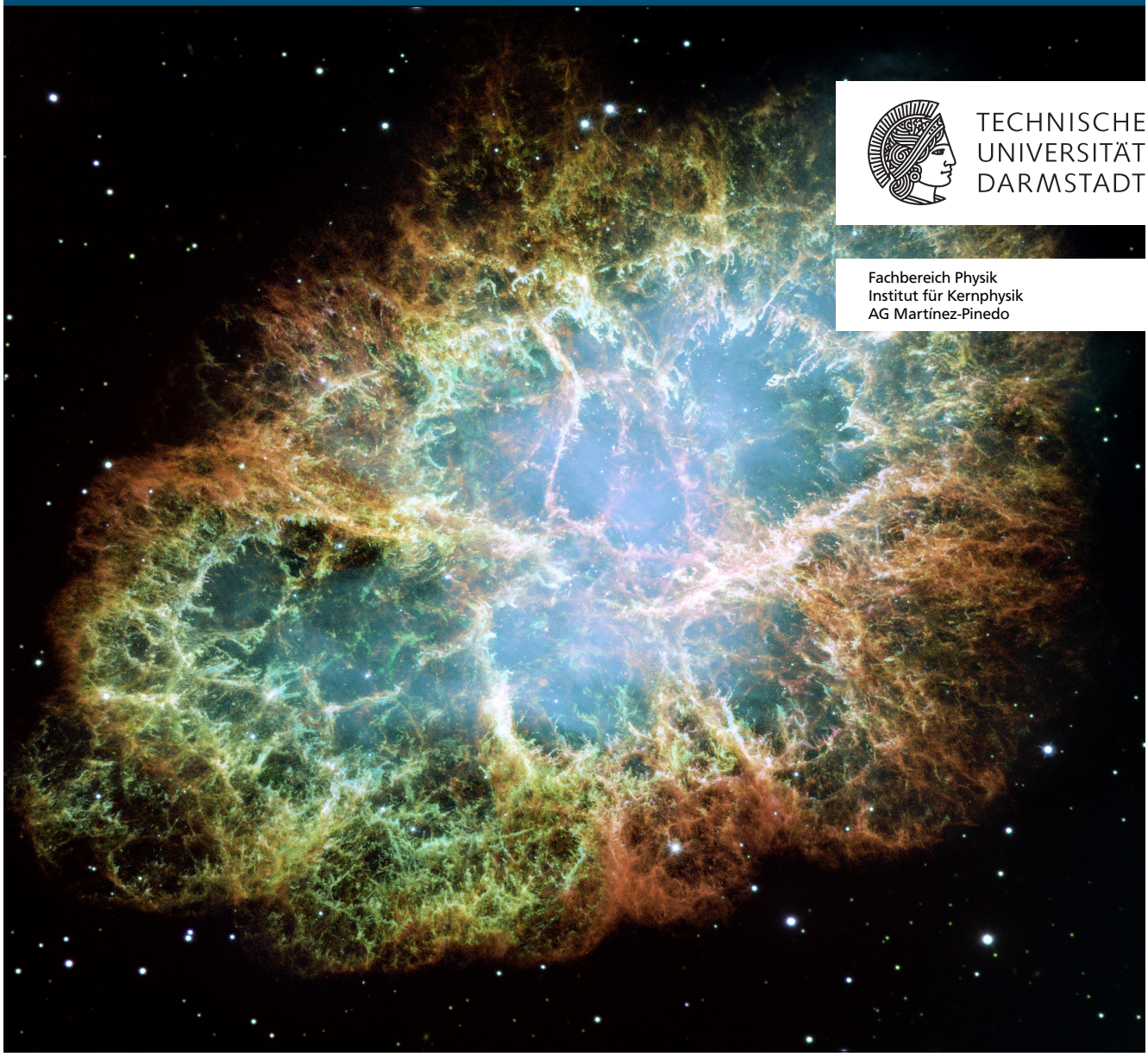

TECHNISCHE UNIVERSITÄT DARMSTADT

Fachbereich Physik
Institut für Kernphysik
AG Martínez-Pinedo

Evolution of Degenerate Oxygen-Neon Cores
Entwicklung Entarteter Sauerstoff-Neon-Kerne

Genehmigte Dissertation von M.Sc. Heiko Möller, geb. in Wiesbaden

1. Gutachten: Prof. Dr. Gabriel Martínez-Pinedo
2. Gutachten: Prof. Dr. Karlheinz Langanke

Tag der Einreichung: 6.2.2017
Tag der Prüfung: 24.4.2017

Darmstadt 2017 — D 17

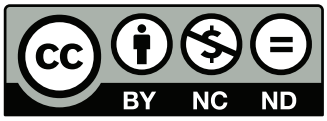

In memory of

David
Magdalena & Ernst

“If all this is true, stars have a life cycle much like animals. They get born, they grow, they go through a definite internal development, and finally they die, to give back the material of which they are made so that new stars may live.”

— H. A. Bethe, Nobel Lecture, 1967

Abstract

Mass-accreting electron-degenerate stellar cores that are composed primarily of the carbon-burning ashes ^{16}O and ^{20}Ne (ONe cores) appear in several astrophysical scenarios. On the one hand, they can be formed during the late evolution of intermediate-mass stars with 8 to 10 solar masses. On the other hand, they can occur in the context of the accretion-induced collapse (AIC) of ONe white dwarfs, where the collapse is induced by mass transfer from a companion star in a binary system or due to cooling of the outer layers of a white dwarf-white dwarf merger remnant. Their evolution is critically depending on electron capture (EC) reactions on nuclei with mass number $A \approx 20$ that become relevant above a density of 10^9 g cm^{-3}. Besides removing electrons—the main pressure support—from the core, EC are also responsible for releasing or absorbing heat. In the canonical picture, the accreting ONe core will undergo compression until EC on the abundant ^{20}Ne are activated. As a consequence, the core becomes gravitationally unstable. Simultaneously, ECs release sufficient heat to ignite oxygen in a thermonuclear runaway, launching an outwards traveling deflagration wave. Nevertheless, the energy release from oxygen fusion is insufficient to halt gravitational collapse. Otherwise, the star would be destroyed by a thermonuclear explosion. Subsequent to collapse, a neutron star is formed and the stellar envelope explodes in an electron-capture supernova (ECSN).

Recent 3D hydrodynamic simulations of the oxygen deflagration in ONe cores have suggested that the outcome of such events—either ECSNe or thermonuclear explosions—depends critically on the ignition density of oxygen ϱ_{ign}. Depending on the treatment of convection, ϱ_{ign} is estimated to be $\approx 2 \times 10^{10}$ g cm^{-3} in case core convection sets in prior to ignition and $\approx 1 \times 10^{10}$ g cm^{-3}, if not. It has been suggested that models corresponding to the first case lead to a collapse, while models corresponding to the second case result in a thermonuclear explosion of the star.

We study accreting ONe cores in the AIC scenario, focusing on open questions regarding the evolution of the core prior to ignition. By including the secondary carbon-burning products ^{23}Na and ^{25}Mg in the initial models, new insights can be gained concerning Urca cooling. While it seems well established that EC processes do not trigger convection in the ONe core, the poorly understood phenomenon of overstable convection could alter this picture and will be assessed by us, in detail. Furthermore, modifications at high densities to the standard set of nuclear reactions, responsible for neon and oxygen burning, are investigated. Previously, reaction channels that become possible due to the presence of ^{20}O, formed by double-EC on ^{20}Ne, have not been considered. Neon burning is modified by the reaction $^{20}\mathrm{O}(\alpha,\gamma)^{24}\mathrm{Ne}$ and oxygen burning can additionally proceed by the fusion involving neutron-rich oxygen isotopes: $^{20}\mathrm{O} + {}^{16/20}\mathrm{O} \rightarrow {}^{36/40}\mathrm{S}^{*}$. In neither case experimental data is available. Further investigations are dedicated to exploring the origin and the consequences of an off-center ignition of the flame, due to EC processes. For our simulations, we make use of the "Modules for Experiments in Stellar Astrophysics" stellar evolution code (MESA). In order to determine the EC and β^- decay rates, we utilize the recently implemented capability of MESA to evaluate weak reaction rates with very high accuracy by solving the phase-space integral directly, only requiring matrix elements and excitation energies of all contributing transitions, either known experimentally or originating from shell-model calculations.

Additionally, it is our aim to study the oxygen deflagration that is potentially followed by an ECSN. This is done by combining the 1D shock-capturing core-collapse-supernova code AGILE-IDSA with a level-set-based flame description, using laminar and turbulent flame velocities based on microscopic calculations. All relevant weak processes on the oxygen-burning ashes are considered, in order to correctly predict the deleptonization and energy generation.

We confirm the accuracy of the direct determination of weak rates in MESA and extend it to the Urca nuclei ^{23}Na and ^{25}Mg. The MESA models of accreting ONe cores show that especially the abundance of ^{25}Mg and the related Urca cooling can affect ϱ_{ign} by 10 %, resulting in values between $8.7 - 9.7 \times 10^9$ g cm^{-3}. Additionally, we investigate the previously reported off-center ignition ($\approx$ 50 km) of the oxygen deflagration, caused by including the second-forbidden transition between the ^{20}Ne and ^{20}F ground states. We conclude that in this case, EC heating on ^{20}Ne acts on much longer timescales ($\approx$ years), giving the core sufficient time to expand and shift the ignition away from the center. Furthermore, we report that overstable convection, treated as a diffusive process, does not affect the evolution of the ONe core. However, applying Kato's linear growth analysis suggests that instabilities could grow on a timescale of around $10-100$ s. This would give enough time for instabilities to develop, as the timescale between the onset of semiconvection in the core, due to EC on ^{20}Ne, and collapse is around 100 years. Also, we find that including a larger reaction network, together with the aforementioned modified set of reactions during neon and oxygen burning, has no impact on the evolution of the ONe core, at least if the burning is initiated by a thermonuclear runaway.

Using spatially high-resolution ONe core models that develop a thermonuclear runaway in the center, we show preliminary results of the oxygen deflagration, simulated with AGILE-IDSA. We further demonstrate the capability of AGILE-IDSA to perform self-consistent ECSN simulations with Nomoto's canonical progenitor model. We want to point out that this approach can efficiently complement expensive 3D simulations by performing parameter studies, allowing for a better targeted use of computer resources in 3D simulations.

Cover picture: Crab Nebula, image credit: NASA, ESA and Allison Loll/Jeff Hester (Arizona State University). Acknowledgment: Davide de Martin (ESA/Hubble). The Crab Nebula is a supernova remnant approximately 6500 light-years away from earth. It hosts the Crab pulsar, a neutron star that was formed by supernova SN 1054. This supernova was seen by Chinese, Japanese as well as Arab astronomers in 1054 AD. Recent studied suggest that the progenitor star of SN 1054 was a super-asymptotic-giant-branch star with a mass between 8 and 10 solar masses that exploded as electron-capture supernova.

Zusammenfassung

Akkretierende, entartete Sternkerne, die hauptsächlich aus den Produkten des Kohlenstoffbrennens Sauerstoff (^{16}O) und Neon (^{20}Ne) bestehen, existieren in verschiedenen astrophysikalischen Szenarien. Auf der einen Seite können sie während der finalen Entwicklung von mittelschweren Sternen mit 8 bis 10 Sonnenmassen entstehen. Andererseits können sie auch im Zusammenhang mit dem Akkretions-induzierten Kollaps von Sauerstoff-Neon-Weißen Zwergen auftreten. Dieser Kollaps wird entweder hervorgerufen durch Massentransfer in einem Doppelsternsystem oder durch das Abkühlen der äußeren Stern-Schichten nach der Verschmelzung zweier Weißer Zwerge. Ihre Entwicklung hängt maßgeblich von Elektroneneinfängen an Kernen mit Massenzahl $A \approx 20$ ab, welche ab einer Dichte von 10^9 g cm^{-3} eintreten. Neben dem Entfernen von Elektronen aus dem Kern, der dominierenden Druckkomponente, sind Elektroneneinfänge auch für die Absorption respektive Emission von Wärmeenergie verantwortlich. Nach allgemeiner Auffassung verdichtet sich ein akkretierender Sauerstoff-Neon-Kern solange, bis es zu Elektroneneinfängen am häufig vorhandenen ^{20}Ne kommt, woraufhin der Stern gravitativ instabil wird. Gleichzeitig setzen Elektroneneinfänge genügend Wärme frei, um Sauerstoff in einem thermonuklearen Durchgehen zu entzünden und eine nach außen gerichtete Deflagrationswelle zu initiieren. Trotzdem reicht die Energiefreisetzung aus dem Sauerstoffbrennen nicht aus, um den Gravitationskollaps aufzuhalten, woraufhin der Stern durch eine thermonukleare Explosion zerstört würde. Im Anschluss an den Kollaps entsteht ein Neutronenstern und die Hülle des Sterns explodiert in einer Elektroneneinfang-Supernova.

Aktuelle hydrodynamische 3D-Simulationen der Sauerstoffdeflagration in Sauerstoff-Neon-Kernen legen nahe, dass der Ausgang, ob nun thermonukleare Explosion oder Elektroneneinfang-Supernova, abhängig ist von der Entzündungsdichte des Sauerstoffs. Je nach Betrachtungsweise wird selbige auf $\approx 2 \times 10^{10}$ g cm^{-3} geschätzt, falls Konvektion im Kern vor der Entzündung einsetzt, und auf 1×10^{10} g cm^{-3}, falls nicht. Man nimmt an, dass Modelle, die dem ersten Fall entsprechen, zu einem Kollaps führen, während Modelle, die dem zweiten Fall entsprechen, in einer thermonuklearen Explosion enden.

Wir untersuchen akkretierende Sauerstoff-Neon-Kerne innerhalb des Akkretions-induzierten Kollapsszenarios, wobei wir uns auf offene Fragestellungen hinsichtlich der Sternentwicklung vor der Sauerstoffentzündung konzentrieren. Durch die Berücksichtigung sekundärer Produkte des Kohlenstoffbrennens, nämlich Natrium (^{23}Na) und Magnesium (^{25}Mg), können neue Erkenntnisse über die sogenannte Urca-Kühlung gewonnen werden. Das Phänomen der überstabilen Konvektion ist bisher wenig verstanden und unsere Analyse könnte die gängige Meinung, dass die Konvektion in Sauerstoff-Neon-Kernen nicht von Elektroneneinfängen ausgelöst wird, revidieren. Zusätzlich erforschen wir Modifikationen der Standardraten von Kernreaktionen bei hohen Dichten, die für das Neon- und Sauerstoffbrennen verantwortlich sind. Reaktionskanäle, die durch das Auftreten von ^{20}O, hergestellt durch den doppelten Elektroneneinfang am ^{20}Ne, möglich werden, wurden in früheren Arbeiten nicht berücksichtigt. Neonbrennen wird dadurch um die Reaktion $^{20}\mathrm{O}(\alpha,\gamma)^{24}\mathrm{Ne}$ erweitert und Sauerstoffbrennen kann zusätzlich mit der Fusion von neutronenreichen Isotopen $^{20}\mathrm{O} + {}^{16/20}\mathrm{O} \rightarrow {}^{36/40}\mathrm{S}^*$ ablaufen. Experimentelle Daten sind jedoch in keinem der beiden Fälle vorhanden. Weiter haben wir uns der Erforschung des Ursprungs und der Konsequenzen einer dezentralen Flammenentzündung gewidmet, welche durch Elektroneneinfangprozesse ausgelöst wird. Für unsere Simulationen verwenden wir den Computercode für Sternentwicklung, genannt “Modules for Experiments in Stellar Astrophysic”, kurz MESA. Um Elektroneneinfang- und β^--Zerfallsraten zu bestimmen, nutzen wir die kürzlich implementierte Möglichkeit von MESA, schwache Wechselwirkungsraten mit hoher Genauigkeit, durch direktes Lösen des Phasenraumintegrals, auszu-

werten. Diese Methode benötigt lediglich die Matrixelemente und Anregungsenergien von allen beteiligten Übergängen, welche entweder experimentell gemessen oder durch Schalenmodell-Rechnungen bestimmt wurden.

Überdies ist es unser Ziel, die Sauerstoffdeflagration, auf die möglicherweise eine Elektroneneinfang-Supernova folgt, zu untersuchen. Dafür kombinieren wir den eindimensionalen Kernkollaps-Supernova Code AGILE-IDSA mit einem Deflagrationsmodell, das laminare und turbulente Flammengeschwindigkeiten, basierend auf mikroskopischen Berechnungen, berücksichtigt. Um die Deleptonisierung und die Energieerzeugung korrekt vorherzusagen, werden alle schwachen Wechselwirkungsprozesse einbezogen, die an den Erzeugnissen des Sauerstoffbrennens stattfinden.

Wir bestätigen die Genauigkeit der direkten Bestimmung der schwachen Wechselwirkungsraten in MESA und erweitern den Formalismus um die Urca-Kerne ^{23}Na und ^{25}Mg. Die MESA Modelle von akkretierenden Sauerstoff-Neon-Kernen zeigen, dass besonders die Häufigkeit von ^{25}Mg, und die damit verbundene Urca-Kühlung, die Entzündungsdichte um bis zu 10 % beeinflussen können, was zu Werten von $8.7-9.7\times10^{9}$ g cm^{-3} führt. Zusätzlich untersuchen wir die dezentrale Entzündung ($\approx$ 50 km) der Sauerstoffdeflagration, welche durch den zweiten verbotenen Übergang zwischen den Grundzuständen von ^{20}Ne und ^{20}F hervorgerufen wird. Wir schlussfolgern, dass in diesem Fall die Aufheizung durch Elektroneneinfänge an ^{20}Ne in einem viel längeren Zeitraum von Jahren stattfindet, was dem Stern genug Zeit gibt, sich auszudehnen und die Entzündung vom Zentrum weg zu verlagern. Ferner berichten wir, dass die überstabile Konvektion, betrachtet als Diffusionsprozess, keinen Einfluss auf die Entwicklung des Sauerstoff-Neon-Kerns hat. Die Verwendung der linearen Wachstumsanalyse von Kato weißt jedoch daraufhin, dass hydrodynamische Instabilitäten in einem Zeitraum von $10-100$ s wachsen könnten. Damit wäre genug Zeit für die Entstehung von Konvektion, da zwischen dem Einsetzen der überstabilen Konvektion im Zentrum, ausgelöst durch Elektroneneinfänge an ^{20}Ne, und dem Kollaps etwa 100 Jahre liegen. Darüber hinaus können wir zeigen, dass es keinen Unterschied macht ein größeres Reaktionsnetzwerk mit zuvor genanntem Satz an modifizieren Reaktionen währen des Neon- und Sauerstoffbrennens zu implementieren, da es keinen Einfluss auf die Entwicklung des Sauerstoff-Neon-Kerns hat, zumindest falls das Brennen in einem thermonuklearen Durchgehen initiiert wurde.

Unter Verwendung von hochauflösenden Sauerstoff-Neon-Kern-Modellen, die ein thermonukleares Durchgehen im Zentrum entwickeln, können wir erste Ergebnisse der mit AGILE-ISDA simulierten Sauerstoffdeflagration vorstellen. Weiterhin demonstrieren wir die Fähigkeit von AGILE-IDSA, selbstkonsistente Elektroneneinfang-Supernova Simulationen durchzuführen. Dies geschieht mit Hilfe des Standard-Vorläuferstern-Modells von Nomoto. Wir möchten darauf hinweisen, dass rechenintensive 3D-Simulationen mit dieser Herangehensweise effizient unterstützt werden können, indem Parameterstudien durchgeführt werden, die eine zielgerichtetere Verwendung von Computerressourcen ermöglichen.

Contents

1 Introduction

Sixty years after the seminal work of Burbidge et al. (1957) and Cameron (1957), we believe to have a profound understanding of how chemical elements heavier than helium are synthesized by nuclear processes in stars (stellar nucleosynthesis) and related explosive events (explosive nucleosynthesis) while hydrogen and helium were formed during the Big Bang at a ratio of 3 to 1 (Big Bang nucleosynthesis). Since then, the interdisciplinary field of nuclear astrophysics—by combining nuclear physics on the smallest scales and astrophysics on the largest scales—aims at improving our understanding of the processes that are responsible for the creation of elements in the universe as we observe them for example in the solar system (Asplund et al., 2009). Progress is made on the one hand by the advancing description of the nuclear processes occurring in the universe—via theory and experiment. And on the other hand, by a better understanding of cosmic phenomena, from computer models as well as the increasing amount and quality of astronomical observations.

In many astrophysical problems, nuclear processes do not only determine the chemical composition but also the dynamical evolution of the system. Hence, the fields of nuclear astrophysics and theoretical astrophysics are closely connected. In particular, this applies to the description of stars. They are not only responsible for the nucleosynthesis of heavy elements but their mere existence depends critically on nuclear reactions. For this reason, it is not surprising that nuclear astrophysics emerged from the question of how the sun produces its energy. The origin of the solar energy source—required to explain why the sun does not collapse due to its own mass—was obscure, before the field of nuclear physics emerged at the turn of the 20^{th} century. The pioneering work of nuclear physicists like Hans Bethe revealed that the sun is releasing energy by fusing four hydrogen atoms into one helium atom with a net energy gain of 26.7 MeV, emitted by photons and neutrinos (Bethe & Critchfield, 1938; Bethe, 1939). As a consequence, stellar structure—with the exception of white dwarfs (WDs, Chandrasekhar, 1931)—and evolution could only be understood, even on the most fundamental level after the discovery of hydrogen burning.

In the field of theoretical astrophysics, one aim has always been to determine the internal structure of stars in coherence with astronomical observations (see e.g. Eddington, 1926; Chandrasekhar, 1939). Unfortunately, stars are giant balls composed of hot and dense plasma, rendering them opaque to light. Despite the fact that millions of stars have been observed, not much is known about their interior. At least in the case of the sun, the observation of neutrinos (see e.g. Haxton et al., 2013) as well as constraints from helioseismology (see e.g. Gizon & Birch, 2005) are able to provide insight into its internal structure. Apart from this, the validity of stellar models can only be directly confronted with observation if they affect the exterior of the star, for example through convective processes that mix chemical elements from the interior into the stellar atmosphere and make them appear in the visible spectrum.

The detailed study of stellar evolution only became feasible with the availability of electronic computers in the early 1960s. It was among the first problems to be tackled in computational astrophysics when it became possible to numerically solve the non-linear system of coupled differential equations governing the evolution of stellar models. The initial computer codes for stellar modeling were developed by Iben & Ehrman (1962); Henyey et al. (1964) and Hofmeister et al. (1964) and results were published shortly thereafter. Since then, the main approach for improving the theoretical understanding of stellar structure and evolution has remained astonishingly similar. Nevertheless, a lot of key ingredients have received important updates over the past years, like stellar opacities, plasma neutrino losses, nuclear reaction rates and the description of convective phenomena, to name just a few.

Physicists and astronomers have always been interested in observing and understanding the cataclysmic explosions that mark the end of the life of certain stars, called supernovae. Because of their enormous luminosity, supernovae were observed already a long time ago. Besides indications that Chinese astronomers observed a supernova in 185 AD (Zhao et al., 2006), a supernova was recorded by multiple astronomers around the world in 1006 AD (Winkler et al., 2003). In 1054 AD, a supernova was seen by Chinese, Japanese as well as Arab astronomers (e.g. Collins et al., 1999). It gave rise to the Crab Nebula (cover picture). It was pointed out for the first time by Baade & Zwicky (1934) that "supernovae represent the transition from ordinary stars to neutron stars". This description has proven to be very accurate for one half of the observed supernovae—core-collapse Supernovae (CCSNe)—which are explosions that follow the gravitational collapse of massive stars to neutron stars (NSs) or black holes (BHs). The other half—thermonuclear supernovae—is attributed to the destruction of WDs in binary systems.

The vast majority of stars do not end their life in a CCSN. Stars that are not massive enough to become gravitationally unstable and collapse, rather develop into WDs, compact stars that are stabilized by the pressure of degenerate electrons. From this bimodality of fates arises the question of where the transition lies between stars that explode as CCSN or those that become WDs. As a consequence, stellar evolution has to follow the life of a star from the beginning of hydrogen burning until the end of its life, in order to correctly predict the stellar remnant. This question is closely related to the topic of this thesis, the evolution of degenerate oxygen-neon stellar cores, as they appear exactly in stars of said transition region.

1.1 Stellar Evolution in a Nutshell

In Woosley et al. (2002) stars are described as "gravitationally confined thermonuclear reactors whose composition evolves as energy is lost to radiation and neutrinos". Star formation left aside, stellar evolution begins with hydrogen burning in hydrostatic equilibrium, where the star will spend the majority of its life, releasing 90% of the total energy that originates in nuclear processes. From this point, the evolution of a star is mainly a function of its initial mass, as illustrated in Figure 1.1, initial composition[1] and rotation. If a star is sufficiently heavy, it will also enter advanced burning stages beyond hydrogen burning that require increasingly higher temperatures to take place. Only if the compression of the stellar material due to its self-gravity is strong enough, the star can enter the subsequent burning stages that burn the following fuel (sorted by operational temperature): hydrogen at 0.02 GK, helium at 0.2 GK, carbon at 0.8 GK, neon at 1.5 GK, oxygen at 2 GK and silicon at 3.5 GK (see e.g. Arnett, 1996).[2]

At the same time, the mass of the stellar core required for advancing to the subsequent burning stage increases as well. This is important to note, because there is a mass limit (called Chandrasekhar mass M_{ch}) beyond which the stellar core becomes gravitationally unstable and collapses:

$$M_{\mathrm{Ch}} \approx 1.456\,(2\langle Y_e\rangle)^2\ \mathrm{M}_\odot{}^3, \tag{1.1}$$

where $\langle Y_e\rangle$ is the average ratio of electrons to nucleons in the core. Notice that already the minimum core mass for initiating carbon burning is very close to M_{Ch}. If a star is more massive than about 11 $\mathrm{M}_\odot$ (massive star), it will proceed through all advanced burning stages and form an inert core of iron-group nuclei. As no energy can be released by fusing the most-strongly bound iron-group nuclei into even heavier elements, the core contracts to densities in excess of 10^9 g cm^{-3} where electrons become increasingly degenerate and represent the dominating source of pressure.[4] At the same time, the lighter

[1] Depending on the generation of the star, it contains an increasing amount of heavy elements ($>{}^4$He)—called metallicity—from previous generations of stars that affect their evolution, for example by catalyzing certain nuclear reactions.

[2] In the context of astrophysical plasma, we will use Kelvin and MeV as a measure of the temperature interchangeably. They are connected via the Boltzmann constant: $1/k_{\mathrm{B}} = 11604.505(20)$ K/eV. Hence, 1 MeV $\equiv 1.1604525 \times 10^9$ K.

[3] Masses of stellar objects are usually given with respect to the mass of the sun. $1\ \mathrm{M}_\odot = 1.98855 \times 10^{33}$ g.

[4] Notice that throughout this thesis, we will make use of the centimeter-gram-second system of units (CGS), whenever astrophysical topics are discussed.

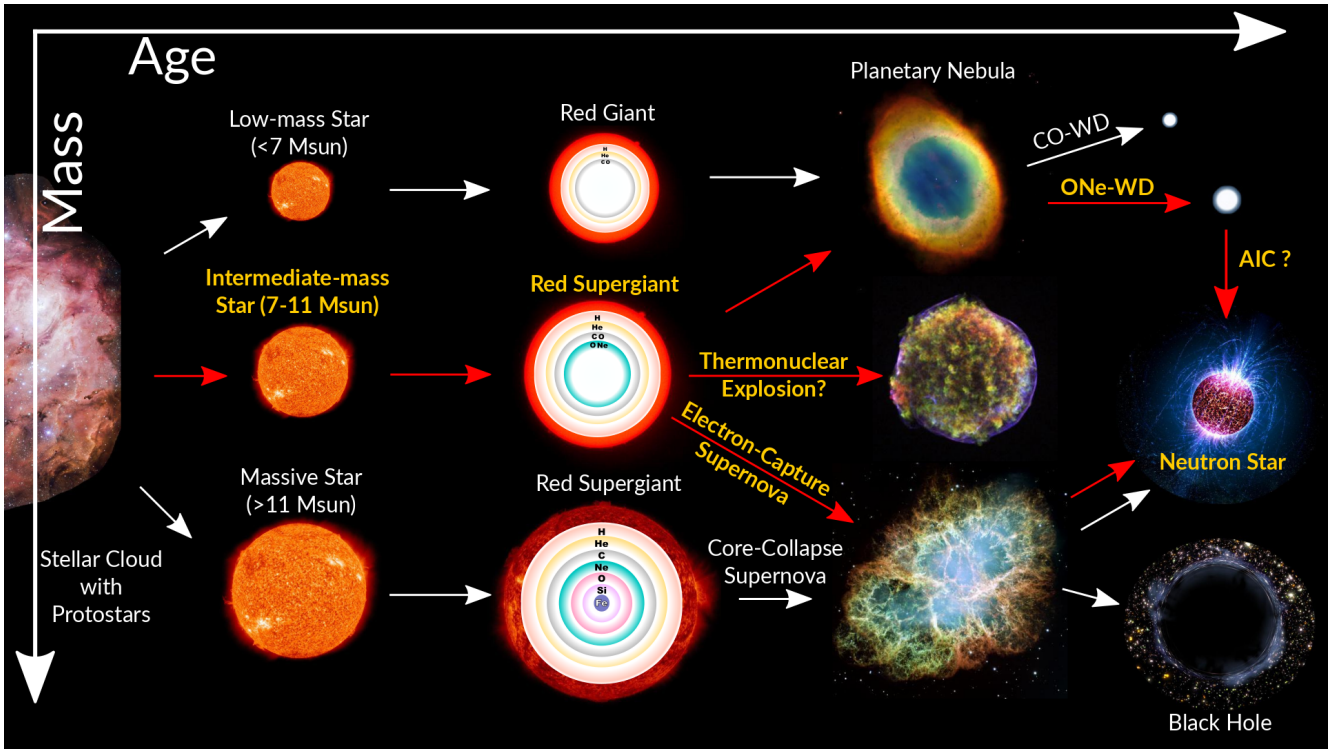

Figure 1.1: Schematic overview of stellar evolution, depending on the initial stellar mass. Low-mass stars ($\lesssim 7\ M_\odot$) ultimately evolve into CO WDs and massive stars ($\gtrsim 11\ M_\odot$) end their live in a CCSN and become NSs or BHs. Intermediate-mass stars (between 7 and 11 $M_\odot$) proceed through carbon burning but fail to ignite the subsequent neon burning stage in their core. They are thought to either become ONe WDs, explode as electron-capture supernova (ECSN) or get destroyed in a thermonuclear explosion due to the oxygen deflagration initiated at the onset of core-collapse. Another path towards the formation of a NS is the accretion-induced collapse (AIC) of ONe WDs.

fuel burns in concentric shells around the core. Due to silicon shell burning, the stellar core will grow and ultimately exceed $M_{\rm ch}$.

Consequently, the star will collapse to nuclear densities and explode as iron-core-collapse supernova (FeCCSN), giving birth to a NS or a BH. This is thought to be the standard evolutionary path for massive stars as indicated by the lower track in Figure 1.1. Low-mass stars, lighter than 7 $M_\odot$, are not massive enough to form an iron core and will lose their outer layers, mainly driven by stellar mass-loss during the asymptotic giant branch phase (AGB), before the core reaches $M_{\rm ch}$ and end up typically as carbon-oxygen WDs. This is indicated by the upper track in Figure 1.1. However, the fate of stars in the transition region between 7 and 11 $M_\odot$ is less clear. These intermediate-mass stars proceed through carbon burning but fail to ignite the subsequent neon-burning stage, implying that they are mainly composed of the carbon burning products oxygen and neon. They are usually referred to as super-asymptotic-giant-branch stars (SAGB) and can either become ONe WDs, explode as electron-capture supernovae (ECSNe) or get destroyed in a thermonuclear explosion due to the oxygen deflagration initiated at the onset of gravitational collapse (see middle track in Figure 1.1). ECSNe are a subtype of CCSNe, which in contrast to FeCCSNe, are not triggered by silicon shell burning, but rather by deleptonizing electron capture (EC) reactions mainly on ^{20}Ne in the dense core that decrease $M_{\rm ch}$ until collapse ensues:

$$(A, Z) + e^- \rightarrow (A, Z-1) + \nu_e. \tag{1.2}$$

It has been speculated that SN 1054, which formed the Crab nebula, had a progenitor star in the range of 8 to 11 $M_\odot$ (Nomoto et al., 1982; Kitaura et al., 2006).

The main characteristic of SAGB stars, which potentially explode as ECSNe, is that they form an electron-degenerate ONe core towards the end of their life, giving rise to a unique evolutionary stage, as lighter stars never reach carbon burning conditions and heavier stars burn carbon under non-degenerate conditions and proceed through the subsequent burning stages of neon, oxygen and silicon burning. This distinct configuration of the stellar core has been subject to research ever since the pioneering work of Miyaji et al. (1980). Earlier studies of similar stars showed an evolution towards central carbon burning in non-degenerate conditions, due to a lack of understanding of neutrino emission processes from the stellar plasma, which was only obtained by Fowler & Hoyle (1964). As it turns out, leptonic neutrino processes are the dominating energy loss mechanism of any star from carbon burning on, leading to more degenerate conditions during the late burning stages than previously anticipated.

1.2 Degenerate Oxygen-Neon Cores

Electron-degenerate ONe stellar cores are composed of the carbon burning ashes ^{16}O and ^{20}Ne, plus some ^{23}Na and ^{24}Mg. Their evolution is initially driven by the balance between compressional heating and cooling by neutrino emission. As the heating is insufficient, they do not reach the critical temperature of 1.5 GK for neon burning and contract, due to the absence of nuclear energy generation, to densities in excess of 10^9 g cm^{-3}. Hence, the core is stabilized mainly by electron degeneracy pressure. Because the central density in the core is continuously growing, it eventually exceeds the threshold for EC from the continuum, first on nuclei with odd mass number. This results in a very efficient cooling mechanism (called Urca process, Tsuruta & Cameron, 1970). Later, also ECs on the even mass number nuclei, i.e. ^{24}Mg and then ^{20}Ne set in, typically releasing considerable amounts of heat. In the extreme-relativistic ultra-degenerate limit, the electron Fermi energy E_F of an electron gas with number density n_e is given by (assuming one electron per two nucleons):

$$E_F = hc\left(\frac{3n_e}{8\pi}\right)^{1/3} \approx 4.1\ \mathrm{MeV}\left(\frac{\varrho}{10^9\ \mathrm{g\ cm^{-3}}}\right)^{1/3}, \tag{1.3}$$

where ϱ is the baryon density. Consequently, at the prevalent conditions, E_F is greater than 4 MeV and eventually large enough to overcome the Q value[5] for the previously mentioned EC reactions (Miyaji et al., 1980). It was further argued that the continuous growth of the ONe core, together with the deleptonization from EC processes, will push the core mass beyond M_{ch} and the core becomes gravitationally unstable. Different from a collapsing iron core, the abundant nuclei in the mass region around $A = 20$ can still release approximately 1 MeV/nucleon of nuclear binding energy by fusion. As a consequence, the heat released by EC on ^{20}Ne will inevitably ignite oxygen burning in the core. Because of the high degeneracy, the burning proceeds in a violent deflagration that transforms the material in the core into iron-group nuclei in a matter of seconds. In the canonical picture, which has not changed since then, the EC-induced deleptonization dominates over the energy liberated during the oxygen deflagration and the star collapses to a NS, marking the standard path towards ECSNe.

Whether and by which means a degenerate ONe core reaches conditions to surpass the threshold energy for EC on ^{20}Ne, depends on the scenario in which they appear. In the canonical SAGB star scenario, the evolution is driven by a growing core due to hydrogen and helium shell burning. As during this phase of evolution the star loses an appreciable mass by stellar winds, it is the competition between core growth and mass loss that determines whether the core of the star can grow sufficiently big to induce gravitational collapse before the whole envelope is shed. In case the mass loss is too high, the SAGB star will end up as an ONe WD, otherwise it will proceed towards an ECSN. Mass-accreting degenerate ONe cores were postulated to appear in other scenarios as well. Nomoto & Kondo (1991)

[5] The ground state-ground state Q value that has to be overcome for the ^{24}Mg-EC is 6.026 MeV and 7.535 MeV for ^{20}Ne (see Section 4.3).

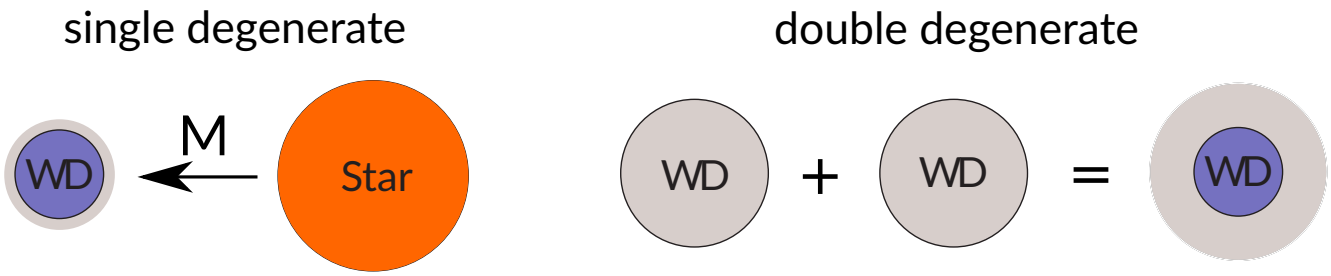

Figure 1.2: Single- and double-degenerate scenarios for the AIC of ONe WDs. The left-hand side depicts the single-degenerate scenario in which an ONe WD in a binary system accrets mass from a companion star, through which the collapse ensues (Nomoto & Kondo, 1991). The right-hand side illustrates the double-degenerate scenario in which the accretion occurs by cooling after a merger of two CO WDs (Saio & Nomoto, 1985).

introduced the accretion-induced collapse scenario (AIC, upper right corner in Figure 1.1), where an ONe WD in a binary system exceeds $M_{\rm ch}$ due to mass accretion from a companion star and explodes in an ECSN as well. Similarly, such a situation may be reached subsequent to a merger of two lighter WDs (Saio & Nomoto, 1985). Both AIC scenarios are illustrated schematically in Figure 1.2. Notice that it was recently concluded by Schwab et al. (2016b) that super-Chandrasekhar-mass WD-merger remnants might not proceed towards an EC-induced collapse, but if the remnant mass stays above $M_{\rm ch}$, a low-mass iron core is formed that collapses to a NS in a FeCCSN. And remnants that loose sufficient mass become massive ONe or Si WDs.

In the seminal work of Miyaji et al. (1980) it was found that the energy released by EC on ^{20}Ne triggers convective fluid motion in the core. As convection can efficiently cool down the central region of the core, the ignition of oxygen is delayed to a density of around 2×10^{10} g cm^{-3}. Unfortunately, one major uncertainty in stellar modeling originates in the poor description of convection—a truly multidimensional phenomenon—in 1D (see Section 2.3.2). Usually, the appearance of convection is determined based on a single criterion (Schwarzschild criterion) that probes whether the temperature gradient of a stratification is too large to be stabilized by radiative energy transport, in which case convective motion will start to appear. Afterwards, in Miyaji & Nomoto (1987) convection was treated differently, taking into account also the stabilizing mean molecular weight gradient (i.e. using the Ledoux criterion for convection). In this case, the ONe core is found to be non-convective all the way until oxygen is ignited. Due to the absence of efficient energy transport by convection, oxygen is ignited at significantly lower densities around 1×10^{10} g cm^{-3}. It was argued by Isern et al. (1991) that the ignition of oxygen at lower densities might not lead to a collapse but rather to a complete disruption of the star in a thermonuclear explosion, possibly leaving behind an iron WD as stellar remnant.

The oxygen-deflagration is an interesting and poorly understood physics problem as such. Very recently, the first 3D hydrodynamic simulations of the oxygen deflagration, for conditions prevalent in degenerate ONe cores, were performed by Jones et al. (2016). It was found that for ignition densities in agreement with Ledoux convection the core does not collapse to NS densities but gets destroyed by the violent oxygen deflagration and leaves behind a bound remnant, while for densities corresponding to Schwarzschild convection the core collapses. Consequently, different from the canonical assumption, the outcome of the competition between deleptonization and oxygen deflagration is far from being known. Only a better understanding of both the pre-ignition phase as well as the oxygen deflagration can answer the question whether ECSNe make NSs, or not. The work presented in this thesis aims to provide valuable input regarding exactly those questions.

1.3 Importance of Understanding Oxygen-Neon Cores

Degenerate ONe cores have been discussed primarily in the context of ECSNe and SAGB star evolution. As a consequence, a main motivation in studying those objects arises from the importance of understanding stars in the 7 to 11 $M_\odot$ range. The classical initial stellar mass function (IMF) of Salpeter (1955) is given by $dN/dM \propto M^{-2.35}$ and suggests that the fraction of stars in the mentioned mass range compared to all stars heavier than 7 $M_\odot$ is approximately 50%.[6] Consequently, the fraction of ECSNe compared to all CCSNe could be rather large as well. Unfortunately, uncertainties in stellar evolution make this number much less certain because it is unclear what fraction of SAGB stars proceeds towards ECSNe and not ONe WDs (see e.g. Poelarends et al., 2008). Hence, the stellar evolution of SAGB stars is an interesting and important topic in its own right. However, detailed studies focusing on their late evolution are sparse, the main reason being uncertainties and caveats that can be avoided when studying both their lighter and more massive counterparts. In particular, during the SAGB phase thousands of thermal pulses (see Section 5.2.2) have to be followed in order to correctly predict the fate of the star (see e.g. Jones et al., 2013).

Knigge et al. (2011) reported on the analysis of X-ray binary systems—a special class of NS-hosting X-ray pulsars. They observed that there is a distinct bimodality regarding their spin periods as well as orbital eccentricities, suggesting that NSs with low orbital eccentricities and spin periods might be remnants of ECSNe, while the others are formed by FeCCSNe. Similarly, Schwab et al. (2010) found a bimodality in the mass distribution of 14 well-known NSs whose masses can be accurately determined. After the conversion to pre-collapse masses (model dependent) they were also suggesting that both populations might originate in the two different CCSN subtypes. Notice that this conclusion is not necessarily supported by the latest results from CCSN modeling (see e.g. Müller, 2016). Additionally, the majority of stars occurs in binary systems where the complex interaction between the stars, i.e. during the common envelope phase, is far from being well understood.

SAGB stars between roughly 9 and 11 $M_\odot$ are thought to be sufficiently massive to proceed towards an ECSN explosion. They are of special importance for the theoretical understanding of the CCSN explosion mechanism as they explode in spherically symmetric supernova models. Such models are still indispensable when sophisticated input physics, like Boltzmann-neutrino transport including a large variety of charged-current and neutral-current weak interactions for all three neutrino flavors, are to be applied. However, only ONe core progenitors explode in one-dimensional neutrino-driven supernova models, whereas it is generally found that iron-core progenitors do not. The canonical pre-ECSN structure is the 8.8 $M_\odot$ ONe(Mg) core progenitor of Nomoto (1984, 1987). Recent simulations by Kitaura et al. (2006); Janka et al. (2008); Fischer et al. (2010) and Möller (2013) demonstrate, that the star explodes in spherically symmetric supernova models.

Especially due to their relatively large abundance, stars in the mass region between 7 and 11 $M_\odot$ are thought to be responsible for the nucleosynthesis of heavy elements, both via the *s*-process (see e.g. Käppeler et al., 2011) and the *r*-process (see e.g. Arnould et al., 2007). It is well established, also from observation, that stars going through the AGB phase (including SAGB) are responsible for the production of *s*-process elements. On the other hand, *r*-process nucleosynthesis has been thought to occur in explosive environments as they are present in CCSNe (Woosley et al., 1994) or the coalescence of NSs (Freiburghaus et al., 1999). ECSNe in particular have been studied extensively as a possible origin of the production of *r*-process elements. But the majority of recent results, especially coming from sophisticated supernova simulations, suggests that ECSNe cannot account for the production of all, especially the heavier, *r*-process elements observed in the solar system. Nucleosynthesis calculations by Wanajo et al. (2011), based on two-dimensional supernova simulations, suggest that ECSNe could

[6] Jennings et al. (2012) studied supernova remnants in the Andromeda galaxy (M31) and indicated that the IMF could be even steeper than the canonical value of Salpeter (1955), rendering the IMF even more bottom heavy.

explain the abundance of elements beyond the iron-peak (Zn, Ge, As, Se, Br, Kr, Rb, Sr, Y and Zr) in the galaxy but typical r-process elements were not produced.

Compared to massive stars, ONe cores in intermediate-mass stars have much higher densities in the same evolutionary stage ($10^9 - 10^{10}$ g cm^{-3} vs. $10^6 - 10^7$ g cm^{-3}). This has various implications regarding the input from nuclear physics as nuclear reactions operate not only at higher densities but also at higher degeneracy. This implies for example that dense plasma effects need to be taken into account for the equation of state (EoS) (Bravo & García-Senz, 1999) as well as weak reaction rates (Schwab et al., 2015). As already said, EC reactions on nuclei in the sd-shell play an important role. At degenerate conditions they are usually dominated by few transitions, making it necessary to calculate the corresponding reaction rates with high accuracy, as otherwise important effects on the stellar evolution might be overlooked entirely (Toki et al., 2013).

1.4 Research Questions and Status of the Field

The relevant research questions regarding the evolution and the fate of degenerate ONe cores can be divided into two categories. First of all, the pre-ignition phase where the uncertainties mainly concern the ignition density of the oxygen deflagration, as well as the stellar evolution modeling of SAGB stars and the question whether the critical density for EC on ^{20}Ne is reached. Secondly, assuming that oxygen is ignited at a certain density in the degenerate ONe core, important research questions are devoted to the propagation of the oxygen deflagration that competes with the gravitational instability. Of course, this is also connected to the question of what the final fate of collapsing ONe cores is—ECSN or thermonuclear explosion.

Pre-ignition phase:

- How large is the probability for ONe cores in SAGB stars to grow beyond $M_{\rm ch}$ and, as a result, what is the ratio of ONe WDs to ECSNe? This question is mainly related to the poorly constrained mass loss during the SAGB phase that competes with the core growth (see e.g. Poelarends et al., 2008). Related to this aspect is also the question of what is the critical initial stellar mass that corresponds to an ONe core exceeding $M_{\rm ch}$. Furthermore it has to be investigated how the critical mass depends on other quantities like metallicity (Doherty et al., 2015).
- Do neon and oxygen burning operate differently at high densities and larger neutron excesses? How important is the ^{20}O made by EC on ^{20}Ne for the evolution of degenerate ONe cores (Möller et al., 2014)? This might be more relevant for the scenario of "failed massive stars", where neon and oxygen burning are ignited off-center prior to gravitational collapse (Jones et al., 2014).
- What is the influence of plasma screening effects both on EC rates as well as the EoS regarding the ignition density (see e.g. Bravo & García-Senz, 1999; Schwab et al., 2015)?
- What is the effect of Urca processes on the thermal evolution of degenerate ONe cores at densities around 2×10^9 g cm^{-3} (Jones et al., 2013; Toki et al., 2013; Denissenkov et al., 2015). Are there differences between SAGB stars and the AIC scenario?
- Determine the influence of EC processes involving ^{24}Mg and ^{20}Ne on the ignition density of oxygen. The ^{24}Mg fraction of ONe cores critically depends on the reaction rates that govern carbon fusion. They final ^{24}Mg abundance has received a significant reduction since the seminal investigations (Gutiérrez et al., 2005; Schwab et al., 2015). A large unknown in the current understanding of ONe cores is related to the second-forbidden transition of the EC on ^{20}Ne (Lam et al., 2014; Martínez-Pinedo et al., 2014; Schwab et al., 2015). This stimulated a determination of the corresponding

transition strength, both experimentally as well as theoretically (Idini et al., 2014; Kirsebom et al., 2017).[7]

- Does convection occur in the degenerate ONe core before the ignition of oxygen? There appears to be a consensus (see Figure 6.4) that applying the Schwarzschild criterion for convection leads to a significantly higher ignition density compared to applying the Ledoux criterion for convection (Miyaji et al., 1980; Miyaji & Nomoto, 1987). In between those two extremes, the occurrence of semiconvection[8] has been suggested (Mochkovitch, 1984), but is far from being well understood. Currently, it seems more likely that convection does not occur (Schwab et al., 2015).

Collapse and deflagration phase:

- In Jones et al. (2016), the authors presented 3D simulations of the oxygen deflagration. It was concluded that models representing the case where semiconvective mixing is efficient prior to ignition show clear signs that the stellar core will collapse to NS densities. However, this appears not to be the case for the preferred assumption of having no convection prior to ignition. In this case, the ONe core is destroyed by the thermonuclear explosion. This strongly suggests to investigate the issue of convection more profoundly.
- The question that has to be answered is whether all degenerate ONe cores collapse and explode in an ECSN. Related is the question of what the lightest stars are that make NSs and if a minimum NS mass can be inferred from stellar evolution and supernova modeling (Lattimer, 2012).
- The ultimate answer to this question can only be given by simulations as in Jones et al. (2016), as many uncertainties related to the hydrodynamic description of the oxygen deflagration remain and have to be addressed in the future. When does the transition occur from the laminar to the turbulent flame regime? How can the results of multidimensional simulations be incorporated into spherically symmetric simulations that are capable of performing exploratory parameter studies.
- How would the deflagration behave for an off-center ignition of oxygen? What is the influence of different flame ignition spots in general, taking into consideration that for the carbon deflagration of WDs, a significant impact was found (see e.g. Fink et al., 2014)?
- What are the uncertainties regarding the EC processes on the (neutron-rich) iron-group material (oxygen-burning ashes) behind the deflagration that quickly deleptonize the core (see e.g. Seitenzahl et al., 2009)? How do they affect the dynamical evolution of the star in the critical phase?

[7] Notice that currently, the transition strength of the ^{20}Ne-EC second-forbidden transition can only be inferred from an experimental upper limit given by Tilley et al. (1998).

[8] Semiconvection is a distinct mode of convection that is thought to occur in regions that are Ledoux stable but Schwarzschild unstable (see Section 2.3.2).

1.5 Thesis Outline

This thesis is organized as follows. In Chapter 2 we will introduce the theoretical background and concepts of stellar structure and evolution. The necessary microphysics will be introduced, specifically for the description of the stellar interior of intermediate-mass stars that form electron-degenerate ONe cores. This includes a discussion of stellar opacity sources, the EoS of degenerate matter, the treatment of convection and a short introduction of corrections arising from Coulomb-interaction effects in dense plasma.

In Chapter 3 we will briefly discuss the nuclear physics concepts that are required for the description of nuclei in astrophysical plasma and reactions among them. Owing to their special relevance for the topic of this thesis, Chapter 4 is devoted to a recapitulation of the various facets in which the weak interaction—EC processes in particular—plays a role for the evolution of degenerate ONe cores, by determining the rate of deleptonization and by releasing or absorbing energy in the stellar plasma.

In Chapter 5 we will review the current understanding of the stellar evolution of stars between 7 and 11 $M_\odot$, as well as the concept of CCSNe with special focus on the explosion of ECSNe.

In Chapter 6 we will present our results regarding the evolution of degenerate ONe cores. We will point out modifications to the standard oxygen and neon burning process at high densities, potentially relevant for the evolution of stars between 7 and 11 $M_\odot$. Then, we will present calculations of the AIC of degenerate ONe cores that were performed with the stellar evolution code MESA and address key uncertainties like the treatment of weak reactions and convection. We will also present preliminary results of modeling the oxygen deflagration in 1D with the CCSN code AGILE-IDSA and demonstrate that it can be used to model ECSNe, based on simulations of Nomoto's canonical 8.8 $M_\odot$ ONe(Mg) progenitor.

Finally, in Chapter 7 we will summarize our results, point out the significance of our findings and pose the relevant questions that should be addressed in future investigations.

2 Basic Concepts of Stellar Structure

In this chapter, we want to introduce the basic concepts required for the theoretical description of stellar structure and evolution. The general discussion will follow the textbooks of Kippenhahn & Weigert (1990) and Weiss et al. (2004). As was already pointed out in the introduction, this thesis will focus mainly on the physics of stars that form electron-degenerate cores, consisting of ^{16}O and ^{20}Ne, that were formed during carbon burning. Hence, topics which are in particular relevant for the understanding of such objects will be treated with special care and in greater detail.

A star is usually described as a self-gravitating, self-luminous objects that has a mass between 10^{-2} to 10^{2} $M_{\odot}$. In Section 2.1, we will examine the nature of stars related to their self-gravity. This will result in the well known stellar structure equations under the assumption of hydrostatic equilibrium. In Section 2.2, an adequate thermodynamic description of the stellar material will be derived, resulting in an EoS that provides a necessary relation between pressure and density in the stellar structure equations. Because stars are also self-luminous objects, the different ways of transporting and producing energy inside stars will be introduced in Section 2.3.[1]

The previous considerations will provide the necessary tools to describe the evolution of stars as a system of coupled differential equations that can be solved numerically (Section 2.4). With the help of this framework, we will be able to qualitatively understand the evolution of stars, with special focus on those that form degenerate ONe cores. This is summarized in the first part of Chapter 5. Furthermore, we follow the evolution of intermediate-mass stars until the point where they will either become WDs or explode in a CCSN. This topic will be dealt with in the second part of Chapter 5.

2.1 Stellar Structure Equations

The stability of stars arises from the the assumption that the gravitational force—due to the stars self-gravity—is balanced at every point inside the star by a sufficient pressure gradient of opposite sign. This balance is usually called hydrostatic equilibrium (or mechanical equilibrium). Consequently, the star will instantly[2] react to any change and enter a state where the pressure gradient counters exactly the influence of all external force fields like gravity. Based on the hydrostatic description, every point in the star is force-free, resulting in a time-independent (i.e. static) configuration of the star. Because of the nature of the gravitational attraction, the star can be described in spherical symmetry leading to the first equation of stellar structure:

$$\frac{dP}{dr} = -G\frac{m(r)\,\varrho(r)}{r^2}, \tag{2.1}$$

where P denotes the pressure, r the radius, ϱ the baryon mass density and m the enclosed mass (i.e. the integrated mass of the star up to radius r). G is the gravitational constant. The baryon mass density can be easily related to the enclosed mass as follows:

$$\frac{dm}{dr} = \varrho(r)\,4\pi r^2. \tag{2.2}$$

[1] Notice that in this context, energy production refers to the amount of energy that is absorbed by the stellar plasma.

[2] In the most general sense, this means that the timescale for the mechanical adaption to a change of the force field happens much faster that any other timescale in the star.

Equations (2.1) and (2.2) are given in the Eulerian form with r as independent variable. In spherically symmetric models, it is however much more convenient to use the the enclosed mass m as an independent variable (Lagrangian form) because local properties of the material like composition are tied to the mass, rather than to spatial coordinates. Consequently, the Lagrangian stellar structure equations are given by:

$$\frac{dP}{dm} = -\frac{Gm}{4\pi r^4}, \tag{2.3}$$

$$\frac{dr}{dm} = \left(4\pi r^2 \varrho\right)^{-1}. \tag{2.4}$$

As stars are luminous, they have to loose energy by radiation. Hence, hydrostatic equilibrium can only be maintained if some process occurs inside the star that provides the energy that is lost on its surface. Such a situation is referred to as a steady-state problem, where the leakage of energy—in this case at the stellar surface—is counterbalanced by an equal source of energy inside. As we will see later, the pressure gradient in Equation (2.1) is maintained mainly by the release of binding energy in nuclear reactions.

As a consequence, whenever energy production and loss are not in equilibrium, the star is expected to change its structure. If that is the case, the concept of hydrostatic equilibrium has to be abandoned and the star has to be described by hydrodynamic equations where besides the directional derivatives, also time derivatives of physical quantities appear in the governing equations. As it turns out, for most phases of stellar evolution, the structural changes are much slower compared to the timescale for hydrostatic equilibrium and hence this concept can still be applied.

2.2 Equation of State of Stellar Interior

In order to solve the stellar structure equations (2.3) and (2.4), it is first of all necessary to provide a third equation that relates at least two of the three unknowns P, ϱ and m with each other in order to make the system of equations determined. This can be achieved by providing an equation of state (EoS) that gives a relationship of the pressure as a function of the density $P(\varrho)$.

By describing the stellar matter as a sum of different statistical ensembles of identical particles in local thermal equilibrium, it is possible to derive simple expressions that relate the matter and radiation content of the star to macroscopic quantities, like pressure and kinetic energy. In this context, thermal equilibrium means that an ensemble within a sufficiently small region of the star can be assigned one definite temperature T, hence it has to contain enough particles of whichever kind, allowing for the application of the well known relations of statistical mechanics. Both conditions are easily fulfilled in stars. Local thermal equilibrium has the advantage that the ambient pressure can be related to the equilibrium distribution function of the different particles that contribute to it. The thermodynamic state of a star can usually be described by the presence of nuclei, electrons & positrons and photons. Neutrinos produced during weak processes, are in most cases assumed to be non-interacting and simply represent an energy sink in the star. Of course, as we will discuss in Section 5.4, this is not true for densities that are present in the center of a massive star, during and after its gravitational collapse.

Hence, the EoS is not only describing the relationship $P(\varrho)$ but also the composition of matter in a mixture of different particle species that each follow their own distribution function, characterized by the same temperature, assuming that all particle species are in local thermodynamic equilibrium. This suggests the following more generic definition for an EoS:

$$(T, \varrho, \text{Composition}) \overset{\text{EoS}}{\Longleftrightarrow} (P, e, s, \dots), \tag{2.5}$$

where s denotes the specific entropy and e the specific energy. In this example, the left-hand side defines the input of the EoS and the right-hand side the output, which is rendered by the EoS. Of course, it

is also possible to use a different set of independent variables for the EoS. Notice that in this chapter, the specific (kinetic) energy e will be defined as the energy per unit mass (erg/g) in order to give an expression that does not change trivially during compression or expansion. The total energy E and the specific energy e are related in the following way: $e = E/(V\varrho)$, where V is the volume. Unfortunately, depending on the reference, the specific energy can have a slightly different definition. Sometimes it denotes the energy per volume E/V, or the energy per baryon $Em_u/(V\varrho)$.

2.2.1 Equation of State of "Dilute" Matter in Stars

The vast majority of stellar matter is sufficiently "dilute" that it can be described as a non-interacting gas. Of course that does not mean that the ions cannot react with each other in "chemical processes", where particles are created or destroyed. Additionally, we will relax this assumption to some extent in Section 2.2.1 and introduce plasma screening corrections to the EoS based on the Coulomb interaction among electrons and charged ions that appear at sufficiently high electron densities.

If matter is even denser, nuclei will eventually become densely packed and start to be affected by the strong interaction (and eventually also become degenerate). Then, a more sophisticated nuclear EoS has to be employed. This will be briefly discussed in Section 2.2.2, as these conditions are met in CCSNe prior to the formation of a NS. By comparing the average distance between nucleons and the range of the strong force, we can roughly define the transition between "dilute" and "dense" matter at 10^{13} g cm^{-3}. Hence, for all aspects of stellar evolution, it is safe to say that ions are sufficiently far apart to be regarded as non-interacting. Additionally, free neutrons and protons do not exhibit their quantum nature, meaning that they can be treated in the non-degenerate limit.

In the case of non-interacting or weakly-interacting gas components, all intensive thermodynamic quantities can be computed by summing up their individual contributions. First of all, the plasma consists of a multitude of ions that can be described by an ideal Boltzmann gas (non-degenerate and non-relativistic). In order for substantial parts of the ions to become relativistic, the temperature has to exceed at least 10^{11} K, something that is never reached during regular stellar evolution. For electrons and positron however, we have to take into account that they can appear with arbitrary degeneracy and relativity for the conditions of interest. Photons can be treated as black body radiation. Thus, the total pressure P is given by:

$$P_{\text{total}} = \sum_i P_{\text{Ion,i}} + P_{\text{ele}} + P_{\text{pos}} + P_\gamma, \tag{2.6}$$

where i runs over all different nuclear species. One additionally simplifying assumption is that all atoms are fully ionized. Because of this constraint, the matter that we want to describe should be hotter than roughly 10^{5-6} K.[3] This is the case for the stellar interior that we study throughout this thesis. Notice that the assumption of local thermodynamic equilibrium implies that all gas constituents i.e ions, electrons/positrons and photons have to thermalize sufficiently fast to be well described by their equilibrium properties. Because of this, the validity of such an EoS will be limited at very low densities. The lower limit will be around 1 g cm^{-3}.

If we are interested in finding the thermodynamically most favorable state in a local volume with certain thermodynamic observables, the principle of minimum energy can be used. It follows directly from the second law of thermodynamics and states that for a closed system at constant temperature T and volume V the Helmholtz free energy F is minimized in thermal equilibrium. In this context, a closed system is a system that can exchange heat but not particles with its surrounding. F is defined as follows:

$$dF(T,V,N_i) = -SdT - PdV + \sum_i \mu_i dN_i. \tag{2.7}$$

[3] The actual degree of ionization depends also on the ambient density due to the effects of pressure ionization.

F is related to E via $F = E - TS$. For the specific free energy f, we easily see that the external variables that characterize our system become $f(T, \varrho, X_i)$, exactly as we introduced in Equation (2.5). The free energy can be also written as the sum of all of its contributions:

$$F_{\text{total}} = \sum_i F_{\text{Ion,i}} + F_{\text{ele}} + F_{\text{pos}} + F_\gamma. \tag{2.8}$$

Abundance and Mass Fraction

Before describing the thermodynamic state of the stellar plasma and in particular that of the ions, it will prove helpful to introduce some concepts that relate the abundance of different isotopes to global properties of the ion gas. This will significantly facilitate the discussion of matter inside stars that is possibly made of hundreds of different nuclear species. First of all, the concept of abundances will be introduced. As the net baryon number (matter - antimatter) is strictly conserved by all interactions, we know that inside a star, the total number of nucleons N_{nucleon} is constant. For this reason, we can introduce the total number density of nucleons (or equivalently baryons) n_{nucleon} which is given by:

$$n_{\text{nucleon}} = \sum_i n_i A_i, \tag{2.9}$$

where n_i is the number density of nuclear species i. Then, the approximation is made, that the total mass of a stellar gas is given by the mass of its charge neutral atoms. Hence, the total mass density ϱ can be related to the number density of the ions n_i, by multiplication with the atomic mass. In this way, the rest mass of the electrons in a charge neutral plasma will be accounted for as well, independent of whether they are bound in an atom or not. It follows that:

$$\varrho \approx n_{\text{nucleon}} m_u = m_u \sum_i n_i A_i. \tag{2.10}$$

The approximation that we just introduced assumes that the weight of an arbitrary ion i is approximately given by $A_i/12$ times the weight of a ^{12}C atom, where A_i is the number of nucleons in the atom considered. In this way, m_u is equivalent to the definition of the unified atomic mass unit (AMU). Of course, assuming that all nuclei have the same nuclear binding energy per nucleon as a ^{12}C atom introduces an (relative) error, usually smaller than 10^{-3}. Now, we introduce an expression for the occurrence of different nuclear species that is independent from the ambient density ϱ, defined as the abundance Y:

$$Y_i = \frac{n_i}{n} = n_i \frac{m_u}{\varrho}. \tag{2.11}$$

The advantage of the definition of the abundance is that the dependence on the ambient density ϱ is factored out in Y and hence, Y remains constant for trivial thermodynamic changes like compression or expansion. Only reactions that explicitly change the particle number of a given nuclear species, will change the abundance. The same is true for processes that mix material of different composition with each other like diffusion or convection. Notice that in the literature, a different definition for the abundance is used quite often, which is better described by the term molar fraction:

$$Y_i = \frac{n_i}{n} = n_i \frac{1}{N_A \varrho}, \tag{2.12}$$

where N_A is the Avogadro constant and hence Y_i will have units of mol g^{-1}. In this case, number and mass density would be related in the following way:

$$n_i = \varrho_i \frac{N_A}{M_i}, \tag{2.13}$$

where M_i is the molar mass. The basic difference in both schemes comes about by using either mass or the number of particles as a reference. Abundance and molar fraction become only equivalent by assuming $M_i \cong A_i$. Furthermore, by using the definition of the abundance as the number fraction of an isotope as given by Equation (2.11), Y_i is conveniently unitless.

In analogy to the abundance, it is useful to introduce a quantity called mass fraction X, that relates the ion mass density ϱ_i to the total mass density ϱ of all ions, rather than the number fraction to the total particle number. Consequently, it is defined in the following way:

$$X_i = \frac{\varrho_i}{\varrho} = \frac{n_i A_i m_u}{\varrho} = Y_i A_i. \tag{2.14}$$

Then, nucleon number conservation implies that:

$$\sum_i Y_i A_i = \sum_i X_i = 1. \tag{2.15}$$

Notice that in the context of stellar physics, it is common to define $X_{\text{hydrogen}} = X$ and $X_{\text{helium}} = Y$ so that it follows:

$$X + Y + Z = 1, \tag{2.16}$$

where Z is called metallicity and is the combined mass fraction of all isotopes heavier than ^{4}He:

$$Z = \sum_{i>\text{He}} X_i. \tag{2.17}$$

Another assumption usually made, is that of a charge neutral plasma, implying that the number of protons N_p has to be equal to the net number of electrons $N_{ele,net} = N_{ele} - N_{pos}$. In other words, at each point in the star, it is required that $n_e = \sum_i n_i Z_i = n \sum_i Y_i Z_i$. If we now introduce the electron abundance Y_e (usually called net electron fraction) in the same way as we introduced Y_i previously, we get $Y_e = \frac{n_e}{n}$. This yields:

$$Y_e = \sum Y_i Z_i. \tag{2.18}$$

Now, we also want to define average quantities of the plasma. A very useful definition in this context is the average weight of the ions, given by:

$$\langle A \rangle = \mu_{\text{Ion}} = \left(\sum_i X_i / A_i \right)^{-1}. \tag{2.19}$$

This quantity is often called mean molecular weight of the ions or average nuclear mass. Notice that μ is usually defined in textbooks including electrons. The mean molecular weight of only the electrons is given by:

$$\mu_{\text{ele}} = \left(\sum_i \frac{X_i Z_i}{A_i} \right)^{-1}, \tag{2.20}$$

hence the total mean molecular weight μ is given by:

$$\mu = \left(\sum \frac{X_i (1 + Z_i)}{A_i} \right)^{-1}. \tag{2.21}$$

μ^{-1} simply determines the amount of particles of any kind (i.e. atoms, ions, electrons minus positrons) per baryon. As we will need this later as well, we also define the mean molecular charge of the total ion content in the star as:

$$\langle Z \rangle = \langle A \rangle \sum_i X_i \frac{Z_i}{A_i}, \tag{2.22}$$

where Z_i is the charge number of the ith ion. This leads to another very useful relation:

$$Y_e = \langle Z \rangle / \langle A \rangle \tag{2.23}$$

If a certain particle species is in local thermal equilibrium, it is often possible to find a simple relation that describes the distribution function of kinetic energies associated with the particle. It is well known from statistical mechanics that in thermodynamic equilibrium, the particle number N per energy interval $(E, E + dE)$ for a non-interacting particle-species can be expressed as follows:

$$dN = \frac{dg}{e^{-\eta + E/k_B T} \pm 1}, \tag{2.24}$$

where dg is the number of possible quantum states (statistical weight), a particle species can have in the energy range $(E, E + dE)$. Here, E is the total energy, hence the kinetic energy plus the particles rest mass. In the case of discrete energy levels like in a nucleus, g can be easily specified. A nucleus with angular momentum quantum number J has $2J + 1$ states that are degenerate in energy, implying that $g = 2J + 1$. The "continuous" statistical weight dg of a free particle in a large box of volume V is given by:

$$dg = g_{\text{discrete}} \cdot V \cdot \frac{p^2 dp d\Omega}{h^3}, \tag{2.25}$$

where g_{discrete} is the discrete statistical weight, p is the momentum and h^3 is the volume of a unit cell in phase space. Hence, the integral over dg determines the number of allowed quantum states in the volume V. For an isotropic distribution—as is the case here—the number density of particles follows from Equations (2.24) and (2.25) and is given by:

$$n = \int_0^\infty \frac{g_{\text{discrete}} \cdot 4\pi p^2}{h^3 \left(e^{-\eta + E(p)/k_B T} \pm 1\right)} dp, \tag{2.26}$$

where kinetic energy and momentum are related in the usual way: $E_{\text{tot}} = mc^2 \left(1 + p^2 m^{-2} c^{-2}\right)^{1/2}$. The positive sign in Equation (2.24) refers to fermions with half-integral spin like electrons, positrons, protons, neutrons or neutrinos. In general, such particles have to be described by Fermi-Dirac statistics. The negative sign refers to bosons, which are particles with integral spin like photons, that have to be described in general by Bose-Einstein statistics. η is the degeneracy parameter, which is given by $\mu/k_B T$, where μ is the chemical potential, which throughout this thesis will be consistently defined including the particles rest mass, unless stated otherwise. Hence in the non-relativistic limit, the rest mass of the particle is irrelevant for the term $E - \mu$ that appears in the exponent of the distribution function.

The physical meaning of the chemical potential is not obvious, but it is related to an energy that is required to add a particle to the thermodynamic system at constant entropy and volume ($\mu = \partial E / \partial N|_{S,V}$). For a dilute system, well described by an ideal gas, the chemical potential will always be negative. This is the case, because adding particles to such a system will always increase the number of accessible states. Thus, in order for the entropy to remain constant, the energy per particle of the system has to be reduced at the same time, implying a negative chemical potential. For a degenerate Fermi gas however, the chemical potential will be positive. Assuming a system at zero temperature, all energy levels up to the Fermi energy E_f are occupied by particles and the entropy is zero as there is only one possible microstate. Adding another particle to the system will consequently cost exactly the energy of the first unfilled state, while the entropy remains zero. It follows that $\mu = E_f$.

Coming back to the distribution function, if $\eta \ll -1$ then the system is said to be non-degenerate. In that case, Equation (2.24) can be simplified to:

$$dN = dg e^{\eta} e^{E/k_b T}. \tag{2.27}$$

Thus, the description of the system simplifies to a "classical" Maxwell-Boltzmann distribution, where quantum effects and thereby also the distinction between bosons and fermions disappear. If $\eta \gg 1$ then the system is said to be highly degenerate. As we already mentioned, conditions where electrons become highly degenerate can be achieved easily in stars (e.g. WDs).

In the following sections, it will be the goal to derive expressions for the pressure and the specific energy (in units of erg g^{-1}) for the different components in our plasma, based on their distribution function.

Ions

The first component of the plasma that we want to describe are the ions, well described by Boltzmann statistics in the classical limit of non-relativistic and non-degenerate particles. This means that $m_{\text{Ion}} \ll E - \mu \ll k_B T$. In general, the pressure P and the particle number N for non-interacting bosons or fermions in statistical equilibrium are given by:

$$PV = k_B T \ln Z = k_B T \sum_k G_k \ln\left[1 \pm e^{(\mu - E_k)/k_b T}\right]^{\pm 1}, \tag{2.28}$$

$$N = \left(\frac{\partial PV}{\partial \mu}\right)_{T,V} = \sum_k \frac{G_k}{e^{(-\mu + E_k)/k_B T} \pm 1}. \tag{2.29}$$

Here, Z is the grand partition function as given above and G_k is the product of the discrete and continuous statistical weights as introduced in Equation (2.25). k sums over all energy states E_k of the particle species, the "+" sign corresponds to fermions and the "-" sign corresponds to bosons. If we now assume that the ions that we want to describe are non-degenerate, meaning that $E_k - \mu \ll k_B T \ \forall \ k$, Equations (2.28) and (2.29) simplify to:

$$PV = k_B T e^{\mu/k_B T} \sum_k G_k e^{-E_K/k_B T}, \tag{2.30}$$

$$N = e^{\mu/k_B T} \sum_k G_k e^{-E_K/k_B T}. \tag{2.31}$$

By combining both equations, the well known ideal gas law can be easily obtained:

$$PV = N k_B T, \tag{2.32}$$

which can be expressed in terms of the number density n_i of a given ion species i:

$$P_i = n_i k_B T. \tag{2.33}$$

Hence, the total ion pressure is simply given by:

$$P_{\text{Ion}} = k_B T \sum_i n_i, \tag{2.34}$$

where i sums over all nuclear species. Now, we can make use of the relations obtained in Section 2.2.1 and eliminate the sum over the different ion species:

$$P_{\text{Ion}} = k_B T \sum_i n_i, \tag{2.35}$$

$$= k_B T \frac{\varrho}{m_u} \sum_i Y_i, \tag{2.36}$$

$$= k_B T \frac{\varrho}{m_u} \frac{\sum_i X_i/A_i}{\sum_i X_i}, \tag{2.37}$$

$$= \frac{k_B \varrho}{m_u \langle A \rangle} T. \tag{2.38}$$

In the case of monoatomic molecules, the ions have only three translational degrees of freedom and the specific kinetic energy per unit mass is given by:

$$e_{\mathrm{Ion,kin}} = \frac{3}{2}\frac{P_{\mathrm{Ion}}}{\varrho} = \frac{3k_B}{2m_u\langle A\rangle}T. \tag{2.39}$$

The chemical potential for an individual ion species is given by:

$$\mu_{\mathrm{Ion}} = m_u c^2 A_{\mathrm{Ion}} + k_B T \ln\left(\frac{n_{\mathrm{Ion}}h^3}{(2\pi A_{\mathrm{Ion}} m_u k_B T)^{3/2}}\right). \tag{2.40}$$

Photons

The photon gas can be perfectly described by the emission and absorption characteristics of a black body in thermal equilibrium, as the photons are continuously scattered, absorbed and re-emitted by the ambient matter. In this context, it is important to note that the photon number is not conserved because the absorption and re-emission of a nucleus can occur via a different number of photons. This directly implies that for a photon gas, the chemical potential μ as well as the degeneracy η have to be zero by definition. Thus, the photons can be characterized by their black body pressure P_{rad} which is given by:

$$P_{\mathrm{rad}} = \frac{8\pi^5 k_B^4}{45c^3h^3}T^4 = \frac{1}{3}aT^4, \tag{2.41}$$

where a is the radiation constant. The specific radiation energy is given by:

$$e_{\mathrm{rad}} = \frac{3P_{\mathrm{rad}}}{\varrho} = \frac{aT^4}{\varrho}, \tag{2.42}$$

and the specific entropy is given by:

$$S_{\mathrm{rad}} = \frac{e_{\mathrm{rad}}}{T} + \frac{P_{\mathrm{rad}}}{T\varrho} = \frac{4}{3}\frac{aT^3}{\varrho} \tag{2.43}$$

Electrons and Positrons

The description of the ion and photon gas for the conditions that we are interested in, is rather trivial. However, this is not true for electrons and positrons and related to the fact, that they are neither non-degenerate, non-relativistic nor non-interacting. Hence, none of the the previously introduced simplifications can be applied. As a consequence, the appropriate formalism has to allow for a relativistic description of electrons (as $m_e \approx k_B T$, they are also not extreme relativistic) as well as for an arbitrary degree of degeneracy η. If electrons and positrons are degenerate, their quantum effects will play a role and they must obey Pauli's exclusion principle, limiting the maximum number of electrons and positrons per unit cell in phase space with volume h^3 to g_{discrete}, which for unpolarized electrons is 2. In a degenerate gas, a considerable amount of these unit cells is filled with particles and is thereby blocking this volume for other identical particles to occupy. Clearly, we expect this blocking to be more pronounced for higher electron densities and less pronounced for higher temperatures, where the amount of accessible microstates in the phase space volume will be larger.

There are several textbooks that describe the thermodynamic properties of an electron-positron gas. An excellent source is in particular Chapter 24 in Weiss et al. (2004). Starting from Equation (2.26), the

number density for electrons and positrons can be expressed as a function of temperature and degeneracy $n_{\mathrm{ele/pos}}\left(T, \eta_{\mathrm{ele/pos}}\right)$:

$$n_{\mathrm{ele/pos}} = \int_0^\infty \frac{8\pi p^2}{h^3} \left\{ \exp\left[-\eta_{\mathrm{ele/pos}} + \frac{m_e c^2}{k_B T} \left(\sqrt{1 + \frac{p^2}{m_e^2 c^2}} - 1 \right) \right] + 1 \right\}^{-1} dp. \tag{2.44}$$

In order to solve above expression in an numerically efficient way, we will introduce a different set of variables x and β.[4] They are given by: $x = E/k_B T$ and $\beta = k_B T/m_e c^2$. Additionally, we will assume that the thermal production of electron-positron pairs via $\gamma \leftrightarrows e^- + e^+$ is in equilibrium. For that reason, it follows directly that: $\mu_{\mathrm{ele}} + \mu_{\mathrm{pos}} = 0$. Notice that, as is done in many references like Timmes & Arnett (1999); Timmes & Swesty (2000), we introduce a "kinetic" or bare electron/positron chemical potential without the electron rest mass, given by: $\mu_{\mathrm{ele/pos,bare}} = \mu_{\mathrm{ele/pos},b} - m_e c^2$. Consequently, $\eta_{\mathrm{ele/pos,bare}}$ are related as follows:

$$\eta_{\mathrm{ele,bare}} = -\eta_{\mathrm{pos,bare}} - 2\beta. \tag{2.45}$$

By using $\eta \equiv \eta_{\mathrm{ele,bare}}$ and rewriting Equation (2.44) in terms of x and β, we find:

$$n_{\mathrm{ele}} = \frac{8\pi\sqrt{2} m_e^3 c^3 \beta^{3/2}}{h^3} \left[F_{1/2}(\eta, \beta) + F_{3/2}(\eta, \beta) \right], \tag{2.46}$$

$$n_{\mathrm{pos}} = \frac{8\pi\sqrt{2} m_e^3 c^3 \beta^{3/2}}{h^3} \left[F_{1/2}(-\eta - 2/\beta, \beta) + \beta F_{3/2}(-\eta - 2/\beta, \beta) \right], \tag{2.47}$$

where $F_k(\eta, \beta)$ is the Fermi-Dirac integral that can be efficiently solved numerically and is given by:

$$F_k(\eta, \beta) \int_0^\infty \frac{x^k (1 + 1/2\beta x)^{1/2}}{\exp(x - \eta) + 1} dx. \tag{2.48}$$

Hence, the lepton number density is given as a function of temperature and degeneracy: $n_{\mathrm{ele/pos}}(T, \eta)$. While the temperature is obviously known, in most applications η has yet to be determined. For this reason, we will relate the net electron density $n_{\mathrm{ele,matter}}$ to the ion density ϱ assuming charge neutrality and complete ionization. In this way, we are subtracting thermally produced electron-positron pairs and ensure lepton number conservation. Using the relations from Section 2.2.1, we find:

$$n_{\mathrm{ele,matter}} = n_{\mathrm{ele}} - n_{\mathrm{pos}} = \sum_i Z_i n_i = \frac{\varrho}{m_u} \sum_i \frac{Z_i X_i}{A_i} = \frac{\varrho}{m_u} \frac{\langle Z \rangle}{\langle A \rangle} = \frac{\varrho}{m_u} Y_e, \tag{2.49}$$

where $n_{\mathrm{ele/pos}}$ is the total electron or positron density including thermally produced pairs. Consequently, η can be recovered by combining Equations (2.46) - (2.47) together with (2.49), to obtain:

$$\frac{\varrho}{m_u} Y_e \frac{h^3}{8\pi\sqrt{2} m_e^3 c^3 \beta^{3/2}} = \left[F_{1/2}(\eta, \beta) + F_{3/2}(\eta, \beta) - F_{1/2}(-\eta - 2/\beta, \beta) - \beta F_{3/2}(-\eta - 2/\beta, \beta) \right], \tag{2.50}$$

which yields η by numerically inverting above expression for given conditions $\{\varrho, Y_e, \beta\}$. Once η is known, n_{ele} and n_{pos} can be easily computed via Equation (2.46) and (2.47).

[4] Only in a few special cases like $T = 0$, the integral over the lepton momentum p can be solved explicitly.

Now, it is possible to obtain additional useful quantities by applying the standard thermodynamic relations. Hence, pressure and specific energy of electrons and positrons are given by:

$$P_{\mathrm{ele}} = \frac{16\pi\sqrt{2}m_e^4c^5\beta^{5/2}}{3h^3}\left[F_{3/2}(\eta,\beta)+\frac{\beta}{2}F_{5/2}(\eta,\beta)\right], \tag{2.51}$$

$$P_{\mathrm{pos}} = \frac{16\pi\sqrt{2}m_e^4c^5\beta^{5/2}}{3h^3}\left[F_{3/2}(-\eta-2/\beta,\beta)+\frac{\beta}{2}F_{5/2}(-\eta-2/\beta,\beta)\right], \tag{2.52}$$

$$e_{\mathrm{ele}} = \frac{8\pi\sqrt{2}m_e^4c^5\beta^{5/2}}{\varrho h^3}\left[F_{3/2}(\eta,\beta)+\beta F_{5/2}(\eta,\beta)\right], \tag{2.53}$$

$$e_{\mathrm{pos}} = \frac{8\pi\sqrt{2}m_e^4c^5\beta^{5/2}}{\varrho h^3}\left[F_{3/2}(-\eta-2/\beta,\beta)+\beta F_{5/2}(-\eta-2/\beta,\beta)\right]+\frac{2m_ec^2n_{\mathrm{pos}}}{\varrho}. \tag{2.54}$$

Remember that in all above expressions, $\eta \equiv \eta_{\mathrm{ele,bare}}$, as defined in Equation (2.45).

Choice of EoS

For the purpose of stellar evolution, a great variety of EoSs is available. Most of them describe matter in a very similar fashion, to what we discussed in the previous sections regarding ions, photons, electrons and positrons. In this case, Equation (2.5) reads as follows:

$$(T,\varrho,\langle A\rangle,\langle Z\rangle) \overset{\mathrm{EoS}}{\Longleftrightarrow} (P,e_{\mathrm{therm}},s,\dots), \tag{2.55}$$

where $\langle A\rangle$ denotes the mean atomic weight, $\langle Z\rangle$ the mean atomic charge of all nuclei and e_{therm} is the specific thermal energy, which is given by:

$$e_{\mathrm{therm}} = e_{\mathrm{Ion,kin}}(T,\langle A\rangle)+e_{\mathrm{rad}}(\varrho,T)+e_{\mathrm{ele+pos}}(T,\varrho,Y_e). \tag{2.56}$$

Notice that the compositional information given by the individual mass fractions X_i can be reduced to the mean atomic weight $\langle A\rangle$ and the mean atomic charge $\langle Z\rangle$ if one is only interested in the specific thermal energy. The total specific rest mass e_{rest} of the plasma consistent with the approximations made in Equation (2.10), is given by:

$$e_{\mathrm{rest}} = \frac{m_uc^2n_{\mathrm{baryon}}}{\varrho} = c^2. \tag{2.57}$$

Remember that the net rest mass energy of the electrons $\left(n_{\mathrm{ele}}-n_{\mathrm{pos}}\right)m_ec^2$ as well as the nuclear binding energy per baryon of ^{12}C are included in m_u. Additionally, the rest mass of the thermally produced electron-positron pairs is included - by choice - in the kinetic energy of the positrons in Equation (2.54). Hence, in order to obtain the total internal energy e_{int}, we still need to correct the energy by the average mass excess of the specific composition, which yields:

$$e_{\mathrm{int}} = e_{\mathrm{therm}}+c^2+\frac{c^2}{m_u}\sum_i\Delta_i\frac{X_i}{A_i}. \tag{2.58}$$

A recent tabulation of Δ_i can be found in Wang et al. (2012). Hence, in order to calculate the correct total energy, it is necessary to know the exact composition of nuclei X_i, which is not surprising as is it exactly the change in binding energy by nuclear reactions that determines the thermodynamic state of the plasma. Then Equation (2.5) reads:

$$(T,\varrho,X_i) \overset{\mathrm{EoS}}{\Longleftrightarrow} (P,e_{\mathrm{int}},s,\dots), \tag{2.59}$$

where X_i are the mass fractions of all nuclei that are considered in the calculation.

Among those EoSs that are compared for example in Timmes & Arnett (1999), the Timmes EoS has the highest accuracy, as it calculates the non-interacting electron-positron EoS without using approximations. As was explained in Section 2.2.1, the lepton contribution to the mixture of particles requires the largest computational effort, because it is necessary to solve $\approx 10^2$ Fermi-Dirac integrals per EoS call. Therefore, it is helpful to construct an approximate EoS that is in good agreement with the Timmes EoS, but at the same time executes much faster. It turns out that for most purposes in stellar evolution, the Helmholtz EoS is the best choice (Timmes & Swesty, 2000). It is based on the Timmes EoS and uses the same equations for the photon and ion part of the EoS. While the Timmes EoS computes the electron-positron gas with no approximations, the Helmholtz EoS routine relies on an EoS table for the lepton part that was computed based on the results obtained with the Timmes EoS. This table is then used in the actual astrophysical simulation together with an efficient interpolation scheme to obtain the required thermodynamic variables and derivatives. Both the Timmes EoS and the Helmholtz EoS can be obtained online (Helmholtz-EoS, 2017). Notice that the Helmholtz EoS is employed for the computations that rely on MESA, as well as the calculations based on AGILE in Chapter 6.

EoS Coulomb Corrections

The degenerate ONe cores that we study in this thesis contain a highly degenerate electron gas. In such conditions, the plasma coupling can become large as well. This makes it necessary to account for the Coulomb interaction among electrons and ions, introducing a non-negligible correction term in the EoS. Then—by definition—the electrons and ions can no longer be correctly described by non-interacting gas statistics, as has to be assumed when applying Fermi-Dirac statistics for electrons or Boltzmann statistics for ions.

The quantification of the interaction effects on the EoS are described in detail in Yakovlev & Shalybkov (1989). The importance of Coulomb corrections for a specific charged particle species in a plasma can be determined by the so-called plasma coupling parameter Γ, defined as the ratio between the Coulomb energy and thermal energy. In the case of $\Gamma > 1$, the plasma is said to be strongly coupled and in case $\Gamma < 1$, it is said to be weakly coupled. For ions with charge Z_i, Γ_i is given by:

$$\Gamma_i = \frac{E_{\text{Coulomb}}}{E_{\text{thermal}}} = \frac{Z_i^2 e^2}{a_{\text{ion}} k_B T}, \tag{2.60}$$

where a_{ion} is the mean distance between two ions and e is the elementary charge. For electrons, the coupling parameter is given by:

$$\Gamma_e = \frac{e^2}{a_e k_B T}, \tag{2.61}$$

where a_e is the mean distance between electrons (also called electron sphere radius), given by $a_e = (4\pi n_e/3)^{-1/3}$. By assuming that every ion with charge Z is surrounded by Z electrons, we can easily relate their number densities and find:

$$\Gamma_i = Z_i^{5/3}\Gamma_e = \frac{Z_i^{5/3} e^2}{(3/(4\pi n_e))^{1/3} k_B T}. \tag{2.62}$$

In a multicomponent plasma with a lot of different nuclear species, it can be useful to define the average ion coupling parameter $\langle\Gamma_{\text{ion}}\rangle$ as:

$$\langle\Gamma_{\text{ion}}\rangle = \Gamma_e \cdot \langle Z^{5/3}\rangle = \frac{\langle Z^{5/3}\rangle e^2}{(3/(4\pi n_e))^{1/3} k_B T} = \frac{\langle Z\rangle^2 e^2}{k_B T}\left(\frac{4\pi\varrho}{3 m_u \langle A\rangle}\right)^{1/3}. \tag{2.63}$$

By using $\langle\Gamma_{\rm ion}\rangle$, a multicomponent plasma will be represented by a one-component plasma with a single representative ion species that carries average properties via $\langle Z\rangle$ and $\langle A\rangle$ and can then be used to calculate Coulomb corrections to the EoS in an easier fashion.

Now, it is possible to compute the Coulomb correction $P_{\rm Ion,c}$ to the total pressure $P_{\rm Ion,0}$ for a non-interacting Boltzmann gas, which we obtained in Equation (2.38). The same can be done in complete analogy for the specific internal energy e and the specific entropy S. The corrected gas pressure is consequently given by: $P_{\rm Ion} = P_{\rm Ion,0} + P_{\rm Ion,c}$. For a multicomponent plasma, the pressure correction has to be computed in principle for each nuclear species individually. By making use of the average ion coupling parameter $\langle\Gamma_{\rm ion}\rangle$ and applying the uniform-electron-background approximation, $P_{\rm Ion,c}$ is given by:

$$P_{\rm Ion,c} = \frac{\varrho}{3} k_B T \cdot u_c\left(\langle\Gamma_{\rm ion}\rangle\right), \tag{2.64}$$

where $u_c\left(\langle\Gamma_{\rm ion}\rangle\right)$ is the Coulomb internal energy per ion which can be parametrized as a function of $\langle\Gamma_{\rm ion}\rangle$. In the next step, we have to distinguish between the strong and weak coupling regime. For $\langle\Gamma_{\rm ion}\rangle \geq 1$, we employ the formula as proposed by Slattery et al. (1982) and Yakovlev & Shalybkov (1989):

$$\frac{u_c\left(\langle\Gamma_{\rm ion}\rangle\right)}{k_B T} = a\langle\Gamma_{\rm ion}\rangle + b\langle\Gamma_{\rm ion}\rangle^{1/4} + c\langle\Gamma_{\rm ion}\rangle^{1/4} + d, \tag{2.65}$$

where the values of the parameters a, b, c, d are given in Ogata & Ichimaru (1987) and Ichimaru (1993). They are $a = -0.898004$, $b = 0.96786$, $c = 0.220703$ and $d = -0.86097$. For the weak coupling regime ($\langle\Gamma_{\rm ion}\rangle \leq 1$), Yakovlev & Shalybkov (1989) suggest to use the following expression:

$$\frac{u_c\left(\langle\Gamma_{\rm ion}\rangle\right)}{k_B T} = -\frac{1}{\sqrt{3}}\langle\Gamma_{\rm ion}\rangle^{3/2} + \frac{\beta}{\gamma}\langle\Gamma_{\rm ion}\rangle^{\gamma}, \tag{2.66}$$

where $\beta = 0.295614$ and $\gamma = 1.98848$. The parameters β and γ are chosen in such a way that both expressions for the weak and the strong coupling regime as derived above, are connected smoothly. This means that both descriptions yield the same value for $u_c\,(1)$ and $du_c/d\langle\Gamma_{\rm ion}\rangle\,(1)$. Of course, the first part of Equation (2.66) reproduces the Debye-Hückel limit for $\langle\Gamma_{\rm ion}\rangle \ll 1$.

It should be noted that the Coulomb correction for the EoS are implemented exactly in this way in the Timmes as well as the Helmholtz EoS (Timmes & Arnett, 1999; Timmes & Swesty, 2000).

2.2.2 EoS of "Hot" and "Dense" Matter in Stars

During the gravitational collapse of a massive star to a NS or BH, the matter density ϱ becomes so large that not only will neutrons and protons become degenerate but they will also start to interact with each other via the strong interaction. Obviously, this means that at some point, the description of the ions as a non-interacting, non-degenerate ideal Boltzmann gas, will break down.

For such extreme conditions of high baryon density and potentially also very high temperatures, the nuclear contribution to the EoS can become substantial. Unfortunately, it is still poorly understood compared to the dilute matter EoS and is an active field of current research. A very recent review article on exactly that subject is given by Oertel et al. (2016). Especially the high-density part of the nuclear EoS is connected with large uncertainties due to the lack of a good understanding of nuclear matter slightly below the nuclear saturation density (i.e densities of roughly $0.01 - 1\ \varrho_{\rm sat}$). Here, $\varrho_{\rm sat}$ is the density of nuclear matter given by 2.04×10^{14} g cm^{-3} (corresponds to a number density in nuclear physics units of 0.122 fm^{-3}). This density region has to describe the transition from a gas of separate but already interacting nuclei, to a uniform nuclear liquid composed of degenerate neutrons and protons. This condensation process gives rise to structure-rich phases that are commonly summarized as "nuclear

pasta" (Ravenhall et al., 1983). Furthermore the EoS deep inside the NS (i.e densities of roughly $\gtrsim 5 \times \varrho_{\text{sat}}$) is even more speculative.

In a typical EoS for dense matter, abundances of nuclear species Y_i will no longer be input to the EoS but rather a result of the thermodynamic conditions. This is the case because first of all any compression of nuclear material to such high densities will heat up the material sufficiently that conditions are reached where nuclear statistical equilibrium (NSE, see Section 3.2.4) is reached. And second of all, as soon as densities close to the saturation point are reached, individual nuclei will clump & break up dynamically and the classical description as individual nuclei will not be valid anymore. Additionally, NSE implies that the elemental abundances can be calculated from the thermodynamical properties and are fully determined by the independent variables ϱ,Y_e and T. Consequently, Equation (2.5) for a hot and dense matter EoS can be written as follows:

$$(T, \varrho, Y_e) \overset{\text{EoS}}{\Longleftrightarrow} (P, e_{\text{int}}, S, \dots). \tag{2.67}$$

The two most commonly used EoSs for the hydrodynamical simulations of CCSNe are the Lattimer-Swesty EoS (Lattimer & Swesty, 1991) and the Shen EoS (Shen et al., 1998). By default, the AGILE-IDSA supernova code that we use in Chapter 6 for the simulation of the oxygen deflagration and also for ECSNe, utilizes the Lattimer-Swesty EoS that is readily available online (LS-EoS, 2017). Note that as of now, there are also several more recent EoSs available, like the one by Hempel & Schaffner-Bielich (2010).

The Lattimer-Swesty EoS is based on the compressible liquid drop model for nuclei as described in Lattimer et al. (1985). It considers nuclei, free neutrons and protons, electrons, positrons and photons together. In order to simplify the model, it is assumed that baryonic matter consists of free neutrons and protons, α particles as well as a single species of heavy nuclei. The α particle represents all light nuclear clusters and the heavy nucleus the average properties of all heavy nuclei (single nucleus approximation). The Wigner-Seitz approximation is used to describe the mixture of different particle species. This means that each heavy ion is surrounded by a charge neutral spherical cell (implying local charge neutrality) containing a gas of neutrons, protons, α particles, electrons and positrons.

2.3 Energy Transport and Production in Stars

So far, Equations (2.3) and (2.4) describe the stellar structure of a star that is not evolving with time. But is it easy to imagine that a non-isotropic energy flux related to radial temperature gradients, has to arise in the star. Hence, we define a net energy per unit time passing outwards through a sphere at radius r as the energy luminosity $l(r)$. For an infinitesimal mass shell in a star, the difference between the luminosity at the outer boundary compared to the inner boundary dl/dm has to be given either by a local production or absorption of energy or by compression or expansion of the shell. As a result, the shell's internal energy can change and mechanical work (PdV) can be exchanged with the neighboring shells. Based on these assumptions, it is possible to obtain a relation for change of the luminosity with respect to the enclosed mass:

$$\frac{\partial l}{\partial m} = \dot{\epsilon} - c_p \frac{\partial T}{\partial t} + \frac{\delta}{\varrho} \frac{\partial P}{\partial t}, \tag{2.68}$$

where

$$c_P = \left(\frac{dq}{dT}\right)_{\text{P=const}}, \qquad \delta = -\left(\frac{\partial \ln \varrho}{\partial \ln T}\right)_{\text{P=const}}. \tag{2.69}$$

Here, $\dot{\epsilon}$ is the energy released per unit mass and time due to local processes. In stars, there are thermonuclear as well as weak reactions which release or absorb energy in the plasma. $\dot{\epsilon}$ is positive if energy

is released and negative if energy is absorbed. As during thermonuclear reactions, all participating reactants are instantly thermalized, their release in energy $\dot{\epsilon}_{\mathrm{nuc,thermo}}$ is directly related to the change of binding energy of the reacting nuclei. This is discussed in detail in Section 3.2.3. The same does not hold true for weak reactions, as all the neutrinos that are produced are assumed to leave the star unhindered and consequently result in a leakage of energy. Neutrinos can be produced in two ways. By weak nuclear reactions (semileptonic processes) where the total energy released per time $\dot{\epsilon}_{\mathrm{semi}}$ is given by the difference between the binding energy change of the involved nuclei and the energy of the produced neutrino: $\dot{\epsilon}_{\mathrm{semi}} = \dot{\epsilon}_{\mathrm{nuc,semi}} - \dot{\epsilon}_{\nu,\mathrm{semi}}$. For a more complete discussion, the reader is referred to Chapter 4. Besides weak nuclear reactions, purely leptonic reactions can occur inside the stellar plasma and release pairs of neutrinos. The energy leakage $\dot{\epsilon}_{\nu,\mathrm{plasma}}$ related to those processes is usually called plasma neutrino loss. The most relevant leptonic neutrino producing processes in stars are:

$$e^+ + e^- \rightarrow \nu + \bar{\nu} \quad \text{(neutrino pair process)}, \tag{2.70}$$

$$\gamma + e^{\pm} \rightarrow e^{\pm} + \nu + \bar{\nu} \quad \text{(photo neutrino process)}, \tag{2.71}$$

$$\gamma^* \rightarrow \nu + \bar{\nu} \quad \text{(plasma neutrino process)}, \tag{2.72}$$

$$e^{\pm} + (A,Z) \rightarrow e^{\pm} + (A,Z) + \nu + \bar{\nu} \quad \text{(bremsstrahlung neutrino process)}, \tag{2.73}$$

$$e^-_{\mathrm{free}} \rightarrow e^-_{\mathrm{bound}} + \nu + \bar{\nu} \quad \text{(recombination neutrino process)}. \tag{2.74}$$

The determination of energy loss rates for above processes was for example done in a series of publications that has been summarized and tabulated by Itoh et al. (1996). As of now, those rates are still considered state of the art for application in stellar evolution codes.

Taking into consideration all effects that release or produce energy locally, the energy production per unit time is given by:

$$\dot{\epsilon} = \dot{\epsilon}_{\mathrm{nuc,thermo}} + \dot{\epsilon}_{\mathrm{nuc,semi}} - \dot{\epsilon}_{\nu,\mathrm{semi}} - \dot{\epsilon}_{\nu,\mathrm{plasma}} = \dot{\epsilon}_{\mathrm{nuc}} - \dot{\epsilon}_{\nu}. \tag{2.75}$$

In the next step, we want to relate the magnitude of the luminosity to temperature gradients in the star, based on the assumption that the microscopic processes that transport heat along those temperature gradients can be approximated by diffusion. As we will see in Section 2.3.1, those processes are radiation by photons and conduction by electrons. In the diffusion approximation, the net particle flux per unit area and time $\vec{j}$ between two places of different number density n is given by:

$$\vec{j} = -D\nabla n, \tag{2.76}$$

where D is the coefficient of diffusion given by:

$$D = \frac{1}{3} v l. \tag{2.77}$$

Here v is the average velocity of the particle species that is diffusing and l is its mean free path. The mean free path can be expresses in terms of an opacity κ by $l = (\varrho\kappa)^{-1}$. Assuming spherical symmetry and looking at the radial energy flux F rather than the particle flux, Equation (2.76) becomes:

$$F = -D\frac{de}{dr}, \tag{2.78}$$

where e is the energy density of the transport particle. If we consider photons for example, e_{rad} can be directly obtained from Planck's law and we find that the flux can be easily related to the temperature gradient:

$$F_{\mathrm{rad}} = -\frac{4ac}{3}\frac{T^3}{\kappa_{\mathrm{rad}}\varrho}\frac{\partial T}{\partial r}. \tag{2.79}$$

Replacing F_{rad} with $l = 4\pi r^2 F_{\text{rad}}$ and using the enclosed mass an independent variable, we obtain the basic equation for radiative transport in a star:

$$\frac{\partial T}{\partial m} = -\frac{3}{64\pi^2 ac}\frac{\kappa_{\text{rad}} l}{r^4 T^3}. \tag{2.80}$$

Until now, it was assumed that photons are exclusively responsible for all energy transport processes in stars. But in degenerate conditions, electrons can contribute significantly to the energy transport in stars, as well. Hence, in addition to the radiative energy flux F_{rad}, we introduce the conductive energy flux F_{cond}, which is defined in analogy to Equation (2.80). Consequently, we can keep all prefactors from the radiative energy flux and rewrite Equation (2.79) in terms of a combined energy flux:

$$F = F_{\text{rad}} + F_{\text{cond}} = -\frac{4ac}{3}\frac{T^3}{\varrho}\left(\frac{1}{\kappa_{\text{rad}}} + \frac{1}{\kappa_{\text{cond}}}\right)\frac{\partial T}{\partial r}. \tag{2.81}$$

Hence, in the general case, where both means of transporting heat are considered, the total opacity κ_{tot} is given by: $\kappa_{\text{tot}} = \left(\kappa_{\text{cond}}^{-1} + \kappa_{\text{rad}}^{-1}\right)^{-1}$ and Equation (2.80) reads:

$$\frac{\partial T}{\partial m} = -\frac{3}{64\pi^2 ac}\frac{\left(\kappa_{\text{cond}}^{-1} + \kappa_{\text{rad}}^{-1}\right)^{-1} l}{r^4 T^3}. \tag{2.82}$$

2.3.1 Stellar Opacity Sources

In the previous section, the opacity κ related to processes involving photons and electrons was introduced. In principle, ions diffuse as well and could also be responsible for transporting heat. But their contribution is in most cases negligible, due to their large rest mass. Similarly, also neutrinos do not contribute to the transport of heat, as it can be usually assumed that they are free streaming and do not interact with the stellar matter. Even if they would interact at a meaningful rate as is the case for example during a CCSN, they are not in local thermodynamic equilibrium and hence their occurrence cannot be described in the diffusion approximation. Consequently, they have to be described by a proper radiation transport theory like the Boltzmann transport scheme (see Chapter 6). Of course, in the stellar atmosphere close to the surface of the star, where material is rather dilute, photons are not in thermal equilibrium anymore and the diffusion approximation breaks down, as well. If one is really interested in the exact properties of the photon-matter interaction in the surface area, radiation transport has to be used as well. However, this is neglected in usual stellar evolution calculations as it does not affect the evolution of the star in its interior and hence is not of major interest.

There are multiple ways for photons to interact with matter and in most conditions, the total opacity is dominated by these radiative processes. Only in very degenerate conditions, this might be different and the heat flux due to electron conduction might be of the same order or even dominating. As this is the case for many of our stellar models, we have to focus on both contributions.

When describing stellar opacities, the most complicated part originates from bound-free and bound-bound transitions. These are interactions of photons with electrons that are bound inside an atom or molecule. We will mention them of course for the sake of completeness, but we will not discuss them in any detail here. For the stellar conditions of our interest, nuclei are in the state of complete ionization where bound-free and bound-bound transitions are consequently irrelevant. It is easy to imagine that the determination of bound-free and bound-bound transitions requires the knowledge of uncountable atomic states in many different nuclei, which in turn makes the calculation of the corresponding opacity sources very cumbersome.

There are two major stellar opacity sources for photons relevant for the conditions present in the stellar core during the late burning stages of intermediate-mass stars. On the one hand, the well known electron scattering that can be described by Thomson scattering for low photon energies and by Compton scattering in the case of high photon energies. On the other hand, free-free absorption can occur, a process which is sometimes called inverse bremsstrahlung. In that case, a photon is absorbed by a free electron in the vicinity of a nucleus and thereby transferring its energy to the electron. As the conditions in which we want to study stellar opacities - dense & degenerate stellar cores - are comparable to certain layers in the NS atmosphere, we will follow the discussion of radiative and conductive opacities in Appendix A of Schatz et al. (1999). For the conditions, that electron scattering is the dominating opacity source, it is well described by simple Thomson scattering. According to Buchler & Yueh (1976), Thomson scattering can be expresses in terms of a fit formula that is valid for $\eta \lesssim 4$:

$$\kappa_{\mathrm{es}} = \frac{\left(n_e + n_p\right)\sigma_0}{\varrho} \bar{G}\left(T, \eta\right) \ \mathrm{cm}^2 \ \mathrm{g}^{-1}, \tag{2.83}$$

where σ_0 is the standard Thomson scattering cross section given by:

$$\sigma_0 = \frac{8\pi}{3}\left(\frac{e^2}{m_e c^2}\right)^2. \tag{2.84}$$

$\bar{G}\left(T, \eta\right)$ is the average inverse dimensionless mean free path that can be approximated by:

$$\begin{aligned} \bar{G}\left(T, \eta\right) = {} & 1.129 + 0.2965\xi - 0.005594\xi^2 + && (2.85)\\ & + \left(11.47 + 0.3570\xi + 0.1078\xi^2\right) T + \\ & + \left(-3.249 + 0.1678\xi - 0.04706\xi^2\right) T^2. && (2.86) \end{aligned}$$

In above expression, $\xi = \exp\left(0.8168\eta - 0.05522\eta^2\right)$. Notice that here, the degeneracy parameter η is defined excluding the electron rest mass. This means $\eta = \left(\mu - m_e c^2\right)/k_B T$.

The next process we want to consider is free-free absorption. According to Clayton (1983), it is given by:

$$\kappa_{\mathrm{ff}} = 0.753 \frac{\varrho_5 Y_e}{T_8^{7/2}} \sum_i \frac{Z_i^2 X_i}{A_i} g_{\mathrm{ff}}\left(Z_i, T, n_e\right) \frac{\mathrm{cm}^2}{\mathrm{g}}, \tag{2.87}$$

where i sums is over all nuclear species, $\varrho_5 = \varrho/10^5$ g cm^{-3}, $T_8 = T/10^8$ K and g_{ff} is the dimensionless free-free Gaunt factor. Based on the work of Itoh et al. (1991) for pure hydrogen, helium, carbon & oxygen plasmas, the authors in Schatz et al. (1999) provide a fitting formula for the Gaunt factor which is given by:

$$g_{\mathrm{ff}}\left(Z_i, T, n_e\right) = 1.16 \left[\frac{0.08 T_8^{3/2}}{Y_e \varrho_5} \ln\left(1 + e^{\eta}\right)\right] \left[\frac{1 - \exp\left(-2\pi\gamma/\sqrt{\Pi + 10}\right)}{1 - \exp\left(-2\pi\gamma/\sqrt{\Pi}\right)}\right] \left[1 + \frac{T_8}{7.7}^{3/2}\right], \tag{2.88}$$

where $\gamma = \left(1.58 \times 10^{-3} Z^2 T_8^{-1}\right)^{1/2}$ and $\Pi\left(\eta\right) = \left[1 + \ln\left(1 + e^{\eta}\right)\right]^{2/3}$.

As we already mentioned, for high electron degeneracy, the energy transport due to conduction can become very efficient. According to Yakovlev & Urpin (1980), the electron conductivity is given by:

$$K = \kappa_{\mathrm{cond}} = \frac{\pi^2 k_B^2 T n_e}{3 m_e^* \left(\nu_{ei} + \nu_{ee}\right)}, \tag{2.89}$$

where ν_{ei} is the electron-ion collision frequency and ν_{ee} is the electron-electron collision frequency. m_e^* is given by:

$$m_e^* = m_e c^2 + \frac{k_B T \eta}{c^2} = \frac{\mu}{c^2}. \tag{2.90}$$

Here μ and η are the chemical potential and the degeneracy including the electron rest mass, respectively. In Chabrier et al. (1997), a fitting formula for the electron-electron collision frequency is derived. It is given by:

$$\nu_{ee} = \frac{3\alpha^2 k_B^2 T^2}{2\pi^3 \hbar m_e^* b_e} J(x, y), \tag{2.91}$$

where $\alpha = e^2/(\hbar c)$, $b_e = \alpha/(\pi\beta)$, $\beta = x/\sqrt{1+x^2}$ and x is the dimensionless Fermi momentum:

$$x = \frac{p_F}{m_e c} = \frac{\hbar\left(3\pi^2 n_e\right)^{1/3}}{m_e c} = 1.009\left(\varrho_6 Y_e\right)^{1/3}, \tag{2.92}$$

where $p_F = \hbar\left(3\pi^2 n_e\right)^{1/3}$ is the regular Fermi momentum. The function $J(x, y)$ can be approximated by:

$$J(x, y) = \left(1 + \frac{6}{5x^2} + \frac{2}{5x^4}\right)\left[\frac{y^3}{3(1+0.07414y)^3} \times \ln\left(\frac{2.810 - 0.810\beta^2 + y}{y}\right) + \frac{\pi^5}{6}\frac{y^4}{(13.91+y)^4}\right], \tag{2.93}$$

where y is given by:

$$y = \frac{\sqrt{3}\hbar\sqrt{4\pi e^2 n_e/m_e^*}}{k_B T}. \tag{2.94}$$

For the conditions where electron conduction is important, the contribution of electron-electron collisions is usually significantly less important than the contribution of electron-ion collisions. In Schatz et al. (1999), the results from Yakovlev & Urpin (1980) are generalized to plasmas with arbitrary mixtures of ions. They obtain an expression for the frequency of electron-ion collisions ν_{ei} as follows:

$$\nu_{ei} = \frac{4e^2 m_e^*}{3\pi\hbar}\frac{\sum_i Y_i Z_i^2}{Y_e}\Lambda_{ei}. \tag{2.95}$$

Here, Λ_{ei} is the Coulomb logarithm given by:

$$\Lambda_{ei} = \Lambda_{ei}^0 - \frac{\hbar^2\left(3\pi^2 n_e\right)^{2/3}}{2m_e^{*2}c^2}, \tag{2.96}$$

where Λ_{ei}^0 reads as follows:

$$\ln\left[\left(\frac{2\pi}{3}\right)^{1/3}\left(\frac{Y_e}{\sum_i Y_i}\right)^{1/3}\left(\frac{3}{\Gamma} + \frac{3}{2}\right)^{1/2}\right]. \tag{2.97}$$

Finally, by using the following relation for Γ, the collision frequency ν_{ei} can be obtained:

$$\Gamma = \frac{e^2}{k_B T}\left(\frac{4\pi}{3}\sum_i n_i\right)^{1/3}\frac{\sum_i n_i Z_i^2}{\sum_i n_i} = 0.49 \times \frac{\sum_i Y_i Z_i^2}{\sum_i Y_i}\frac{\left(\varrho_7 \sum_i Y_i\right)^{1/3}}{T_8}. \tag{2.98}$$

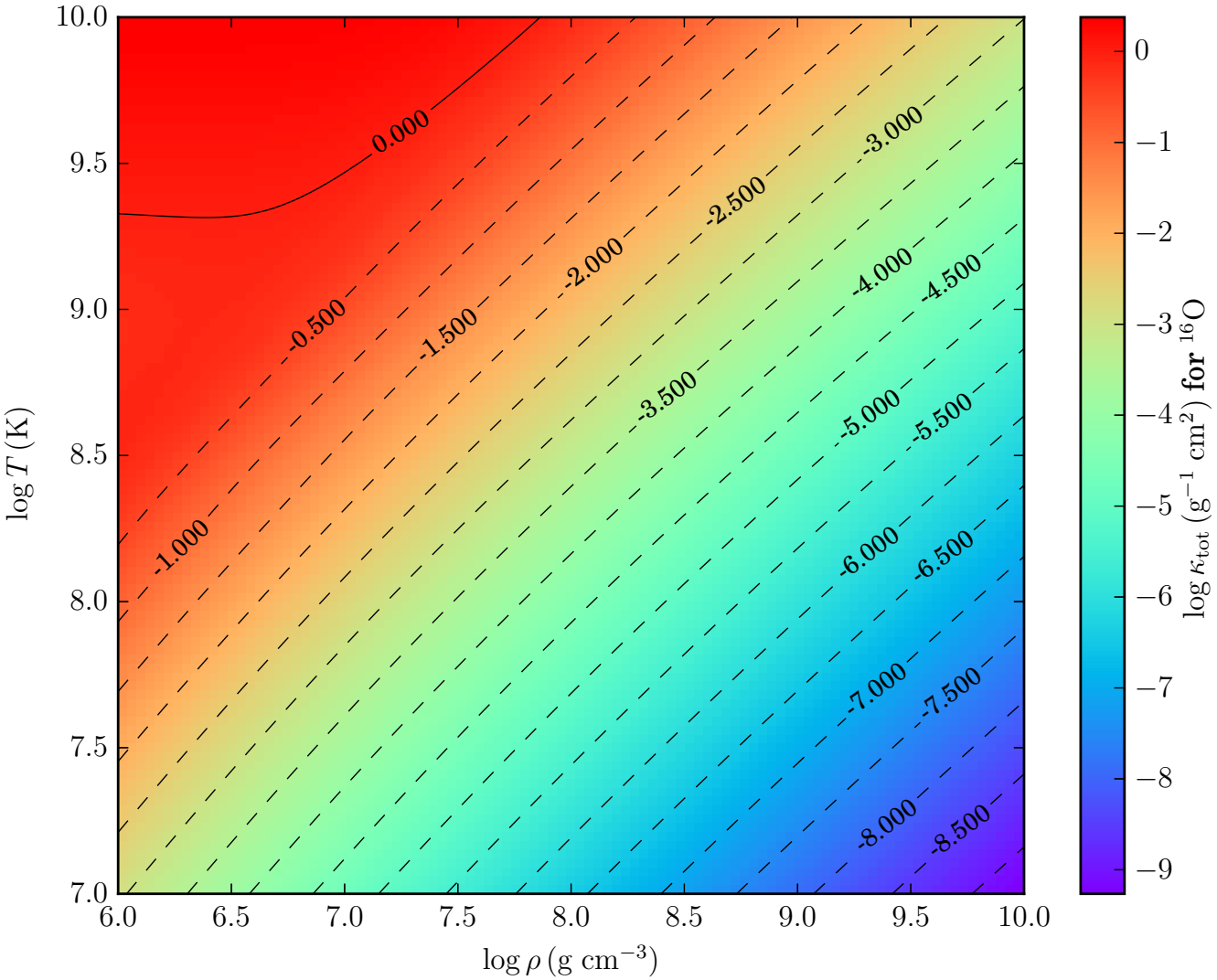

Figure 2.1: Stellar opacity κ for a pure ^{16}O-gas as a function of temperature and density. The total opacity κ_{tot} is given by $\kappa_{\text{tot}} = \left(\kappa_{\text{cond}}^{-1} + \kappa_{\text{rad}}^{-1}\right)^{-1}$, where κ_{rad} is the opacity due to radiation and κ_{cond} is the opacity due to electron conduction.

By incorporating all previously mentioned effects, we can express the total radiative and conductive opacity by:

$$\kappa_{\text{tot}} = \left(\kappa_{\text{cond}}^{-1} + \kappa_{\text{rad}}^{-1}\right)^{-1} = \left(\frac{1}{\kappa_{\text{es}} + \kappa_{\text{ff}}} + \frac{1}{\kappa_{\text{ee}} + \kappa_{\text{ei}}}\right)^{-1}. \tag{2.99}$$

In Figure 2.1, we compute the stellar opacity, based on the previously mentioned contributions for a pure oxygen gas over a density and temperature regime that first of all represents the conditions in degenerate ONe cores and second of all ensures that no other processes are dominating. It becomes clear that especially for very degenerate conditions (i.e. high density and low temperature), the star becomes comparably transparent for electrons. This can be seen in Figure 2.1, as the combined opacity is decreasing with increasing density. The reason for this behavior is that on the one hand, electrons become extreme relativistic and on the other hand, they cannot exchange momentum with the plasma anymore because in such degenerate conditions, many momentum states are Pauli-blocked.

2.3.2 Convection

Besides the transport of energy via microscopic particles, energy can also be transported inside the star via "blobs" of matter. This macroscopic process of particle movement is called convection. Obviously, during the process of convection, not only energy can be transported but also layers of different composition can be mixed. As we already concluded earlier that diffusion of ions can be neglected on the relevant evolutionary timescales in stars, convection is the only viable mechanism of mixing material from the interior of the star to the outside or vice versa, during the regular burning stages of a star.

Stability Criteria in Stars

In order to describe the mechanism of convection, it is necessary to understand which criteria have to be fulfilled in order to enable convection in a star in the first place. Our considerations will be closely related to the question of the stability of a small mass element in a star, against non-spherical perturbations. If a local perturbation occurs, there are certain conditions that allow its growth and result in a macroscopic non-spherical motion. If that should be the case, the stellar material is said to be unstable and if the perturbation gets suppressed, the stellar material is stable.

The first instability that we will discuss in detail, is the so-called dynamical instability. It is given when a local perturbation—assuming that it gets displaced and grows—has insufficient time to exchange heat with the surrounding material. Consequently, it can be described by an adiabatic motion. In the initial situation, it is assumed that a small mass element obtains a different temperature compared to its surrounding material through microscopical fluctuations. The fluid element will react by either expanding or compressing.[5] Hence, the internal pressure is regulated to the same pressure than the surrounding material and the bubble has obtained a different density than the ambient medium. Subsequently, it will get displaced due to the buoyancy force and either rise or sink. Of course, during this process, the bubble will enter different layers of the star with varying thermodynamic properties.

The direction of the buoyancy force can either be anti-aligned or aligned with the velocity of the mass element. In the first case, the buoyancy force pulls the displaced element back to its original position, indicating that the layer that it originates from is stable. In the second case, the mass element gets accelerated in the direction of motion and the layer that it originates from is dynamically unstable. The occurrence of dynamical instabilities can be predicted by a stability criterion:[6]

$$\nabla \leq \nabla_e + \frac{\varphi}{\delta}\nabla_\mu. \tag{2.100}$$

Here, φ and δ represent two thermodynamic derivatives that are given by:

$$\varphi = \left(\frac{\partial \ln \varrho}{\partial \ln \mu}\right)_{P,T=\text{const}} \quad \text{and} \quad \delta = -\left(\frac{\partial \ln \varrho}{\partial \ln T}\right)_{P,\mu=\text{const}}. \tag{2.101}$$

The three temperature gradients ∇ that appear in the stability criterion are given by:

$$\nabla = \left(\frac{d \ln T}{d \ln P}\right)_{\text{sourrounding}}, \quad \nabla_\mu = \left(\frac{d \ln \mu}{d \ln P}\right)_{\text{sourrounding}} \quad \text{and} \quad \nabla_e = \left(\frac{d \ln T}{d \ln P}\right)_{\text{mass element}}, \tag{2.102}$$

where the derivatives are taken along the motion of the displaced bubble either with respect to the bubble itself or with respect to the surrounding material. By assuming that the displaced mass element

[5] As discussed in Section 2.1, this process happens on the timescale of reaching mechanical equilibrium, which typically is very fast.

[6] A derivation is given for example in Chapter 6 of Kippenhahn & Weigert (1990).

moves adiabatically (i.e. at constant entropy), ∇_e is simply given by ∇_{ad}, that is defined in the following way:

$$\nabla_{\mathrm{ad}} = \left(\frac{P}{T}\frac{dT}{dP}\right)_{\mathrm{S=const}} = \frac{P\delta}{T\varrho c_P}. \tag{2.103}$$

If one is interested in determining when a non-convective zone will become convective, it is valid to assume that ∇ is entirely given by the transport of radiation (and conduction). Consequently, $\nabla = \nabla_{\mathrm{rad}}$. The radiative temperature gradient can be easily obtained by combining Equations (2.3) and (2.82):

$$\nabla_{\mathrm{rad}} = \left(\frac{d\ln T}{d\ln P}\right)_{\mathrm{rad}} = \frac{P}{T}\frac{\partial T/\partial m}{\partial P/\partial m} = \frac{3}{16\pi acG}\frac{\kappa l P}{mT^4}. \tag{2.104}$$

As long as effects of varying mean molecular weight μ are ignored, these considerations result in the well-known Schwarzschild criterion for dynamical stability, given by:

$$\nabla_{\mathrm{rad}} < \nabla_{\mathrm{ad}}, \tag{2.105}$$

and by also taking into account that the mass element can move through material with varying mean molecular weight μ, the Ledoux criterion is obtained:

$$\nabla_{\mathrm{rad}} < \nabla_{\mathrm{ad}} + \frac{\varphi}{\delta}\nabla_\mu. \tag{2.106}$$

Based on the Schwarzschild (SS) and the Ledoux (L) criterion for dynamical stability, it is possible to classify the behavior of every layer in the star into four different regimes

$$\left.\begin{aligned}\nabla_{\mathrm{rad}} &< \nabla_{\mathrm{ad}} \\ \nabla_{\mathrm{rad}} &< \nabla_{\mathrm{ad}} + \tfrac{\varphi}{\delta}\nabla_\mu\end{aligned}\right\} \Longrightarrow \text{radiative (SS + L stable)}, \tag{2.107}$$

$$\left.\begin{aligned}\nabla_{\mathrm{rad}} &> \nabla_{\mathrm{ad}} \\ \nabla_{\mathrm{rad}} &> \nabla_{\mathrm{ad}} + \tfrac{\varphi}{\delta}\nabla_\mu\end{aligned}\right\} \Longrightarrow \text{convective (SS + L unstable)}, \tag{2.108}$$

$$\left.\begin{aligned}\nabla_{\mathrm{rad}} &> \nabla_{\mathrm{ad}} \\ \nabla_{\mathrm{rad}} &< \nabla_{\mathrm{ad}} + \tfrac{\varphi}{\delta}\nabla_\mu\end{aligned}\right\} \Longrightarrow \text{semiconvective (SS unstable + L stable)}, \tag{2.109}$$

$$\left.\begin{aligned}\nabla_{\mathrm{rad}} &< \nabla_{\mathrm{ad}} \\ \nabla_{\mathrm{rad}} &> \nabla_{\mathrm{ad}} + \tfrac{\varphi}{\delta}\nabla_\mu\end{aligned}\right\} \Longrightarrow \text{thermohaline mixing (SS stable + L unstable)}. \tag{2.110}$$

The first two regimes simply denote the two limiting cases where energy is either transported by radiation or in the other case primarily by convection. This is the case, because typically convective energy transport is significantly more efficient than radiative energy transport for the same conditions, given that convection is allowed. While we will not discuss thermohaline mixing, some additional considerations regarding the semiconvective regime will be of particular importance for the topic of this thesis.

Semiconvection

In a semiconvective region, regular convection is prohibited by a stabilizing mean molecular weight gradient ∇_μ, which can enable interesting phenomena. First, it will be necessary to investigate what happens to a displaced mass element in a region that is dynamically stable. Based on the discussion in the previous Section, we know that a semiconvective region is dynamically stable. In a dynamically stable region, a displaced bubble will always return to its original position. But as it is continuously driven by the buoyancy force during that process, it will start to "overshoot" its original position and start to

oscillate. As long as the mass element is not allowed to exchange heat (simply because we assume that it moves adiabatically) with the surrounding material, then this perturbation will always grow. One can easily show that the frequency of such an oscillation is given by the so-called Brunt-Väisälä frequency:

$$\omega_{\mathrm{ad}}^2 = \frac{g\delta}{H_P}\left(\nabla_{\mathrm{ad}} - \nabla + \frac{\varphi}{\delta}\nabla_\mu\right), \tag{2.111}$$

where g is the gravitational acceleration, and H_P is the pressure scale height given by:

$$H_P = -P\frac{dr}{dP}. \tag{2.112}$$

But the longer the mass element is oscillating, the more time it has to actually exchange heat with the surrounding material. Consequently, the assumption of adiabaticity for the displaced mass element has to be relaxed at some point. Then, it is possible to show that for a region that is Schwarzschild and Ledoux stable, any heat exchange between the displaced mass element and the ambient medium (independent of its magnitude) will always lead to a damping of the oscillation until is disappears.

This however is not necessarily the case for a region that is semiconvective. Here, in some cases, the heat exchange with the surrounding material can even boost the oscillation amplitude. Such a situation is called overstability or vibrational instability. Now, it is also possible to obtain a criterion for the occurrence of the vibrational instability in a semiconvective region:

$$\nabla_{\mathrm{ad}} < \nabla < \nabla_{\mathrm{ad}} + \frac{\varphi}{\delta}\nabla_\mu. \tag{2.113}$$

Consequently, a layer for which above criterion is met (this can by definition only be in a semiconvective region) will be dynamically stable but vibrationally unstable. The growth of a vibrational instability is governed by the timescale τ_{adj} for a mass element to adjust thermally to its surrounding material. Typically, this is much longer than the timescale for the growth of a dynamical instability that is given by $\tau_{\mathrm{dyn}} = (H_P/g)^{1/2}$. In Kippenhahn & Weigert (1990), τ_{adj} of a perturbed mass element is estimated to be:

$$\tau_{\mathrm{adj}} = \frac{\kappa\varrho^2 c_P d^2}{16acT^3}, \tag{2.114}$$

where d is the diameter of a spherical "blob" of matter. Per se, d is not known and hence τ_{adj} can only be calculated as a function of d.

Convective Energy Transport and Mixing

We already quantified the energy transport via radiation in Equation (2.82). In this Section it will be the goal to introduce a theory that is able to yield a similar expression in the case of convective heat transport. So far, we only discussed criteria that can determine the onset or end of convective motion in stars in Section 2.3.2. Unfortunately, the actual description of convective motion is much more challenging to describe and is connected to a lot of shortcomings, due to the description of a truly multidimensional phenomenon in spherical symmetry.

The usual implementation of convective motion in stellar evolution models is done via the so-called mixing length theory, dating back to work of Ludwig Prandtl from 1925. In this simple picture, convection is treated in complete analogy to a microscopic means of transport, with the only difference that the transport particles are now "blobs" of matter instead of photons or electrons. In general, if convection is also present in the star, Equation (2.81) for the total energy flux F_{tot} has to be modified and is now given by:

$$F_{\mathrm{tot}} = F_{\mathrm{rad}} + F_{\mathrm{conv}} = \frac{4acG}{3}\frac{T^4 m}{\kappa P r^2}\nabla_{\mathrm{rad}}, \tag{2.115}$$

where $\nabla_{\rm rad}$ has now a contribution also from convection. Then, the radiative flux is now related only to ∇, not to $\nabla_{\rm rad}$:

$$F_{\rm rad} = \frac{4acG}{3}\frac{T^4 m}{\kappa P r^2}\nabla. \tag{2.116}$$

Consequently, the goal of any theory of convection has to be to determine ∇ in the presence of convection. In Chapter 7 of Kippenhahn & Weigert (1990), this is achieved based on the description of Böhm-Vitense (1958) and will be briefly sketched here. The simple picture of convection as described above, depends on a crucial parameter, the mixing length l_m which describes how long a displaced mass element moves until it disperses in the surrounding material. It is possible to show that the average velocity $v_{\rm blob}$ of such a mass element is given by:

$$v_{\rm blob} = \left((\nabla - \nabla_e)\, g\, \delta \frac{l_m^2}{8 H_P} \right)^{1/2}, \tag{2.117}$$

and furthermore, the convective flux $F_{\rm conv}$ is given by:

$$F_{\rm conv} = 32^{-1/2}\, \varrho c_P T\, (g\delta)\, l_m^2 H_P^{-3/2}\, (\nabla - \nabla_e)^{3/2}. \tag{2.118}$$

By considering the temperature change inside a displaced mass element, due to an adiabatic expansion and radiative energy exchange with the surroundings, another equation can be obtained that relates the different ∇'s with each other:

$$\frac{\nabla_e - \nabla_{ad}}{\nabla - \nabla_e} = \frac{6acT^3}{\kappa \varrho^2 c_P l_m v_{\rm blob}}. \tag{2.119}$$

The set of five Equations (2.115) - (2.119) can now be solved for its five unknown quantities $F_{\rm rad}, F_{\rm conv}, v, \nabla_e$ and ∇, with l_m serving as a free parameter that has to be guessed appropriately.

Besides the already mentioned characteristic of convection to transport energy rather efficiently in the star, it is also responsible for mixing materials of different chemical composition with each other. In a convective zone, convection (and hence also mixing) extends from mass coordinate m_1 to m_2 which denote the lower and upper boundary of the convection zone. If it is furthermore assumed that inside a convective layer, all elemental abundances are instantaneously mixed. The average mass fraction inside a mixed layer $\langle X_i \rangle$ is defined as:

$$\langle X_i \rangle = \left(\int_{m_1}^{m_2} X_i \right) \left(\sum_i \int_{m_1}^{m_2} X_i \right)^{-1}. \tag{2.120}$$

Consequently, the abundance change in a convective layer is given by:

$$\frac{\partial \langle X_i \rangle}{\partial t} = (m_2 - m_1)^{-1} \left[\int_{m_1}^{m_2} \left(\frac{\partial X_i}{\partial t} \right)_{\rm nuclear} dm + \frac{\partial m_2}{\partial t} (X_{i2} - \langle X_i \rangle) - \frac{\partial m_1}{\partial t} (X_{i1} - \langle X_i \rangle) \right], \tag{2.121}$$

where X_{i1} and X_{i2} are the mass fractions of the material that is directly below the inner and directly above the outer boundary of the convective zone, respectively. In this fashion, this formula does not only take into account nuclear burning but also changes in size of the convective layer.

Above considerations regarding energy transport and mixing are only valid in a regime that is dynamically unstable. In a semiconvective region, the situation is more complicated. Unfortunately, due to the complicated nature of this process, semiconvection is usually implemented in stellar evolution codes

(e.g. in MESA) based on a description of Langer et al. (1983). Here, the complicated process of the vibrational instability as introduced in Section (2.3.2) and as described in detail by Kato (1966), is highly simplified and treated as an additional diffusive process with a diffusion constant given by:

$$D_{\text{semiconv}} = \alpha_s \frac{K_{\text{rad}}}{6c_p\varrho}\frac{\nabla - \nabla_S}{\nabla_L - \nabla} = \frac{4acT^3}{18\kappa c_P \varrho^2}\frac{\nabla - \nabla_S}{\nabla_L - \nabla}. \tag{2.122}$$

Here, $\nabla_S = \nabla_{\text{ad}}$ is the temperature gradient corresponding to Schwarzschild convection and $\nabla_L = \nabla_{\text{ad}} + (\varphi/\delta)\nabla_\mu$ is the temperature gradient corresponding to Ledoux convection. In this picture, semiconvection simply connects the two limiting cases of pure Schwarzschild convection and Ledoux convection, based on the value of the parameter α_S, that quantifies the efficiency of semiconvection.

If semiconvection is inefficient (i.e α_S small), then a semiconvective layer will behave like a convectively stable layer and $\nabla = \nabla_{rad}$ (i.e Ledoux convection without semiconvection). If semiconvection would turn out to be very efficient (i.e α_S large), it would result in a behavior similar to regular convection arising from a dynamical instability as described by the Schwarzschild criterion.[7] Typically α_S is assumed to have values around unity (see e.g. Yoon et al., 2006), in which case it is considerably less efficient than ordinary convection due to dynamical instability.

2.4 Differential Equations of Stellar Evolution

Now, we have all the necessary ingredients to name a set of coupled differential equations which describes the evolution of a star together with the right initial and boundary conditions. Adopting the notation from Kippenhahn & Weigert (1990), we obtain:

$$\frac{\partial r}{\partial m} = \frac{1}{4\pi r^2 \varrho}, \tag{2.123}$$

$$\frac{\partial P}{\partial m} = -\frac{Gm}{4\pi r^4} - \frac{1}{4\pi r^2}\frac{\partial^2 r}{\partial t^2}, \tag{2.124}$$

$$\frac{\partial l}{\partial m} = \dot{\epsilon}_{\text{nuc}} - \dot{\epsilon}_\nu - c_P\frac{\partial T}{\partial t} + \frac{\delta}{\varrho}\frac{\partial P}{\partial t}, \tag{2.125}$$

$$\frac{\partial T}{\partial m} = -\frac{GmT}{4\pi r^4 P}\nabla, \tag{2.126}$$

$$\frac{\partial X_i}{\partial t} = \left(\frac{\partial X_i}{\partial t}\right)_{\text{mixing}} + \left(\frac{\partial X_i}{\partial t}\right)_{\text{nuclear}}. \tag{2.127}$$

Equations (2.123) and (2.124) simply are the stellar structure Equations as given by Equation (2.3) and (2.4) with the only difference that the term $\left(-4\pi r^2\right)^{-1}\partial^2 r/\partial t^2$ was introduced to account for a situation where the hydrostatic equilibrium is not fulfilled. Equation (2.125) is simply given by Equation (2.68) and Equation (2.126) represents Equation (2.80) rewritten in terms of ∇. If the energy transport is only due to radiation and conduction, then $\nabla = \nabla_{\text{rad}}$, as given by Equation (2.104). In case a given layer in the star is dynamically unstable, then ∇ has to be determined also by mixing length theory, as described by Equations (2.115) - (2.119). Finally, Equation (2.127) determines the abundance change due to nuclear reactions and mixing.

In addition to these equations, we need to use well-known thermodynamic relations to obtain c_P, δ and ∇_{ad} (enters in Equation (2.126)), an EoS to obtain $P(\varrho)$ and stellar opacities to obtain κ that enters Equation (2.126). $\dot{\epsilon}_{\text{nuc}}$, $\dot{\epsilon}_\nu$ and $\partial X_i/\partial t$ are determined by nuclear reactions and neutrino losses.

[7] Even though this is highly unlikely as the growth timescale for dynamical instability is usually much smaller than the one for vibrational instability.

Using the proper techniques of discretization and numerical solving of differential equations, a computer code can then follow the evolution of a star with a given set of initial conditions, like initial mass, rotation or metallicity.

3 Nuclear Reactions in Astrophysics

In this Chapter, we introduce the main nuclear physics aspects that are relevant for the studies in this thesis. Notice that it is not the goal to present the broad field of nuclear theory in an unnecessary degree of detail but rather focus on the phenomenological description of nuclei, regardless whether they can be accessed by experiment or have to be described by theoretical models. In astrophysics, the required input from nuclear physics can be very roughly classified in two different categories. On the one hand, properties of individual nuclei and on the other hand, reactions among nuclei that occur in astrophysical plasma. Those nuclear reactions that are mediated by the strong and the electromagnetic force will be discussed in Section 3.2 of this chapter while reactions involving the weak force are discussed in more detail in Chapter 4, due to their special relevance for dense stellar cores, as will be pointed out in Chapter 6. The majority of concepts that will be introduced in Section 3.1 about nuclear properties are covered by any elementary nuclear physics textbook, for example Wong (1998) or Greiner & Maruhn (1996). Nuclear reactions in stars are presented in great detail by Cowan et al. (manuscript in preparation).

3.1 Properties of Nuclei

Despite the fact that neutrons and protons are composite particles made of u and d quarks, the relevant degrees of freedom in nuclei at the energies of interest in stellar physics, are nucleons, not quarks. In turn, a nucleus can be thought of as a composite object of A nucleons, of which N are neutrons and Z are protons. The relevant forces in nuclei are the strong nuclear force involving all nucleons and the electromagnetic repulsion of the charged protons. The strong nuclear force can be considered as the residual part of the strong interaction between quarks, as described by QCD, after having formed baryonic bound states, in this case neutrons and protons. Conceptually, this is similar to van der Waals forces, which in a highly simplified view, denote the residual electromagnetic interaction between charge-neutral molecules composed of equal numbers of protons and electrons. With the nucleus being a bound state of nucleons, the strong force needs to be attractive at distances that corresponds to the inter-nucleon spacing in nuclei, which is roughly 1 fm.

A nucleus is said to be stable, if it does not exhibit any form of radioactivity, meaning that in the absence of external forces, it will remain forever in its designated state.[1] If it is energetically favorable and not quantum mechanically forbidden to convert a neutron into a proton inside the nucleus or vice versa, then nuclei are unstable with respect to the weak interaction and can decay via $e^{\pm}$-emission or -absorption. Due to the nature of the weak interaction, those processes are typically rather slow and those nuclei exhibiting no other decay modes can have very long lifetimes. Another type of radioactivity involves the emission of nucleons. Among such processes are for example the emission of neutrons, protons, α-particles or spontaneous fission. In this case, reactions involve the strong nuclear force, suggesting that they occur on a significantly shorter timescale compared to weak decays. Concerning the emission of charged particles (p, α, fission), tunneling through the Coulomb barrier can make corresponding decay rates slow, as well. The last important nuclear decay mode is γ-radiation between two states of different excitation energy of the same nucleus. Such processes are mediated by the electromagnetic interaction and occur typically very fast.[2]

[1] The stability of a nucleus is usually defined with respect to its ground state.

[2] A notable exception is for example the metastable state of ^{180}Ta, having the longest half-life (lower limit) of all isomers in nature.

The main property of a nucleus is the mass of its ground state M_{gs}. Excited states of nuclei are labeled according to their excitation energy E_{ex} compared to M_{gs}. Notice that in astrophysics, nuclei appear in the context of hot plasma, where excited states can be populated thermally by the ambient photon gas, making their knowledge particularly important. Because nuclei are bound states, their mass has to be smaller than the mass of their individual constituents and the difference between both is called nuclear binding energy. As the binding energy compares the mass of the nucleus with that of all nucleons being separated to infinity, this concept is not a good measure of the stability of nuclei. Instead, it is helpful to compare the mass of a nucleus with the mass of the same system, where one nucleon has been removed. This difference is called neutron or proton separation energy. As soon as a nucleus can release energy by emitting nucleons, it is extremely unstable only exist for a very short time. By marking the last neutron-rich isotope that is still not gaining energy by emitting neutrons for each element, the neutron dripline can be constructed, beyond which the neutron separation energy becomes smaller than 0. As nuclei beyond the dripline are extremely unstable with respect to neutron emission, the dripline indicates the neutron-rich limit of the nuclear chart.

Besides their ground state mass M_{gs} and excitation energy E_{ex}, it is customary to characterize nuclei by quantum numbers, arising from their quantum mechanical nature that gives rise to discrete energy levels. These are the isospin T, the isospin projection T_z, the total angular momentum J, the angular momentum projection M, and its parity Π. They will be briefly introduced in the following.

3.1.1 Isospin Formalism

Ii was discovered very early in the history of nuclear physics that neutrons and protons have similar masses. While the proton has a mass of $938,2720813(58)$ MeV, the neutron has a mass of $939,5654133(58)$ MeV. Furthermore, both neutrons and protons have a spin of $1/2$. Consequently, they exhibit the same quantum mechanical properties as elementary fermions. Bearing this in mind and supported by the observational evidence that neutrons and protons are indistinguishable with respect to the strong interaction, it was pointed out by Heisenberg (1932) that it is customary to think of neutrons and protons inside a nucleus as the same particle, the nucleon. Of course, as this is not true for the electromagnetic interaction, it has to be left out of consideration, for now.

In analogy to the spin that will be introduced in Section 3.1.2, the nucleonic isospin t can be defined via two basis states, the neutron $|n\rangle$ and the proton $|p\rangle$ in the two-dimensional isospin space:

$$|n\rangle = |t = 1/2,\ t_z = +1/2\rangle = \begin{pmatrix} 1 \\ 0 \end{pmatrix}, \tag{3.1}$$

$$|p\rangle = |t = 1/2,\ t_z = -1/2\rangle = \begin{pmatrix} 0 \\ 1 \end{pmatrix}, \tag{3.2}$$

where t_z is the projection of t onto the third axis and the sign of the neutron/proton isospin projection in above definition is convention.[3] In analogy to the spin operators (Pauli matrices), three basic isospin operators $\hat{t}_x, \hat{t}_y$ and $\hat{t}_z$ exist:

$$2\hat{t}_x = \hat{\tau}_x = \begin{pmatrix} 0 & 1 \\ 1 & 0 \end{pmatrix},\ 2\hat{t}_y = \hat{\tau}_y = \begin{pmatrix} 0 & -i \\ i & 0 \end{pmatrix},\ 2\hat{t}_z = \hat{\tau}_z = \begin{pmatrix} 1 & 0 \\ 0 & -1 \end{pmatrix}. \tag{3.3}$$

The physical meaning of $\hat{t}_z$ follows directly from its definition. It simply evaluates the isospin projection eigenvalue of the nucleonic state:

$$\hat{t}_z|n\rangle = +1/2|n\rangle, \tag{3.4}$$

$$\hat{t}_z|p\rangle = -1/2|p\rangle. \tag{3.5}$$

[3] As we will see in Chapter 4, this convention has the advantage that β^+ decay can be associated with the $\hat{t}_+$ operator and β^- decay with the $\hat{t}_-$ operator.

Furthermore, $\hat{t}_x$ and $\hat{t}_y$ can be used to define two additional operators $\hat{t}_\pm$:

$$\hat{t}_\pm = \hat{t}_x \pm i\hat{t}_y, \tag{3.6}$$

that are either raising or lowering the isospin projection of a nucleon. For this reason, they are called isospin lowering operator $\hat{t}_-$ and isospin raising operator $\hat{t}_+$. They act on neutron and proton states in the following way:

$$\hat{t}_+|n\rangle = 0, \tag{3.7}$$
$$\hat{t}_+|p\rangle = |n\rangle, \tag{3.8}$$
$$\hat{t}_-|n\rangle = |p\rangle, \tag{3.9}$$
$$\hat{t}_-|p\rangle = 0. \tag{3.10}$$

This behavior can be conveniently summarized by a single expression:

$$\hat{t}_\pm|t, t_z\rangle = \left[t\,(t+1) - t_z\,(t_z \pm 1)\right]^{1/2}|t, t_z \pm 1\rangle. \tag{3.11}$$

Now, the concept of nucleonic isospin can be generalized to the whole nucleus, consisting of A nucleons. In that case, the nuclear isospin operator is given by:

$$\hat{T} = \sum_{i=1}^{A} \hat{t}_i, \tag{3.12}$$

and regarding the total isospin projection, the eigenvalue is simply the sum of the projection for each individual nucleon. Hence it follows:

$$T_Z = \frac{1}{2}(N - Z). \tag{3.13}$$

For a given total isospin T, the eigenstates for different T_Z represent nuclei with the same mass number A but a different neutron and proton number. Under the assumption that the Coulomb repulsion can be neglected, these states would be expected to be degenerate in energy, because the strong interaction phenomena are invariant under isospin transformations. Such states are indeed found in light nuclei where Coulomb effects are small. They are called isobaric analog states (IAS). A priori, it is not possible to say which isospin multiplet a given state belongs to, as only the projection of the isospin T_Z is observed and the $\hat{t}_i$'s can couple in many different ways. Nevertheless, we can obtain the following relation

$$\frac{1}{2}(N + Z) \geq T \geq \frac{1}{2}(N - Z) = T_z. \tag{3.14}$$

As it turns out, there is a natural ordering of the energy of states with the same number of nucleons and the same T_z but different T. This is related to the nuclear symmetry energy, which indicates that nuclei with equal number of neutrons and protons are favored over asymmetric configurations. Because of this, the isospin multiplet corresponding to $T = T_{\text{min}} = 1/2\,(N - Z)$ (singlet for $T = 0$) is situated below the multiplet with $T = 1/2\,(N - Z) + 1/2$, and so on.

3.1.2 Spin, Angular Momentum and Parity

The analogy to the spin was already used in the previous section to introduce the concept of isospin. As was already mentioned, nucleons have an intrinsic spin of $s = 1/2$ (in units of $\hbar$). Additionally, nucleons can also carry an integer valued orbital angular momentum l. l and s can be coupled to a total

angular momentum $\vec{j} = \vec{l} + \vec{s}$. Hence, nucleonic states with a given orbital angular momentum l and are characterized by doublet of $j_1 = |l - 1/2|$ and $j_2 = |l + 1/2|$.

For a nucleus with A nucleons, the total angular momentum J is given by:

$$\vec{J} = \sum_{n=1}^{A} \vec{j} = \sum_{n=1}^{A} \vec{s} + \sum_{n=1}^{A} \vec{l}. \tag{3.15}$$

The projection of the angular momentum quantum number J onto the third axis is given by the magnetic quantum number M, which can have values of:

$$M \in \{-J, -J+1, \ldots, J-1, J\}. \tag{3.16}$$

In astrophysical problems where external magnetic fields are not considered, the angular momentum projection M is not of particular interest, because all states with different M are degenerate in energy and represent a multiplet with respect to J whose degeneracy is given by $2J + 1$.

In the absence of a microscopic description of the nucleus, it is not possible to determine the coupling of $\vec{l}$ and $\vec{s}$ to the observed angular momentum J of a given nuclear state. Of course, in many cases, J can be measured in the lab. Nevertheless it is possible to make an educated guess for the ground state nuclear spin J of a nucleus. By virtue of the nuclear shell model, it is known that neutrons and protons inside a nucleus occupy discrete single particle energy levels that can be filled with a limited number of nucleons because of Pauli's exclusion principle. Furthermore, it is energetically favored for nucleons in the same shell of given j to form anti-aligned pairs with $J_{\text{pair}} = 0$. Consequently, even-N even-Z nuclei should have a $J = 0$ ground state, as is observed in nature. In odd-A nuclei, the remaining unpaired nucleon determines the total angular momentum of the ground state (J is half-integer) and in odd-N odd-Z nuclei, two unpaired nucleons exist that result in an integer J.

The parity Π of a nucleon depends on the symmetry behavior of its wave function under a point reflection in space (i.e. multiplying all space components with -1). It is given by:

$$\Pi = (-1)^l. \tag{3.17}$$

The parity is a multiplicative quantum number and the parity of the nuclear ground state can be guessed as well by knowing that paired nucleons have even parity. Notice that nuclear states are usually labeled by the spectroscopic notation, which is given by J^π. Then even-N even-Z are expected to have a ground state of 0^+. Analogously, for odd-A nuclei, the parity is given by $(-1)^l$ of the unpaired nucleon and for odd-N odd-Z nuclei, it is given by the two unpaired nucleons.

3.1.3 Nuclear Mass and Binding Energy

The knowledge of nuclear masses (i.e. ground state energy), or more precisely the mass difference Q between neighboring nuclei, is of crucial importance for calculating reaction rates and chemical equilibrium distributions of nuclei. Notice that many astrophysical processes that involve nuclear reactions like hydrostatic burning in stars, operate at very low temperatures and can be dominated by few resonances. In that case, the knowledge of the resonance energy is important, as well.

Except for the r-process and similar extreme nucleosynthesis events, the ground state masses of the involved nuclear species have been measured experimentally with a very high level of precision. Consequently, this is also the case for the stellar evolution calculations performed in Chapter 6. Only when a stellar core collapses gravitationally, neutron-rich nuclei far off stability are formed, which are hard to access experimentally. A recent review on nuclear mass measurements can be found in Blaum (2006).

If nuclei cannot be explored in the lab, their masses have to be determined theoretically with a suitable method in large-scale calculations (see e.g. Pearson et al., 2013).[4] As the most precise measurements of nuclei are done in their atomic state, important tabulations like the "AME2012" by Wang et al. (2012) provide the atomic mass rather than the nuclear mass. In many astrophysical problems, the temperature is sufficiently high to ensure a fully ionized plasma. For this reason, it is useful to give a relation between the nuclear mass and the atomic mass, which has to contain mass and binding energy of the atomic electrons, as well:

$$m_{\text{atom}}(A,Z) = m_{\text{nuclear}}(A,Z) + m_{\text{ele}}(Z) - B_{\text{ele}}(Z), \tag{3.18}$$
$$\approx m_{\text{nuclear}}(A,Z) + m_e(Z), \tag{3.19}$$

where the binding energy of the electrons $B_{\text{ele}}(Z)$ at the level of precision required in astrophysical application is usually neglected. The main contribution of the nuclear mass is given by the mass of its constituents. Hence it is customary to define a quantity - the nuclear binding energy - as the difference in mass of a given nucleus compared to its individual constituents. Consequently, we define the "atomic-mass based nuclear binding energy" in the usual way as the difference between the atomic mass of a nucleus and the atomic mass of its constituents:

$$B_{\text{nuc}}(A,Z) = c^2\left[Z\cdot m_{\text{atom}}\left({}^1H\right) + (A-Z)\cdot m_{\text{atom}}\left({}^1n\right) - m_{\text{atom}}(A,Z)\right]. \tag{3.20}$$

Notice that above definition results always in a positive binding energy for nuclei. Analogously, the nuclear binding energy can be expressed in terms of bare neutrons, protons and electrons:

$$B_{\text{nuc}}(A,Z) = c^2\left[Z\cdot m_{\text{atom}}\left({}^1H\right) + (A-Z)\cdot m_{\text{atom}}\left({}^1n\right) - m_{\text{atom}}(A,Z)\right], \tag{3.21}$$
$$\approx c^2\left[Z\cdot\left(m_p+m_e\right) + (A-Z)\,m_n - m_{\text{nuc}}(A,Z) - Z m_e\right], \tag{3.22}$$
$$= c^2\left[Z m_{\text{p}} + (A-Z)\,m_{\text{n}} - m_{\text{nuc}}(A,Z)\right]. \tag{3.23}$$

Another quantity that is often used in astrophysics, is the so-called mass excess Δ. It is defined as the difference in rest mass energy[5] of a given nucleus with A nucleons compared to the mass of the ${}^{12}C$ atom scaled with $A/12$:

$$\Delta(A,Z) = c^2\left[m_{\text{atom}}(A,Z) - \frac{A}{12}m_{\text{atom}}\left({}^{12}C\right)\right], \tag{3.24}$$
$$= c^2\left[m_{\text{atom}}(A,Z) - A\,m_u\right], \tag{3.25}$$

where m_u (or u or AMU) is the unified atomic mass unit. It has a value of $1.660539040(20)\times10^{-24}$ g. The atomic binding energy with respect to the mass excess is given by:

$$B_{\text{nuc}}(A,Z) = Z\cdot\Delta\left({}^1H\right) + (A-Z)\cdot\Delta\left({}^1n\right) - \Delta(A,Z). \tag{3.26}$$

3.1.4 Excited States and Partition Function

As already mentioned, the knowledge of nuclear excited states is especially important in the astrophysical context of hot plasma, as they can be populated by thermal excitations. Of course, many excited states of nuclei have been measured experimentally, but especially for high excitation energies, few to none

[4] Among the first global determination of nuclear masses, was the Semi-empirical Bethe-Weizsäcker mass formula, as described in Bethe & Bacher (1936). It relies on the classical picture of the nucleus as a liquid drop and incorporates some effects that are known from the quantum nature of nucleonic systems.

[5] Δ is usually tabulated in units of keV or MeV.

excited states are known. In this case, they have to be determined theoretically. Based on the knowledge of the excited states, it is then possible to calculate the grand partition function of the nucleus and calculate the fractional abundance of a certain excited state compared to the total abundance of the nucleus as a function of the temperature T.

Based on the assumption that the different excited states in a nucleus are in thermal equilibrium, we know that the statistical ensemble of a certain nucleus will populate states according to the Boltzmann distribution. In the stellar environment, this is achieved by an equilibrium of γ-excitation and γ-deexcitation. The fraction or probability of finding this nucleus in its excited state i is given by:

$$p_i(Z,A,T) = \frac{g_i(Z,A)\, e^{-E_i/k_B T}}{G(Z,A,T)}. \tag{3.27}$$

$G(Z,A,T)$ is the grand (canonical) partition function and is given by:

$$G(Z,A,T) = \sum_i g_i(Z,A)\, e^{-E_i/k_B T}, \tag{3.28}$$

where the $\sum_i$ runs over all possible excited states. $g_i(A,Z)$ is the (degeneracy) number of nuclear states that have the same energy E_i. As nuclear states are usually degenerate with respect to their total intrinsic angular momentum J, the multiplicity of such a state is given by $2J+1$. Hence $G(Z,A,T)$ is given by:

$$G(Z,A,T) = \sum_i (2J+1)\, e^{-E_i/k_B T}. \tag{3.29}$$

I reality, the situation is somewhat more complicated because usually, only the lowest excited states of a nucleus are known, if at all. It this case, the partition function is defined in the following way:

$$G(Z,A,T) = \sum_{i=0}^{n} (2J+1)\, e^{-E_i/k_B T} + \int_{E_n}^{E_{\max}} (2J+1)\, e^{-\epsilon/k_B T}\, \varrho(Z,A,\epsilon)\, d\epsilon, \tag{3.30}$$

where here $\varrho(Z,A,\epsilon)$ is the nuclear level density and the integral goes from the last experimentally or otherwise determined state E_n to some maximum energy $E_{\max}$ that is chosen appropriately (for more details, see e.g. Rauscher & Thielemann, 2000).

3.2 Nuclear Reactions in Stars

In this section, the basic nuclear properties that were derived in Section 3.1 will be combined with the thermodynamic relations for ions in a plasma, obtained in Section 2.2.1 in order to describe the occurrence of nuclear reactions in the stellar environment on a phenomenological level. Additionally, nuclear reactions can be applied to predict the global composition changes as well as their impact on the thermodynamic state of the plasma in which they occur. Many aspects of the discussion are based on the corresponding chapter in Cowan et al. (manuscript in preparation).

It was pointed out in Section 2.3 that inside a star, energy is liberated by transmutation of one nuclear species into another to stabilize it against its own gravitational pull. During such a process, rest mass is converted into kinetic energy, or vice versa. In the earlier case, the reaction would be exothermic, in the latter case, endothermic. Besides this, nuclear reactions are of course also responsible for the nucleosynthesis of elements in the universe heavier that neutrons and protons. Consequently, it will be important to examine in which ways nuclei can react with each other in order to form other nuclei.

In a more strict definition, the nuclear reactions that we want to discuss in this section involve the strong or the electromagnetic force. In the context of astrophysics, they are called "thermonuclear reactions" as the reactants obtain their necessary energy to react due to their thermal motion. Usually, nuclear reactions involving the weak interaction (i.e. those turning a neutron into a proton or vice versa) are treated separately as they involve leptons and have to be described differently. They will be discussed in the next chapter, also because they are of particular importance for our work. Seminal work concerning a complete description of thermonuclear reaction rates for astrophysical problems was performed by Fowler et al. (1967, 1975); Harris et al. (1983); Caughlan et al. (1985); Caughlan & Fowler (1988). Usual nuclear reactions that are relevant in the context of astrophysics - except for certain decays - do not occur at room temperature. Considering a reaction of two charged ions, they become sufficiently energetic only at high-temperature conditions, that allow for tunneling through the potential barrier of the Coulomb repulsion. Another exception would be reactions involving neutrons, as they can react especially well at low energies. They are however usually not very abundant and mainly play a role in scenarios where free neutrons are available in large numbers (e.g. *s*-process or *r*-process).

The following enumeration will give a short overview of the most important nuclear reactions that occur during the evolution of stars as well as during the nucleosynthesis processes in explosive events at the end of a stellar life ($A, B, C, \cdots$ stand for nuclei):

$$\begin{aligned}
\text{fusion}: &\quad A + B \rightarrow C + \{\gamma, n, p, \alpha, \dots\} \\
\text{sp. fission}: &\quad A \rightarrow B + C + \{n, 2n, 3n, \dots\} \\
\text{n—ind fission}: &\quad A + n \rightarrow B + C + \{n, 2n, 3n, \dots\} \\
\gamma\text{—ex./deex.}: &\quad A + \gamma \rightarrow B + \gamma \\
\text{transfer}: &\quad A + \{n, p, \alpha, \dots\} \rightarrow B + \{n, p, \alpha, \dots\} \\
\text{capture}: &\quad A + \{n, p, \alpha, \dots\} \rightarrow B + \gamma \\
\text{photodisint.}: &\quad A + \gamma \rightarrow B + \{n, p, \alpha, \dots\} \\
\text{weak decay}: &\quad A \rightarrow B + e^- / e^+ + \bar{\nu}_e / \nu_e \\
\text{weak capture}: &\quad A + e^- / e^+ \rightarrow B + \nu_e / \bar{\nu}_e \\
\alpha\text{—decay}: &\quad A \rightarrow B + \alpha
\end{aligned}$$

Notice that the γ-excitation and deexcitation processes do not have to be considered explicitly if this process is assumed to be in equilibrium, as will be the case throughout this thesis. For this reason, the equilibrium can be used to determine the probability of populating excited states in nuclei, as was done in Section 3.1.4. Nevertheless, in case the nucleus gets excited by a photon into an excited state from which it can react further, this is taken into account. Such a process would be for example photodisintegration. Excited states that are so high in energy that the nucleus can deexcite via the emission of nucleons, are said to be above the threshold for particle separation.

During any reaction ($i \rightarrow f$), total energy $E = E_{\text{int}} + E_{\text{kin}}$ and total momentum $\vec{p}$ have to be conserved:

$$\sum_i E_i = \sum_f E_f, \tag{3.31}$$

$$\sum_i \vec{p}_i = \sum_f \vec{p}_f, \tag{3.32}$$

where i sums over all reactants in the initial channel and f sums over all reactants in the final channel. This directly leads to a classification of nuclear reactions, originating in the question whether they are releasing or absorbing energy. This means that either kinetic energy is transformed into internal energy

or vice versa. In this context, it is customary to define the Q value of a reaction, which is usually given by the difference in total kinetic energy of the system before and after the reaction:[6]

$$Q = \sum_f E_{\text{kin,f}} - \sum_i E_{\text{kin,i}}. \tag{3.33}$$

If the Q value is negative, the system loses kinetic energy (endothermic) and if the Q value is positive, the system gains kinetic energy (exothermic). Using energy conservation, the Q value can also be calculated from the internal energy of the reactants:

$$Q = \sum_i E_{\text{int,i}} - \sum_f E_{\text{int,f}}. \tag{3.34}$$

$$\tag{3.35}$$

3.2.1 Reaction Rates

A more generic classification of nuclear reactions besides their exact type can be done regarding the number of reactants in the incoming channel, leading to the following scheme:

$$\begin{aligned} A &\to X + \cdots \quad \text{(decay)}, \\ A + B &\to X + \cdots \quad \text{(two-body)}, \\ A + B + C &\to X + \cdots \quad \text{(three-body)}, \end{aligned}$$

where X stands for any arbitrary reaction product. If we think of a nuclear experiment with a beam and a target, a two-body reaction can be described by the reaction cross section σ that is defined in the following way:

$$\sigma = \frac{\text{number of reactions per target nucleus and time}}{\text{flux of incoming particles}}. \tag{3.36}$$

For a constant velocity $v = |\vec{v}_i - \vec{v}_j|$ between reactants i and j, the cross section would be consequently given by:

$$\sigma_{ij} = \frac{r/n_i}{n_j v}, \tag{3.37}$$

where n are the number densities and r is the number of reactions per unit volume. In the context of astrophysics, the velocities of projectile and target follow a certain distribution function. This leads to a more generic expression for the reaction rate r_{ij}:

$$r_{ij} = \frac{1}{1+\delta_{ij}} \int \sigma(v) \cdot |\vec{v}_i - \vec{v}_j| dn_i dn_j, \tag{3.38}$$

where δ_{ij} is zero if i and j are distinguishable particles and one if they are identical. If i and j are nuclei, they can be usually described by a Maxwell-Boltzmann distribution. Hence, their velocity distribution is independent from their number density and depends solely on the temperature. Then, a binary nuclear reaction rate (of type $A + B \to X$) is given by:

$$r_{ij} = \frac{1}{1+\delta_{ij}} n_i n_j \langle \sigma v \rangle_{ij}, \tag{3.39}$$

[6] Notice that for the weak processes considered in Chapter 4, the Q value is defined in a slightly different way.

where $\langle \sigma v \rangle_{ij}$ is the astrophysical two-body reaction rate in units of $\mathrm{cm}^3\mathrm{s}^{-1}$. It can be determined by integrating the velocity dependent cross section $\sigma(v)_{ij}$ over the velocity distribution of the particles. For reactants with similar mass, that each follow a Maxwell-Boltzmann distribution, $\langle \sigma v \rangle_{ij}$ can be written in terms of the center of mass kinetic energy E of projectile and target:

$$\langle \sigma v \rangle_{ij} = \left(\frac{8}{\pi m_{ij}} \right)^{1/2} (k_B T)^{-3/2} \int_0^\infty \sigma_{ij}(E) \cdot E \cdot e^{-E/k_B T} dE, \tag{3.40}$$

where the reduced mass is given by $m_{ij} = \frac{m_i m_j}{m_i + m_j}$ and $\sigma_{ij}(E)$ is now the energy-dependent cross section for the respective reaction channel. By introducing the astrophysical S-factor $S(E)$, the cross section can be written as:

$$\sigma(E) = \frac{S(E)}{E} e^{-2\pi\eta(E)}. \tag{3.41}$$

The factor $\eta(E)$ is the so-called Sommerfeld parameter given by:

$$\eta(E) = \left(\frac{m_{ij}}{2E} \right)^{1/2} \frac{Z_i Z_j e^2}{\hbar}, \tag{3.42}$$

where Z denotes the ion charge. Consequently, $\langle \sigma v \rangle_{ij}$ can be rewritten as follows:

$$\langle \sigma v \rangle_{ij} = \left(\frac{8}{\pi m_{ij}} \right)^{1/2} (k_B T)^{-3/2} \int_0^\infty S(E) e^{-E/k_B T} e^{-2\pi\eta(E)} dE. \tag{3.43}$$

The astrophysical S-factor as such has no physical meaning, but it has the advantage that compared to the cross section, the dominating energy dependency related to the Coulomb barrier penetration, is factored out. Hence, the S-factor should in principle be a more slowly varying function of energy and primarily probe the strong interaction physics of the two reactants or indicate where the rate is dominated by resonances.

At finite temperature, the nuclear excitation spectrum has to be taken into account as well, when determining the cross section. An individual cross section σ only connects two nuclei in a distinct nuclear state with a certain excitation energy. Hence, the total cross section is obtained by summing over all final states and averaging over all initial states of the nucleus, where the probability of finding a nucleus in a certain excited state has to be considered as given by Equation (3.27). Then, the stellar cross section $\sigma^*(E)$ is defined in the following way:

$$\sigma^*(E) = \frac{1}{G(T)} \sum_l (2J_l + 1) \sigma^l(E) e^{-E^l/k_B T} \tag{3.44}$$

where l sums over all possible initial states with excitation energy E^l. Based on Equation (3.44), the the stellar reaction rate $\langle \sigma v \rangle^*_{ij}$ follows directly:

$$\langle \sigma v \rangle^*_{ij} = \left(\frac{8}{\pi m_{ij}} \right)^{1/2} (k_B T)^{-3/2} \int_0^\infty \sigma^*(E) \cdot E \cdot e^{-E/k_B T} dE. \tag{3.45}$$

Notice that we will not enter into the discussion on how individual cross sections can be either measured or calculated. Experimentally, one problem that frequently occurs, is that projectile energies that correspond well to typical astrophysical conditions in terms of temperature, are usually very low and hence their experimental determination can be very challenging. In many cases, the cross section has to be

extrapolated to low energies in order to allow for the determination of astrophysical reaction rates at the appropriate conditions.

The next step will be to determine the abundance changes related to a certain binary reaction $A+B \rightarrow X$. Using the abundance definition as introduced in Section 2.2.1, the basic abundance evolution equation has the following form:

$$\frac{dY_a}{dt} = -\frac{\varrho}{m_u} Y_a Y_b \langle \sigma v \rangle_{AB \rightarrow X}, \tag{3.46}$$

where $m_u^{-1}\langle \sigma v \rangle$ has units of $\mathrm{cm}^{-3}\ \mathrm{s}^{-1}\ \mathrm{g}^{-1}$.[7] Even though, three-body reactions were not discussed in detail, a trinary reaction is represented by the following abundance evolution equation:

$$\frac{dY_A}{dt} = -\left(\frac{\varrho}{m_u}\right)^2 Y_A Y_B Y_C \langle ABC \rangle, \tag{3.47}$$

where $m_u^{-2}\langle ABC \rangle$ has units of $\mathrm{cm}^6\ \mathrm{s}^{-1}\ \mathrm{g}^{-2}$.

Now, we want to discuss reactions that can be described by a decay. Of course, there are "true decays" like α, β-decay, where the nucleus is radioactive by itself. Then, the only relevant quantity is its decay rate λ. But more importantly, also reactions, where a photon is in the incoming channel, can be described as "decays". This originates from the fact that the momentum transfer of the photon to the nucleus is typically neglected. Then, a reaction like photodisintegration can be described as the decay of a nucleus from an excited state after the absorption of a photon ($A \rightarrow X$). The rate $r_{\gamma A \rightarrow X}$ of a photodisintegration reaction can be expressed as follows:

$$r_{\gamma A \rightarrow X} = \frac{n_A}{\pi^2 c^2 \hbar^3} \int_0^\infty \sigma\left(E_\gamma\right) E_\gamma^2 \frac{1}{e^{E_\gamma / k_B T} - 1}, \tag{3.48}$$

$$= n_A \lambda_\gamma\left(E_\gamma\right). \tag{3.49}$$

In that case and for all other types of decays, the abundance change of the decaying nuclear species is given by:

$$\frac{dY_A}{dt} = -\lambda_{A \rightarrow X} Y_A, \tag{3.50}$$

where $\lambda_{A \rightarrow X}$ is the decay constant in units of s^{-1}.

Analogous to chemical reactions, every nuclear reaction can occur in the reverse direction with a certain probability, as well (e.g. $A + B \leftrightarrows C + D$). Of course, both reaction cross sections could be measured or computed independently. This approach is not only more cumbersome but also makes it more likely that at conditions, where both reactions might be in chemical equilibrium (see Section 3.2.4), the equilibrium configuration is wrong. Nevertheless, there is a handy way to relate both processes via "detailed balance". For reactions of type $A + B \leftrightarrows C + D$, the stellar reaction rates can be related with each other in the following way:

$$\langle \sigma v \rangle_{CD} = \frac{1 + \delta_{CD}}{1 + \delta_{AB}} \frac{G_A G_B}{G_C G_D} \left(\frac{m_{AB}}{m_{CD}}\right)^{3/2} e^{-Q/k_B T} \langle \sigma v \rangle_{AB}, \tag{3.51}$$

[7] Notice that in many references like Cyburt et al. (2010), a binary reaction rate is given as $N_A\langle \sigma v \rangle$ which means it has units of $\mathrm{cm}^{-3}\ \mathrm{s}^{-1}\ \mathrm{mol}^{-1}$. In this way, the abundance Y would also be defined as the molar fraction (mole per gram). Then the basic abundance evolution equation for a reaction $A + B \rightarrow X$ would be given by: $dY_A/dt = -\varrho N_A Y_A Y_B \langle \sigma v \rangle_{AB \rightarrow X}$. Following this definition makes it hard to understand dY/dt as particle flux.

where $Q = c^2\,(m_A + m_B - m_C - m_D)$, G are the nuclear partition functions as defined in Section 3.1.4 and m are the reduced masses. For a reaction involving photons (e.g. $A + B \leftrightarrows C + \gamma$), it can be shown that:

$$\lambda_C = \frac{G_A G_B}{G_C\,(1+\delta_{AB})}\left(\frac{m_A m_B}{m_C}\right)^{3/2}\left(\frac{k_B T}{2\pi\hbar^2}\right)^{3/2} e^{-Q/k_B T}\,\langle\sigma\,v\rangle_{AB}, \tag{3.52}$$

and in this case, Q is given by $Q = c^2\,(m_A + m_B - m_C)$.

Finally, it may be useful to estimate the timescale τ_{nuc} of a nuclear reaction given by the rate $\langle\sigma\,v\rangle_{AB\to X}$. this can be done in the following way:

$$\frac{1}{\tau_{\mathrm{nuc}}} = \left|\frac{1}{Y_a}\frac{dY_a}{dt}\right| = \left(\frac{\varrho}{m_u}\right) Y_B \langle\sigma\,v\rangle_{AB\to X}. \tag{3.53}$$

3.2.2 Nuclear Reaction Networks

In an astrophysical plasma, a multitude of different reactions can occur at the same time and every nuclear species can be created or destroyed by many different reactions. If one is interested in tracking the abundance evolution for i different isotopes, then this will result in i coupled differential equations. By accounting for all possible one-, two- or three-body reactions, as defined in Section 3.2, the abundance change of species i is given by:

$$\frac{dY_i}{dt} = \sum_j N_i \lambda_j Y_j + \sum_{j,k} \frac{N_i}{|N_j|!\;|N_k|!}\left(\frac{\varrho}{m_u}\right)\langle\sigma\,v\rangle_{jk} Y_j Y_k + \tag{3.54}$$

$$+ \sum_{j,k,l} \frac{N_i}{|N_j|!\;|N_k|!\;|N_l|!}\left(\frac{\varrho}{m_u}\right)^2 \langle\sigma\,v\rangle_{jkl} Y_j Y_k Y_l, \tag{3.55}$$

where j, k, l run over all reactions that either produce or destroy nucleus i. Additionally, N_i counts the amount of nuclei of species i created or destroyed in this reaction.

Computationally, this problem is very challenging as soon as a lot of different nuclear species have to be considered. The reason is that a nuclear reaction network represents an extraordinarily stiff system of coupled non-linear differential equations, where the standard solution techniques either fail or are very inefficient. A lot of details concerning the computational challenge in solving nuclear reaction networks are discussed for example in Timmes (1999).

For astrophysical simulations that require large nuclear reaction networks, it is customary to rely on reaction rate libraries that contain all experimentally measured and theoretically determined reaction rates, typically parametrized as a function of temperature. In this context, the most up-to-date and complete tabulation of nuclear reaction rates is the "JINA Reaclib" database (Cyburt et al., 2010). Other databases are for example the BRUSLIB database (Xu et al., 2013). As the JINA Reaclib database will be used throughout this thesis, it is useful to briefly introduce its rate parametrization. All reaction rates (decay,two-body,three-body) are given by a seven-parameter fit as a function of temperature:

$$\lambda(T) = \exp\left[a_0 + \sum_{i=1}^{5} a_i \left(\frac{T}{10^9\ \mathrm{K}}\right)^{(2i-5)/3} + a_6 \ln\left(\frac{T}{10^9\ \mathrm{K}}\right)\right], \tag{3.56}$$

where λ has units of of s^{-1} for a decay, units of of $\mathrm{cm}^{-3}\ \mathrm{g}^{-1}\ \mathrm{s}^{-1}$ for a two-body reaction and units of of $\mathrm{cm}^{6}\ \mathrm{g}^{-2}\ \mathrm{s}^{-1}$ for a three-body reaction.

3.2.3 Energy Generation

In many cases, the energy release from nuclear reactions is a crucial ingredient for the correct solution of an astrophysical problem, like for stellar evolution (see Equation (2.125)). Hence, it is important to determine the energy generation $\dot{q}$ (energy per unit mass and time) due to thermonuclear reactions (excluding weak reactions). As already pointed out, the energy generated in thermonuclear reactions corresponds to the change of the total ion mass. Hence, it follows directly that $\dot{q}$ is given by:

$$\dot{q}_{\text{thermo,mass}} = -\frac{1}{m_u} \sum_i \frac{dY_i}{dt} m_i c^2, \tag{3.57}$$

or in terms of energy per unit time and baryon:

$$\dot{q}_{\text{thermo,baryon}} = -\sum_i \frac{dY_i}{dt} m_i c^2. \tag{3.58}$$

Notice that for thermonuclear reactions, meaning that no leptons are involved, m_i can be either the atomic mass, the nuclear mass, or the mass excess as defined in Equation (3.25), because the total amount of electrons in conserved and their binding energy is neglected. For weak processes, this is not the case and this is reflected in their energy generation, as will be discussed in Section 4.4.2.

3.2.4 Nuclear Statistical Equilibrium

Under certain conditions, thermonuclear reaction rates (forward and reverse rates) proceed sufficiently fast that the timescale to reach chemical equilibrium is shorter than other relevant timescales in the problem of interest (e.g. the hydrodynamic evolution timescale). In the context of nuclear burning processes in stars, this chemical equilibrium is called nuclear statistical equilibrium (NSE, see Clifford & Tayler, 1965). Typically, it is present when temperatures exceed $4-5 \times 10^9$ K. In such conditions, capture reactions (p, n, α) will proceed very rapidly because particles are energetic enough to overcome Coulomb barriers. Additionally, there are sufficiently many high-energy photons in the Planck distribution to ensure that the photodisintegration of nuclei will occur at a high rate, as well. As a consequence, all nuclear abundances will eventually reach a chemical equilibrium state where individual reaction rates become irrelevant and the abundance of nuclei depends exclusively on few local thermodynamic variables (i.e. T, ϱ, Y_e). Notice that this equilibrium only refers to nuclear reactions that are mediated by the strong and the electromagnetic interaction, not the weak interaction. This has essentially two reasons. First of all, weak reactions typically occur on a significantly longer timescale and hence do not reach an equilibrium comparably fast. And second of all, they would continuously produce neutrinos that under most conditions escape from the location of interest and thereby represent an energy leakage. Therefore, such an equilibrium can only be achieved if not only the neutrino producing reactions are in equilibrium but also the neutrino absorbing reactions. In present time, this would require extremely high densities in excess of 10^{13} g cm^{-3} that can only be achieved inside an object as dense as a NS.[8] In NSE, the only nuclear input that is required in such a situation, are the nuclear masses and the nuclear partition functions G (see Section 3.1.4).

If all reactions are in chemical equilibrium, then - by definition - the free energy F is at its minimum. This directly leads to the following expression that relates the chemical potentials μ of all nuclei with each other.

$$\sum_{i=1} \mu_i dY_i = 0. \tag{3.59}$$

[8] Notice that in the early universe weak equilibrium was attained as well, despite much lower densities. Neutrinos decoupled from the rest of the universe ≈ 1 s after Big Bang.

In order to find the correct minimum of F, it is important to take the two following constraints for the minimization into account:

$$\sum_i A_i Y_i = \sum_i X_i = 1, \tag{3.60}$$

$$\sum_i Z_i Y_i = Y_e. \tag{3.61}$$

Equation (3.60) and (3.61) together constrain ϱ and Y_e that have to be given as input for the determination of the NSE composition. If all reactions are in equilibrium, then obviously also the following two relations have to be valid for each nucleus that is abundant:

$$\mu(Z,N) + \mu_n = \mu(Z,N+1), \tag{3.62}$$

$$\mu(Z,N) + \mu_p = \mu(Z+1,N). \tag{3.63}$$

Hence, the chemical potential of each nucleus can be directly given by the neutron and proton chemical potential, resulting in the following expression:

$$N \cdot \mu_n + Z \cdot \mu_p = \mu(Z,N). \tag{3.64}$$

If we assume that all nuclei are described by a Maxwell-Boltzmann distribution, we can rewrite Equation (2.40) in terms of an abundance Y_i and get:

$$\mu_i = m_i \cdot c^2 + k_B T \times \ln\left[\frac{\varrho}{m_u}\frac{Y_i}{G_i}\left(\frac{2\pi\hbar^2}{m_i k_B T}\right)^{3/2}\right]. \tag{3.65}$$

Combining Equations (3.64) and (3.65), and assuming that $m_n \approx m_p \approx m_u$, yields a general expression for the abundance of any nucleus $Y(Z,N)$ in NSE:

$$Y(Z,N) = G(T,Z,N)\left(\frac{\varrho}{m_u}\right)^{A-1}\frac{A^{3/2}}{2^A}\left(\frac{2\pi\hbar^2}{m_u k_B T}\right)^{1.5(A-1)}\exp\left[\frac{B_{\mathrm{nuc}}(Z,N)}{k_B T}\right]Y_n^N Y_p^Z, \tag{3.66}$$

where $B_{\mathrm{nuc}}(Z,N)$ is the nuclear binding energy as defined in Equation (3.20) and the partition function G is defined as in Equation (3.29). Hence, for given T and ϱ, we can relate every nuclear abundance entirely to the abundance of free neutrons and protons, which has yet to be determined. As a consequence, for a system with N_{nuc} different nuclear species, we end up with $(N_{\mathrm{nuc}}-2)$ times Equation (3.66) together with Equations (3.60) and (3.61). This system of equations is determined and can be solved exactly through iteration by guessing Y_n and Y_p. The solution is found by adjusting their ratio if the obtained Y_e is wrong and adjusting their product if $\sum_i X_i$ is wrong. In total, the NSE abundance depends only on three independent and local variables, being T, ϱ and Y_e.

It should be added that, even though NSE occurs at high temperatures, conditions at high densities ($\varrho \gtrsim 10^8$ g cm^{-3}) that host nuclei in NSE with large average charge number $\langle Z \rangle$ can make it necessary to incorporate Coulomb corrections into the description of the NSE abundances. This is because the Coulomb interaction of the ions in the dense plasma becomes non-negligible. In Bravo & García-Senz (1999), this is discussed in detail. In Section 4.4.5, the ion Coulomb correction is quantified in terms of an ion chemical potential shift μ_C, that can be readily incorporated into the description of NSE abundances. Consequently, Equation (3.65) can be rewritten as:

$$\mu_i = m_i \cdot c^2 + \mu_{i,C} + k_B T \times \ln\left[\frac{\varrho}{m_u}\frac{Y_i}{G_i}\left(\frac{2\pi\hbar^2}{m_i k_B T}\right)^{3/2}\right], \tag{3.67}$$

and Equation (3.66) is consequently given by:

$$\begin{aligned} Y(Z,N) = G(T,Z,N)\left(\frac{\varrho}{m_u}\right)^{A-1}\frac{A^{3/2}}{2^A}\left(\frac{2\pi\hbar^2}{m_u k_B T}\right)^{1.5(A-1)} \times \\ \times \exp\left[\frac{B_{\mathrm{nuc}}(Z,N) + N\mu_{n,C} + Z\mu_{p,C} - \mu_C(N,Z)}{k_B T}\right]Y_n^N Y_p^Z. \end{aligned} \tag{3.68}$$

4 Electron Capture and Emission in Stars

4.1 Weak Interaction

The weak interaction is one of the four fundamental forces and responsible for a diversity of observable phenomena in physics, the most prominent process being the radioactive β-decay of nuclei. According to the Standard Model of particle physics (SM), the weak interaction is mediated by the exchange of force carriers, the $W^{\pm}$ and Z gauge bosons. The weak interaction can be unified with the electromagnetic interaction in the framework of the electroweak theory. The fact that the $W^{\pm}$ and Z bosons have—in contrast to the photon, which mediates the electromagnetic interaction—a non-vanishing mass of $m_W = 80.385$ GeV and $m_Z = 91.1876$ GeV, respectively, is explained via the "spontaneous symmetry breaking Higgs mechanism". Like the other force carriers, the $W^{\pm}$ and Z bosons are vector bosons, meaning that they have a spin of 1 (in units of $\hbar$).

Besides gravity, the weak interaction is the only force that acts on all observed fermions [1]. If a particle participates in the weak interaction, it has to posses a corresponding "charge" that is usually called weak isospin T_3 (there are also other naming conventions for the weak isospin). During any weak interaction process, the total weak isospin T_3 is a conserved quantity. As the weak bosons have a very large mass, they only exist for a very short time (about 10^{-25} s). Consequently, the range of the force is limited as well. We can approximate the range to be $r_{\text{weak}} = \hbar / \left(m_{W^{\pm},Z}\, c\right) \approx 2.5 \times 10^{-3}$ fm. As already indicated by its name, the weak force is "weak" compared to other forces, meaning that the strength of the interaction is several orders of magnitude smaller compared to processes involving the strong or the electromagnetic force. As a direct consequence, weak processes can only become relevant if processes which are mediated by the strong or electromagnetic force cannot occur. For example, charged pions $\pi^{\pm}$ can only decay "weakly", mainly via the muonic channel: $\pi^{\pm} \rightarrow \mu^{\pm} + \nu_{\mu}/\bar{\nu}_{\mu}$. As the neutral pion π^0 can also decay electromagnetically, mainly via $\pi^0 \rightarrow \gamma + \gamma$, we would intuitively expect that it has a much shorter lifetime than the charged pion, which is indeed the case. While $\pi^{\pm}$ mesons have a mean lifetime of 2.6×10^{-8} seconds, the lifetime of the π^0 meson is only 8.4×10^{-17} seconds. However, only the weak interaction can change the flavor state of quarks via the exchange of $W^{\pm}$ bosons. The best known example is of course the β^- decay in a nucleus where a d quark inside a neutron is converted into an u quark, hence transforming the nucleon into a proton. The involved W^- boson decays into an electron and an electron antineutrino.

One achievement of the SM is the above mentioned unification of the electromagnetic and the weak interaction into one electroweak interaction. The SM of particle physics is a gauge quantum field theory based on the symmetry group $SU(3)_c \otimes SU(2)_L \otimes U(1)_Y$ that contains all known fundamental particles, being leptons, quarks, gauge bosons and the Higgs boson, together with their interactions except gravity (electromagnetic, weak & strong). The SM can explain the majority of observable phenomena in physics with some well known exceptions like non-vanishing neutrino masses & neutrino oscillations. As it does not incorporate aspects of general relativity, it also fails to explain several aspects of cosmology like the accelerated expansion of the universe.

In the SM, not only the weak interaction but all contained interactions are mediated via vector bosons. While the $SU(3)_c$ part describes the strong force with eight massless gluons, the $SU(2)_L \otimes U(1)_Y$ part gives rise to the electroweak force with the massless photon and the three massive bosons $W^{\pm}$ & Z.

[1] There are proposed particles like the sterile neutrino, which only interact gravitationally.

All SM fermions are listed in Table 4.1 together with their properties in the symmetry broken sector in terms of the electric charge Q, the weak isospin T_3, their color content and their chirality (left-handed or right-handed, short explanation follows). Both leptons and quarks are each structured in three families (or generations) of fermions which, except for their mass & flavor, have identical properties. Within each family, the left-handed fields are doublets ($T_3 = -1/2, 1/2$) with respect to the weak isospin and the right-handed fields are singlets ($T_3 = 0$). Hence, all left-handed leptons ($e^-, \mu^-, \tau^-, \nu_e, \nu_\mu, \nu_\tau$) form a doublet and the charged leptons (e^-, μ^-, τ^-) form a weak isospin singlet. Notice that in the SM, right-handed neutrinos do not exist. In a similar manner, the quarks can be grouped into a left-handed isospin doublet and a right-handed isospin singlet.

chirality	LH fermions / RH antifermions			RH fermions / LH antifermions		
type/generation	1st	2nd	3rd	1st	2nd	3rd
quarks	$u/\bar{u}$	$c/\bar{c}$	$t/\bar{t}$	$u/\bar{u}$	$c/\bar{c}$	$t/\bar{t}$
mass (GeV)	0.0023	1.275	173.07	0.0023	1.275	173.07
weak isospin T_3	$+\frac{1}{2}/-\frac{1}{2}$	$+\frac{1}{2}/-\frac{1}{2}$	$+\frac{1}{2}/-\frac{1}{2}$	0	0	0
electric charge Q	$+\frac{2}{3}/-\frac{2}{3}$	$+\frac{2}{3}/-\frac{2}{3}$	$+\frac{2}{3}/-\frac{2}{3}$	$+\frac{2}{3}/-\frac{2}{3}$	$+\frac{2}{3}/-\frac{2}{3}$	$+\frac{2}{3}/-\frac{2}{3}$
color (strong int.)	yes	yes	yes	yes	yes	yes
quarks	$d/\bar{d}$	$s/\bar{s}$	$b/\bar{b}$	$d/\bar{d}$	$s/\bar{s}$	$b/\bar{b}$
mass (GeV)	0.0048	0.095	4.18	0.0048	0.095	4.18
weak isospin T_3	$-\frac{1}{2}/+\frac{1}{2}$	$-\frac{1}{2}/+\frac{1}{2}$	$-\frac{1}{2}/+\frac{1}{2}$	0	0	0
electric charge Q	$-\frac{1}{3}/+\frac{1}{3}$	$-\frac{1}{3}/+\frac{1}{3}$	$-\frac{1}{3}/+\frac{1}{3}$	$-\frac{1}{3}/+\frac{1}{3}$	$-\frac{1}{3}/+\frac{1}{3}$	$-\frac{1}{3}/+\frac{1}{3}$
color (strong int.)	yes	yes	yes	yes	yes	yes
leptons	$\nu_e/\bar{\nu}_e$	$\nu_\mu/\bar{\nu}_\mu$	$\nu_\tau/\bar{\nu}_\tau$	$(\nu_e/\bar{\nu}_e)$ [2]	$(\nu_\mu/\bar{\nu}_\mu)$	$(\nu_\tau/\bar{\nu}_\tau)$
mass (GeV)	0	0	0	0	0	0
weak isospin T_3	$+\frac{1}{2}/-\frac{1}{2}$	$+\frac{1}{2}/-\frac{1}{2}$	$+\frac{1}{2}/-\frac{1}{2}$	0	0	0
electric charge Q	0 [3]	0	0	0	0	0
color (strong int.)	no	no	no	no	no	no
leptons	e^-/e^+	μ^-/μ^+	τ^-/τ^+	e^-/e^+	μ^-/μ^+	τ^-/τ^+
mass (GeV)	0.0005111	0.105658	1.77682	0.0005111	0.105658	1.77682
weak isospin T_3	$-\frac{1}{2}/+\frac{1}{2}$	$-\frac{1}{2}/+\frac{1}{2}$	$-\frac{1}{2}/+\frac{1}{2}$	0	0	0
electric charge Q	$-1/+1$	$-1/+1$	$-1/+1$	$-1/+1$	$-1/+1$	$-1/+1$
color (strong int.)	no	no	no	no	no	no

Table 4.1: Fermions and antifermions in the Standard Model of particles.

In the context of the weak interaction, the above mentioned handedness is related to the (Lorentz-invariant) chirality of the fermions (not to be confused with their helicity). The weak interaction is a chiral interaction, meaning it distinguishes the chirality (or handedness) of the involved fermions. As we will see later, this is an observational fact that has been used to formulate the electroweak theory. From Table 4.1, we can see that left- and right handed particles in the SM do not have the same weak isospin T_3, hence they will not couple in the same way to the weak interaction. The chirality of a fermion is an abstract concept that follows from its quantum mechanical description as Dirac spinors, where the wave function of a Dirac particle can be decomposed into a left-handed chirality and a right-handed chirality

[2] There is no established mechanism to produce chiral right-handed neutrinos or chiral left-handed anti-neutrinos. If they would exist, they would not interact via any of the SM forces. That holds true even if we account for their non-vanishing mass, because the right-handed coupling of the weak force due to the Z boson requires the particle to have electric charge.

[3] Within the SM, neutrinos are massless and therefore do not oscillate.

part. The general meaning of chirality is not easy to understand unless the particles are massless. In this case, the helicity and the chirality of the particle are equivalent. The helicity of a particle is simply defined as the projection of its angular momentum onto the translational momentum. For elementary fermions with spin $1/2$, positive helicity simply means that spin and momentum vector are aligned, and negative helicity that they are anti-aligned. It is clear that for massive particles, the helicity is not a Lorentz-invariant quantity as there is always a frame of reference that moves faster in the direction of the particles motion than the particle itself. In this frame of reference, the particle can be observed with opposite helicity. The chirality of a particle in contrast, is an internal property that, as we learned before, cannot be changed by a Lorentz-boost.

One peculiarity of the SM is that the prevalent gauge symmetry is spontaneously broken by the vacuum via the Higgs mechanism below a critical energy scale:

$$SU(3)_c \otimes SU(2)_L \otimes U(1)_Y \xrightarrow{SSB} SU(3)_c \otimes U(1)_{QED}. \tag{4.1}$$

This leads to various consequences. First of all, the Higgs mechanism generates the masses of the weak gauge bosons which requires the introduction of a scalar boson (Spin=0) in the SM, the so-called "Higgs particle". Additionally, it also generates the fermion masses and mixings. Initially, the unbroken electroweak interaction is given by the $SU(2)_L \otimes U(1)_Y$ gauge group. The corresponding gauge bosons are the W_1, W_2, W_3 bosons that form a triplet of weak isospin T_3 generated by the $SU(2)$ part and the B boson singlet of the weak hypercharge Y, which is the generator of the $U(1)_Y$ group. All of them are by definition massless. Note that all existing fermions have a weak hypercharge different from 0. Due to spontaneous symmetry breaking, the $W^{\pm}$ and Z bosons and the photons are created.[4] The generator of $U(1)_{QED}$ is given by the electric charge $Q = Y/2 + T_3$. The observable electroweak bosons can now be expressed in terms of the bosons in the unbroken sector:

$$\begin{pmatrix} \Psi_\gamma \\ \Psi_Z \end{pmatrix} = \begin{pmatrix} \cos\Theta_W & \sin\Theta_W \\ -\sin\Theta_W & \cos\Theta_W \end{pmatrix} \begin{pmatrix} \Psi_B \\ \Psi_W \end{pmatrix}, \tag{4.2}$$

and

$$\begin{pmatrix} \Psi_{W^+} \\ \Psi_{W^-} \end{pmatrix} = \frac{1}{\sqrt{2}} \begin{pmatrix} 1 & i \\ 1 & -i \end{pmatrix} \begin{pmatrix} \Psi_{W^1} \\ \Psi_{W^2} \end{pmatrix}. \tag{4.3}$$

The only unknown in this scheme is the so-called Weinberg mixing angle or weak mixing angle Θ_W, which cannot be extracted from the SM and has to be measured experimentally.[5] As already mentioned, the Higgs mechanism gives the $W^{\pm}$ & Z bosons its mass. The ratio of their masses can be used to calculate Θ_W as follows: $\cos\Theta_W = m_W/m_Z \approx 0.8768$. The mass of the $W^{\pm}$ bosons is 80.385 GeV and the Z boson has a mass of 91.1876 GeV.

The Weinberg mixing also has consequences for the coupling strength (here Q) of the gauge bosons to the corresponding charge. For $W^{\pm}$ bosons it is given by

$$Q_W = g\,T_3 \tag{4.4}$$

and for the Z boson by

$$Q_Z = \frac{g}{\cos\Theta_W}\left(T_3 - Q\sin^2\Theta_W\right), \tag{4.5}$$

where g is the weak coupling constant.

[4] This symmetry breaking phase has probably occurred during the quark epoch in the early universe, shortly after the Big Bang.

[5] Note that Θ_W is in general a function of the momentum transfer q.

One important point that we addressed briefly already, is the fact that the weak interaction distinguishes the chirality of the particles that are involved in the interaction. Only left-handed fermions and right-handed antifermions couple to the $W^{\pm}$ boson, as their counterparts with opposite chirality carry no weak charge ($T_3 = 0$). If this is true, the weak force has to break parity-symmetry. First, this has been found experimentally by Wu et al. (1957) and was consequently incorporated into the theory of weak interaction. As mentioned before, the $W^{\pm}$ boson completely distinguishes between right-handed and left-handed particles/antiparticles. This means that the weak interaction involving the $W^{\pm}$ boson, breaks parity maximally. At this point, it should be mentioned that the Z boson couples also to right-handed fermions and left-handed antifermions via the Weinberg mixing, in case they carry an electric charge (see Equation (4.5)). In the electroweak unification of the weak interaction, it can be shown that the Z boson contains a component of the B_0 boson that acts also in the electromagnetic sector and is not parity violating. As a consequence, the weak interaction involving the Z boson is in general not maximally parity violating. Even though parity is not conserved in the weak interaction, it was thought that the combined symmetry of charge and parity (CP) would still obey a conservation law. However, not much later, it was shown experimentally that CP symmetry is violated by the weak interaction as well (Christenson et al., 1964). This can be incorporated into the SM by introducing a complex phase δ_{13} into the quark mixing matrix that we will introduce in the next section.

4.2 Weak Processes

The weak interaction can be divided into several subgroups based on the nature of its occurrence. First of all, if a weak process involves the $W^{\pm}$ bosons, it is called a "charged-current interaction", as these bosons carry an electric charge of $Q = 1$. If the interaction is mediated by the charge-neutral Z boson ($Q = 0$), it is called the "neutral-current interaction". In a second step, weak interactions can be classified based on their participating elementary fermions. If only leptons are participating, the reaction is called leptonic, if only quarks (or quark bound states such as baryons & mesons) are participating, it is called hadronic (or non-leptonic) and in case quarks as well as leptons participate, the reaction is called semi-leptonic. Charged currents can only transform particles within the same doublet. For the three leptonic doublets

$$\begin{pmatrix} \nu_e \\ e \end{pmatrix}, \begin{pmatrix} \nu_\mu \\ \mu \end{pmatrix}, \begin{pmatrix} \nu_\tau \\ \tau \end{pmatrix}, \tag{4.6}$$

the W^+ boson climbs up and the W^- climbs down in T_3. For hadronic processes (i.e. the flavor conversion of quarks), the three doublets look as follows:

$$\begin{pmatrix} u \\ d' \end{pmatrix}, \begin{pmatrix} c \\ s' \end{pmatrix}, \begin{pmatrix} t \\ b' \end{pmatrix}. \tag{4.7}$$

The $W^{\pm}$ bosons act in the same way as for the leptonic doublets. Nevertheless, there is an important difference. The quark doublets are only eigenstates of the weak interaction (for the lower part of the doublet indicated as quark$'$), but not of free quarks themselves, which in contrast are mass eigenstates and non-dashed in our notation. It can be shown that the dashed quark states relate to the non-dashed quark states via a generalized rotation (implying that the transformation is unitary) described by the CKM matrix:

$$\begin{pmatrix} d' \\ s' \\ b' \end{pmatrix} = V_{\mathrm{CKM}} \begin{pmatrix} d \\ s \\ b \end{pmatrix} = \begin{pmatrix} V_{ud} & V_{us} & V_{ub} \\ V_{cd} & V_{cs} & V_{cb} \\ V_{td} & V_{ts} & V_{tb} \end{pmatrix} \begin{pmatrix} d \\ s \\ b \end{pmatrix}. \tag{4.8}$$

Notice that it would be analogous to define the CKM-matrix in Equation (4.8) with up-type quarks, as the definition with down-type quarks is arbitrary. Defining the matrix in the above way means that for up-type quarks the interaction eigenstates and the mass eigenstates are equal:

$$\begin{pmatrix} u' \\ c' \\ t' \end{pmatrix} = \begin{pmatrix} u \\ c \\ t \end{pmatrix} \tag{4.9}$$

According to the particle data group (Patrignani, 2016), the best current fit (omitting the explicit statement of the errors which are given in the reference) of the absolute values of the CKM matrix elements is given by:

$$|V_{\mathrm{CKM}}| = \begin{pmatrix} 0.97427 & 0.22536 & 0.00355 \\ 0.22522 & 0.97343 & 0.0414 \\ 0.00886 & 0.0405 & 0.99914 \end{pmatrix}. \tag{4.10}$$

One example for a leptonic process is the muon decay: $\mu^- \rightarrow e^- + \bar{\nu}_e + \nu_\mu$. Here, the muon decays into an muon neutrino and a W^- boson, with the latter decaying into an electron and an electron antineutrino. A semileptonic process is for example the β-decay, which on the quark level has the form: $d \rightarrow u + e^- + \bar{\nu}_e$. A hadronic process is the Kaon decay: $K^+ \rightarrow \Pi^0 + \Pi^+$ (or on the quark level: $u + \bar{s} \rightarrow u + \bar{u} + u + \bar{d}$). Notice that all of these examples were charged current processes. As the Z bosons carries neither weak isospin nor electric charge, it usually describes scattering processes like neutrino-electron scattering: $\nu_e + e^- \longleftrightarrow \nu_e + e^-$. One should also mention, that there is no neutral-current mixing between quarks of different generations as is the case for charged-current reactions.

4.3 Electron and Positron Emission and Capture

On earth, the weak interaction occurs most notably via β-decay involving unstable nuclei. However, there are astrophysical events with extreme conditions like CCSNe or neutron-star mergers, where neutrino-induced weak reactions can become relevant. Under normal conditions, quarks are confined in color-free objects, i.e. hadrons of which only neutrons and protons are abundant. The free neutron can decay via a weak process into a proton, but not vice versa, because the neutron is about 1.5 MeV heavier than the proton. Proton decay is only possible inside a nucleus, where a distinct shell structure exists that makes such kind of decay energetically favorable. Hence, if we want to investigate the nature of β-decay at low energies, the relevant degrees of freedom are neutrons and protons. This implies that the understanding of processes like β-decay is tightly connected to nuclear physics. Here, the weak interaction is of particular interest because of all processes involving nuclei, only the weak interaction is capable of changing the isospin projection T_z of a given nucleus (see Section 3.1) and by doing so, turning a proton inside the nucleus into a neutron or vice versa. Compared to strong and electromagnetic processes, nuclear β-decay is considerably slower, hence it only becomes observable if other processes are prohibited.

In addition to β-decay, also another process exists, which is called electron capture (EC). Under normal conditions, this process occurs when proton-rich nuclei absorb an electron from the atomic electron cloud, usually from the K or L shell. Thereby a proton changes into a neutron and simultaneously emits an electron neutrino. The same process can also occur in astrophysical plasma, where the electron number density is sufficiently high to make it likely for a nucleus to capture an electron from the surrounding plasma. In the following, the focus will be on stellar weak reactions. In particular, this means that EC always refers to the absorption of an electron from the continuum of electron states in the plasma and not to the capture of an electron from the atomic shell. In a very hot plasma, where positrons are thermally produced by pair production, they can be captured by nuclei as well (positron capture, PC). Both

β-decay and EC/PC are semi-leptonic charged-current processes. On the elementary level of quarks, they can be described as follows:

$$\begin{aligned}
\beta^-\text{—decay} &: (udd) \rightarrow (uud) + e^- + \bar{\nu}_e, && (4.11)\\
\text{positron capture} &: (udd) + e^+ \rightarrow (uud) + \bar{\nu}_e, && (4.12)\\
\beta^+\text{—decay} &: (uud) \rightarrow (udd) + e^+ + \nu_e, && (4.13)\\
\text{electron capture} &: (uud) + e^- \rightarrow (udd) + \nu_e. && (4.14)
\end{aligned}$$

Confined inside a nucleus with mass number A, neutron number N and proton number Z, the processes look like this:

$$\begin{aligned}
\beta^-\text{—decay} &: A(Z,N) \rightarrow A(Z+1,N-1) + e^- + \bar{\nu}_e, && (4.15)\\
\text{positron capture} &: A(Z,N) + e^+ \rightarrow A(Z+1,N-1) + \bar{\nu}_e, && (4.16)\\
\beta^+\text{—decay} &: A(Z,N) \rightarrow A(Z-1,N+1) + e^+ + \nu_e, && (4.17)\\
\text{electron capture} &: A(Z,N) + e^- \rightarrow A(Z-1,N+1) + \nu_e. && (4.18)
\end{aligned}$$

In terms of energetics, the Q value of a reaction is of particular interest. From Section 3.2, it is known that the Q value of a reaction is typically defined as the difference between the kinetic energies of initial and final particles. Thus, a reaction is exothermic if the kinetic energy increases during the process and endothermic if it decreases (see e.g. Wong, 1998). If we exclude the neutrino rest mass, the recoil energy of the nucleus and the electron binding energy (all of them usually being small corrections), we find for the Q value in terms of atomic masses:

$$\begin{aligned}
Q_{\beta^-} &= E_\nu + E_e = m_{\text{atom}}(Z,N)\,c^2 - m_{\text{atom}}(Z+1,N-1)\,c^2 + E_i - E_f, && (4.19)\\
Q_{pc} &= E_\nu - E_p = m_{\text{atom}}(Z,N)\,c^2 - m_{\text{atom}}(Z+1,N-1)\,c^2 + 2m_e c^2 + E_i - E_f, && (4.20)\\
Q_{\beta^+} &= E_\nu + E_p = m_{\text{atom}}(Z,N)\,c^2 - m_{\text{atom}}(Z-1,N+1)\,c^2 - 2m_e c^2 + E_i - E_f, && (4.21)\\
Q_{ec} &= E_\nu - E_e = m_{\text{atom}}(Z,N)\,c^2 - m_{\text{atom}}(Z-1,N+1)\,c^2 + E_i - E_f, && (4.22)
\end{aligned}$$

where E_i and E_f are the excitation energy of the parent and daughter nucleus, respectively. These expressions are valid independently, if considering this reaction to happen among neutral atoms or fully ionized nuclei, as we are ignoring the contribution of the electron binding energy on both sides of the equation.

In the context of weak reactions in a stellar plasma, it is nevertheless more convenient to avoid the explicit appearance of the electron mass in the expression of the Q value, as we will see later. Hence, the Q value is simply defined as the energy available in the weak process due to the nuclear transition. This has the advantage that the Q value is the same for all four processes:

$$Q_{if} = \left(M_p - M_d\right)c^2 + E_i - E_f. \tag{4.23}$$

4.3.1 Cross Section and Rate Determination

In the beginning of this subsection, we want to derive an expression for the transition probability W of an EC process. This will work analogously for the three related processes. Note that some level of detail will be omitted here and the interested reader should be redirected to the standard textbooks like Wong (1998) or Greiner & Müller (2009), which also serve as guidance for this section. The transition probability is related to the half-life of the nucleus as follows:

$$t_{1/2} = \frac{\ln 2}{W}. \tag{4.24}$$

If a certain nucleus decays, it can populate different excited states (characterized by their excitation energy E_i) of the daughter nucleus. Hence, the total transition probability is given by summing over all individual transition probabilities to different final states. In astrophysics, the decay from one individual initial state (e.g. the ground state) is usually not of the only interest, as nuclei can occur in a plasma with high temperatures, that allow the parent nucleus to become thermally excited from its ground state (resulting in a thermal excitation spectrum). Consequently, the transition probability has to be averaged over the population of this excitation spectrum as well, in order to get an averaged transition probability. This is explained in detail in Section 4.4.1. For now, we will consider only single transitions from one nuclear state to another.

Both electromagnetic and weak interactions can usually be treated as perturbations of the initial quantum state of the nuclear system. Hence, they can be dealt with in the framework of time-dependent perturbation theory, where the external weak field can be regarded as a time-dependent perturbation of the nuclear many-body wave function. This approach leads to the formulation of Fermi's golden rule, which in general gives an expression for the transition probability W:

$$dW = \int \frac{2\pi}{\hbar} |M_{if}|^2 \times (\text{Phase Space}), \tag{4.25}$$

$$= \int \frac{2\pi}{\hbar} |\langle f | \hat{H}_{\text{weak}} | i \rangle|^2 \times (\text{Phase Space}), \tag{4.26}$$

where M_{if} is the nuclear transition matrix element and $|i\rangle$ and $|f\rangle$ are the wave functions of the initial or final state of the system, composed of the two leptons and the parent and daughter nucleus, respectively. Hence the square of the transition matrix element is simply given by:

$$|M_{if}|^2 = |\langle f | \hat{H}_{\text{weak}} | i \rangle|^2, \tag{4.27}$$

where it should be noted that depending on the nature of the process, $|M_{if}|^2$ will be obtained by averaging over the possible initial and summing over the possible final quantum states that are connected via $|\langle f | \hat{H}_{\text{weak}} | i \rangle|$. This will be introduced later. For a decay process (here β^--decay), this is identical to the decay rate λ and Fermi's golden rule is given by:

$$\lambda = \frac{2\pi}{\hbar} \int |M_{if}|^2 (2\pi\hbar)^3 \, \delta^{(4)} \left(p_f + p_e + p_\nu - p_i \right) \frac{d^3 p_f}{(2\pi\hbar)^3} \frac{d^3 p_e}{(2\pi\hbar)^3} \frac{d^3 p_\nu}{(2\pi\hbar)^3}, \tag{4.28}$$

where p are the individual momenta (the δ function goes over the four-momenta). For lepton absorption (here EC), we have to write Fermi's golden rule in terms of a cross section σ. It is given by:

$$\sigma = \frac{2\pi}{\hbar v_e} \int |M_{if}|^2 (2\pi\hbar)^3 \, \delta^{(4)} \left(p_f + p_\nu - p_i - p_e \right) \frac{d^3 p_f}{(2\pi\hbar)^3} \frac{d^3 p_\nu}{(2\pi\hbar)^3}, \tag{4.29}$$

where v_e is the velocity of the incoming electron or positron.

Starting from Fermi's golden rule, we first have to find an adequate representation of the interaction Hamiltonian $\hat{H}_{\text{weak}}$ that respects the symmetries (or broken symmetries) of our interaction. Then, we need to describe the wave functions of the involved particles and finally we have to consider the allowed phase space of the involved particles. In the final step, we can describe the average rate in an astrophysical plasma, by considering all possible (and allowed) transitions from exited states of the parent nucleus to excited states of the daughter nucleus with the correct statistical averaging.

As we discussed earlier in Section 4.1, charged-current processes are maximally parity breaking, meaning that the wave functions change their sign under a parity transformation. It turns out that if the interaction

contains operators that are either scalars, pseudoscalars or tensors, leptons of both helicities will be produced under a parity transformation. As this was not observed experimentally, we can constrain the operators of which the Hamiltonian is composed of, to be either of vector (V, parity conserving) or axial-vector type (A, parity violating). Hence, the general form of the interaction is given by a $V-A$ structure. This ensures that any interaction build from these vectors violates parity maximally. Hence, the interaction Hamiltonian has a polar vector part with coupling constant G_V and an axial vector part with coupling constant G_A. In order to relate G_V and G_A to the elementary weak coupling constant g, we first introduce the so-called Fermi constant G_F, which is given by:

$$G_\mathrm{F} = \frac{\sqrt{2}}{8}\frac{g^2}{m_\mathrm{W}^2} = 8.96181(8) \times 10^{-44}\ \mathrm{MeV\ cm^3}, \tag{4.30}$$

where m_W is the mass of the W boson. This coupling constant can be measured for example in the muon decay which is a purely leptonic process. The Fermi constant describes the weak interaction accurately, when the momenta of the involved particles are small compared to the mass of the W boson. If we consider the decay of the d quark for example ($d \rightarrow u + e^- + \bar{\nu}_e$), the T-matrix is given by (see e.g. Towner & Hardy, 1995):

$$T_{fi} = \frac{g^2}{8} V_{ud} \bar{\psi}_u \gamma_\mu (1-\gamma_5) \psi_d \frac{\delta_{\mu\nu} + q_\mu q_\nu / m_W^2}{q^2 + m_W^2} \bar{\Psi}_{e^-} \gamma_\nu (1-\gamma_5) \Psi_{\bar{\nu}_e}, \tag{4.31}$$

where q is the momentum transferred between the hadrons and the leptons. If we make the same assumption and say that $q \ll m_W$, Equation (4.31) simplifies to:

$$T_{fi} = \frac{g^2}{8 m_W^2} V_{ud} \bar{\psi}_u \gamma_\mu (1-\gamma_5) \psi_d \bar{\Psi}_{e^-} \gamma_\mu (1-\gamma_5) \Psi_{\bar{\nu}_e}. \tag{4.32}$$

$$= \frac{G_F}{\sqrt{2}} V_{ud} J_\mu^h J_l^\mu, \tag{4.33}$$

where J_μ^h and J_l^μ are the hadronic and the leptonic currents. Additionally, both currents can be related to a vector and an axial vector current, as was imposed before:

$$J_\mu^h = \bar{\psi}_u \gamma_\mu (1-\gamma_5) \psi_d \equiv V_\mu^h - V_\mu^h, \tag{4.34}$$

$$J_\mu^l = \bar{\psi}_{e^-} \gamma_\mu (1-\gamma_5) \psi_{\bar{\nu}_e} \equiv V_\mu^l - V_\mu^l. \tag{4.35}$$

If we remember the quark mixing nature of the weak interaction, it becomes clear that the observed β-decay strength cannot be the fundamental interaction strength itself but has to be adjusted to account for the quark mixing angle. Considering the decay of an u quark into a d quark, we remember from section 4.1 that the created quark state d' contains an admixture from s and b quarks as well:

$$u \rightarrow d' = V_{ud} \cdot d + V_{us} \cdot s + V_{ub} \cdot b. \tag{4.36}$$

As long as it is not energetically allowed to create a hyperon (for example the Lambda *sud* state), only the $u \rightarrow d$ channel has a non-vanishing phase space and the transition scales with V_{ud}, leading exactly to the scaling of the weak interaction with V_{ud}.

The interaction strength above was derived based on the interaction Lagrangian for free quarks and leptons. Inside a nucleon the situation is more complicated, as they are composite objects of three quarks. So in analogy to the hadronic current for free quarks, we write the current for neutrons and protons as (again $n \rightarrow p + e^- + \bar{\nu}_e$):

$$J_\mu^H = \bar{\psi}_n \gamma_\mu \left[G_V\left(q^2\right) - G_A\left(q^2\right) \gamma_5 \right] \psi_p, \tag{4.37}$$

where $G_V\left(q^2\right)$ and $G_A\left(q^2\right)$ are somewhat like form factors and depend on the momentum transfer q^2. We shall not enter into much detail at this point, but in the limit of low momentum transfer, Equation (4.37) is accurate and $G_V(0)$ and $G_A(0)$ can be determined. This is discussed in great detail in Towner & Hardy (1995).

By using the so-called conserved vector current hypothesis (CVC), it can be shown that even inside a nucleus, $G_V(0) = 1$. The situation for the axial vector coupling constant G_A is more complicated. We do not expect G_A to be exactly 1, as in the case of free quarks because of the residual strong interaction between the nucleons. This stems from the fact that there should be corrections to the standard $n-p-W$ vertex coupling, due to the simultaneous exchange of pions, which are effectively mediating the residual strong force in the nucleus. This connection can be established via the partially conserved axial-vector current (PCAC) hypothesis, resulting in the so-called Goldberger-Trieman relation that predicts a ratio g_A between G_A and G_V:

$$g_A \equiv \frac{G_A}{G_V} = \frac{f_\pi g_{\pi N}}{m_N c^2} \approx 1.31,^{6} \tag{4.38}$$

where m_N is the nucleon mass, f_π is the pion decay constant and $g_{\pi N}$ is the pion-nucleon coupling constant. This also explains why the corrections of the residual strong force are not negligible. The pion-nucleon coupling constant is $g_{\pi N}^2/4\pi \approx 14$ which is large compared to radiative (EM) corrections for example, that arise in leptonic and semi-leptonic weak interactions. Radiative corrections play a role as well, but they are strongly suppressed because the relevant coupling constant α (fine-structure constant) is on the order of $\alpha \approx 10^{-2}$.

Based on Fermi's Theory of β-decay, it (and the other related processes) is best described by a four-fermion point interaction for which the so-called current-current description is adequate. The operator in the current-current representation is given by:

$$\hat{H}_{\text{weak}} = \frac{G_F V_{ud}}{\sqrt{2}} \int J_h^\mu(\vec{x}) J_\mu^l(\vec{x})\, d^3x, \tag{4.39}$$

From our previous considerations, we already know how $J_h^\mu(\vec{x})$ and $J_l^\mu(\vec{x})$ look inside a nucleus and hence we get:

$$\hat{H}_{\text{weak}} = \frac{G_F V_{ud}}{\sqrt{2}} \int \left[\bar{\psi}_{p/n}(\vec{x})\gamma^\mu(1-g_a\gamma_5)\psi_{n/p}(\vec{x})\right] \times \left[\bar{\psi}_{e/p}(\vec{x})\gamma_\mu(1-\gamma_5)\psi_{\nu_e/\bar{\nu}_e}(\vec{x})\right] d^3x. \tag{4.40}$$

The nuclei involved in the EC process can be characterized by their quantum numbers. These are the Spin J, the third projection of the Spin M, the isospin T and the third projection of isospin T_z which has a trivial physical representation: $T_z = (N-Z)/2$ (for details see Section 3.1). Additionally, we know that EC or β-decay processes raise or lower T_z by 1. So for EC for example, we characterize the initial and final states in the following way:

$$|i\rangle = |J_i, M_i, T_i, T_{z_i}; e^-\rangle, \tag{4.41}$$

$$|f\rangle = |J_f, M_f, T_f, T_{z_f}; \nu_e\rangle. \tag{4.42}$$

Notice that in terms of the nuclear matrix element, processes (4.15),(4.16),(4.17) & (4.18) will be equivalent. On the one hand, antiparticle wave functions are the complex conjugates of the particle wave functions. And on the other hand, we will eliminate all dependencies on the leptons in the matrix

[6] Experimentally, one finds values closer to ≈ 1.26. Interestingly, when studying β-decay in heavier nuclei , g_a appears to be significantly smaller than that, having values close to the vacuum value of 1. This phenomenon is known als the "in-medium quenching of the axial vector coupling constant" (for details, see e.g. Osterfeld, 1992).

element and hence, whether an electron (or positron) is in the initial or final state will only affect the phase space integral.

Now, we want to evaluate the wave function part of the leptons. To a good approximation, we can say that the electron and the neutrino are plane waves traveling with the wavenumbers $\vec{k}_e$ and $\vec{k}_\nu$, meaning that $\Psi_{e,\nu_e}(\vec{x}) = V^{-1/2} e^{-i\vec{k}\vec{x}}$. Here, V is an arbitrary volume so that for example $\langle e|e\rangle = \int_V \Psi_e^* \Psi_e d^3x = \int_V d^3x = 1$. In the plane wave picture, Coulomb effects are ignored. Later, we will reintroduce them via a correction term. In this case it follows that (remember that $\vec{k} = \vec{p}/\hbar$):

$$\langle \nu_e | J_\mu^l | e\rangle = e^{-i(\vec{p}_e - \vec{p}_\nu)\vec{x}/\hbar}\, \bar{u}_\nu \gamma_\mu (1-\gamma_5) u_e = e^{-i\vec{q}\vec{x}/\hbar}\, \bar{u}_\nu \gamma_\mu (1-\gamma_5) u_e, \tag{4.43}$$

where u are spinors and $\vec{q}$ (here for EC kinematics) is now the combined momentum between electron and neutrino, which amounts to the nuclear recoil momentum. As this is comparably small ($\vec{p}_e - \vec{p}_\nu = \vec{q} \approx \vec{0}$), we can make use of a common approach and expand the product of the two plane waves in terms of spherical harmonics:

$$e^{-i\vec{q}\vec{x}/\hbar} = \sum_{\lambda=0}^{\infty} [4\pi(2\lambda+1)]^{-1/2} i^\lambda j_\lambda(qx/\hbar) Y_{\lambda 0}(\theta, 0), \tag{4.44}$$

where θ is the angle between $\vec{p}_e$ and $\vec{p}_\nu$. Here, the spherical harmonics become independent of the azimuthal angle ϕ by choosing $\cos\phi = 0$. Making use of the long-wavelength approximation, we only need to keep the first term in the expansion of the spherical Bessel function:

$$j_\lambda(qx/\hbar) \approx \frac{(qx/\hbar)^\lambda}{(2\lambda+1)!!}. \tag{4.45}$$

The combined wave equation for both leptons is then given by:

$$e^{-i\vec{q}\vec{x}/\hbar} \approx 1 + i\left(\frac{4\pi}{3}\right)^{1/2} (qx/\hbar) Y_{10}(\Theta, 0) + O\left(q^2x^2/\hbar^2\right) + \dots \quad . \tag{4.46}$$

By approximating $1 + i\left(\frac{4\pi}{3}\right)^{1/2}(qr/\hbar) Y_{10}(\Theta,0) + \dots \approx 1$, one finds:

$$\langle \nu_e | J_\mu^l | e\rangle = e^{-i(\vec{p}_e + \vec{p}_\nu)\vec{x}/\hbar}\, \bar{u}_\nu \gamma_\mu (1-\gamma_5) u_e \approx \bar{u}_\nu \gamma_\mu (1-\gamma_5) u_e = l_\mu. \tag{4.47}$$

Above approximation of the lepton wave function is called “allowed approximation”. One can easily see that the higher order terms in Equation (4.46) correspond to solutions of the leptonic wave function, where the lepton pair carries at least one unit of angular momentum ($\vec{L} = 1, 2, 3, \dots$), while the first (allowed) term corresponds to a combined angular momentum of $\vec{L} = 0$. Then the matrix element $\langle f|\hat{H}_{\text{weak}}|i\rangle$ is given by:

$$\langle f|\hat{H}_{\text{weak}}|i\rangle = \frac{G_F V_{ud}}{\sqrt{2}} l_\mu \int \langle J_f, M_f, T_f, T_{z_f}|J_h^\mu|J_i, M_i, T_i, T_{z_i}\rangle d^3x. \tag{4.48}$$

Obtaining the nuclear part of the β-decay operator is more complicated, consequently we will not derive it here in full detail. This is done for example in Greiner & Müller (2009, p. 260 - 271). We already know that it can only contain a polar vector and an axial vector term, but the form will be more complicated compared to free quarks, as the interaction happens in terms of nucleons in a dense medium. As has been discussed earlier, this also implies that the weak coupling constants will be different compared to the vacuum values. Due to the nature of β-decay (i.e. transforming a proton into a neutron and vice versa), it is not far fetched to assume that the isospin raising or lowering operator $t_\pm$ will be an integral

part of the required expression. Another point worth mentioning is that no explicit form of the nuclear wave function has to be given. It will be sufficient to assume that they are sharply localized in space. Then, one can show that $\hat{H}_{\text{weak}}$ is given by:

$$\hat{H}_{\text{weak}} = \frac{G_F V_{ud}}{\sqrt{2}} \sum_{k=1}^{A} \left(l_0 \hat{1}^k + g_a \vec{l} \hat{\sigma}^k \right) \hat{t}_{\pm}^k. \tag{4.49}$$

Here, $\hat{t}_{\pm}^k$ is the isospin lowering/raising operator and $\vec{\sigma}_k$ is the Pauli spin matrix. Thus, the weak interaction couples to the nucleon spin. l_0 and $\vec{l}$ are different components of l_μ. $\sum_k$ runs over the number of nucleons from 1 to A. At this point, we define—as usual—the first part of this equation to be the Fermi transition operator and the second part to be the Gamov-Teller transition operator.

Here, we have to take into account that we are not measuring the spin projections M_i and M_f of the nuclei and also not the spins of the electron S_{e^-} and the neutrino S_{ν_e}. For this reason, we have to sum over all possible final spins and projections and average over the initial spin projections. By accounting for that choice in Equation (4.27), the square of the matrix element is now given by:

$$|M_{if}|^2 = \frac{1}{2J_i + 1} \sum_{S_{e^-}, \nu_e} \sum_{M_i, M_f} |\langle f | \hat{H}_{\text{weak}} | i \rangle|^2, \tag{4.50}$$

$$= \frac{G_F^2 V_{ud}^2}{2(2J_i + 1)} \sum_q \sum_{M_i, M_f} |\langle J_f M_f T_f T_{z_f} | \sum_{k=1}^{A} \left[\left(l_0 \hat{1}^k + g_a \vec{l} \hat{\sigma}_q^k \right) \hat{t}_{\pm}^k \right] | J_i M_i T_i T_{z_i} \rangle|^2, \tag{4.51}$$

where we used that the summation over the lepton spins is equivalent to the summation over the different components of σ.

In order to evaluate the expression even further, we can integrate over all solid angles of the produced neutrino if one is not interested in its direction. The dependence of the matrix element on the lepton angles is obtained by integrating over the time and space parts of the leptonic current (l_0 and l). By doing so, we get:

$$\int |M_{if}|^2 \frac{d\Omega_\nu}{4\pi} = \frac{G_F^2 V_{ud}^2}{2} \left[B(F)_{if} + B(GT)_{if} \right], \tag{4.52}$$

where $B(F)_{if}$ is the reduced Fermi matrix element (vector part) and $B(GT)_{if}$ is the reduced Gamov-Teller matrix element (axial vector part). $B(GT)_{if}$ is then given by:

$$B(GT)_{if} = \frac{g_A^2}{2J_i + 1} \sum_q \sum_{M_i, M_f} |\langle J_f M_f T_f T_{z_f} | \sum_{k=1}^{A} \vec{\sigma}_q^k \hat{t}_{\pm}^k | J_i M_i T_i T_{z_i} \rangle|^2. \tag{4.53}$$

After evaluating the sums over M_i,M_f and $q \in \{-1, 0, 1\}$, the Gamov-Teller matrix element is given by:

$$B(GT)_{if} = \frac{g_A^2}{2J_i + 1} |\langle J_f T_f T_{z_f} || \sum_{k=1}^{A} \vec{\sigma}^k \hat{t}_{\pm}^k || J_i T_i T_{z_i} \rangle|^2. \tag{4.54}$$

In general, it is not possible to evaluate this matrix element in an simple way. Hence, it has to be either measured specifically for the involved transition or computed with a suitable method like shell-model calculations. Recent calculations were performed among others by Langanke & Martínez-Pinedo (2000) or Suzuki et al. (2016). For the EC on protons, the Gamov-Teller matrix element simplifies to $B(GT)_{if} = 3g_a^2$.

The Fermi part $B(F)_{if}$ is given by:

$$B(F)_{if} = \frac{1}{2J_i+1} \sum_{M_i,M_f} \langle J_f M_f T_f T_{z_f} || \sum_{k=1}^{A} \hat{t}_{\pm}^k || J_i M_i T_i T_{z_i} \rangle^2. \tag{4.55}$$

In Section 3.1, the isospin raising or lowering operator was introduced with the convention that: $\hat{t}_+ |p\rangle = |n\rangle$ and $\hat{t}_- |n\rangle = |p\rangle$. Furthermore, if we assume that isospin is a good quantum number in our calculations (i.e. that it is conserved), it follows that the whole Fermi transition strength has to come from the isobaric analog state (IAS) of the parent nucleus. This approximation is usually good to about 0.5 %. In this case, the Fermi transition matrix element can be further simplified as we can evaluate the summation over k explicitly and get:

$$B(F)_{if} = \Big[T_i(T_i+1) - T_{z_i} T_{z_f} \Big] \delta_{J_i,J_f} \delta_{T_i,T_f} \delta_{T_{z_f},T_{z_i}\pm 1}, \tag{4.56}$$

where again, T denotes the isospin of the nucleus and T_z its projection.

The last factor in Equation (4.25) is the phase space integral, which in the following will be denoted with Φ. We already wrote down the explicit form of the phase space integral for the emission of electrons (Equation (4.28)) and the absorption of electrons (Equation (4.29)). Here, we will carry out the evaluation of Fermi's golden rule for the EC process, exemplarily. For the emission process, the evaluation follows analogously. First of all, we want to rewrite Equation (4.29) in terms of the energy of the incoming electron E_e:

$$\sigma(E_e) = \frac{2\pi}{\hbar v_e} \int |M_{if}|^2 (2\pi\hbar)^3 \, \delta^{(4)}\left(p_f + p_\nu - p_i - p_e\right) \frac{d^3p_f}{(2\pi\hbar)^3} \frac{d^3p_\nu}{(2\pi\hbar)^3}. \tag{4.57}$$

Here, the integral has to be taken over all possible final states that are consistent with conservation of energy and momentum, which is enforced by the delta function $\delta^{(4)}\left(p_f + p_\nu - p_i - p_e\right)$.

First of all, we will integrate over the nuclear momenta of the final state p_f, assuming that the integrand is (to a good level of precision) independent of p_f. Hence, we get:

$$\begin{aligned}
\sigma(E_e) &= \frac{2\pi}{\hbar^4 (2\pi)^3 v_e} \int |M_{if}|^2 \delta^{(4)}\left(p_f + p_\nu - p_i - p_e\right) d^3p_f d^3p_\nu, && (4.58)\\
&= \frac{2\pi}{\hbar^4 (2\pi)^3 v_e} \int |M_{if}|^2 \delta^{(3)}\left(p_f + p_\nu - p_i - p_e\right) \delta^{(1)}\left(E_f + E_\nu - E_i - E_e\right) d^3p_f d^3p_\nu, && (4.59)\\
&= \frac{2\pi}{\hbar^4 (2\pi)^3 v_e} \int_{p_f} \delta^{(3)}\left(p_f + p_\nu - p_i - p_e\right) d^3p_f \int_{p_\nu} |M_{if}|^2 \delta^{(1)}\left(E_f + E_\nu - E_i - E_e\right) d^3p_\nu, && (4.60)\\
&= \frac{2\pi}{\hbar^4 (2\pi)^3 v_e} \int_{p_\nu} |M_{if}|^2 \delta^{(1)}\left(E_f + E_\nu - E_i - E_e\right) d^3p_\nu. && (4.61)
\end{aligned}$$

Notice that the momenta in $\delta^{(3)}\left(p_f + p_\nu - p_i - p_e\right)$ are regular three-momenta. Additionally, we know that $E_f + E_\nu - E_i - E_e \Leftrightarrow -Q_{if} + E_\nu - E_e$, where Q_{if} is given as defined in Equation (4.23). This is only valid, if the recoil energy of the daughter nucleus is assumed to be negligible. Furthermore, by replacing d^3p_ν with $p_\nu^2 dp_\nu \frac{d\Omega_\nu}{4\pi}$, we get:

$$\sigma(E_e) = \frac{2\pi\, 4\pi}{\hbar^4 (2\pi)^3 v_e} \int |M_{if}|^2 \delta^{(1)}\left(-Q_{if} + E_\nu - E_e\right) p_\nu^2 dp_\nu \frac{d\Omega_\nu}{4\pi}. \tag{4.62}$$

Now, we insert Equation (4.52), which gets rid of the integration over Ω_ν and yields the following expression:

$$\sigma(E_e) = \frac{G_F^2 V_{ud}^2}{2\pi\hbar^4 v_e} \int [B(F) + B(GT)]\, \delta^{(1)}\left(-Q_{if} + E_\nu - E_e\right) p_\nu^2 dp_\nu. \tag{4.63}$$

Using $p_\nu^2 dp_\nu = c^{-3} E_\nu^2 dE_\nu$, we get:

$$\sigma(E_e) = \frac{G_F^2 V_{ud}^2}{2\pi c^3\hbar^4 v_e} \int [B(F) + B(GT)]\, \delta^{(1)}\left(-Q_{if} + E_\nu - E_e\right) E_\nu^2 dE_\nu. \tag{4.64}$$

$$= \frac{G_F^2 V_{ud}^2}{2\pi c^3\hbar^4 v_e} [B(F) + B(GT)] \left(E_e + Q_{if}\right)^2, \tag{4.65}$$

where we evaluated $\delta^{(1)}\left(-Q_{if} + E_\nu - E_e\right)$, giving us the condition that $E_\nu = E_e + Q_{if}$. Now, we want to calculate a rate based on the cross section expression above. This will require us to know the distribution function of the electrons in the scenario where we want to evaluate the reaction rate. For an experiment in the lab, this could be given by a monochromatic electron beam and in the stellar plasma, we can simply use the thermal equilibrium distribution function of the electrons as derived in Section 2.2.1.

For the EC problem, we know that the number of reactions per unit of volume is given by (for details see Section 3.2.1):

$$r_{ec} = \int \sigma(E_e)\, v dn_A dn_e. \tag{4.66}$$

Here, v is given by $v = |\vec{v}_e - \vec{v}_A|$. As the electron mass is much smaller than the nucleon mass and electrons are extremely relativistic, v can be approximated with $v \approx |\vec{v}_e|$. Then above expression reduces to:

$$r_{ec} = n_A \int \sigma(E_e)\, v_e dn_e. \tag{4.67}$$

As we are rather interested in the rate per nucleus λ_{ec} and not the rate per volume r_{ec}, we make use of their relation which is given by:

$$\lambda_{ec} = r_{ec}/n_A = \int \sigma(E_e)\, v_e dn_e. \tag{4.68}$$

Now, we need to give an expression for the number density of the electrons. Inside a star, we can assume that electrons and positrons follow Fermi-Dirac statistics. Then, the number density of electrons is given by:

$$\frac{dn_e(p_e)}{dp_e} = \frac{1}{\pi^2\hbar^3} p_e^2 f(E_e), \tag{4.69}$$

where $f(E_e)$ is the electron distribution function and μ_e is the electron chemical potential. In general, $f_{e/p}\left(E_{e/p}\right)$ is given by:

$$f_{e/p} = \left(1 + \exp\left(\frac{E_{e/p} \mp \mu_e}{kT}\right)\right)^{-1}, \tag{4.70}$$

where the positron chemical potential μ_p is given by the relation $\mu_e = -\mu_p$. The chemical potentials have to be calculated, for example by numerically inverting the following relationship:

$$n_{e,net} = n_e - n_p = \frac{\varrho Y_e}{m_u} = \frac{1}{\pi^2}\left(\frac{m_e c}{\hbar}\right)^3 \int_0^\infty \left(f_e - f_p\right) p^2 dp. \tag{4.71}$$

Now, we are rewriting Equation (4.69) as a function of energy, i.e. using $dp_e = E_e dE_e / \left(p_e c^2\right)$. It follows that:

$$\frac{dn_e(E_e)}{dE_e} = \frac{1}{\pi^2 \hbar^3 c^2} p_e E_e f(E_e), \tag{4.72}$$

and by plugging Equation (4.72) in Equation (4.68), we find:

$$\lambda_{ec} = \frac{1}{\pi^2 \hbar^3 c^2} \int E_e p_e \sigma(E_e) v_e dE_e. \tag{4.73}$$

Now, we insert Equation (4.65) into (4.73) and get:

$$\lambda_{ec} = \frac{G_F^2 V_{ud}^2}{2\pi^3 \hbar^7 c^6} [B(F) + B(GT)] \int E_e p_e f(E_e) E_\nu^2 dE_e. \tag{4.74}$$

Usually, above expression is written in the following way:

$$\lambda_{ec} = \frac{\ln 2}{K} [B(F) + B(GT)] \Phi_{ec}, \tag{4.75}$$

where the constant K is defined as:

$$K = \frac{2\pi^3 (\ln 2) \hbar^7}{G_F^2 V_{ud}^2 g_V^2 m_e^5 c^4}. \tag{4.76}$$

Experimentally, K can be determined to be $K = 6146 \pm 6$ s. The normalized phase space integral Φ_{ec} is consequently given by:

$$\Phi_{ec} = m_e^{-5} c^{-10} \int E_e p_e f(E_e) E_\nu^2 dE_e, \tag{4.77}$$

$$= \int wpf(w) \left(w + q_{if}\right)^2 dw. \tag{4.78}$$

Here, w is the total energy of the electron in units of $m_e c^2$ and $p = \left(w^2 - 1\right)^{1/2}$ is the electron momentum in units of $m_e c^2$. The Q value (here q_{if})is also given in units of $m_e c^2$:

$$q_{if} = \frac{Q_{if}}{m_e c^2}. \tag{4.79}$$

It has to be noted, that the lower bound of the integral over the electron energy in Equation (4.78) has to be considered carefully. It has to be sufficiently high to make sure that there is always enough energy for the reaction to take place. For EC we easily see that the electron needs to have at least an energy of $-q_{if}$. If this value is smaller than the electron rest mass, we have to make sure that the integral does not start below the electron rest mass. Hence, the lower bound is given by: $\max\left(-q_{if}, 1\right)$ (in units of $m_e c^2$). Therefore, the phase space integral reads as:

$$\Phi^{ec} = \int_{\max\left(-q_{if}, 1\right)}^{\infty} wp \left(q_{if} + w\right)^2 f_e(w) dw. \tag{4.80}$$

So far, we said that we will neglect Coulomb effects for the leptons involved in the reaction, effectively treating them as plain waves. As mentioned before, we will conveniently introduce a correction factor into the phase space integral, the so-called Fermi Coulomb function $F(Z, w)$ which is taking into account

the fact that the electron feels the presence of the positively charged nuclear core. The correction factor is given by:

$$F(Z,w) = 2(1+\gamma)(2pR)^{-2+2\gamma}\frac{|\Gamma(\gamma+iy)|^2}{|\Gamma(2\gamma+1)|^2}e^{\pi y}, \tag{4.81}$$

where $y = \alpha Z w/p$, $\gamma = \left(1-(\alpha Z)^2\right)^{1/2}$, α is the fine structure constant and $R \approx 1.2 \times A^{1/3}$ is the nuclear radius.

The last factor that could appear in the phase space integral, is the final state blocking of the neutrinos. While for most applications (densities below $\varrho \approx 10^{11}$ g cm^{-3}), the final state neutrino blocking is irrelevant, it can become important for example during the gravitational collapse of a massive star. So in general, we have to introduce a blocking term that looks as follows: $(1-f_\nu(E_\nu))$. For EC and in units of $m_e c^2$, the blocking term is $\left(1-f_\nu\left(q_{if}+w\right)\right)$. Including this term, we arrive at the well-known form of phase space factor for nuclear EC as given for example in Fuller et al. (1980):

$$\Phi^{ec} = \int_{\max(-q_{if},1)}^{\infty} wp\left(q_{if}+w\right)^2 F(Z,w) f_e(w)\left(1-f_\nu\left(q_{if}+w\right)\right)dw. \tag{4.82}$$

Consequently, the whole rate is given by:

$$\lambda_{ec} = \frac{\ln 2}{K}\left[B(F)+B(GT)\right]\int_{\max(-q_{if},1)}^{\infty} wp\left(q_{if}+w\right)^2 F(Z,w) f_e(w)\left(1-f_\nu\left(q_{if}+w\right)\right)dw. \tag{4.83}$$

Even though we carried out the derivation only in the example of the EC, we could do the same for the other processes, as well. It is important to note that for allowed transitions, the matrix elements are the same for all four processes and the only factor that changes the rate is the phase space integral, where we have to take into account that the reacting particles are different. The phase space factor for all four processes is given by:

$$\Phi^{ec} = \int_{\max(-q_{if},1)}^{\infty} wp\left(q_{if}+w\right)^2 F(Z,w) \qquad f_e(w)\left(1-f_\nu\left(q_{if}+w\right)\right)dw, \tag{4.84}$$

$$\Phi^{\beta^+} = \int_{1}^{q_{if}} wp\left(q_{if}-w\right)^2 F(-Z+1,w)\left(1-f_p(w)\right)\left(1-f_\nu\left(q_{if}-w\right)\right)dw, \tag{4.85}$$

$$\Phi^{\beta^-} = \int_{1}^{q_{if}} wp\left(q_{if}-w\right)^2 F(Z+1,w) \quad (1-f_e(w))\left(1-f_{\bar{\nu}}\left(q_{if}-w\right)\right)dw, \tag{4.86}$$

$$\Phi^{pc} = \int_{\max(-q_{if},1)}^{\infty} wp\left(q_{if}+w\right)^2 F(-Z,w) \qquad f_p(w)\left(1-f_{\bar{\nu}}\left(q_{if}+w\right)\right)dw. \tag{4.87}$$

Notice that for the two processes that emit two leptons (i.e. $\beta^\pm$-decay) the upper bound of the integral over the electron energy has to be chosen carefully, as well. This is because the combined energy of the two produced leptons can be q_{if} at most. Hence, the maximum electron energy is q_{if}, as well (neglecting the non-vanishing neutrino mass). Consequently, the rate for any of the four processes is given by:

$$\lambda^{EC/PC/\beta^-/\beta^+} = \frac{\ln 2}{K}\left[B(F)+B(GT)\right]\Phi^{EC/PC/\beta^-/\beta^+}. \tag{4.88}$$

Besides the reaction rate itself, there is another useful quantity, the so-called "comparative half-life" or ft-value, which is defined as follows:

$$ft = f \times t_{1/2} = \Phi \times t_{1/2} = \frac{\ln 2}{\lambda}\Phi = \frac{K}{\left[B(F)+B(GT)\right]}. \tag{4.89}$$

The advantage of this quantity is that it is independent from the phase space integral Φ and inverse proportional to the nuclear weak interaction matrix element.[7] At this point, it is also clear why it is called comparative half-life, as the ft-value can be easily compared between different transitions and indicates how strong they are without having the dominating influence of the phase space integral.

4.3.2 Selection Rules

In this section, we want to derive "selection rules" for EC and β-decay processes, by looking at the operator structure of the transition matrix elements $B(F)$ and $B(GT)$. In this way, we can tell which states of the parent and daughter nuclei can or cannot be connected via Fermi or Gamov-Teller transitions. First of all, as they are both allowed transitions, we know that the combined angular momentum of the leptons must be $\vec{L} = 0$. As they both have a spin of $1/2$, their combined spins can be either aligned ($\vec{S} = 1$) or anti-aligned ($\vec{S} = 0$). For allowed transitions, this means that the total angular momentum transported by the leptons is $\vec{J}_l = 0, 1$. As we will see soon, the earlier case corresponds to a Fermi transition and the latter case to a Gamov-Teller transition. This also implies that for allowed transitions, as the lepton system will not carry away any angular momentum L, the total angular momentum of the parent J_i and the daughter nucleus J_f can only differ by 0 or 1.

By looking at the Fermi operator (Equation (4.56)), we directly see, that $J_i = J_f$ and $T_i = T_f$, taking into account that the operator vanishes for $T_i = T_f = 0$. As a first consequence, the lepton spins have to couple to $\vec{S} = 0$. Hence, the Gamov-Teller matrix element corresponds to $\vec{S} = 1$. Additionally, we find that $T_{z_i} = T_{z_f} \pm 1$ and the parity of the nuclei remains the same, as the lepton pair carries no angular momentum. The angular momentum and isospin selection rules for a Fermi-type decay are summarized in Table 4.2.

$J_i = J_f$	($\Delta J = 0$)
$T_i = T_f$	($\Delta T = 0$, but $T_i = 0 \rightarrow T_f = 0$ is forbidden)
$T_{z_i} = T_{z_f} \pm 1$	($\Delta T_z = 1$)
$\Delta\pi = 0$	(no parity change)

Table 4.2: Angular momentum and isospin selection rules for Fermi-type weak transitions.

The same analysis can be done for the Gamov-Teller transition operator (Equation (4.54)), but in contrast to the Fermi transition, it cannot be evaluated that trivially. Hence, the results will be displayed in Table 4.3 without further explanation. For details, see e.g. Wong (1998).

$\Delta J = 0, 1$	(but $J_i = 0 \rightarrow J_f = 0$ is forbidden)
$\Delta T = 0, 1$	(but $T_i = 0 \rightarrow T_f = 0$ is forbidden)
$T_{z_i} = T_{z_f} \pm 1$	($\Delta T_z = 1$)
$\Delta\pi = 0$	(no parity change)

Table 4.3: Angular momentum and isospin selection rules for Gamov-Teller-type weak transitions.

4.3.3 Forbidden Transitions

In Section 4.3.1, it was pointed out that for allowed transitions, the leptons always carry an angular momentum of $\vec{L} = 0$. By considering higher order terms in Equation (4.46), we step away from the

[7] f denotes the phase space integral in the original notation from Feenberg & Trigg (1950), hence the name ft-value.

allowed approximation and include lepton pairs with $\vec{L} \geq 1$. The transition corresponding to a lepton pair with $\vec{L} = n$, is called nth forbidden transition. Consequently, depending on the spin alignment, they can carry a total angular momentum of $\vec{J}_l = \{n-1, n, n+1\}$. It is observed, that forbidden transitions are highly suppressed, roughly by a factor of 10^{3n}, because of the angular momentum barrier that inhibits the emission of leptons for $\vec{L} \geq 0$. Notice that in general, forbidden transitions will always contain contributions from the Fermi as well as the Gamov-Teller matrix element, unless one of both is prohibited by selection rules. In Table 4.4 the selection rules for forbidden transitions are displayed.

Decay type	ΔJ	ΔT	$\Delta\pi$
Allowed	0, 1	0, 1	no
First forbidden	0, 1, 2	0, 1	yes
Second forbidden	1, 2, 3	0, 1	no
Third forbidden	2, 3, 4	0, 1	yes
Fourth forbidden	3, 4, 5	0, 1	no

Table 4.4: Angular momentum and isospin selection rules for forbidden weak transitions.

It is worth mentioning, that nearly all β-decays that can be observed in nature, will be mixtures of Fermi and Gamow-teller type transitions. In the case that a transition occurs from a 0^+ state to a 0^+ state (excluding the case $T_i = T_f = 0$), we know from the selection rules that it can be only a Fermi type transition with $\vec{L}_l = 0$ and $\vec{S}_l = 0$. Hence, it is a unique transition that is only sensitive to the vector coupling constant G_V of the weak interaction. Such transitions are also known as superallowed β-decays. Note that in this case, there cannot even be a small contribution from a forbidden transition, as this can be excluded from the selection rules for forbidden transitions in Table 4.4. Pure Gamov-Teller transitions exist as well. For example, as one can easily see, all transitions where $\Delta J = \pm 1$ and the parity of parent and daughter nuclei stay the same ($\Delta\pi$ = no), have to be always of Gamov-Teller type and consequently they are only sensitive to the axial-vector coupling constant G_A.

Another important class of transitions that are only sensitive to a single matrix element are the so-called unique forbidden transitions. Assuming that $\Delta J \geq 2$, then we also know that $\vec{L}_l \geq 1$, as otherwise, the transition would not be possible. If the parity of initial and final nuclear state are different (just for this example, it works analogously for constant parity), then we know that only forbidden transitions with uneven lepton angular momentum can contribute (i.e. $\vec{L}_l = 1, 3, 5, \ldots$). If for example $\Delta J = 2$, then only $\vec{L}_l = 1, 3$ are allowed, implying that $\vec{S}_l = 1$. Hence, in such a situation only the Gamov-Teller matrix element contributes to the transition. Such transitions are usually called "unique" nth-forbidden transitions.

Because forbidden transitions can connect two nuclear states which differ in J by more than one unit, there could be situations, where allowed transitions are energetically disfavored by Q-value arguments. In such a situation, a forbidden transition could give the major contribution to the total rate. It was pointed out first by Lam et al. (2014); Martínez-Pinedo et al. (2014); Schwab et al. (2015) that such peculiar conditions could be present in degenerate ONe cores, where the 2nd forbidden transition of the EC on ^{20}Ne could dominate the total rate for a relevant range of conditions. This topic will be discussed in detail in Chapter 6. Nevertheless, it should be pointed out, that it is very difficult to measure or calculate the matrix element for this forbidden transition. In Martínez-Pinedo et al. (2014), the rate was estimated by using the experimental upper limit for the transition matrix element.

4.4 Weak Rates in Astrophysics

4.4.1 Average Reaction Rate

Previously, we have computed the weak interaction reaction rate that connects a nucleus in a given state to another nucleus in its given state. This is however not very meaningful in an astrophysical context, where nuclei are excited thermally. Hence, it would be more useful to consider all transitions of one certain type (i.e. β^-, β^+, EC, PC) from one nucleus to another. This means that we have to quantify the probability to populate a given excited state E_i of the parent nucleus and take this into consideration when computing the reaction rate. We define the reaction rate from a given excited state i to a given excited state j as: $\lambda_{ij}^{EC/PC/\beta^-/\beta^+}$ and the total reaction rate as $\lambda^{EC/PC/\beta^-/\beta^+}$. Then, they are connected by the following relation:

$$\lambda^{EC/PC/\beta^-/\beta^+} = \sum_i P_i \sum_j \lambda_{ij}^{EC/PC/\beta^-/\beta^+}, \tag{4.90}$$

where P_i is the probability to find the parent nucleus with excitation energy E_i in the excited state i at a given temperature T. In this way, we average the rate over all possible initial states and sum over all final states. P_i can be easily related to the energy partition function G of the parent nucleus:

$$P_i = \frac{(2J_i+1)\, e^{-E_i/k_BT}}{G\left(Z_p, A_p, T\right)} = \frac{(2J_i+1)\, e^{-E_i/k_BT}}{\sum_l (2J_l+1)\, e^{-E_l/k_BT}}, \tag{4.91}$$

where l sums over all included excited states.

Finally, if we want to calculate the total change per unit time of a given nuclear species characterized by its abundance $Y(A,Z)$ due to all four weak processes that we described earlier, we get the following relation:

$$\begin{aligned}\frac{dY(A,Z)}{dt} = {} & Y(A,Z)\left(-\lambda^{EC}_{(A,Z)\to(A,Z-1)} - \lambda^{PC}_{(A,Z)\to(A,Z+1)} - \lambda^{\beta^-}_{(A,Z)\to(A,Z+1)} - \lambda^{\beta^+}_{(A,Z)\to(A,Z-1)}\right) + \\ & + Y(A,Z-1)\left(+\lambda^{PC}_{(A,Z-1)\to(A,Z)} + \lambda^{\beta^-}_{(A,Z-1)\to(A,Z)}\right) + \\ & + Y(A,Z+1)\left(+\lambda^{EC}_{(A,Z+1)\to(A,Z)} + \lambda^{\beta^+}_{(A,Z+1)\to(A,Z)}\right).\end{aligned} \tag{4.92}$$

4.4.2 Energy Generation and Neutrino Losses

Weak reactions are not only responsible for changing the net amount of electrons (i.e. $N_{\text{ele}} - N_{\text{pos}}$) in an astrophysical plasma, but they also affect the plasma by releasing or absorbing energy. Here, we have to distinguish two different concepts. In the first step, we will only look at the energy of the absorbed and produced leptons for an individual reaction. Because of energy conservation, this can be summarized into one single quantity, the average energy of the produced neutrino $\langle E_\nu^{EC/PC/\beta^-/\beta^+}\rangle$. Afterwards, we want to study the impact of a given EC rate on the thermodynamic properties of the plasma.

In the first part, we will restrict ourselves to the question of how much energy is on average carried away by a (potentially) produced electron/positron and the neutrino. If the kinetic energy of all produced particles in a reaction is reabsorbed in the plasma (as is usually the case for strong and electromagnetic reactions), then the only effect of a reaction is to convert internal energy of the nucleons (i.e. binding energy or excitation energy) into kinetic energy of the produced particles, if the reaction is exothermic or vice versa, if the reaction is endothermic. The situation is different however, if neutrinos are produced. As has been mentioned, in most scenarios, the plasma is not dense enough for the neutrinos to interact with it at a meaningful rate. Hence, the neutrinos produced in a star will simply radiate away energy and

always reduce the total energy of the plasma. For this reason, it is useful to define the average neutrino energy loss rate ϵ_ν (energy per nucleus per time) for a given reaction as:

$$\epsilon_\nu^{EC/PC/\beta^-/\beta^+} = \sum_i P_i \sum_j \epsilon_{\nu,ij}^{EC/PC/\beta^-/\beta^+}, \tag{4.93}$$

where $\epsilon_{\nu,ij}$ is the energy loss rate for a single transition and P_i is given by Equation (4.91). In analogy to Equation (4.75), $\epsilon_{\nu,ij}$ is given by:

$$\epsilon_{\nu,ij} = \frac{(\ln 2)\, m_e c^2}{K} \left[B(F) + B(GT)\right] \Psi. \tag{4.94}$$

Ψ is the phase space integral which is chosen appropriately and in analogy to Equations (4.84) - (4.87) to yield the energy of the emitted neutrino in terms of $m_e c^2$. Ψ is given by:

$$\Psi^{ec} = \int_{\max(-q_{if},1)}^{\infty} wp\left(q_{if}+w\right)^3 F(Z,w) \qquad f_e(w)\left(1-f_\nu\left(q_{if}+w\right)\right) dw, \tag{4.95}$$

$$\Psi^{\beta^+} = \int_1^{q_{if}} wp\left(q_{if}-w\right)^3 F(-Z+1,w)\left(1-f_p(w)\right)\left(1-f_\nu\left(q_{if}-w\right)\right) dw, \tag{4.96}$$

$$\Psi^{\beta^-} = \int_1^{q_{if}} wp\left(q_{if}-w\right)^3 F(Z+1,w) \quad (1-f_e(w))\left(1-f_\nu\left(q_{if}-w\right)\right) dw, \tag{4.97}$$

$$\Psi^{pc} = \int_{\max(-q_{if},1)}^{\infty} wp\left(q_{if}+w\right)^3 F(-Z,w) \qquad f_p(w)\left(1-f_\nu\left(q_{if}+w\right)\right) dw. \tag{4.98}$$

Note that the only difference of Ψ compared to Φ, the phase space integral for the reaction rate λ, is obviously one additional power of the neutrino energy E_ν in terms of $m_e c^2$. Then, the average energy per produced neutrino (i.e. the average total energy lost per reaction) in any of the four processes is given by:

$$\langle E_\nu^{EC/PC/\beta^-/\beta^+} \rangle = \frac{\epsilon^{EC/PC/\beta^-/\beta^+}}{\lambda^{EC/PC/\beta^-/\beta^+}}. \tag{4.99}$$

As said in the beginning, the average neutrino energy is only a measure for the amount of energy leakage from the plasma. It will be however more interesting to know, whether the kinetic energy of the plasma constituents has increased or decreased during the reaction. This will ultimately tell us, if the reaction results in an increase or decrease in temperature. For this consideration, we have to assume that the timescale of weak interactions is much longer than the timescale to retain local thermodynamic equilibrium after the reaction has occurred. Then, we can start from the elementary weak interaction process where we already know its energetics and deduce its impact onto the stellar plasma. Due to the particles involved, the thermalization process occurs in a two-fold way. On the one hand, by distorting the population probability of excited states in the parent and daughter nucleus. The return to the new thermodynamic equilibrium configuration takes place by releasing or absorbing gamma rays. On the other hand, the absorbed or produced electrons/positron during the weak interaction will thermalize, as well. And again, by bringing back a distorted distribution function to its equilibrium distribution, energy will be either absorbed or released. At this point, the chemical potentials of the nuclei as well as electrons and positrons have to be taken into account.

Now, we will study the impact of a single weak reaction on the local thermodynamic equilibrium in our system. This means that except for the leaking neutrinos, there is no energy transport in and out of the

cell (i.e. for now we ignore a possible net energy luminosity). Then, we can use the following basic thermodynamic relation:

$$\frac{dQ}{dt} = k_B T \frac{dS}{dt} + \sum_i \mu_i \frac{dN_i}{dt}, \tag{4.100}$$

where Q is the heat that is added or removed from the system during the process considered, S is the entropy in units of k_B, and N_i is the total particle number of species i. All processes that we consider destroy a parent nucleus and create one daughter nucleus and either create or destroy an electron/positron. Lets exemplarily consider an EC process, then Equation (4.100) reads as:

$$\frac{dQ}{dt} = k_B T \frac{dS}{dt} + \frac{dN_e}{dt}\left(+\mu_p - \mu_d + \mu_e\right). \tag{4.101}$$

Notice that on the level of distribution functions, we do not distinguish between different excited states of nuclei anymore. They are accounted for in their distribution by their corresponding partition function that enters in the determination of n_{Ion}. As we discussed in Section 2.2.1, for our applications, nuclei are well described by an ideal Boltzmann gas. Thus, their chemical potential is given by (see also Equation (2.40)):

The chemical potential for an individual ion species is given by:

$$\mu_{\mathrm{Ion}} = m_u c^2 A_{\mathrm{Ion}} + k_B T \ln\left(\frac{n_{\mathrm{Ion}} h^3}{(2\pi A_{\mathrm{Ion}} m_u k_B T)^{3/2}}\right). \tag{4.102}$$

Consequently, the expression $\mu_p - \mu_d$ is given by:

$$\mu_p - \mu_d = \left(M_p - M_d\right)c^2 + k_B T \ln\left(\frac{n_p}{n_d}\right). \tag{4.103}$$

For the conditions that we are mostly interested in, it is valid to assume that $\left(M_p - M_d\right)c^2$ is much larger than the concentration-difference term in Equation (4.103) that scales with $k_B T$. Then, Equation (4.23) will be sufficiently accurate. Note that in conditions with temperatures well above 5 GK, this simplification is not accurate anymore and also in case of significantly different concentrations of n_p and n_d, this term has to be taken into account. For now, we write Equation (4.101) as:

$$\frac{dQ}{dt} = k_B T \frac{dS}{dt} + \frac{dN_e}{dt}\left(+M_p - M_d + \mu_e\right). \tag{4.104}$$

Obviously, $M_p - M_d$ is simply the ground state to ground state Q value $Q_{gs\to gs}$ of the weak reaction, hence we find:

$$\frac{dQ}{dt} = k_B T \frac{dS}{dt} + \frac{dN_e}{dt}\left(Q_{gs\to gs} + \mu_e\right). \tag{4.105}$$

As has been discussed before, the only particle that does not thermalize, is the produced neutrino. In this case, we can relate the average neutrino energy to the heat loss rate dQ/dt of the system:

$$\frac{dQ}{dt} = \langle E_\nu \rangle \frac{dN_e}{dt}. \tag{4.106}$$

Taking into account the sign of $\frac{dN_e}{dt}$ and $\mu_e = -\mu_p$ we find for the EC processes:

$$k_B T \frac{dS}{dt} = -\frac{dN_e}{dt}\left(Q_{gs\to gs} + \mu_e\right) + \langle E_\nu \rangle \frac{dN_e}{dt}, \tag{4.107}$$

$$= \frac{dN_e}{dt}\left(-Q_{gs\to gs} - \mu_e + \langle E_\nu \rangle\right) \tag{4.108}$$

$$= \left|\frac{dN_e}{dt}\right| \epsilon_{ec}. \tag{4.109}$$

Hence, ϵ_{ec} corresponds to the energy generation per each EC. Analogously, we find for all four processes:

$$\epsilon_{ec} = Q_{gs\to gs} + \mu_e - \langle E_\nu \rangle, \tag{4.110}$$
$$\epsilon_{\beta^+} = Q_{gs\to gs} + \mu_e - \langle E_\nu \rangle, \tag{4.111}$$
$$\epsilon_{\beta^-} = Q_{gs\to gs} - \mu_e - \langle E_\nu \rangle, \tag{4.112}$$
$$\epsilon_{pc} = Q_{gs\to gs} - \mu_e - \langle E_\nu \rangle. \tag{4.113}$$

4.4.3 Weak Rates for Astrophysical Problems

Over the past decades, several approaches have emerged to provide weak reaction rates for application in astrophysics. Due to the importance of this subject for the work presented in this thesis, we will shortly review the three most prominently used approaches. Note that in all cases, neutrino loss rates have to be provided as well. Nevertheless, as we can always use Equation (4.99) to relate the neutrino loss rate to the reaction rate, it will be in most cases more consistent and more accurate to provide $\langle E_\nu^{EC/PC/\beta^-/\beta^+} \rangle$ which is only very mildly depending on the thermodynamic conditions. Then, $\epsilon^{EC/PC/\beta^-/\beta^+}$ can be easily recovered from $\lambda^{EC/PC/\beta^-/\beta^+}$. Hence, we can restrict ourselves in the following discussion to the different ways to provide $\lambda^{EC/PC/\beta^-/\beta^+}$ in the most efficient and accurate way possible.

The first and most straight-forward method, is to evaluate Equation (4.88) explicitly and then tabulate the values of the rate for different thermodynamic conditions. As we can see from the phase space integral, the rates depend on temperature T as well as the electron density ϱ_e, which in a charge neutral plasma is related to the baryon density by $\varrho_e = Y_e \cdot \varrho$. The first extensive (and still used) stellar weak interaction rate tabulation was provided by Fuller et al. (1980, 1982a,b, 1985). Here, the reaction rates and energy production rates are tabulated on a grid of temperature and electron density for nuclei around stability from mass number $A = 21$ up to $A = 60$. A more recent rate tabulation that is still commonly used, was published by Oda et al. (1994). The tabulated rates are available for the mass numbers $A = 17$ to $A = 39$ (i.e. sd-shell). Later, in Caurier et al. (1999); Langanke & Martínez-Pinedo (2000) more recent rates were published for nuclei in the pf-shell (mass range $A = 45 - 65$). Very recently, Suzuki et al. (2016) have published extensive tabulations (on a much finer grid) for sd-shell nuclei (see also Toki et al. (2013) from the same authors). As we will see later, tabulations on a finer temperature and especially density grid may become necessary under certain conditions. Most importantly, the Urca process requires a very fine rate tabulation for the narrow regime in which it operates. Juodagalvis et al. (2010) calculated exclusively EC rates (as tabulations), specifically designed for the use in the collapse-phase during CCSN simulations. Here, the range in mass number is $A = 45 - 110$.

Despite the fact that rate tabulations in general are a very fast method for weak rates to be implemented in astrophysical codes, they severely lack precision in some cases. This stems from the fact that the rates are in general very strongly varying as a function of temperature and density. In fact, they can vary easily by more than 10 orders of magnitude for very similar conditions (e.g. neighboring grid points in the tabulation). This problem was already pointed out by Fuller et al. (1985). The temperature dependence originates mainly from the thermal population of excited states in the parent nucleus and also the phase space integral that reflects the temperature dependence of the Fermi-Dirac distribution of the involved leptons.

While β^+-decay rates to not exhibit a strong dependence on the astrophysical conditions, this is not the case for the β^--decay in strongly degenerate conditions, where the decay can be heavily suppressed due to the final state blocking of the produced electrons. This is especially true if the Q-value of the reaction is small, meaning that the maximum electron energy could be well below the Fermi energy of the electron gas. Inaccuracies in the rate tabulation in this regime are nevertheless not so important, as the rates are expected to be small, due to the blocking.

For EC and PC rates however, the situation is more severe. First of all, they show the same temperature sensitivity as $\beta^{\pm}$-decay rates, introduced through the thermal population of excited states of the parent nucleus. The largest uncertainty arises however, due to their strong density dependence, especially for degenerate conditions. Here, the electron distribution function is basically "frozen" and the electrons occupy all available energy states up to the Fermi energy. In order to be captured, the electrons need to have a kinetic energy equal or larger than the Q-value of the reaction. This means that they will most likely not be able to participate in the EC process until the electron density reaches a critical threshold value and the electrons start to populate states with energies above the Q-value of the specific reaction. For zero temperature, the electron Fermi energy only depends on the electron density ($E_f \propto \varrho_e^{1/3}$) and the phase space integral will be approximately zero until a certain threshold density. Beyond such density, the rate will rise dramatically. Especially this peculiarity of the EC rates makes their interpolation around the threshold density very inaccurate and can lead to large errors. This was recently discussed by Jones et al. (2013); Toki et al. (2013); Jones et al. (2014); Denissenkov et al. (2015). The authors pointed out that the standard tabulations fail entirely to reproduce the feature of rapid Urca cooling for certain conditions in degenerate stellar cores, as they are drastically miscalculating the relevant EC and β-decay rates. Of course, the easiest solution would be to tabulate the rate on a considerably finer grid, especially in density. In Suzuki et al. (2016), exactly this was done.

Obviously, there are more accurate methods to evaluate the weak interaction rates in astrophysical application, compared to simple rate tabulations (if affordable). The most precise possibility to provide a reaction rate would be to calculate on-the-fly the phase space integral for all transitions from and to different excited states that matter and then multiply Φ with the individual matrix element of the transition and finally sum over all final states and average over all initial states. This is equivalent to simply providing $[B(F)+B(GT)])_{ij}$ for all contributing transitions.[8] Despite this method being very accurate, it is also the one which is computationally most demanding, as the phase space integral has to be evaluated numerically. Thus, the calculation of a single reaction rate could involve several thousand evaluations of the integrand in Equation (4.88). For this reason, this method is only feasible (and necessary), if it is known that only very few transitions contribute to the total reaction rate. This is typically true for low-temperature conditions and weak rates involving light nuclei. One example is the EC on sd-shell nuclei in highly degenerate stellar cores. In the recent publications of Lam et al. (2014) and Martínez-Pinedo et al. (2014), a formalism was developed, to approximate the phase space integral analytically. This method was subsequently implemented into the stellar evolution code MESA (see Paxton et al. (2015); Schwab et al. (2015)), in order to provide both accurate and reasonably fast EC rate evaluations that can be used whenever the regular tabulations are insufficient. It should be noted that in the two aforementioned publications, the formalism was implemented, including two minor mistakes. After this was pointed out by us, the corrections were implemented into MESA. For details, see the corresponding errata (Paxton et al., 2016; Schwab et al., 2016a).

Unfortunately, for high temperature conditions, the previously mentioned approach will not be feasible anymore because too many transitions from and to excited states might be important and would have to be taken into account for an accurate rate determination. Hence, an approach would be preferable that does not have to evaluate the phase space integral for every single transition. This can be achieved by making use of the ft value. It was already pointed out in the previous paragraph that the rate, even for a single transition, can vary strongly with temperature and density. This is true especially for EC rates, where careless interpolation of the tabulated rate can lead to large errors. However, this is not the case for the ft-value, which as we have seen in Section 4.3.1, is defined in a way that it is independent of the phase space integral, hence constant for a given transition. This was the motivation, to introduce the concept of "effective rates", as done by Fuller et al. (1985), that allow for a more reliable and accurate rate interpolation. Hence, it is customary to introduce an effective ft-value where the approximate

[8] Usually, such level of precision is only required for low-temperature conditions where the weak rate is dominated by a few transitions ($\lesssim 10$).

phase-space dependence of the total rate is factored out. We would expect that this value varies only very slightly with temperature and density. The effective ft-value $\langle ft \rangle$ is then defined as:

$$\langle ft \rangle = \frac{\ln 2}{\lambda_{\text{tot}}} \Phi_{gs \to gs}. \tag{4.114}$$

In this way, the total rate can be easily approximated from the tabulated values of $\langle ft \rangle$ together with solving a single Fermi-integral $\Phi_{gs \to gs}$. It has proven reliable to use the phase space integral for the ground-state to ground-state transition it this approach, as additional simplifications can be made to speed up its calculation. Then, the rate can be easily recovered from the effective rate by the following relation:

$$\lambda_{\text{tot}} = \frac{\ln 2}{\langle ft \rangle} \Phi_{gs \to gs}. \tag{4.115}$$

It is important to mention, that the solely purpose of $\Phi_{gs \to gs}$ is to remove the largest part of the temperature and density dependence from the rate expression, and not to be overly correct. Basically, one can think of it as dividing the entries in the original rate table with a function that is well-chosen but in principle arbitrary. Later, during the astrophysical simulation, the rate is recovered by multiplying again with the same function. The only relevant factor in the end is, how accurate a chosen function can approximate the $\langle ft \rangle$-value (assuming that no error is made in dividing and multiplying by same arbitrary function).[9] It should be stressed that, by combining the "effective rate" approach together with the recent effort to find analytical approximations to the phase space integral, both an accurate and fast way to use weak rates in astrophysical simulations could be developed.

4.4.4 Deleptonization and Energy Generation in Nuclear Statistical Equilibrium

There are many astrophysical situations where the fast strong and electromagnetic processes are in equilibrium. Then, we can use the concept of NSE as we introduced it in Section 3.2.4 and consequently the abundances of nuclei can be given explicitly as a function of $Y(T, \varrho, Y_e)$. Hence, despite the fact that weak equilibrium is not given, we can use Equation (3.66) to obtain a relation of the total change of Y_e as a function of T, ϱ, Y_e and find that:

$$\dot{Y}_e(T, \varrho, Y_e) = \frac{dY_e}{dt}(T, \varrho, Y_e) = \sum_{N_i} \frac{dY_{N_i}}{dt}(T, \varrho, Y_e), \tag{4.116}$$

where the sum runs over all nuclei N_i that exist for the given NSE conditions. Such values can be handily tabulated with reasonable precision and used in calculations where NSE is present and the leptonization/deleptonization is studied along with the energy generation rate. The total energy generation rate in NSE is purely given by weak processes as by definition, all thermonuclear reactions are assumed to be in equilibrium and hence cannot contribute at all to the energy generation. The rate of energy generation is given by:

$$\dot{E}(T, \varrho, Y_e) = \frac{dE_e}{dt}(T, \varrho, Y_e) = \sum_{N_i} \frac{dE_{N_i}}{dt}(T, \varrho, Y_e). \tag{4.117}$$

Note that here, the nuclear neutrino losses have already been accounted for. Additionally, it is also important to mention that even though the total energy of the plasma can only become smaller because of exactly the neutrino losses, the simultaneous change of the nuclear composition during weak processes can also liberate or consume nuclear binding energy. As a consequence, the total change of kinetic energy of the plasma which determines its temperature could be still positive (in case nuclear binding energy is released) and potentially lead to an increase in temperature.

[9] Strictly speaking, this also means that the author that provides the effective rate, uses the exact same method to obtain $\Phi_{gs \to gs}$, as the user.

4.4.5 Coulomb Corrections in Dense Plasma

As mentioned in the introduction, conditions exist, where the effects of a dense Coulomb plasma have to be taken into account. We already described the Coulomb correction to the EoS in Section 2.2.1. Additionally, the Coulomb interaction also leads to a correction in the determination of the weak rates, by affecting the dynamics of the capture and emission processes of electrons and positrons in the vicinity of a dense electron liquid. In Juodagalvis et al. (2010), the implementation of such screening corrections is discussed in great detail, but exclusively for the EC process. Nevertheless, this can be easily generalized for the other weak processes as well. Hence, we will follow the discussion in Appendix A of Juodagalvis et al. (2010), together with the discussions in Bravo & García-Senz (1999). Most of the theoretical framework is discussed in one of the rare comprehensive reviews of this topic by Yakovlev & Shalybkov (1989).

Based on the ion coupling parameter, we can now compute the Coulomb correction $\mu_{i,c}$ to the ion chemical potential $\mu_{i,0}$ for a non-interacting Boltzmann gas, which we get from Equation (2.40). Then, the corrected chemical potential is given by: $\mu_i = \mu_{i,0} + \mu_{i,c}$. For a given nuclear species, $\mu_{i,c}$ is given by $\mu_{i,c} = k_B T \cdot f_c(\Gamma_i)$, where $f_c(\Gamma_i)$ is the Coulomb free energy per ion which can be parametrized as a function of Γ_i. Now, we have to distinguish again between the strong and weak coupling regimes. For $\Gamma \geq 1$, we employ the formula as proposed by Slattery et al. (1982) and Yakovlev & Shalybkov (1989):

$$\frac{f_c(\Gamma_i)}{k_B T} = a\Gamma_i + 4\left(b\Gamma_i^{1/4} - c\Gamma_i^{-1/4}\right) + d\ln\Gamma_i + e, \tag{4.118}$$

where the values of the parameters a, b, c, d, e are given in Ogata & Ichimaru (1987) and Ichimaru (1993). They are $a = -0.898004$, $b = 0.96786$, $c = 0.220703$, $d = -0.86097$ and $e = -2.52692$. For the weak coupling regime ($\Gamma \leq 1$), Yakovlev & Shalybkov (1989) suggest to use the following expression:

$$\frac{f_c(\Gamma_i)}{k_B T} = -\frac{1}{\sqrt{3}}\Gamma_i^{3/2} + \frac{\beta}{\gamma}\Gamma_i^{\gamma}, \tag{4.119}$$

where $\beta = 0.295614$ and $\gamma = 1.98848$. The parameters β and γ are chosen is such a way that both expressions for the weak and the strong coupling regimes as derived above, are connected smoothly (i.e. they produce the same value and same derivative for $\Gamma = 1$). Of course, the first part of Equation (4.119) reproduces the Debye-Hückel limit for $\Gamma \ll 1$. In Schwab et al. (2015), the chemical potential shift of the ions was calculated in a similar way, following a series of publications by Chabrier & Potekhin (1998); Potekhin & Chabrier (2000); Potekhin et al. (2009). This is also how the corrections to the ion chemical potential are implemented into the stellar evolution code MESA. Both descriptions are equivalent.

After the correction for each nucleus $\mu_{i,c}$ is determined, Equation (4.23) can be rewritten, taking into account the screening corrections:

$$Q_{ij} = \left(M_p - M_d\right)c^2 + E_i - E_j + \mu_{c,p} - \mu_{c,d}. \tag{4.120}$$

Notice that μ_c is scaling with Z, meaning that it is larger for increasing Z. Hence, it is easy to conclude that qualitatively, the correction $\Delta\mu = \mu_{c,p} - \mu_{c,d}$ will be negative for EC and β^+ decay and positive for PC and β^- decay. For EC rates for example, this means that the Coulomb corrections increase the EC threshold and hence reduce the reaction rate compared to the "unscreened" rate.

Besides the screening effect on the ions, one should also consider what happens to the chemical potential of the electrons in a plasma where Coulomb effects are important. The density of electrons close to the ions is somewhat larger than the ambient electron density n_e. For a reaction where an electron has to either be captured inside the ion or escape from it, this will result in a shift of its "effective" chemical potential as it is seen by the participants of the reaction. In Itoh et al. (2002), the screening correction to

the chemical potential of electrons was calculated using linear response theory. The "screened" electron chemical potential is given by:

$$\mu_{e,s} = \mu_e + V_s. \tag{4.121}$$

It is important to add that this modified chemical potential $\mu_{e,s}$ will only enter in the phase space integral for determining the rate and the average neutrino energy. For calculating the energy generation for example, it does not enter the expression, as the electrons that are absorbed or created during the weak interaction, still come from the "unscreened" Fermi see of electrons that are well described by their real chemical potential. In Itoh et al. (2002), an analytic approximation is given to obtain $V_s(r, Z_i, A_i, \varrho)$, where i is the ion index corresponding to the nucleus that sees the electron (i.e. parent for capture and daughter for emission processes). As the relevant effective electron energy is the one at the nuclear radius $r = r_{\rm nuc} = 1.2A^{1/3}$, we have to determine $V_s(r = r_{\rm nuc}, Z_i, A_i, \varrho)$, which is given by:

$$V_s(r, Z_i, A_i, \varrho) = 7.525 \times 10^{-3} Z_i \left(\frac{Z_i}{A_i \varrho_6}\right)^{1/3} \times J(r, Z_i, A_i, \varrho), \tag{4.122}$$

where $\varrho_6 = \frac{\varrho}{10^6 \text{ g cm}^{-3}}$. In general, $J(r, Z_i, A_i, \varrho)$ is an integral that has to be solved numerically. Nevertheless, it can be rewritten in terms of two independent variables r_s and R:

$$J(r, Z_i, A_i, \varrho) = J(r_s, R), \tag{4.123}$$

where $r_s = 1.388 \times 10^{-2} \left(\frac{A_i}{Z_i \varrho_6}\right)^{-1/3}$ and $R = 6.3 \times 10^{-3} Z_i^{1/3} \varrho_6^{1/3}$ for $r = r_{\rm nuc}$. The analytic approximation of J is then given by 121 coefficients a_{ij} which are tabulated in Itoh et al. (2002) and yield an expression of V_s in the following way:

$$J(r_s, R) = \sum_{i,j=0}^{10} a_{ij} s^i u^j = \sum_{i,j=0}^{10} a_{ij} \left(0.5 \log_{10} r_s + 1.5\right)^i (R/25 - 1)^j. \tag{4.124}$$

The range of applicability of this fit ranges from $10^{-5} \leq r_s \leq 10^{-1}$ and $0 \leq R \leq 50$. Hence, the variables s and u are chosen exactly in such a way that the fit is applicable from $-1 \leq u, s \leq 1$, improving the quality of the fit. In terms of the physical variables, we find:

$$\begin{aligned} V_s(r = r_{\rm nuc}, Z_i, A_i, \varrho_6) \approx\ & 7.525 \times 10^{-3} Z_i \left(\frac{Z_i}{A_i \varrho_6}\right)^{1/3} \times \\ & \times \sum_{i,j=0}^{10} a_{ij} \left[0.5 \log_{10}\left(1.388 \times 10^{-2} \left(\frac{A_i}{Z_i \varrho_6}\right)^{-1/3}\right) + 1.5\right]^i \times \\ & \times \left[\left(6.3 \times 10^{-3} Z_i^{1/3} \varrho_6^{1/3}\right)/25 - 1\right]^j. \end{aligned} \tag{4.125}$$

Now, it is trivial to correct the expressions of the phase space integral for the four weak interaction processes as described by Equations (4.84) - (4.87):

$$\Phi_s^{ec} = \int_{\max(-q_{if,s},1)}^{\infty} wp \left(q_{if,s} + w\right)^2 F(Z, w) \qquad f_e\left(w + \frac{V_s}{m_e c^2}\right)\left(1 - f_\nu\left(q_{if,s} + w\right)\right) dw, \tag{4.126}$$

$$\Phi_s^{\beta^+} = \int_1^{q_{if,s}} wp \left(q_{if,s} - w\right)^2 F(-Z + 1, w)\left(1 - f_p\left(w - \frac{V_s}{m_e c^2}\right)\right)\left(1 - f_\nu\left(q_{if,s} - w\right)\right) dw, \tag{4.127}$$

$$\Phi_s^{\beta^-} = \int_1^{q_{if,s}} wp \left(q_{if,s} - w\right)^2 F(Z + 1, w) \quad \left(1 - f_e\left(w + \frac{V_s}{m_e c^2}\right)\right)\left(1 - f_\nu\left(q_{if,s} - w\right)\right) dw, \tag{4.128}$$

$$\Phi_s^{pc} = \int_{\max(-q_{if,s},1)}^{\infty} wp \left(q_{if,s} + w\right)^2 F(-Z, w) \qquad f_p\left(w - \frac{V_s}{m_e c^2}\right)\left(1 - f_\nu\left(q_{if,s} + w\right)\right) dw, \tag{4.129}$$

where $q_{if,s} = q_{if} + \mu_{c,p} - \mu_{c,d}$ and V_s is given for the parent nucleus by Equation (4.125). The same has to be done for the phase space integral that enters the determination of the average neutrino energy in Equations (4.95) - (4.98).

$$\Psi_s^{ec} = \int_{\max(-q_{if,s},1)}^{\infty} wp\left(q_{if,s}+w\right)^3 F\left(Z,w\right) \quad f_e\left(w+\frac{V_s}{m_e c^2}\right)\left(1-f_\nu\left(q_{if,s}+w\right)\right)dw, \tag{4.130}$$

$$\Psi_s^{\beta^+} = \int_{1}^{q_{if,s}} wp\left(q_{if,s}-w\right)^3 F\left(-Z+1,w\right)\left(1-f_p\left(w-\frac{V_s}{m_e c^2}\right)\right)\left(1-f_\nu\left(q_{if,s}-w\right)\right)dw, \tag{4.131}$$

$$\Psi_s^{\beta^-} = \int_{1}^{q_{if,s}} wp\left(q_{if,s}-w\right)^3 F\left(Z+1,w\right) \quad \left(1-f_e\left(w+\frac{V_s}{m_e c^2}\right)\right)\left(1-f_\nu\left(q_{if,s}-w\right)\right)dw, \tag{4.132}$$

$$\Psi_s^{pc} = \int_{\max(-q_{if,s},1)}^{\infty} wp\left(q_{if,s}+w\right)^3 F\left(-Z,w\right) \quad f_p\left(w-\frac{V_s}{m_e c^2}\right)\left(1-f_\nu\left(q_{if,s}+w\right)\right)dw. \tag{4.133}$$

A final remark should be made regarding tabulated "effective" rates (i.e. tabulation of $\langle f\,t\rangle$). As we already showed, the rate can be recovered from the effective rate by the following expression:

$$\lambda = \frac{\ln 2}{\langle f\,t\rangle}\Phi_{gs\to gs}. \tag{4.134}$$

If the tabulated rates do not include screening corrections, they can be easily incorporated if we make the assumption that $\langle f\,t\rangle$ is unaffected by the screening corrections. Then, the screened rate can be calculated based on the unscreened tabulation of $\langle f\,t\rangle$ in the following way:

$$\lambda_s = \frac{\Phi_{gs\to gs,s}}{\Phi_{gs\to gs}}\lambda = \frac{\Phi_{gs\to gs,s}}{\Phi_{gs\to gs}}\frac{\ln 2}{\langle f\,t\rangle}\Phi_{gs\to gs} = \lambda = \frac{\ln 2}{\langle f\,t\rangle}\Phi_{gs\to gs,s}. \tag{4.135}$$

Hence, the determination of the rate still requires only the evaluation of a single phase space integral which now includes all the screening corrections.

5 Stars on a Knife Edge

In Chapter 2 the basic theoretical concepts for the description of stellar structure and evolution were formulated. This chapter will be devoted to a summary of the current understanding of the evolution and fate of stars, based on numerical models that rely in large part on the derivations in Chapter 2. Because stars that develop a degenerate core of oxygen and neon towards the end of their evolution are of particular interest for the work of this thesis, the discussion will focus on stars with initial masses between 7 and 12 $M_\odot$.[1] Consequently, this interval should contain all those stars that are massive enough to proceed through carbon burning, but at the same time sufficiently light not to reach temperature conditions for the subsequent neon burning stage. In terms of the expected stellar remnant, stars that form a degenerate ONe core are thought to be on the knife's edge between forming WDs and NSs following the gravitational collapse triggered by EC processes. Such stars are usually referred to as SAGB stars and will be discussed in detail in Sections 5.2.1 and 5.2.2. Stars that are massive enough to proceed through neon burning, will form an iron core and inevitably undergo gravitational collapse, as well. They will be mentioned briefly in Section 5.3 about massive stars. In the second part of this chapter, the fate of stars with degenerate ONe cores will be investigated. As the heaviest SAGB stars are believed to undergo gravitational collapse, the most important concepts of CCSNe will be recapitulated. Here, special emphasis will be put on ECSNe, the characteristic supernova explosion of collapsing ONe cores.

5.1 Stellar Evolution: Introduction

Stars are formed by collapsing gas clouds after exceeding the critical Jeans mass for gravitational stability. During the pre-main sequence evolution, they reach conditions where hydrogen can be fused into helium in the core in hydrostatic equilibrium. The critical mass for hydrogen burning M_H is about 0.1 $M_\odot$. The vast majority of stars are heavy enough to reach such conditions. Initially, a star contains the elemental distribution from the Big Bang plus what has been synthesized by earlier generations of stars and related events. For relatively young stars (late generation) like the sun, the elemental composition is given by: $X_{\text{hydrogen}} \approx 0.7$, $X_{\text{helium}} \approx 0.28$ and $X_Z \approx 0.02$ (as defined in Section 2.2.1).

As soon as the contracting star is hot enough to start fusing hydrogen into helium in its core, it enters the main sequence, where it will stay for most of its life in hydrostatic equilibrium, maintained by the energy released in hydrogen burning. For a given evolutionary stage, a star is typically hottest in its center and coldest at its surface. Additionally, more massive stars are hotter than their lighter counterparts at the same evolutionary stage, because burning has to proceed faster in order to counterbalance the stronger gravitational pull. For this reason, more massive stars are hotter and more luminous during the main sequence and burn hydrogen at a larger rate compared to lighter stars. For solar-metallicity stars below $\approx 1.3\ M_\odot$, helium is synthesized mainly via the proton-proton chain (lower main sequence) while for stars above this threshold, hydrogen is burned mainly by the CNO cycle (upper main sequence). As soon as the hydrogen in the core of a star has been transmuted into helium, the star will leave the main sequence and evolve on a path that is mainly determined by its initial mass and additional factors like rotation, metallicity or binary interaction.

When the hydrogen fuel for nuclear burning in the core ceases, the stabilizing radiative energy supply vanishes as well and the star contracts. During that process, the core becomes hotter and denser until

[1] Notice that the initial mass of a star refers to the mass after it has entered the main sequence (ZAMS mass).

eventually conditions are reached where helium can start to fuse into carbon (only if the star is massive enough). Due to the Coulomb repulsion, increasingly larger temperatures are required to initiate the next stage of nuclear fusion in stars, involving elements with successively higher charge number Z. Consequently, the different burning stages will proceed in an order that is determined by their mainly charge-dependent ignition temperature.[2]

The consecutive burning stages with their characteristic temperatures are: hydrogen ($T = 0.02$ GK), helium ($T = 0.2$ GK), carbon ($T = 0.8$ GK), neon ($T = 1.5$ GK), oxygen ($T = 2.0$ GK) and silicon burning ($T = 3.5$ GK). Between each burning stage the star will resume contraction because the stabilizing source of energy will disappear together with the corresponding fuel. The intensity of this post-burning contraction depends critically on the strength of the gravitational force that is acting on the stellar core that grows with increasing initial stellar mass. At the same time, the core is continuously losing energy by radiation (dominant until helium burning) as well as by neutrino emission (dominant from carbon burning on). The subsequent behavior of the star can be roughly divided into two cases. If the compression originating from the contraction is only moderate, then the temperature cannot rise sufficiently high to reach the critical value for the next burning stage. If that happens, the compression will only stop once the dominating pressure support comes from degenerate electrons and the star will contain an unreactive core consisting of the ashes of the last active burning stage. If on the other hand, the star is more massive, the contraction can proceed sufficiently fast to ensure that the compressional heating lifts the temperature beyond the threshold for the successive burning stage.

Depending on the duration of the contraction, the next fuel can be ignited either in non-degenerate or degenerate conditions. Owing to a sufficiently fast contraction, fuel will get ignited under non-degenerate conditions, in which case the burning occurs as a self-regulated process in hydrostatic equilibrium (as is the case for hydrogen burning). In a radiation dominated environment, $P \propto T^4$ (see Equation (2.41)). For this reason, the local temperature increase from to the onset of nuclear burning causes an immediate expansion and cooling of the same material, thereby regulating the temperature. In this way, a new hydrostatic equilibrium is quickly obtained, where the star remains for the duration of the currently active burning stage.

The situation is different however, if the core is already degenerate once it exceeds the temperature threshold for the next burning stage. In the degenerate limit, the pressure is insensitive to the temperature. Consequently, the temperature increase due to a local ignition of the fuel cannot proceed as a self-regulated process by expansion, as in the case of a radiation-dominated environment (see Section 2.2.1). In this case, the nuclear burning leads to an even larger increase in temperature and the whole fuel in the ignition region is burned faster than the material can respond to it by expanding (thermonuclear runaway). As a result, a nuclear flame develops that ignites the nearby fuel due to heat transport across the flame front. Consequently, the flame travels through all of the remaining unburned fuel in a short time. Notice that heat transport can become very efficient in degenerate conditions due to electron conduction, as illustrated in Figure 2.1.

In theory, the previously introduced pattern of contraction and fuel re-ignition repeats for all successive burning stages. While the stellar core typically burns the heaviest nuclei at the highest temperatures, the lighter materials are burned in shells around the stellar core. If the star is massive enough, the core will eventually burn silicon into iron-group nuclei, from which point on no fusion reactions can liberate additional binding energy. Thus, elements beyond iron cannot be produced during the regular burning stages in stars (with the exception of the s-process). Consequently, sufficiently massive stars will ultimately develop an inert core of iron that contracts until it reaches densities where it is stabilized by electron-degeneracy pressure. Because of the active burning shells around the iron core, it grows until it eventually reaches the Chandrasekhar mass M_{ch}. Notice that besides shell burning, also EC processes

[2] The corresponding reaction rates are varying smoothly as a function of temperature. But because they exhibit a very steep temperature dependence that can be approximated by a power law $\lambda \propto T^x$ ($x \approx 10-100$), it is possible to define a characteristic temperature for each burning stage (see e.g. Arnett, 1996, , page 163).

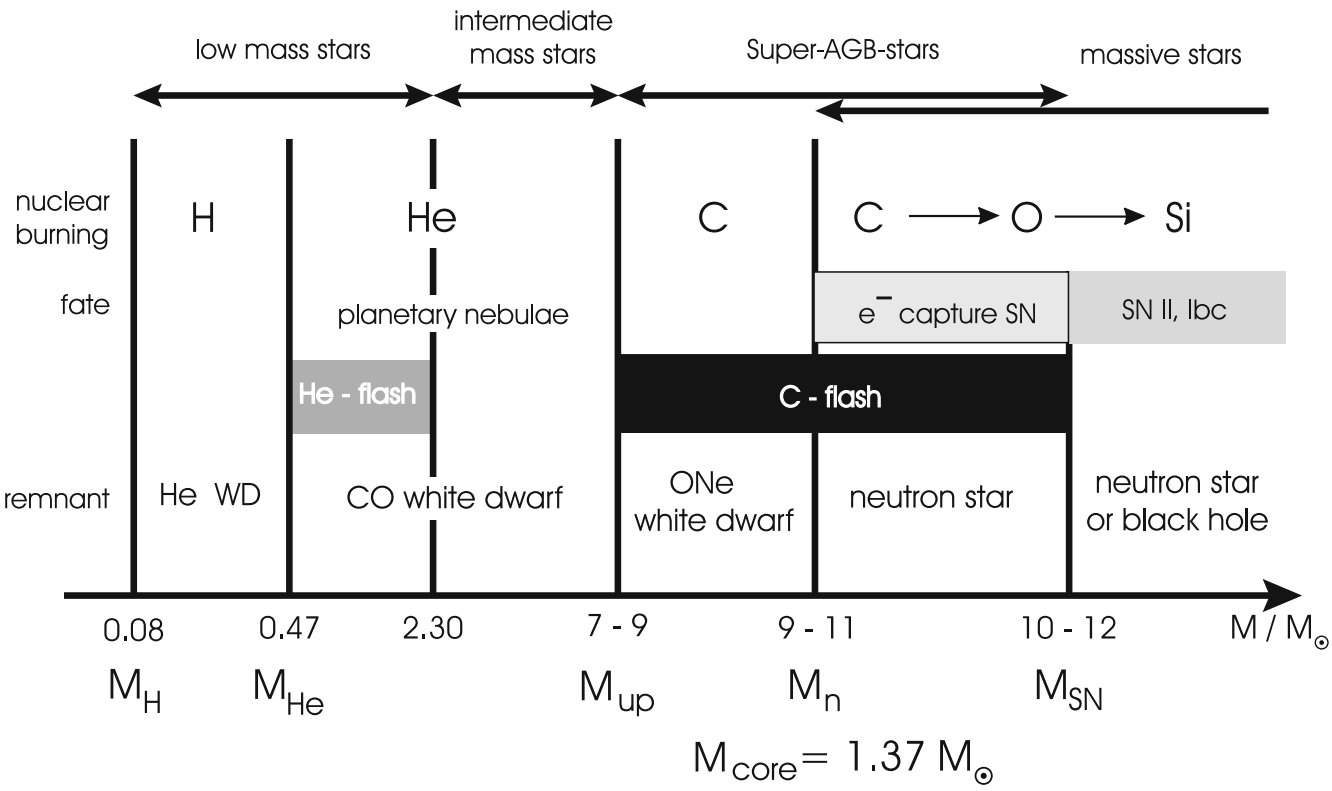

Figure 5.1: Relation of possible stellar evolution outcomes with respect to the initial stellar mass, focusing on low- and intermediate-mass stars. Figure from Siess (2006a). M_{H} is the minimum mass for hydrogen burning, M_{He} the minimum mass for helium burning, M_{up} the minimum mass for carbon burning, M_{n} the minimum mass for gravitational collapse and M_{SN} is the minimum mass for iron-core formation and explosion in an FeCCSN.

have an influence on M_{Ch} as these reactions remove electrons from the interior of the star. They start to occur if the density exceeds $\approx 10^9$ g cm^{-3}:

$$e^- + (A, Z) \rightarrow (A, Z-1) + \nu_e + \gamma, \tag{5.1}$$

5.2 Evolution of Low- and Intermediate-Mass Stars

In the previous section, the schematic evolution of stars through the consecutive burning stages was introduced. It should be pointed out again, that the question if and how a star reaches its different burning stages is mainly related to its initial mass. The same statement can be made about the nature of the stellar remnant. In this section, predictions based on current stellar evolution models are utilized to classify stars depending on their initial mass. As we are primarily interested in stars with masses between 7 and 12 $M_\odot$, we will adopt the notation of Siess (2006a) that is displayed in Figure 5.1. Due to large uncertainties especially regarding the stellar mass loss, it is difficult to give an exact relation between the initial mass and the fate of a star. Hence, the above mentioned interval, adapted from Figure 5.1 can only be regarded as an orientation. Details regarding stellar mass loss and its uncertainties are for example discussed in Chapter 9 of Kippenhahn et al. (2012).

It was already stated in the previous section that the minimum stellar mass for hydrogen burning M_H is about 0.1 $M_\odot$. In order to ignite helium, the star has to be at least as massive as ≈ 0.5 $M_\odot$. If the mass is lower, the star will end up as a degenerate He WD. In Figure 5.1, this threshold corresponds to M_{He}. If the star is less massive than 2.3 $M_\odot$, the core becomes degenerate before helium is ignited. In this

case, the burning proceeds in a helium flash. Stars that are less massive than this threshold are typically called low-mass stars. Above this limit, stars burn helium in hydrostatic equilibrium. Helium burning proceeds in general via the triple-alpha process and enriches the core with carbon and oxygen. For stars less massive than approximately 7 to 9 $M_\odot$, the so-formed carbon and oxygen core will continuously grow and compress but never reach conditions to ignite the next burning stage, which would be carbon burning. In Figure 5.1, this transition is indicated by $M_{\rm up}$. According to this scheme, all stars that burn helium non-degenerately but fail to ignite carbon are called intermediate-mass stars and comprise a relatively large initial mass interval of 6 $M_\odot$ (in width). Due to stellar mass loss, a single star that burns helium but not carbon will always end up as a regular CO WDs, usually well below the Chandrasekhar mass limit $M_{\rm Ch}$. The vast majority of observed WDs are thought to be CO WDs. As we will discuss in detail in Section 5.2.1, intermediate-mass stars will enter distinct evolutionary stages after they leave the main sequence, most notably the AGB.

Above an initial mass of about $10-12\ M_\odot$, stars ignite carbon in non-degenerate conditions and proceed through all the subsequent burning stages until they form an iron core. Stars more massive than this limit $M_{\rm SN}$ are called massive stars. Based on the current understanding, all stars above this critical mass will grow an iron core via silicon shell burning which will eventually exceed $M_{\rm Ch}$ and become gravitationally unstable. Ultimately, they collapse and explode as FeCCSNe, leaving behind either a NS or a BH.

Unfortunately, the fate of stars in the transition region between $7-9\ M_\odot$ and $10-12\ M_\odot$ is less clear. While most of these stars will end as ONe WDs, some of them might undergo a supernova explosion. Of particular interest in this mass region are SAGB stars with masses between about 8 and 10 $M_\odot$ that are believed to explode as ECSN and form a NS, if they are heavy enough. SAGB stars are defined as stars that burn carbon in a flash, as a consequence of a core contraction that could proceed sufficiently long before carbon ignition. During carbon burning, the composition of the core changes predominantly to ^{16}O and ^{20}Ne, while helium and hydrogen are burned in shells around the core. However, the core fails to proceed to the next neon-burning stage and becomes increasingly degenerate. In Figure 5.1, the threshold between exploding and non-exploding SAGB stars is called M_n and is situated between 9 and 11 $M_\odot$, with the largest uncertainty being related to the stellar mass loss. Despite the fact that collapse and explosion of ONe cores resemble that of their massive counterparts (i.e. stars with iron core), they have been dubbed ECSNe. In this case, the reason for collapse is not silicon shell burning but the removal of electron pressure support in the core due to EC reactions on ^{20}Ne that are only enabled at densities in excess of $\approx 4 \times 10^9$ g cm^{-3}. ECSNe will be described in detail in Section 5.4.2.

5.2.1 Asymptotic-Giant-Branch Stars

The post-main-sequence evolution of low-mass stars above $M_{\rm He}$ and intermediate-mass stars, including stars that form ONe cores, shows similar characteristics. Hence, we confine our discussion in this section to stars between initial masses of $M_{\rm He}$ and $M_{\rm SN}$. As will become clear soon, they will all enter a distinct evolutionary phase, called Asymptotic Giant Branch (AGB), where the star is visible as a luminous red giant. An extensive review of the stellar evolution of AGB stars is given by Herwig (2005).[3]

When a low- or intermediate-mass star exhausts the supply of hydrogen in its core, it leaves the main sequence. Due to the absence of nuclear fusion processes, the core contracts, resulting in an increase in temperature in the core. In the current understanding, the energy transfer to stellar layers at large radii is greatly enhanced, driving an expansion of the stellar envelope. Consequently, the star expands to a much larger radius and turns into a red giant, following a track across the so-called Hertzsprung gap towards the upper-right hand corner in the Hertzsprung-Russel diagram (HR diagram). The whole evolution of a typical 5 $M_\odot$ AGB star after the main sequence is illustrated in the HR diagram in Figure 5.2. Evolving on the red giant branch, the core of the star is continuously contracting and at the same time hydrogen

[3] Pioneering work on the the stellar evolution of AGB stars was performed by Iben & Renzini (1983).

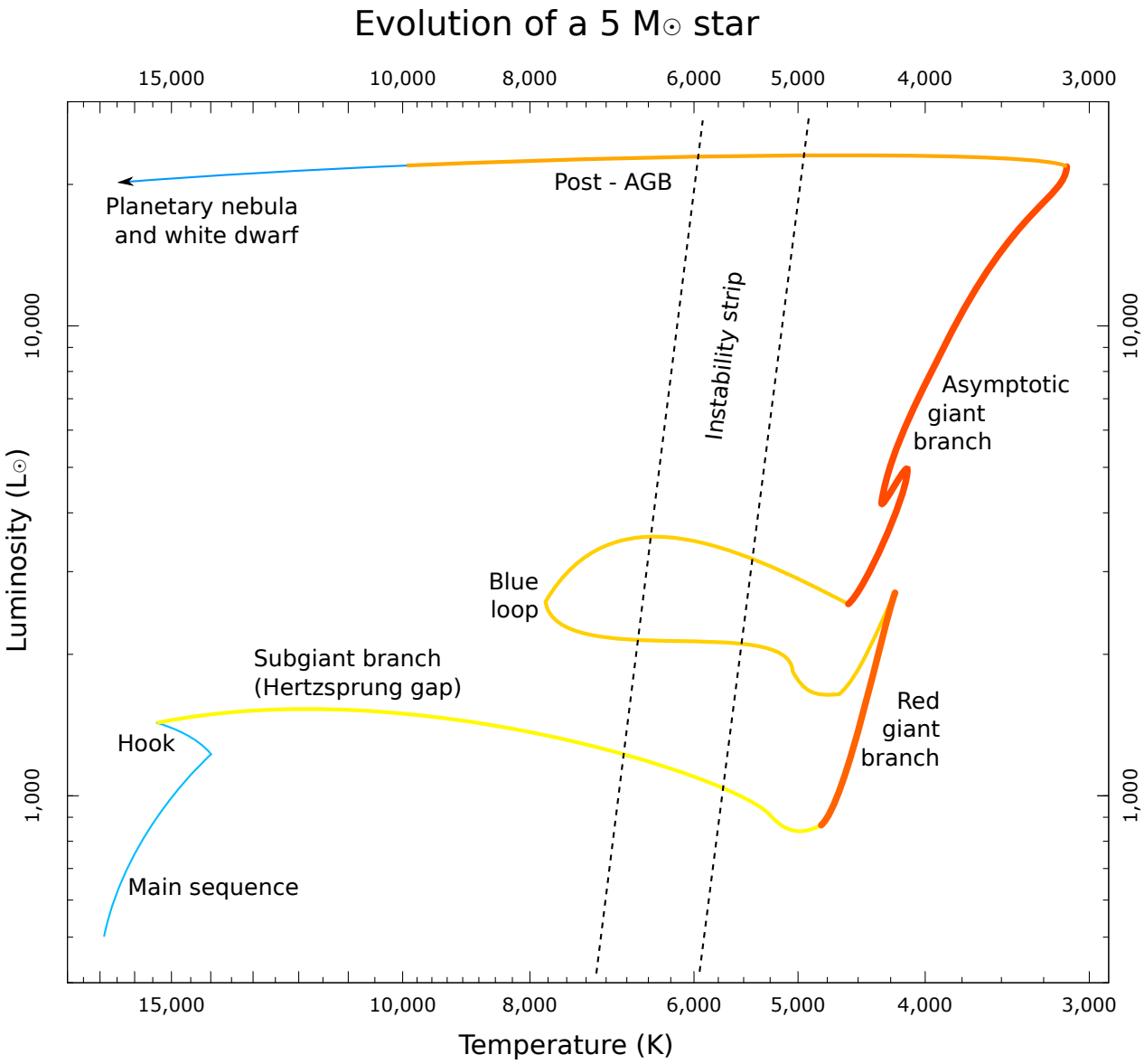

Figure 5.2: Post-main-sequence evolution of a 5 $M_\odot$ star in the HR diagram, from Wikipedia (2016). This figure illustrates the predicted evolution of a 5 $M_\odot$ AGB star from leaving the main sequence until the formation of a CO WD. After core hydrogen burning, the star leaves the main sequence and evolves towards the red giant branch. At the onset of core helium burning, the star proceeds via the blue loop and settles down in the asymptotic giant branch (AGB) once a CO core has formed. It will stay in the AGB and burn hydrogen and helium in exterior shells until stellar winds have removed the envelope and the star becomes a CO WD.

burns in a shell above the helium core. As soon as the core gets hotter than roughly $T = 3 \times 10^8$ K, helium fusion via the triple-α process sets in. Depending on the degeneracy of the material in the core, this proceeds as hydrostatic burning or in a He-flash. Additionally, after the end of hydrogen burning in the core, when the star enters the red-giant branch from the main sequence, the convective envelope can become sufficiently deep to penetrate into the helium core of the star. This process is referred to as the "first dredge-up". During such a "dredge-up" event, the extended surface convection zone causes mixing of material into the envelope that originates from deep inside the star. Hence, a certain fraction of fusion products can appear in the observable spectrum of the star that is emitted from its surface.

Helium burning halts contraction in the core and depending on the initial mass, prevents the star from cooling further in the outer layers. In that case, the star would move temporarily to the left of the HR diagram, again (blue loop, see Figure 5.2). Notice that during core helium burning, the main luminosity source is still hydrogen shell burning. During helium burning, low- and intermediate-mass stars stars will form cores that consist mostly of carbon and oxygen. Once helium in the core is exhausted, further contraction is prevented by degenerate-electron pressure and helium burning takes place in a shell above an unreactive CO core. Due to the similarity (He vs. CO core with burning shells above) with the red giant phase, this phase is called asymptotic giant branch (AGB). By looking at the HR diagram in Figure 5.2, it becomes obvious that the AGB phase is the asymptotic continuation of the red giant branch to larger luminosities. Similar to the red giant phase, at the beginning of the AGB phase, a second dredge-up may occur once core helium fusion ceases. The second dredge-up is believed to occur in stars between about 4 and 8 $M_\odot$ and to be especially strong in very massive AGB stars. As an immediate effect, the second dredge-up reduces the size of the helium core below the critical mass that is required for later reaching neon burning conditions. In fact, the strength of the second dredge-up is one of the key differences between AGB stars and massive stars, where the second dredge-up does not occur. This means that even though a massive AGB star and a low-mass massive star have very similar initial masses (e.g. 8 and 10 $M_\odot$), the mass difference of the helium core at the onset of core carbon burning might nevertheless be comparably large. Hence, in a massive star, the helium core is larger, leading to higher temperatures in the center and carbon, oxygen and later neon-burning take place. But for AGB stars, having a strong second dredge-up that effectively reduces the helium core mass, appears to be an important requirement for the formation of degenerate CO cores or in the case of SAGB stars, for the formation of degenerate ONe cores.

During the whole AGB phase, helium and hydrogen shell burning take place above a growing CO core. In the beginning, during the early AGB phase (E-AGB), helium shell burning is the dominating energy source of the star. But as helium is burned faster than it is produced by the hydrogen burning shell above, the helium shell becomes geometrically thin after some time. This marks the onset of the thermally-pulsing AGB phase (TP-AGB, see e.g. Iben & Renzini, 1983). During the TP-AGB phase, the energy generation from nuclear burning proceeds in a complicated interplay between hydrogen and helium shell burning, called thermal pulses. This shell instability is occurring because the burning of helium proceeds sufficiently fast to make the layers above expand and thereby extinguish hydrogen shell burning. Once there is no helium left to burn in the thin helium shell, both layers contract again, until hydrogen burning is eventually reignited. As as consequence, the helium layer grows until helium is re-ignited in an unstable manner (due to the thin-shell instability), called helium shell flash, and the cycle repeats.

The recurrent thermal pulses have two effects. First, the CO core grows during each cycle due to helium shell burning. And second, material from the outermost CO layer can be mixed into the stellar envelope. This repetitive mixing event is called third dredge-up, even if the second dredge-up did not occur. Thermal pulses and dredge-ups also drive an appreciable mass loss, eventually shedding the whole envelope from the star. The dynamics of burning and mixing in the intershell region are thought to be responsible for bringing large amounts of hydrogen into layers mainly composed of the helium burning ashes, carbon and oxygen. Consequently, this allows for the occurrence of the reaction chain $^{12}C\,(p,\gamma)^{13}N\,(\beta^+\nu)\,C^{13}\,(\alpha,n)\,O^{16}$. This set of reactions is thought to be responsible for the release of

large amounts of neutrons that can be captured by seed nuclei to form heavy elements in the *s*-process. More details regarding nucleosynthesis in AGB stars can be found in the comprehensive reviews of Gallino et al. (1998) and Busso et al. (1999). Recent stellar yields from AGB stars are presented in Karakas (2010).

AGB stars, by definition do not ignite carbon and based on the current understanding, all AGB stars will eventually run out of fuel to power any nuclear reaction and also not become dense enough to trigger EC processes in their core. Hence they will cool down and contract after they have expelled most of their envelope and become CO WDs.

5.2.2 Super-Asymptotic-Giant-Branch Stars

Even though AGB stars below the carbon burning threshold M_{up} are not of major relevance throughout this thesis, they were introduced in the previous section because their heavier counterparts - SAGB stars - share most of the evolutionary characteristics with them until the ignition of carbon. Because of this, we can start their discussion at this point and refer to Section 5.2.1 for the evolutionary stages prior to carbon burning. As was already mentioned in Section 5.2, SAGB stars are by definition heavy enough to ignite a carbon flash in the core during the late AGB phase and thus form a degenerate core of oxygen and neon. Seminal work on the detailed description of the late evolutionary stages of SAGB stars was first obtained in a series of publications by Garcia-Berro & Iben (1994); Ritossa et al. (1996); García-Berro et al. (1997); Iben et al. (1997); Ritossa et al. (1999). Further investigations regarding the stellar evolution of SAGB stars have been performed by Siess (2006b, 2007, 2010) and more recently by Doherty et al. (2010, 2014a,b, 2015). Additional important studies where published by Poelarends et al. (2008) as well as Jones et al. (2013) and Takahashi et al. (2013). The latter two publications focus especially on the final phase of evolution prior to the speculated gravitational collapse of a SAGB star whose core grows beyond M_{Ch}. Before it was possible to study the complicated evolution of SAGB stars with its thousands of thermal pulses in detail, it was already pointed out that stars that form ONe cores could become gravitationally unstable due to EC reactions on material in the dense core. For this reason, the pioneering publications focused rather on the onset of collapse and the subsequent supernova explosion of the degenerate ONe core, than on a detailed study of stellar evolution prior to collapse. The seminal work was performed by Miyaji et al. (1980); Nomoto (1981, 1984); Hillebrandt et al. (1984); Nomoto (1987); Miyaji & Nomoto (1987). Because the gravitational collapse was triggered by EC reactions on ^{24}Mg and ^{20}Ne, these supernova explosions are called ECSNe. They will be addressed in detail in Section 5.4.2.

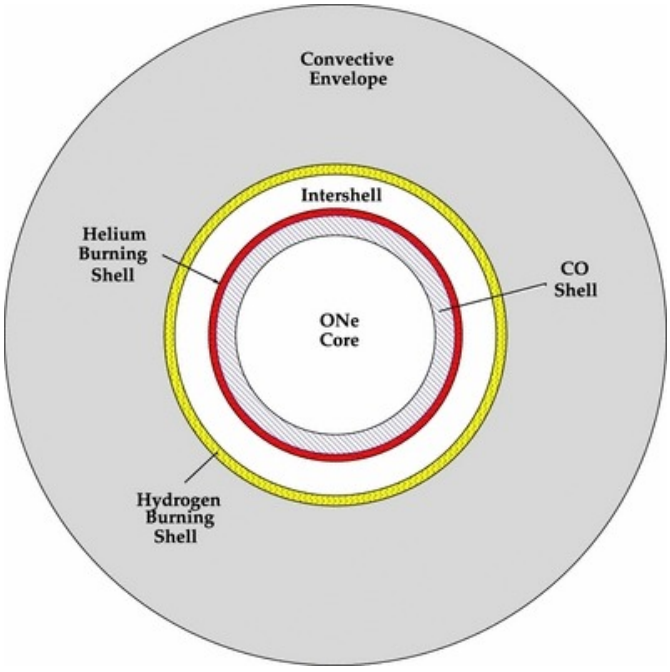

Figure 5.3: Slice through an intermediate-mass star during the SAGB phase, from Lugaro et al. (2012). On top of the ONe core that is surrounded by a small CO shell, hydrogen and helium shell burning proceed via thermal pulses (see Section 5.2.1) and result in the growth of the inert core.

In Figure 5.3, an illustration of a SAGB star is shown for the late evolutionary phase where an ONe core has already been formed by a carbon flash. Due to a temperature inversion caused by plasma

neutrino cooling in the center of the core, the carbon flame is typically found to be ignited off-center and consequently moves inward (see e.g. Nomoto, 1984; García-Berro et al., 1997). Nevertheless, in the recent work of Jones et al. (2013), only the lowest mass SAGB star model with $M = 8.2\ M_\odot$ ignites carbon off-center, while the more massive SAGB star models ignite carbon centrally, in resemblance to low-mass massive stars. After the carbon in the core of an SAGB star has been processed by nuclear reactions, the core will consist of approximately equal parts ^{16}O and ^{20}Ne. Because the core is not compressing sufficiently fast to reach the temperatures needed for the ignition of neon, the neutrino cooling will eventually dominate and the core becomes increasingly degenerate. As shown in Figure 5.3, the ONe core is enclosed by several shells of different composition (CO, He and H shells) and surrounded by a large convective envelope. Similar to less massive AGB stars, nuclear burning takes place mostly in the hydrogen and the helium shell via recurring thermal pulses. The size of the thermal pulses and third dredge-ups are reduced compared to lower-mass AGB stars, while the frequency of the thermal pulses increases significantly, posing a big numerical challenge to stellar evolution studies (Jones et al., 2013). For this reason, synthetic SAGB (and AGB) models have been employed in many studies that do not model individual thermal pulses but rather estimate their asymptotic behavior with respect to core growth and nucleosynthesis (see e.g. Herwig, 2005; Woosley & Heger, 2015).

Once the ONe core has been formed, it grows by He-shell burning in thermal pulses. As H-shell burning is providing the helium fuel, the core growth is ultimately determined by H-shell burning. At the same time, stellar winds drive a mass loss and eventually shed the envelope from the core of the star. This in turn, sets an upper limit for the mass of the core. Details regarding the rather uncertain stellar mass-loss rate during the (S)AGB phase are for example discussed in Poelarends et al. (2008). Obviously, the larger the mass-loss rate during the SAGB phase, the shorter its duration. A we will discuss in the next section, the final mass of the ONe core is of critical importance for the fate of SAGB stars and mainly limited by the intensity of the stellar wind.

Fate of SAGB stars

The special relevance of SAGB stars arises not only from their interesting stellar evolution but also from the fact that they represent the dividing line between stars that will end as WDs and stars that explode in a CCSN and give birth to a NS. This means that, if the mass-loss during the AGB phase dominates over the core growth, the star will end up as an ONe WD, as neither neon nor oxygen burning conditions are met during the evolution of SAGB stars.

The key question regarding the fate of SAGB stars is consequently whether the ONe core that corresponds to a star with a given initial mass reaches the critical mass for becoming gravitationally unstable or not. If the ONe core of an SAGB star grows sufficiently large, it has the potential to explode in an ECSN. Unfortunately, the relation of the initial stellar mass and the mass of the core at a given time is not at all clear, especially for stars that potentially suffer from strong dredge-up events. It was for example pointed out in Poelarends et al. (2008), that the effectiveness of the second dredge-up can strongly affect the maximum core mass of SAGB stars. While it is clear that an iron core of a massive star will inevitably grow beyond $M_{\rm Ch}$, the situation is less obvious for ONe cores. It was first pointed out by Miyaji et al. (1980), that a degenerate stellar core composed of oxygen and neon can get sufficiently dense to exceed the threshold density to trigger EC reactions on first ^{24}Mg and then ^{20}Ne. Because these processes remove electrons, they also remove the main pressure support of a degenerate core. It was shown by Nomoto (1984, 1987) that the critical core mass for EC and the subsequent gravitational collapse is given by $M_{\rm ec} \approx 1.37\ M_\odot$. Consequently, if the mass-loss would be very high, the core cannot grow big enough before its whole envelope is lost and hence never reaches the critical mass of $M_{\rm ec}$. If on the other hand, the mass-loss rate would turn out to be small, then the mechanism for core-growth during the SAGB

phase can operate longer and also less massive SAGB stars could reach $M_{\rm ec}$. For this purpose, we can define the ratio of SAGB stars that end up as ONe WDs and those that end their life in an ECSN by:

$$R_{\rm ECSN/ONeWD} = \frac{M_{\rm SN} - M_{\rm n}}{M_{\rm n} - M_{\rm up}}. \tag{5.2}$$

Notice that this value varies quite a lot among different studies and is far from being well constrained and has a dependence on the metallicity as well. As a consequence, the initial mass range for ECSNe the literature varies between 0 and 1.5 $M_\odot$ (width). In fact, it is not even known whether ECSNe will occur after all. In the recent study by Doherty et al. (2015), it was concluded that the vast majority of stars that go through the thermally pulsing SAGB phase will end their life as ONe WDs and that the channel for ECSNe is very small ($\approx 0.2\ M_\odot$), resulting in a ratio of $R_{\rm ECSN/ONeWD}$ well below 0.1. This is illustrated in detail in Figure 5.4. Since low-mass stars are significantly more abundant than massive stars, ECSNe could nevertheless constitute a large proportion of all observed CCSNe, despite the channel being small compared to the formation of ONe WDs (Eldridge & Tout, 2004).

The exact dividing line between SAGB and low-mass massive stars is not only given by the mass-loss rate and the dredge-up efficiency, but also by additional stellar evolution channels that might have to be considered. The dividing line between SAGB stars and massive star that explode as regular CCSNe is not necessarily given by the dividing line between off-central and central carbon ignition, as for example indicated in Figure 5.1. Rather, the question whether neon burning will occur or not should be adopted as the main criterion. In Jones et al. (2014), the authors investigated stars that could potentially exist between SAGB stars and low-mass massive stars. In the studied models between 8.8 and 9.5 $M_\odot$, neon and oxygen burning was ignited off-center in a flame and the question whether these stars evolve towards ECSNe or FeCCSNe depends critically on the dynamics of the flame. If contrary to the naïve expectation, a model that ignites neon and oxygen off-center would evolve towards an ECSN, such an evolution would produce "failed massive stars". This channel can only exist, if the flame does not burn fully towards the center, whereas stars where this is the case will presumably form an iron core and explode as a FeCCSN.

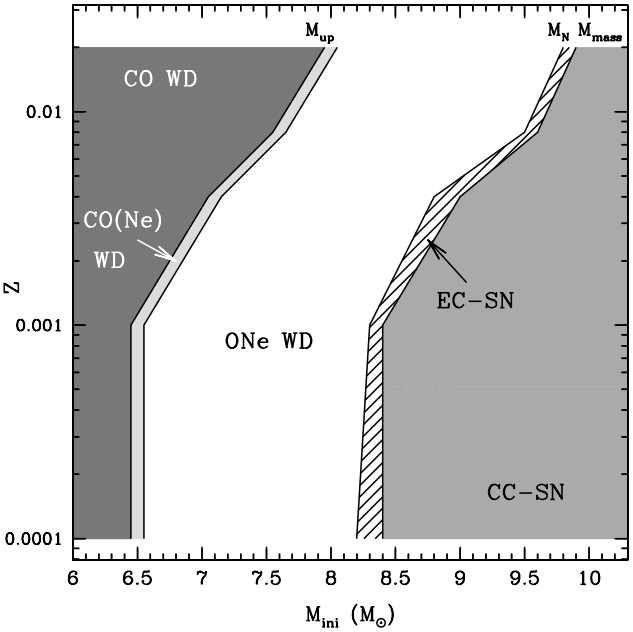

Figure 5.4: Fate of stars as a function of initial mass between $M_{\rm ZAMS} = 6 - 10\ M_\odot$ and metallicities ranging from $Z = 0.0001 - 0.02$. Figure and underlying models from Doherty et al. (2015). The window for ECSNe is predicted to be very small ($\approx 0.2\ M_\odot$).

The main conclusion of Miyaji et al. (1980) was that once the ONe core reaches the critical mass $M_{\rm EC}$ for the onset of EC reactions on ^{24}Mg and ^{20}Ne would exceed $M_{\rm Ch}$ on a very short timescale and the gravitational collapse of the star would be an inevitable consequence of the removal of the electron-degeneracy pressure in the core. It turns out however, that the situation is more complicated for several reasons and it is still under current investigation, how the star will behave after the onset of ECs. The main complication arises from the fact that EC reactions on even-A sd-shell nuclei tend to release a lot of heat into the stellar plasma and hence increase the temperature in the core. As the conditions are highly degenerate, the oxygen in the core will be ignited in a violent flash that releases even more energy, as it burns the whole fuel into NSE. As a consequence, the collapse of the core could be prevented if

the oxygen flame proceeds sufficiently fast. The details of this oxygen deflagration have not been fully explored and turbulent effects have just been started to be investigated recently (Jones et al., 2016). As chapter 6 will be devoted to this discussion in a more general context of ONe cores, independent of their stellar origin, we will follow the canonical assumption that all SAGB stars that trigger EC on ^{24}Mg and ^{20}Ne collapse and subsequently explode as ECSNe.

5.3 Evolution and Fate of Massive Stars

Stars above M_{SN} ($\approx 10-12\ M_\odot$) are called massive stars.[4] They are characterized by carbon burning in non-degenerate conditions in the core. Massive stars have been subject to extensive research both in terms of their stellar evolution as well as in terms of their collapse and their subsequent FeCCSN. Important reviews that focus on the stellar evolution of massive stars are for example given by Woosley & Weaver (1995) and Woosley et al. (2002). It should be noted that the evolution of stars with main-sequence masses in excess of $\approx 100\ M_\odot$ proceeds significantly different and possibly leads to so-called pair-instability supernovae. Some details regarding these very massive stars are discussed in Woosley et al. (2002), as well.

Due to a strong self-gravity, the central temperature of massive stars is increasing sufficiently fast after each core burning stage to reach the threshold temperatures for the fusion of heavier elements before the pressure is dominated by degenerate electrons (i.e. compressional heating dominates over γ/ν-cooling). Ignoring the scenario of failed massive stars, the common wisdom is that stars heavy enough to ignite carbon non-degenerately will also form an iron core by proceeding through the subsequent stages of neon, oxygen and silicon burning. As a consequence, nuclear fusion processes will cease only once the most strongly bound iron-group nuclei are produced in the stellar core. As the temperature in the star is decreasing with increasing radii, an onion-like structure is formed with iron-group nuclei being ultimately present in the core of the star, surrounded by active burning shells of increasingly lighter nuclei. Subsequently, the iron core of a massive star is growing by silicon burning in the first shell above the core. As soon as the iron core exceeds M_{Ch}, the core becomes gravitationally unstable and inevitably collapses. This is the standard path towards FeCCSNe.

It is important to point out that the evolution of SAGB stars and low-mass massive stars ($\lesssim 15\ M_\odot$) is rather similar prior to the ignition of carbon. Only afterward, the evolution starts to diverge more significantly, which is—among other things—related to the absence of the second dredge-up in massive stars. This feature has been observed for example in a comparison of SAGB and low-mass massive star models in Jones et al. (2013, Figures 3 and 4). While the 8.2 $M_\odot$ SAGB star model in this publication shows a strong second dredge-up that reduces the helium core mass from 2.2 to only about 1.2 $M_\odot$ at the onset of carbon burning, the 12 $M_\odot$ massive star model suffers from virtually no second dredge-up and the helium core mass remains at 3.2 $M_\odot$.[5] Consequently, the core of the massive star has to burn its fuel much faster to maintain hydrostatic equilibrium and is consequently significantly hotter but less dense compared to the SAGB star during the same burning stage.

5.4 Core-Collapse Supernovae

Throughout the course of this thesis, we will refer to supernovae based on their explosion engine, not their spectroscopic properties, as is often done. Here, CCSNe denote the entirety of supernovae following the gravitational collapse of a stellar core to nuclear densities. In that case, a compact stellar object is left behind, being either a NS or a BH. In particular, this definition includes the standard FeCCSN

[4] Based on the classification in Figure 5.1, stars heavier than M_n are called massive stars. But as many other authors (see e.g. Woosley et al., 2002), we adopt non-degenerate carbon burning as criterion for massive stars.

[5] The helium core denotes the whole core that has already undergone hydrogen burning.

of massive stars as well as the ECSN channel of SAGB stars. This definition has the advantage that FeCCSNe and ECSNe are regarded as a subtype of CCSNe. This reflects the fact that they are very similar events, except for the progenitor structure outside of the core prior to collapse as well as the different trigger mechanism for gravitational collapse (silicon shell burning compared to EC on ^{20}Ne). Due to the similarities of the involved physics subsequent to collapse, both phenomena can be discussed together. The explosion mechanism for CCSNe is addressed in Section 5.4.1. Of course, we will also focus on ECSNe and all peculiarities compared to FeCCSNe will be discussed in detail in Section 5.4.2. Regarding the astronomical supernova taxonomy, CCSNe are thought to correspond to supernovae of spectroscopic Type Ib/c and all different kinds of Type II supernovae.

CCSNe are the most luminous individual events in the universe with a peak power of approximately 10^{53}erg s^{-1}. They are of large importance for the understanding of the nucleosynthesis of heavy elements in the universe and its impact on galactic chemical evolution. In addition, they are responsible for the creation of extreme states of matter - NSs or BHs. Understanding the mechanism behind supernova explosions requires a profound knowledge of all four fundamental interactions. The historically most important insight into supernovae originates from astronomical observation, mainly by measuring supernova light curves.[6] However, as photons only decouple from matter at very low densities, the supernova becomes optically visible only when the explosion reaches the stellar surface. In turn, the observed photons cannot probe the interior of the star. Nevertheless, their detection can provide useful information like the supernova explosion energy or the composition of the visible material in the star.

Direct probes for the interior of a CCSN are given by neutrinos, gravitational waves, and the formation of heavy elements in the neutrino-heated ejecta. The neutrinos and anti-neutrinos that are created during the explosion do not only carry nearly all the gravitational binding energy released during core collapse, but they also serve as probes for the interior of the supernova, as they decouple from matter at very high densities deep inside the stellar core. Thus, they can help to reveal information about the supernova explosion mechanism. Due to their very small cross section and the distant event location, it is very challenging to detect supernova neutrinos. So far, the only time that a CCSN neutrino signal has been measured on earth, was the detection of supernova SN 1987A. In total, three different neutrino detectors measured 24 $\bar{\nu}_e$'s in a time interval of 13 s, despite SN 1987A being only about 50 kpc (1.6×10^{23} cm) away (Hirata et al., 1987; Bionta et al., 1987; Aglietta et al., 1987). Nevertheless, the neutrino signal provided valuable information and confirmed the key role of neutrinos in the explosion mechanism of CCSNe. Another possible way of probing the inside of a supernova is the detection of gravitational waves. Gravitational waves originate from any collective, non-spherical, accelerated motion of matter, as for example in the center of a CCSN, and their amplitude scales with the second derivative of the mass-quadrupole moment. By virtue of the first two LIGO detections of coalescing BHs (Abbott et al., 2016a,b), it is hoped that the gravitational-wave signature of a CCSN can be detected with future gravitational-wave detectors like Advanced LIGO, as well.[7] It is expected that it is possible to constrain the explosion mechanism based on the shape of the gravitational-wave signal (Ott, 2009; Janka, 2012). Additionally, the gravitational-wave signal might be able to provide a better understanding of the high-density and high-temperature EoS.

Complementary to the advancing supernova astronomy, CCSNe can be explored by performing numerical simulations on a computer. Nowadays, simulations can be carried out in three spatial dimensions and successively more advanced input physics, like sophisticated ν-transport or larger nuclear reaction networks. Relevant reviews about the progress in the understanding of the CCSN explosion mechanism have been published by Woosley & Weaver (1986); Bethe (1990); Burrows et al. (1995); Janka et al. (2007); Janka (2012) and Müller (2016). Regarding nucleosynthesis in the ejected matter from CCSNe,

[6] This is the energy luminosity of the light being emitted by the supernova over time. If possible, the luminosity is measured frequency dependent to reveal spectroscopic information, as well.

[7] At the time of publication, further LIGO detections have been published, including the first ever measurement of a binary neutron star merger.

the review of Thielemann et al. (1996) should be mentioned. Notice that contrary to the consensus of 20 years ago, nearly all recent CCSN nucleosynthesis calculations find conditions unsuitable for the occurrence of the r-process.

The theory of supernovae is closely related to the understanding of NSs, that were first anticipated by Landau (1932), calling for the existence of a "gigantic nucleus" and predicted by Baade & Zwicky (1934) as the possible remnant of a supernova explosion. The concept of the gravitational collapse was introduced by Zwicky (1938) shortly after. One of the first systematic descriptions of the "Synthesis of Elements in Stars" including supernovae was given by Burbidge et al. (1957). Nevertheless, by that time not much was known about the explosion mechanism itself and the dominating picture was that of a prompt explosion sufficiently powered by the bounce shock itself (introduced in Section 5.4.1). This scenario however could be ruled out, as it requires an unphysical soft high-density EoS. As the initial kinetic energies of the matter would prove insufficient to explain the explosion, it became clear that the shock wave will stall within a few milliseconds after bounce. Only with the progress made in neutrino physics in the 1960s, it could be understood that the neutrinos created during collapse could be the key in explaining the explosion mechanism as they carry away about 99% of the gravitational binding energy released in the CCSN. This idea manifested in the first CCSN simulation on a computer by Colgate & White (1966), drawing the picture of a prompt shock driven by diffusion of neutrinos, which later turned out to be inaccurate, as the neutrino diffusion timescale was too large. Since then, the ongoing increase in computational power has allowed for the development of successively more advanced numerical models. On the one hand, more sophisticated input physics can be considered, like an accurate implementation of weak interactions or a microscopic high-density EoS. On the other hand, the number of considered spatial dimensions in a supernova simulation was found to have a strong influence on the explosion dynamics. Consequently, the transition from spherically symmetric via two-dimensional to three-dimensional models with as little as necessary drawbacks considering microphysics was made. This also includes the question whether and with which level of approximation general relativity is considered. Following both approaches at the same time is as of now, beyond the reach of current supercomputers.

When a star above M_n (see Figure 5.1) has successively passed through all its burning stages and no fuel is left to maintain hydrostatic equilibrium, the core of the star will become degenerate and collapse as soon as it exceeds M_{Ch}. The contraction will proceed until the core reaches nuclear densities ($\varrho_0 \approx 2.6 \times 10^{14}$ g cm^{-3}) and the repulsion due to the strong interaction stops a further contraction of the innermost regions of the star. As a consequence, the infalling matter will rebound and a shock wave is formed that propagates outward through the star. In the current understanding, the shock wave will loose its energy by colliding with accreting matter from outer layers of the star until it finally stalls. The subsequent revival of the stalled shock can bee seen as "the supernova problem" and several mechanisms have long been explored in order to explain why CCSNe explode. All scenarios have to account for a mechanism that can explain additional energy transfer to the baryonic matter behind the shock in order to revive it. After the shock wave has been revived, the star finally explodes and considerable amounts of matter are ejected into the interstellar medium. This means that the release of gravitational binding energy due to the contraction of the core ($\Delta E_{\mathrm{grav}} \approx 10^{53}$ erg) is sufficient to make the outer layers of the star explode ($E_{\mathrm{kin}} \approx 10^{51}$ erg), despite nearly all energy being radiated away by neutrinos. In the center of the supernova a protoneutron star (PNS) will form, that settles down to a NS shortly after. If the remnant gets too compact, it will collapse (instantly or after some time due to fallback) further to a stellar mass BH.

Since it was clear that the key in understanding the supernova explosion mechanism is a model that explains the shock revival, many theories have been proposed. The delayed neutrino-driven explosion mechanism was introduced by Bethe & Wilson (1985). It relies on the assumption that the neutrinos created during the supernova transfer a small fraction of their energy to the baryonic matter and thereby provide the little extra energy to drive the explosion. Even though the neutrino-driven explosion mech-

anism is the most favorable explosion scenario, simulations in spherical symmetry including up to date nuclear physics input and neutrino transport generally fail to reproduce explosions. Only the lightest SAGB progenitor stars that become gravitationally unstable, provide conditions for successful ECSNe in one dimension (Nomoto, 1984, 1987; Kitaura et al., 2006; Fischer et al., 2010; Möller, 2013). More recently, simulations in two and three spatial dimensions could be established. Multidimensional effects like convection, mixing and hydrodynamic instabilities are generally expected to increase the efficiency of neutrino heating and thus support the delayed neutrino-driven mechanism. As a consequence, many studies showed that two-dimensional and later three-dimensional simulations are able to obtain successful explosions, despite falling short in obtaining the canonical explosion energy of 10^{51} erg. A detailed analysis regarding the effects of dimensionality in supernova simulations was performed for example by Nordhaus et al. (2010) and Hanke et al. (2012). Only very recently has it become apparent that in CCSN models simulated in two dimensions, an explosion could be obtained somewhat easier than in three dimensions, different from previous considerations. This is thought to originate in the behavior of the turbulent cascade. While in two dimensions, energy from turbulent fluid motion is reshuffled from small to large scales, the opposite effect occurs in three dimensions. The recent review by Janka et al. (2016) discusses this aspect in some detail.

A lot of different supernova engines were proposed besides the neutrino-driven explosion. The most prominent alternative approach is to consider magnetic fields in supernova simulations.[8] This idea goes back to LeBlanc & Wilson (1970), who proposed that the missing energy that is required to power the explosion comes from the conversion of energy stored in magnetic fields in a rotating supernova scenario, resulting in jet-like explosions. The so-called Magneto Hydro Dynamics (MHD) have been a framework of significant importance ever since and deliver a description of the dynamics of matter under strong magnetic fields, not only in the case of CCSNe. While magnetic-field-driven CCSN models can robustly obtain successful explosions, the initial magnetic field strength in the core is rather obscure and poorly constrained. A recent study was performed by Winteler et al. (2012). In Burrows et al. (2006), a completely new approach towards CCSNe was suggested. The authors proposed that acoustic power created in the inner core contributes to the energy transfer towards matter and could help to drive the explosion. Their simulations show that the acoustic power that is generated inside the core, originates mainly in sonic damping of self-exited g-mode oscillations of the NS, and is sufficiently strong to trigger an explosion. In Sagert et al. (2009), Fischer et al. (2011), and Nishimura et al. (2012), CCSN explosions of massive stars are explored, which are powered by a quark-hadron phase transition that sets in shortly after the core bounce deep inside the stellar core.

5.4.1 Neutrino-Driven Explosion Mechanism

The onset of gravitational collapse is schematically shown in the top left panel of Figure 5.5 and occurs once the core exceeds M_{Ch} and becomes gravitationally unstable. During the early phase of the collapse, Y_e is further decreased from slightly below 0.5 due to EC on iron group nuclei.[9] This in turn lowers the electron degeneracy pressure and accelerates the collapse even further. Another effect resulting in an acceleration of the collapse, that is increasingly important for more massive stars, is the photodisintegration of iron-group nuclei into α particles during the onset of collapse. Because this process absorbs a lot of radiative energy, the core shows less resistance against contraction originating from compressional heating. During the collapse, the central density of the star quickly rises by several orders of magnitude. As soon as the core reaches densities of about 10^{12} g cm^{-3}, the neutrinos that are created in weak

[8] More accurately, this approach is often regarded as complimentary to the neutrino mechanism and is supposed to explain a subclass of CCSNe with strong magnetic fields.

[9] This is also true for ECSN progenitors, as the oxygen and neon in the core are burned into iron-group nuclei during the oxygen deflagration while collapsing.

processes become trapped, meaning that their diffusion timescale becomes comparable to the collapse timescale, as is illustrated in the top right panel of Figure 5.5.

Before the core reaches nuclear matter densities, all nuclei will be dissolved into neutrons and protons. They will then start to repel each other due to the short-distance behavior of the strong interaction as well as nucleon degeneracy pressure. Because bulk nuclear matter has a very low compressibility, the collapse will stop rather abruptly and the first response will be a rebounding behavior of the part of the core where matter is already above nuclear matter density. By this time, the core has typically nearly twofold nuclear density ($\approx 4-5\times10^{14}$ g cm^{-3}). The duration of the core collapse is typically between 0.15 and 0.35 s, starting from the homologous collapse of the core. The time of the core bounce is defined as the moment of the highest central density in the core. Subsequently, an outward moving shock wave forms because the outer layers of the core are still falling in with already supersonic velocities (see middle left panel in Figure 5.5).

After the shock wave has formed, it travels through the still rapidly accreting matter of the outer core and heats it up. When layers composed of silicon or iron-group nuclei are dissociated into free neutrons and protons by the shock wave, about 8 MeV of nuclear binding energy is absorbed by each nucleon and removes kinetic energy from the shock. Additionally, the effect of neutrino emission originating from behind the shock has to be considered. During the shock propagation, as soon as the supernova shock runs across the neutrinospheres,[10] most of the neutrinos that originate from the local production via EC on free protons: $e^- + p \rightarrow n + \nu_e$, are now released as they become free-streaming. It is important to notice that the protons only become abundant as soon as the shock wave has dissociated the matter. This results in a very distinct neutrino signal, called deleptonization burst (or ν_e-burst) and reaches luminosities of up to several times 10^{53} erg s^{-1} on a very short timescale of 0.01 to 0.02 s. This feature is illustrated in the middle right panel in Figure 5.5). During that process, the neutrinos carry away most of the energy available in the shock and the shock wave turns into a standing accretion shock at the outer boundary of a hot and dense PNS.

Starting from the moment of the stalling shock wave, the delayed neutrino-driven explosion mechanism is trying to explain an energy transfer from neutrinos to matter that is sufficiently high to allow the shock to propagate further through the star and drive the explosion. Considering that nearly all gravitational binding energy ($\approx 10^{53}$ erg) is radiated away by neutrinos, only a small percentage of this energy has to be transferred to the matter to account for the canonical value of the kinetic energy of the ejecta of 10^{51} erg. The radius R_s of the standing accretion shock has typically values between 100 and 200 km and is following the contraction of the nascent PNS. Hence, the shock radius is considerably larger than that of the neutrinospheres which have typical radii between 50 and 80 km. This leads to a situation, in which the matter behind the shock is subject to continuous interactions with neutrinos coming from the inside of the PNS. The main interactions by this time are charged-current reactions with free nucleons:

$$\nu_e + n \rightleftharpoons e^- + p, \tag{5.3}$$

$$\bar{\nu}_e + p \rightleftharpoons e^+ + n, \tag{5.4}$$

where reactions going from the left to the right ($\nu/\bar{\nu}$-absorption) transfer energy from neutrinos to matter and are called neutrino heating reactions. Their reverse processes (e^-/e^+-capture) going from right to left transfer energy from matter to neutrinos and are thus called neutrino cooling reactions. The net energy transfer depends strongly on the ratio between the heating and cooling rates q^+ and q^-,

[10] The neutrinosphere is the average radius where the neutrinos decouple from equilibrium with the surrounding baryonic matter, corresponding to $\approx 10^{12}$ g cm^{-3} for CCSNe.

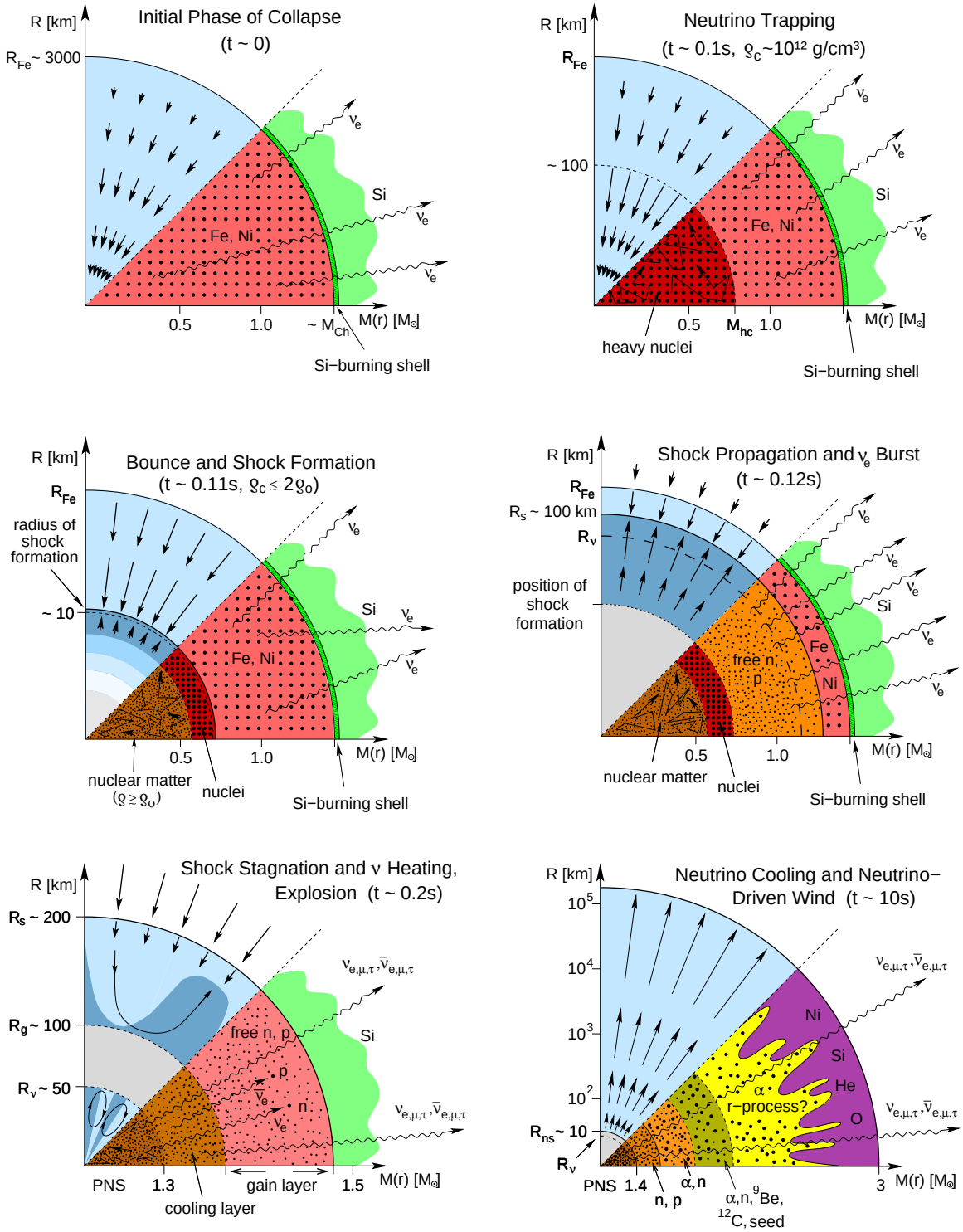

Figure 5.5: Illustration of the different CCSN stages, from Janka et al. (2007). From left top to right bottom is depicted the collapse, the neutrino trapping, the bounce, the shock propagation, the shock stagnation and revival, and the neutrino-driven wind phase. The upper half of each panel shows the dynamical evolution as function of radius and the lower half shows the composition of matter together with neutrino interactions as function of mass. $M_{\rm hc}$ denotes the mass of the homologous inner core, $R_{\rm Fe}$ is the radius of the iron core, $R_{\rm S}$ the shock radius, $R_{\rm g}$ the gain radius, $R_{\rm ns}$ the NS radius, and R_ν the neutrinosphere radius.

respectively. The heating and cooling rates per nucleon, considering only the processes in Equation (5.3) and (5.4), are given by the following estimates (Janka, 2001):

$$q^{+}_{\nu_e+\bar{\nu}_e} \approx 100 \, \frac{L_{E,\nu}}{10^{52}\,\mathrm{erg/s}} \left(\frac{r}{100\,\mathrm{km}}\right)^{-2} \left(\frac{\langle E_\nu \rangle}{10\,\mathrm{MeV}}\right)^{2} \frac{\mathrm{MeV}}{\mathrm{s}}, \tag{5.5}$$

$$q^{-}_{\nu_e+\bar{\nu}_e} \approx 145 \left(\frac{T}{2\,\mathrm{MeV}}\right)^{6} \frac{\mathrm{MeV}}{\mathrm{s}}, \tag{5.6}$$

where $\langle E_\nu \rangle$ is the mean neutrino energy and $L_{E,\nu}$ the neutrino energy luminosity. Since the matter temperature T in Equation (5.6) is roughly proportional to the inverse of the radius, it becomes obvious that the cooling rates fall off roughly with r^{-6} while the heating rates scale with r^{-2}. Consequently, there has to be a certain radius above which the neutrino heating will dominate over the cooling. This radius R_g is called gain radius and is located somewhere in between the PNS and the standing shock. This is displayed in detail in the lower left panel of Figure 5.5. In effect, this means that there is a gain layer behind the shock (between R_g and R_s) where neutrinos deposit energy and eventually contribute to the revival of the shock which, as consequence leads to a successful supernova explosion. Based on the brief discussion in Section 5.4, it becomes clear that multidimensional effects of convective flows behind the shock can increase the energy transfer from neutrinos considerably. Turbulent motion can bring more cold material into the gain region where it is subject to neutrino heating.

After the shock wave has been revived, it travels outward and deposits energy into the outer shells of the star, that are only loosely bound by gravity. Hence, a certain amount of matter reaches velocities that are sufficiently large to escape from the gravitational potential of the star and mix into the interstellar medium. The ejecta from the outer layers of the star consist mostly of the elements of the different shell burning stages and thereby contribute to the synthesis of elements in the universe up to iron-group nuclei. In the same time, the PNS is starting to cool and slowly—by continuous deleptonization due to EC reactions on protons—transforms into a NS. During that process, the NS will contract further to a final size of about 10 to 15 km until it is entirely stabilized by the neutron degeneracy pressure. Depending on the mass of the stellar progenitor and the compactness of the PNS after the CCSN, it is possible that a BH forms after the core collapse. For a BH with mass M, zero charge and zero angular momentum, the critical radius to form a BH is given by the Schwarzschild radius r_s:

$$r_\mathrm{s} = \frac{2GM}{c^2} \approx \frac{2.95}{\mathrm{km}} \frac{M}{M_\odot}. \tag{5.7}$$

It is still unclear whether the BH forms during the supernova explosion or or afterwards due to the fallback of matter onto the PNS. A recent study on the progenitor dependency of BH formation can be found in Ertl et al. (2016). While the PNS is cooling, it emits a considerably large amount of neutrinos on a timescale of 10 s after the core collapse (typically $L_{E,\nu_e} \approx L_{E,\bar{\nu}_e} \approx 10^{51}$ erg s^{-1}). It is exactly this setup together with a zone of comparatively low density between the PNS surface and the supernova shock that gives rise to the so-called neutrino-driven wind which is illustrated in the lower right panel of Figure 5.5. For a long time, it was believed, that this setup is a possible site of heavy element nucleosynthesis via the r-process. As recent studies consistently show that the conditions in neutrino-driven winds from CCSNe are not suitable to account for a full r-process, other nucleosynthesis scenarios like the νp-process are considered (Fröhlich et al., 2006). Currently, the main-component of the r-process is thought to occur in NS-NS mergers (see e.g. Just et al., 2015).

5.4.2 Electron-Capture Supernovae

Stars between 8 and 10 $\mathrm{M}_\odot$ are thought to be the lightest stars that end their life with a gravitational collapse leading into a CCSN. This mass range represents also the transition region between SAGB stars

forming electron-degenerate ONe cores and massive stars that form non-degenerate iron cores. In Section 5.2.2, we already introduced ECSNe as the possible fate of SAGB stars that become gravitationally unstable due to EC reactions on magnesium and neon. It was also pointed out that it is unclear what exact fraction of SAGB stars becomes gravitationally unstable due to ECs after all. Additionally, the question was raised whether the ONe core will collapse to NS densities after becoming unstable. The answer depends critically on the details of the oxygen deflagration that is initiated by the thermonuclear runaway during the collapse. Unfortunately, no review dedicated entirely to ECSNe exists, which is why the reader is referred to the recent CCSN review of Müller (2016) that dedicates a rather long section to ECSN progenitor models and simulations.

The difference between FeCCSNe of massive stars and ECSNe originates mainly from the different progenitor structure of SAGB stars compared to their massive counterparts. As SAGB stars remove most of their envelope during their evolution, the standard mechanism of exceeding M_{Ch} solely by shell burning above the core cannot work. Hence, for those stars, another path towards core collapse was first suggested by Miyaji et al. (1980). It was shown that EC reactions in an degenerate ONe core of a star could trigger core collapse by proceeding in the following way:

$$^{24}\mathrm{Mg}\left(e^{-}, \nu_e\right)^{24}\mathrm{Na}\left(e^{-}, \nu_e\right)^{24}\mathrm{Ne}, \tag{5.8}$$

$$^{20}\mathrm{Ne}\left(e^{-}, \nu_e\right)^{20}\mathrm{F}\left(e^{-}, \nu_e\right)^{20}\mathrm{O}. \tag{5.9}$$

Notice that the threshold density for the onset of EC is roughly 4×10^9 g cm^{-3}. Hence, if the core-growth during the SAGB phase pushes the core above this threshold, that corresponds to a core mass of about $M_{\mathrm{ec}} \approx 1.37\ M_{\odot}$, EC on ^{24}Mg and ^{20}Ne, that are greatly abundant in the ONe core, start to operate. In this stellar environment, the EC reactions have two main effects. First of all, they lead to a strong increase in temperature in the central region of the star. Second of all, they reduce the number of free electrons in the system and thereby decrease Y_e in the core. Hence, the continuous deleptonization is reducing the electron degeneracy pressure and destabilizes the core until it finally exceeds M_{Ch} and becomes gravitationally unstable. Note that the Chandrasekhar mass limit scales with Y_e^2 which means that in the moment of the onset of collapse, the core mass can be significantly lower than 1.4 $\mathrm{M}_{\odot}$. Regarding the heating of the core, it was concluded in Miyaji et al. (1980) that the collapse is expected to start prior to the ignition of an oxygen flame.

The first study of stellar progenitors that collapse and supposedly explode in an ECSN scenario was performed by Nomoto (1984, 1987). In Miyaji & Nomoto (1987), the ignition density of the oxygen deflagration that is initiated by the EC reactions is studied in detail, properly taking into account the convective behavior in the star. It was later shown explicitly by Mayle & Wilson (1988), that an ECSN explosion can be successfully modeled in computer simulations, relying on stellar progenitor data from Nomoto (1987). Despite the fact that the helium star models of Nomoto (1987) left many complications of stellar models that go all the way from the main-sequence to the SAGB phase untouched, they still give rise to the canonical pre-supernova structure for ECSN simulations, also due to the absence of more recent models that were simulated sufficiently far until collapse. Notice that Takahashi et al. (2013) produced ECSN progenitor models that are very similar to Nomoto's 8.8 $\mathrm{M}_{\odot}$ star.

As already indicated, an important characteristic of SAGB stars is that they expel large parts of their hydrogen-rich envelope while climbing up the AGB, so that in the final stage of their evolution, the stellar core is surrounded by a very dilute envelope. For example, the total mass of Nomoto's 8.8 $\mathrm{M}_{\odot}$ star below the hydrogen-rich envelope prior to collapse is only about 1.37 $\mathrm{M}_{\odot}$. Consequently, there is a very steep density gradient on the edge of the carbon layer, where the density drops by many orders of magnitude. This aspect is illustrated in Figure 5.6, where several low-mass progenitor models are compared. While the density profile in the core of the star is rather similar for various stellar models between 8 and 15 $M_{\odot}$, the outer layers and the stellar envelope can differ significantly. In the case of Nomoto's 8.8 $\mathrm{M}_{\odot}$ progenitor, no envelope was considered at all. This distinct feature of ECSN progenitors, facilitates the

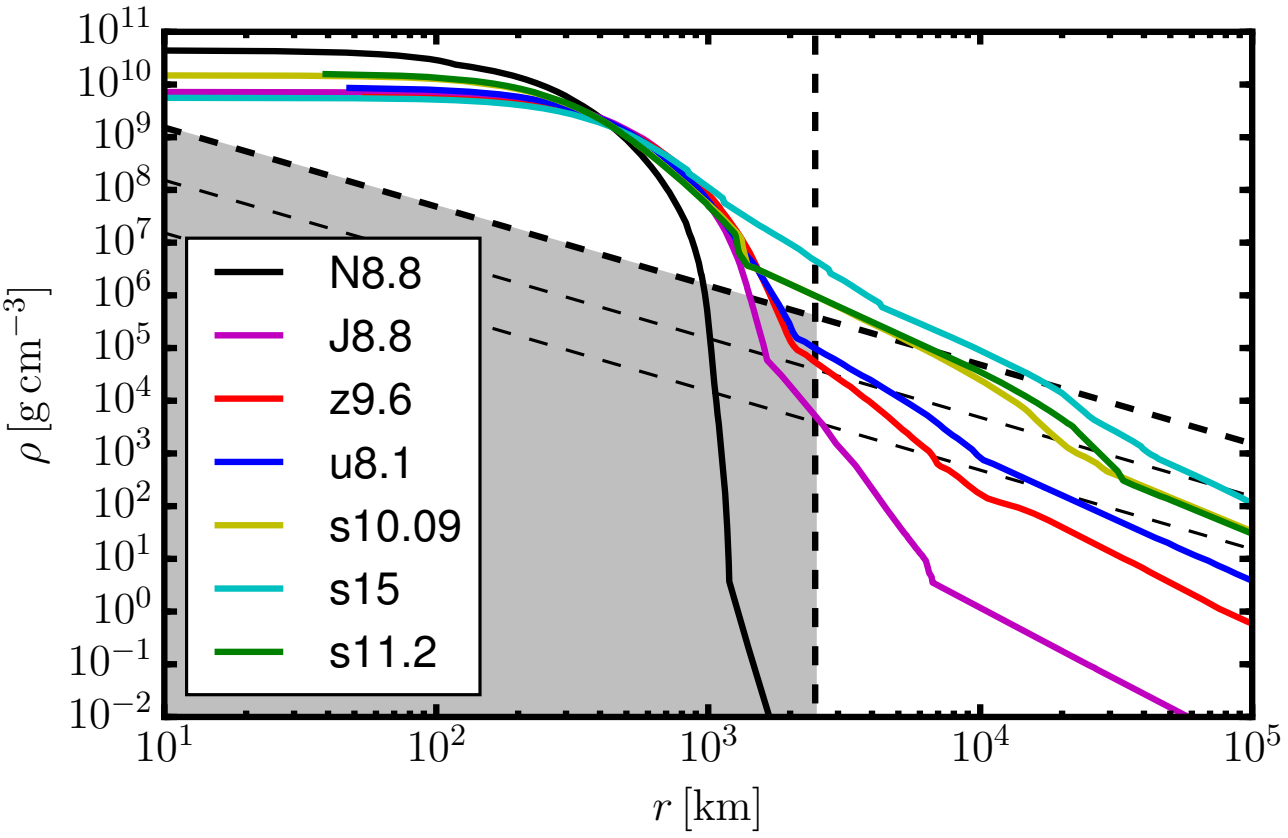

Figure 5.6: Density profiles of selected low-mass supernova progenitors (8.1 to 15 $M_\odot$), from Müller (2016). Progenitor models by references therein. Stellar profiles that intersect the gray-shaded area are thought to explode in an ECSN-like scenario, applying only to stellar models $\lesssim 10\ M_\odot$. The different explosion characteristics between ECSNe and FeCCSNe are related to the density and the thickness of the remaining stellar envelope at the onset of core-collapse. The canonical ECSN progenitor (N8.8, Nomoto, 1984) has virtually no envelope remaining.

revival of the supernova shock after it has stalled, due to the reason that the ram pressure from the still collapsing outer layers onto the shock front is much smaller compared to massive stars. This in turn is very interesting for self-consistent CCSN simulations, as in contrast to massive stars, ECSNe explode in spherically symmetric models without artificially powering the explosion. This has been confirmed by all recent ECSN simulations (Kitaura et al., 2006; Fischer et al., 2010; Möller, 2013).

It is unquestioned nowadays that the key in robustly and quantitatively explaining the neutrino-driven explosion mechanism for a large variety of progenitors has to be performing multidimensional simulations. Nevertheless, certain studies critically rely on physics that are still mainly accessible via one-dimensional simulations that can be carried out for several seconds post-bounce and use detailed neutrino transport and large nuclear reaction networks. Because self-consistent studies of CCSNe in one dimension are only available for the lightest supernova progenitors, ECSNe are especially suitable for nucleosynthesis studies.

For a long time, it was speculated that ECSNe could be responsible for the r-process in neutrino driven-winds subsequent to the supernova explosion. In early nucleosynthesis studies, it was suggested (not based on simulations) that the r-process could occur in explosions of ONe cores Wheeler et al. (1998). However, in Wanajo et al. (2003), a spherically-symmetric Newtonian supernova simulation was performed and no r-process was found for self-consistent explosion models. The authors in Ning et al. (2007) suggested that the r-process could potentially occur in the shocked surface layers of the ONe core

subsequent to an ECSN. This was however based on an artificial shock model, not on a self-consistent simulation. Consequently, in Janka et al. (2008), this issue was investigated in more detail on the basis of hydrodynamic simulations in one and two dimensions and it was concluded that the occurrence of the r-process in shocked surface layers of ONe cores is unlikely. In all recent nucleosynthesis studies of ECSNe based on realistic and self-consistent supernova explosion models, it was concluded that the r-process in unlikely to occur in the neutrino-driven wind after an ECSN. This was shown by several publications, most notably by Kitaura et al. (2006); Wanajo et al. (2009); Hüdepohl et al. (2010) and Wanajo et al. (2011). Consequently, it was among others suggested by Hansen et al. (2012), that ECSNe could nevertheless have a weak contribution to the observed r-process abundances while the main component comes from a different nucleosynthesis site.

6 Evolution and Fate of Degenerate Oxygen-Neon Cores

This chapter contains the main results regarding the evolution and fate of degenerate ONe cores. Section 6.1, will be devoted to a discussion of the different evolutionary stages of degenerate ONe cores, focusing in particular on the weak processes that are relevant in each stage. In Section 6.2, we propose possible modifications to the standard neon and oxygen burning phases in high-density conditions, as they occur during the late evolution of intermediate-mass stars ($7-11\ M_{\odot}$). In Section 6.3, we present results of mass-accreting ONe WDs in the AIC scenario (on the basis of the initial models by Schwab et al. (2015) that evolve towards the ignition of oxygen. This study was conducted with the help of the stellar evolution code MESA, which will be introduced briefly in Section 6.3.1. In particular, we made use of the recently implemented on-the-fly weak rate determination (Paxton et al., 2015). The main purpose of this study is to assess uncertainties related to weak reactions (particularly Urca processes), thermonuclear reactions (including the modifications presented in Section 6.2), as well as convection. Another goal of this study has been generating initial models of ONe cores that ignite oxygen in the center for different accretion rates $\dot{M}$. These can then be used to study the subsequent phase of the oxygen deflagration in spherically-symmetric hydrodynamic models. For this purpose, we will present preliminary results of such simulations with the shock-capturing CCSN code AGILE-IDSA and furthermore demonstrate (based on the work in Möller (2013) that AGILE-IDSA is capable of obtaining self-consistent ECSN explosions, using the canonical progenitor of Nomoto (1984).

6.1 Oxygen-Neon Core Evolution - The Canonical Picture

Degenerate ONe Cores have already been introduced in Chapter 1. Here, we want to approach the topic in a chronological order, starting after the formation of an ONe core, investigating what happens to such a system under the accretion of mass and the continuous increase of the central density ϱ_c. Following the seminal work of Miyaji et al. (1980), we will divide the evolution into different phases and refine the scheme that was developed in Miyaji et al. (1980). The canonical SAGB (left panel, 8.75 and 8.8 $M_{\odot}$, Jones et al., 2013) and AIC (right panel, Schwab et al., 2015) models that are displayed in Figure 6.1 will serve us as guideline for the following discussion, both hosting mass-accreting degenerate ONe cores.

SAGB vs. AIC - Mechanism of Core Growth

In the canonical SAGB star scenario, the ONe core is formed by a carbon burning flame[1] at densities around $\varrho_c \approx 10^{6-7}$ g cm^{-3}. Afterwards, due to the absence of nuclear burning, the core is contracting until electron-degeneracy pressure becomes dominating at $\varrho_c \approx 10^{9}$ g cm^{-3}. In the meantime, the evolution of the star is driven by a growing core due to exterior shell burning. Recent studies of SAGB stars that also cover the late evolutionary phase, were performed for example by Takahashi et al. (2013) and Jones et al. (2013). While the core growth rate $\dot{M}$ (usually measured in $M_{\odot}$ yr^{-1}) is ultimately set by hydrogen burning and can in principle be accurately determined by simulating the thermal pulses during the SAGB phase, the stellar mass loss from the envelope is rather uncertain (for details see Section 5.2.2). Due to a strong mass loss, it might happen that the phases of evolution after carbon burning, which we want to study in this chapter, will not occur, resulting in an ONe WD. Hence, we will ignore

[1] In Farmer et al. (2015), carbon burning in SAGB stars is investigated in great detail.

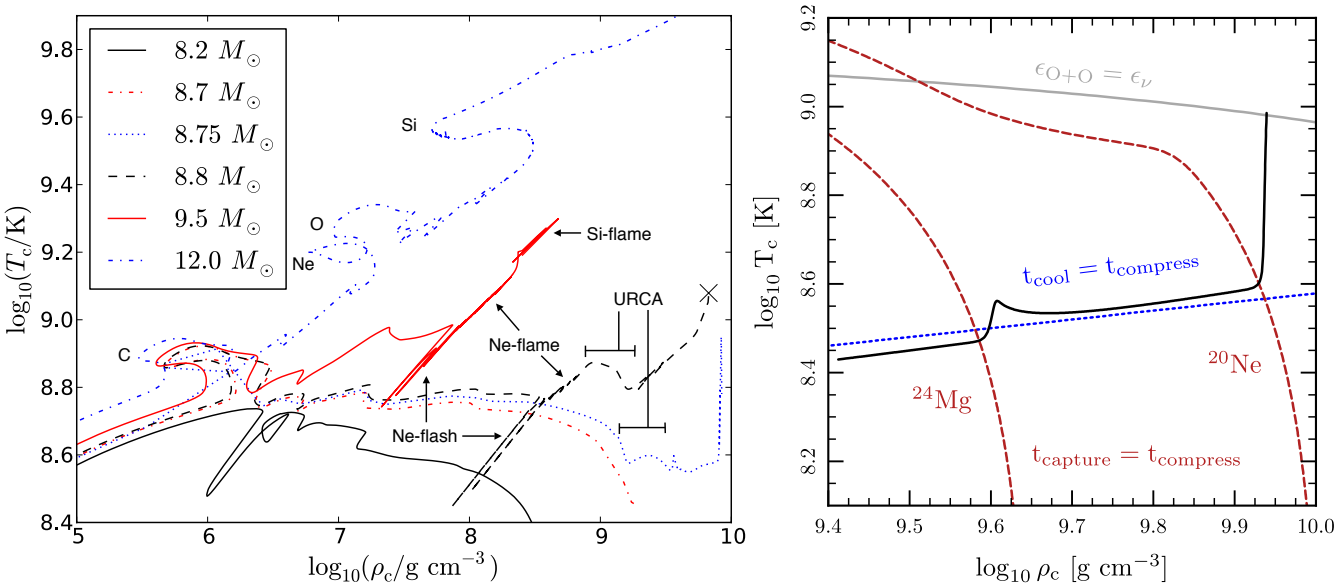

Figure 6.1: Left panel: Canonical intermediate-mass stellar models from Jones et al. (2013). The late stellar evolution is illustrated in a central density-central temperature diagram. The 8.75 and 8.8 $M_\odot$ models are SAGB stars that eventually trigger EC on ^{20}Ne and ignite oxygen burning in the core and potentially proceed towards an ECSN. Both models are also subject to Urca cooling prior to the ignition of oxygen. Right panel: Canonical AIC evolution from Schwab et al. (2015) in a central density-central temperature diagram. In the illustrated model, the accretion rate is $\dot{M} = 10^{-6}\ M_\odot\ \mathrm{yr}^{-1}$ and only EC on ^{24}Mg and ^{20}Ne are considered. The central temperature evolves by the balance of compressional heating and plasma neutrino cooling ($t_{cool} = t_{compress}$), as indicated by the blue dashed line. The two red dashed lines mark the balance between the EC timescale of ^{24}Mg (or ^{20}Ne) and $t_{compress}$. Above the gray line, oxygen fusion releases more energy than is removed by neutrinos, marking the onset of the oxygen deflagration in these models.

this uncertainty completely and assume that there is sufficient material available for the stellar core to always proceed through the whole depicted evolution and ultimately exceed M_{ch}.

The other scenario for accreting ONe cores is the AIC of an ONe WD. It was introduced by Nomoto & Kondo (1991) in the context of a binary system, where an ONe WD accretes matter from a regular companion star, as well as in the context of the cooling phase of a massive WD, subsequent to a merger of two lighter CO WDs (Saio & Nomoto, 1985).[2] In both cases, the system is expected to exceed M_{ch} due to the mass accretion and collapse to a NS while exploding in an ECSN. Notice that this has to be seen in contrast to mass accretion onto regular CO WDs, where a similar evolution leads to a disruption of the star in a thermonuclear explosion, driven by the carbon flame.[3] Important additional publications concerning the AIC of ONe WDs are given by Dessart et al. (2006); Fryer et al. (1999); Bravo & García-Senz (1999) and very recently by Schwab et al. (2015).

Despite the different scenarios in which mass-accreting degenerate ONe cores can appear, their evolution is very similar and determined by the same set of input physics, mostly related to weak processes. The main difference is mostly the reason for the growth of the core and the question whether the core grows beyond the critical mass for the onset of EC processes on ^{24}Mg and ^{20}Ne. Studies that consider the ONe core isolated from exterior processes (as they occur in SAGB stars) usually refer to the AIC of ONe cores (Isern et al., 1991; Gutierrez et al., 1996, see e.g.) but if one leaves the very complicated thermally pulsing phases in SAGB stars aside and parametrizes the core growth by an extrapolated rate $\dot{M}$ (similar to synthetic AGB models, as discussed in Section 5.2.1), their discussion becomes equivalent to the AIC

[2] Seminal work was already performed by Canal & Schatzman (1976), where the non-explosive collapse of CO WDs was discussed, mostly based on timescale arguments.

[3] The events are most likely observed as regular Type 1A supernovae.

scenario. Hence, it is justified to to study the evolution of degenerate ONe cores independent from the origin of accretion, as we will do in this chapter.[4]

Core Growth - Relevant Timescales

Initially, the evolution of ONe cores is driven by the balance between compressional heating and cooling by plasma neutrino emission. As the heating is insufficient, the core does not reach the critical temperature of 1.5 GK for neon burning and contracts due to the absence of nuclear energy generation to densities in excess of 10^9 g cm^{-3}, where the main pressure is due to degenerate electrons. At that time, the core mass is already very close to $M_{\rm Ch}$ ($M_{\rm core} \approx 1.3\ M_\odot$). Subsequently, the compression in the degenerate core is driven by the accretion of mass at a rate $\dot{M}$ that sets the relevant timescale of the evolution of the system. The compression timescale (corresponding to the e-folding time of the central density ϱ_c) is given by:

$$\tau_{\rm compress} = \left(\frac{d\ln\varrho_c}{dt}\right)^{-1} = \left(\frac{d\ln\varrho_c}{d\ln M_{\rm core}}\right)^{-1}\frac{M_{\rm core}}{\dot{M}}. \tag{6.1}$$

In Schwab et al. (2015), an empirical for fit for $\tau_{\rm compress}$ was derived for zero-temperature WDs that is valid in the relevant density regime between $10^9 \lesssim \varrho_c/{\rm g\ cm^{-3}} \lesssim 10^{10}$:

$$\tau_{\rm compress}/{\rm yr} \approx 5\cdot 10^4 \left(\frac{\varrho_c}{10^9\ {\rm g\ cm^{-3}}}\right)^{-0.55}\left(\frac{\dot{M}}{10^{-6}M_\odot{\rm yr}^{-1}}\right)^{-1}. \tag{6.2}$$

In order to obtain the correct temporal evolution (for now ignoring nuclear reactions), plasma neutrino cooling has to be accounted for. Hence, the cooling timescale due to neutrino emission has to be provided. It is given by:

$$\tau_{\rm cool} = \frac{c_P T}{\dot{\epsilon}_\nu(\langle A\rangle, \langle Z\rangle, \varrho, T)}, \tag{6.3}$$

where c_P is the specific heat at constant pressure and $\dot{\epsilon}_\nu$ is the neutrino loss rate as introduced in Section 2.3. If the core evolution is set by these two timescales, then a unique temperature-density relation can be obtained by equating $\tau_{\rm compress}$ and $\tau_{\rm cool}$. This should be reflected in the trajectory of such an accreting ONe core in a central density-central temperature diagram. In the right panel of Figure 6.1, a canonical AIC model of the study by Schwab et al. (2015) is illustrated. It is visible that the temperature evolution of an accreting ONe core follows exactly the blue line, that is set by this equilibrium, unless weak processes occur that release or absorb energy in the plasma on a shorter timescale. This is clearly the case for the periods where EC on ^{24}Mg and ^{20}Ne occur (illustrated as well in the right panel of Figure 6.1).

Initial Composition

ONe cores are mainly composed of the carbon burning ashes ^{16}O and ^{20}Ne. At the end of carbon burning, their mass fractions are given by $X(^{16}{\rm O}) \approx 0.5$ and $X(^{20}{\rm Ne}) \approx 0.4$. Furthermore, ^{24}Mg, ^{23}Na, ^{25}Mg and ^{27}Al are produced in smaller but non-negligible amounts of up to several percent. For details regarding the involved nuclear reactions and the synthesized elements during carbon burning, the reader is referred to the discussion in Iliadis (2007, page 472 and following). Of course, the exact elemental abundances after carbon burning also depend on the conditions in which carbon burning operates, i.e. density, degeneracy, and its duration. Consequently, the outcome can vary from star to star, especially when comparing carbon burning in massive stars with carbon burning in SAGB stars, where the densities are significantly higher. In Jones et al. (2013), the 8.75 and 8.8 $M_\odot$ SAGB star models have abundances

[4] This also implies that the accretion rate $\dot{M}$ is a free parameter that can be varied within some reasonable limits, inferred for example from SAGB star models that model all the thermal pulses.

of $X(^{24}\mathrm{Mg}) \approx 0.05$, $X(^{23}\mathrm{Na}) \approx 0.03$, $X(^{25}\mathrm{Mg}) \approx 0.02$ and $X(^{27}\mathrm{Al}) \approx 0.01$ in the post-carbon burning material, at most. Hence, the values will serve as upper limits regarding the study of their impact on the evolution of the ONe core (see Section 6.3.3).

In earlier publications, ^{24}Mg was believed to have a significantly larger mass fraction in the core compared to the current canonical value. This is mainly related to a better experimental determination of key reaction rates during carbon burning. Hence, ONe(Mg) cores are usually called ONe cores nowadays, although they were previously called ONeMg cores (see e.g. Miyaji et al., 1980). Typical levels of ^{24}Mg are given by $X(^{24}\mathrm{Mg}) \approx 0.05$ (same as the canonical value given in the previous paragraph). In Gutiérrez et al. (2005); Schwab et al. (2015), the impact of the ^{24}Mg mass fraction on the evolution of ONe(Mg) cores was studied in great detail. In the second publication, it was concluded that only for $X(^{24}\mathrm{Mg})$ above 7% (a value that is rather unlikely to achieve in the light of the most up-to-date nuclear reaction rates), the core evolution would be significantly altered due to EC on ^{24}Mg at a density of $\log_{10}\left(\varrho/\mathrm{g\ cm^{-3}}\right) \approx 9.6$. Between $0.07 \lesssim X(^{24}\mathrm{Mg}) \lesssim 0.2$, the onset of EC on ^{20}Ne is delayed to considerably higher densities, while for $X(^{24}\mathrm{Mg})$ in excess of 0.2, the heating due to EC on ^{24}Mg triggers oxygen burning directly, at significantly lower densities. This outcome was already predicted by Miyaji & Nomoto (1987).

Electron Capture on *sd*-Shell Nuclei

The central density in the core, mainly composed of the *sd*-shell nuclei ^{16}O and ^{20}Ne, is continuously growing due to mass accretion, starting from initial values around $\log_{10}\left(\varrho/\mathrm{g\ cm^{-3}}\right) = 9$. In the extreme-relativistic ultra-degenerate limit (zero-temperature), the Fermi energy E_F of an electron gas with number density n_e is given by (assuming $Y_e \approx 0.5$):

$$E_F = hc\left(\frac{3n_e}{8\pi}\right)^{1/3} \approx 4.1\ \mathrm{MeV}\left(\frac{\varrho}{10^9\ \mathrm{g\ cm^{-3}}}\right)^{1/3}. \tag{6.4}$$

In degenerate conditions, E_F and the chemical potential of the electrons (here μ) can be related by a power series expansion in k_BT/E_F (see e.g. Fetter & Walecka, 1971, page 48):

$$\mu = E_F\left[1 - \frac{\pi^2}{12}\left(\frac{k_BT}{E_F}\right)^2 + \cdots\right], \tag{6.5}$$

where only the first two terms of the power series are given. At the characteristic temperatures around 0.3 GK, the electron chemical potential μ is hence given to a very good approximation by the Fermi energy E_F ($(k_BT/E_F)^2 \approx 10^{-4}$) and both terms can be used interchangeably. Looking at the characteristic evolution of the central density between $10^9 \lesssim \varrho_c/\mathrm{g\ cm^{-3}} \lesssim 10^{10}$, the electron chemical potential increases during this phase from roughly 4 MeV to 9 MeV.

Consequently, this environment allows for the occurrence of EC reactions on the abundant nuclei once the electrons have enough energy to overcome the Q value of the reaction. For the ^{24}Mg-EC, the Q value is 6.026 MeV and for ^{20}Ne, it is 7.535 MeV (considering the ground state-ground state transition). Notice that in Table 6.3, among other quantities, EC and β decay Q values of the abundant nuclear species in ONe cores are listed. Now, it is possible to define a threshold density $\varrho_{\mathrm{threshold}}$ for each nuclear transition at which E_F equals exactly the Q value of the associated EC process. Without going into more detail at this point, we would expect a certain EC process to be inhibited below $\varrho_{\mathrm{threshold}}$ due to the absence of electrons with sufficiently high kinetic energies to overcome the Q value of the reaction.

This simple picture is however somewhat incomplete. First of all, several transitions can contribute to the total EC rate at such conditions and the ground state-ground state transition might be forbidden by selection rules. Additionally, finite temperate effects result in a non-zero reaction rate at sub-threshold densities, because of the high-energy tail of the electron distribution function that is increasing exponentially with temperature. (This is illustrated for the ^{20}Ne and ^{24}Mg EC in the left panel of Figure

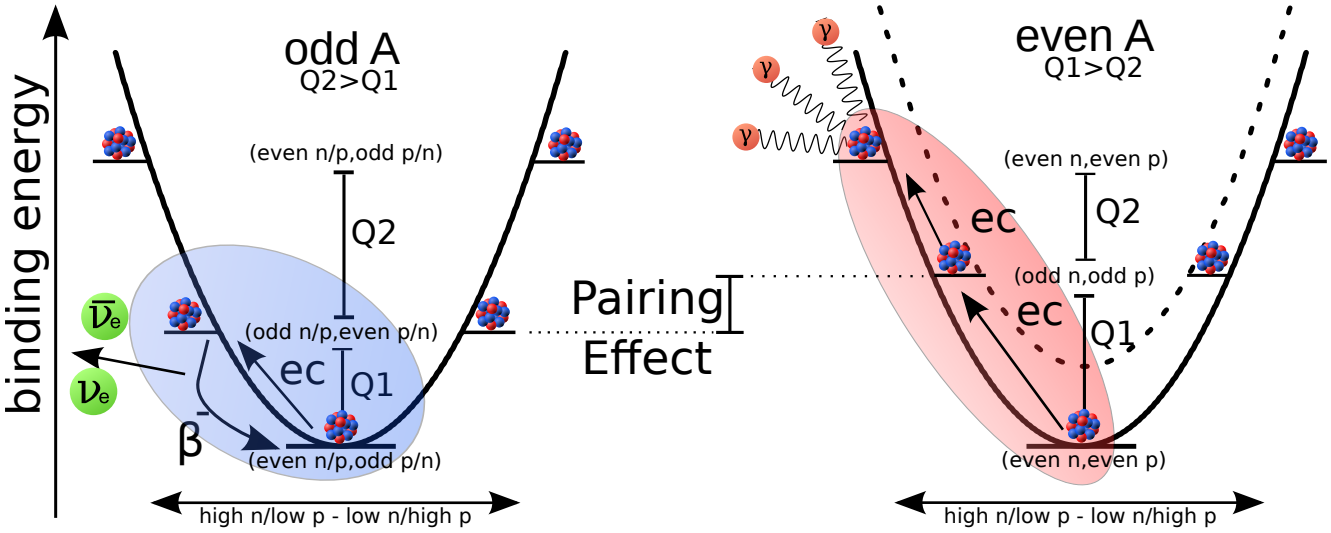

Figure 6.2: Illustration of the mass parabola for an isobaric chain of nuclei in the *sd*-shell, focusing on the implications for EC and β-decay processes that occur in dense stellar plasma. The left side depicts odd-*A* nuclei, the right side even-*A* nuclei. The most stable nucleus is situated in the apex of the parabola. For an odd-*A* chain, the Q value between the most stable nucleus and its neighbors (Q1) is typically smaller that the Q value between the nearest neighbor and the next to nearest neighbor (Q2). For an even-*A* chain, it is the opposite. In the right conditions, as they occur on degenerate ONe cores, this leads to Urca cooling for EC on odd-*A* nuclei and a strong heating effect for EC on even-*A* nuclei.

6.3). For the two most abundant nuclei in the core, $\varrho_{\text{threshold}}$ is given by $\log_{10}\left(\varrho/\text{g cm}^{-3}\right) \approx 9.6$ for ^{24}Mg and $\log_{10}\left(\varrho/\text{g cm}^{-3}\right) \approx 9.95$ for ^{20}Ne. Here, it was taken into account, that in both cases, the ground state-ground state transition is forbidden by selection rules (see Figure 6.3). Referring back to the canonical SAGB and AIC models in Figure 6.1, we can easily see, that these values compare very well to the displayed evolution of the ONe core. In both cases, the onset of EC on first ^{24}Mg and then ^{20}Ne after reaching $\varrho_{\text{threshold}}$ marks the onset of a brief phase, where the core is subject to heating. In the case of ^{20}Ne, this effect is so strong that it leads to the ignition of neon and oxygen.

The main effect of EC processes in stellar cores is that they lower Y_e by removing electrons. As this occurs in a system supported by electron degeneracy pressure, this drives the system towards even higher densities and brings it closer to gravitational collapse by reducing M_{Ch}. In addition to that, EC reactions are also responsible for heating or cooling the plasma in which they occur. In Section 4.4.2, we derived expressions that quantify the energy release associated with weak processes in detail. From Equation (4.110), we know that the energy release of an EC reaction is given by:

$$\epsilon_{ec} = Q_{gs\to gs} + \mu_e - \langle E_\nu \rangle, \tag{6.6}$$

where $\langle E_\nu \rangle$ is the average energy of the neutrino produced in the reaction. Obviously, an EC reaction occurring around the threshold density ϱ_{thresh} (at low temperatures) will neither release nor produce a lot of energy, because $\varrho_{\text{threshold}}$ was exactly defined by $Q_{gs\to gs} + \mu_e = 0$. And in addition to that, the captured electrons have just enough energy to overcome the Q value (even though they stem from the high-energy tail of the distribution function). Consequently, the energy of the produced neutrino will be small, as well. Regarding EC reactions setting in around threshold density, a naive expectation would be that they do not have a large impact on the temperature evolution of the star. Of course, this contradicts the statement that ECs on *sd*-shell nuclei in stars are responsible for heating or cooling the plasma. As it turns out, these effects can only be understood if also secondary EC and β^- decay processes are taken into account.

The basic mechanism of these processes is displayed in Figure 6.2. It depicts the mass parabola for an isobaric chain of nuclei, where the most stable nucleus is situated in the apex of the parabola. Due to

the pairing effect in nuclei, the general appearance of the mass parabola for odd-*A* isotopes (left panel) is different from the one of even-*A* isotopes (right panel). For an odd-*A* chain, the Q value between the most stable nucleus and its two neighboring nuclei (Q1) is typically smaller that the Q value between the neighboring nucleus and the next to nearest neighbor (Q2). For an even-*A* chain, this is exactly the opposite. In the right conditions, as they occur on degenerate ONe cores, this leads either to Urca cooling due to EC on odd-*A* nuclei and a strong heating effect due to EC on even-*A* nuclei.

As the density grows and the electron Fermi energy increases, EC processes set in first on nuclei of odd-*A* chains, assuming that they are abundant. Here, the capture threshold is comparably low (see left panel of Figure 6.2). However, the electron energy at this moment is not large enough to allow for a second EC to occur on the just produced nucleus and eventually, it will decay back to the original nucleus, producing an Urca cycle (Tsuruta & Cameron, 1970):

$$(A,Z)+e^- \rightarrow (A,Z-1)+\nu_e, \tag{6.7}$$
$$(A,Z-1) \rightarrow (A,Z)+e^-+\bar{\nu}_e. \tag{6.8}$$

In this Urca cycle, two neutrinos are emitted, carrying away energy from the stellar plasma. The result of this is the very efficient Urca cooling mechanism. Because the β^- decay channel is quickly blocked by final state electron blocking (with increasing density), the Urca mechanism can only occur for a very brief period in density. In the left panel of Figure 6.1, it can be seen that ONe cores of SAGB stars are subject to Urca cooling, as well. Reaching densities of $1-3\times10^9$ g cm^{-3}, Urca cooling occurs, predominantly involving the following odd-*A* nuclei that are abundant after carbon burning in the star :^{23}Na, ^{25}Mg, ^{27}Al. Hence, the main EC and β decay reaction channels are given by (sorted by Q value):

$$^{27}\mathrm{Al}+e^- \rightarrow {}^{27}\mathrm{Mg}+\nu_e, \quad {}^{27}\mathrm{Mg} \rightarrow {}^{27}\mathrm{Al}+e^-+\bar{\nu}_e, \quad \left(Q^{ec}_{gs\rightarrow gs}=-3.121\ \mathrm{MeV}\right), \tag{6.9}$$
$$^{25}\mathrm{Mg}+e^- \rightarrow {}^{25}\mathrm{Na}+\nu_e, \quad {}^{25}\mathrm{Na} \rightarrow {}^{25}\mathrm{Mg}+e^-+\bar{\nu}_e, \quad \left(Q^{ec}_{gs\rightarrow gs}=-4.346\ \mathrm{MeV}\right), \tag{6.10}$$
$$^{23}\mathrm{Na}+e^- \rightarrow {}^{23}\mathrm{Ne}+\nu_e, \quad {}^{23}\mathrm{Ne} \rightarrow {}^{23}\mathrm{Na}+e^-+\bar{\nu}_e, \quad \left(Q^{ec}_{gs\rightarrow gs}=-4.886\ \mathrm{MeV}\right). \tag{6.11}$$

However, the situation is different for an even-*A* chain of nuclei. Because of the significantly larger capture threshold on stable nuclei, EC on even-even nuclei set in at higher densities compared to the odd-*A* chain. Once the electron Fermi energy becomes large enough to produce a capture on the even-even nucleus, it is followed immediately by a second capture on the odd-odd nucleus (see Figure 6.2), as the second Q value is much smaller than the first one:

$$(A,Z)+e^- \rightarrow (A,Z-1)+\nu_e, \tag{6.12}$$
$$(A,Z-1)+e^- \rightarrow (A,Z-2)+\nu_e. \tag{6.13}$$

For the second step in this chain, the electron Fermi energy E_F is much higher than the capture threshold. As a consequence, the even-even nucleus is produced in a highly excited state that decays by gamma emission, releasing energy that is transformed into heat in the star. As even-even nuclei are significantly more abundant in the stellar core than odd-*A* nuclei, once EC on even-*A* nuclei are present, there is always a net source of heating that contributes to raising the temperature in the star. First, ^{24}Mg is converted into ^{24}Ne and later EC on ^{20}Ne occur. The corresponding reaction chains are given by (sorted by Q value):

$$^{24}\mathrm{Mg}+e^- \rightarrow {}^{24}\mathrm{Na}+\nu_e, \quad {}^{24}\mathrm{Na}+e^- \rightarrow {}^{24}\mathrm{Ne}+\nu_e, \quad \left(Q^{ec}_{gs\rightarrow gs}=-6.026\ \mathrm{MeV}\right), \tag{6.14}$$
$$^{20}\mathrm{Ne}+e^- \rightarrow {}^{20}\mathrm{F}+\nu_e, \quad {}^{20}\mathrm{F}+e^- \rightarrow {}^{20}\mathrm{O}+\nu_e, \quad \left(Q^{ec}_{gs\rightarrow gs}=-7.536\ \mathrm{MeV}\right). \tag{6.15}$$

Due to their special relevance for ONe cores, the EC rates on ^{20}Ne and ^{24}Mg have recently been reevaluated by Martínez-Pinedo et al. (2014). It was pointed out that the second-forbidden transition between

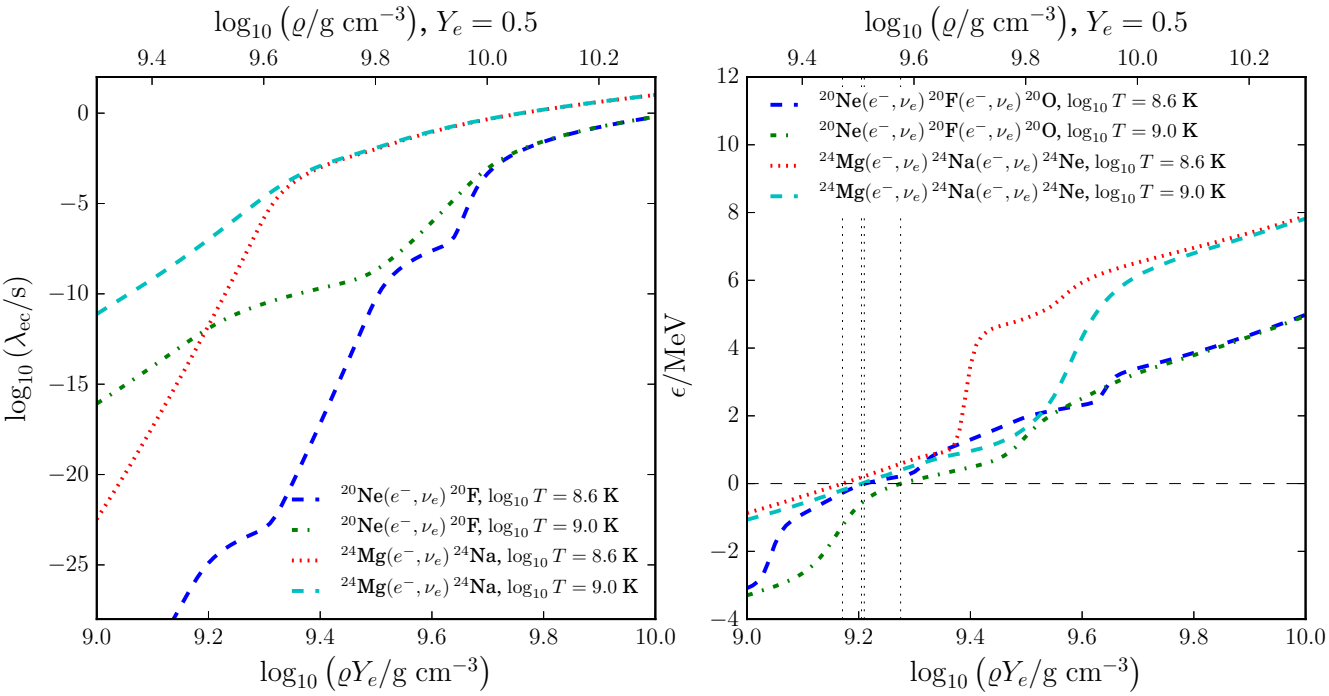

Figure 6.3: Reaction rate λ_{ec} (left panel, in s^{-1}) and energy release ϵ_{2ec} (right panel, MeV/reaction) for the EC on ^{24}Mg and ^{20}Ne. The left panel shows λ_{ec} as a function of ϱ (assuming $Y_e = 0.5$) and ϱY_e for two characteristic temperatures of 0.4 and 1 GK. The right panel depicts the energy release per EC process and is taking into account the energy release from the secondary EC process that occurs together with the first one (see Figure 6.2). Reaction rate and energy release are calculated based on the transition matrix elements presented in Martínez-Pinedo et al. (2014). The threshold density for (positive) energy production is indicated by a dashed vertical line.

the ground states of ^{20}Ne and ^{20}F could play a crucial role for the evolution of the core at temperatures below 0.9 GK. This transition can result in a rate that is—by several orders of magnitude—larger than the previously used rates in stellar evolution calculations (Takahara et al., 1989).[5] The reaction and the heating rates of the EC on ^{20}Ne and ^{24}Mg (based on the calculation of Martínez-Pinedo et al. (2014)) are displayed in Figure 6.3 as a function of density for two characteristic temperatures of 0.4 and 1 GK. The previously mentioned heating effect for the two relevant double ECs is apparent. For both reaction channels and both temperatures, the threshold density for energy production (indicated by dashed vertical lines) are significantly lower than the corresponding capture threshold $\left(\log_{10}\varrho/\mathrm{g\ cm^{-3}}\right) \approx 9.6$ for ^{24}Mg and $\left(\log_{10}\varrho/\mathrm{g\ cm^{-3}}\right) \approx 9.95$ for ^{20}Ne).

Because ^{20}Ne is very abundant in the core, the EC process that consumes it, is responsible for a strong heating of the core. As explained in Section 5.1, a degenerate stellar plasma cannot regulate the temperature increase by expanding, since the pressure is nearly independent from the temperature. After the core reaches $\varrho_{\mathrm{thresh}}$ for EC on ^{20}Ne, the temperature is elevated so much that oxygen is ignited, eventually, resulting in a thermonuclear runaway (typically in the center of the core). This behavior can be observed for both the SAGB star and the AIC model in Figure 6.1, where oxygen is ignited in the center. The onset of the oxygen deflagration also marks the end of evolution that can be covered by a stellar evolution code and hence, the ONe core evolution cannot be continued at this point.

[5] Notice that in the recent weak rate tabulation by Suzuki et al. (2016), the effect of the second forbidden transition, as discussed by Martínez-Pinedo et al. (2014), has been included.

Quasi-Dynamic Collapse and Thermonuclear Runaway

It was further argued by Miyaji et al. (1980) that the continuous growth of the ONe core, together with the deleptonization from EC processes, will inevitable push the core mass beyond $M_{\rm ch}$ and the core becomes gravitationally unstable. Different from a collapsing iron core, the abundant nuclei in the mass region around $A = 20$ can still release ≈ 1 MeV/nucleon of nuclear binding energy by burning processes. As a consequence, oxygen burning will release additional energy. Due to the high degeneracy, the burning proceeds in a violent deflagration that fuses the material in the core into iron-group nuclei in a matter of seconds. In the canonical picture, that has not changed since the seminal work by Miyaji et al. (1980), the EC-induced deleptonization dominates over the energy liberated during the oxygen deflagration and the star collapses to a NS, marking the standard path towards ECSNe. After the oxygen deflagration wave has transformed the core into iron-group material, EC on those nuclei have to be considered, as they occur on a very high rate in these conditions. While for the gravitational collapse of massive stars, it is usually sufficient to consider only EC processes (usually, the tabulation by Juodagalvis et al. (2010) is used), this is not the case for the possible collapse of an ONe core. Here, also the β^- decay direction has to be considered (see e.g. Jones et al., 2016).

The oxygen deflagration wave propagates with very high flame speeds, either in a laminar manner, driven by heat conduction or by turbulent fluid motion that enlarges the reactive surface area of the fuel. Nevertheless, the details of this oxygen deflagration are still poorly understood and subject to current research (Jones et al., 2016).

Core-collapse vs. Oxygen Deflagration

Burning oxygen and neon to iron releases roughly 1 MeV of binding energy per nucleon. Hence, it has been speculated that the energy released by the oxygen deflagration could be sufficient to halt the collapse of the core and prevent the formation of a NS (see e.g. Isern et al., 1991). In that case, the ONe core would be entirely or partially destroyed by a thermonuclear explosion. Observationally, it would probably be very similar to a type 1A supernova, that is connected to the thermonuclear explosion of a CO WD in the canonical scenario.[6]

But, as already indicated, in the common wisdom, the deleptonization of the core will overwhelm the effect of the outwards burning flame and make the star collapse and subsequently explode in an ECSN, leaving behind a NS. It was pointed out by many authors that the most crucial criterion for the question whether the core collapses or not, is related to the ignition density of oxygen $\varrho_{\rm ign}$. In Miyaji et al. (1980), the Schwarzschild criterion for convection was assumed. In this case, the core can efficiently cool down after the onset of EC on ^{20}Ne delaying the ignition of oxygen to comparably high densities around $\varrho_{\rm ign} = 2 \times 10^{10}$ g cm^{-3}. If on the other hand, the Ledoux criterion for convection is applied (Miyaji & Nomoto, 1987), the stabilizing mean molecular weight gradient prevents convection from appearing prior to the ignition of oxygen, which leads to a rather early ignition density of oxygen of around $\varrho_{\rm ign} = 1 \times 10^{10}$ g cm^{-3}. In the recent study by Schwab et al. (2015), assuming Ledoux convection, the ignition density was found to be exactly in above mentioned regime, as illustrated by their fiducial model in the right panel of Figure 6.1. In Figure 6.4, the ignition density of relevant studies involving degenerate ONe cores is summarized as a function of the year of appearance of the publication. Except for the peculiar case of Takahashi et al. (2013), the bimodality is rather clear. Assuming Schwarzschild convection, the ignition density is roughly a factor of two larger compared to models assuming Ledoux convection.

It is easy to imagine that the oxygen deflagration is more likely to disrupt the star, if it gets ignited at lower densities. In the other case, an ignition at very high densities will hardly be able to prevent the stellar core from collapsing to a NS. Even though, the ignition density (by looking at Figure 6.4)

[6] A review about thermonuclear supernovae is for example given by Hillebrandt & Niemeyer (2000).

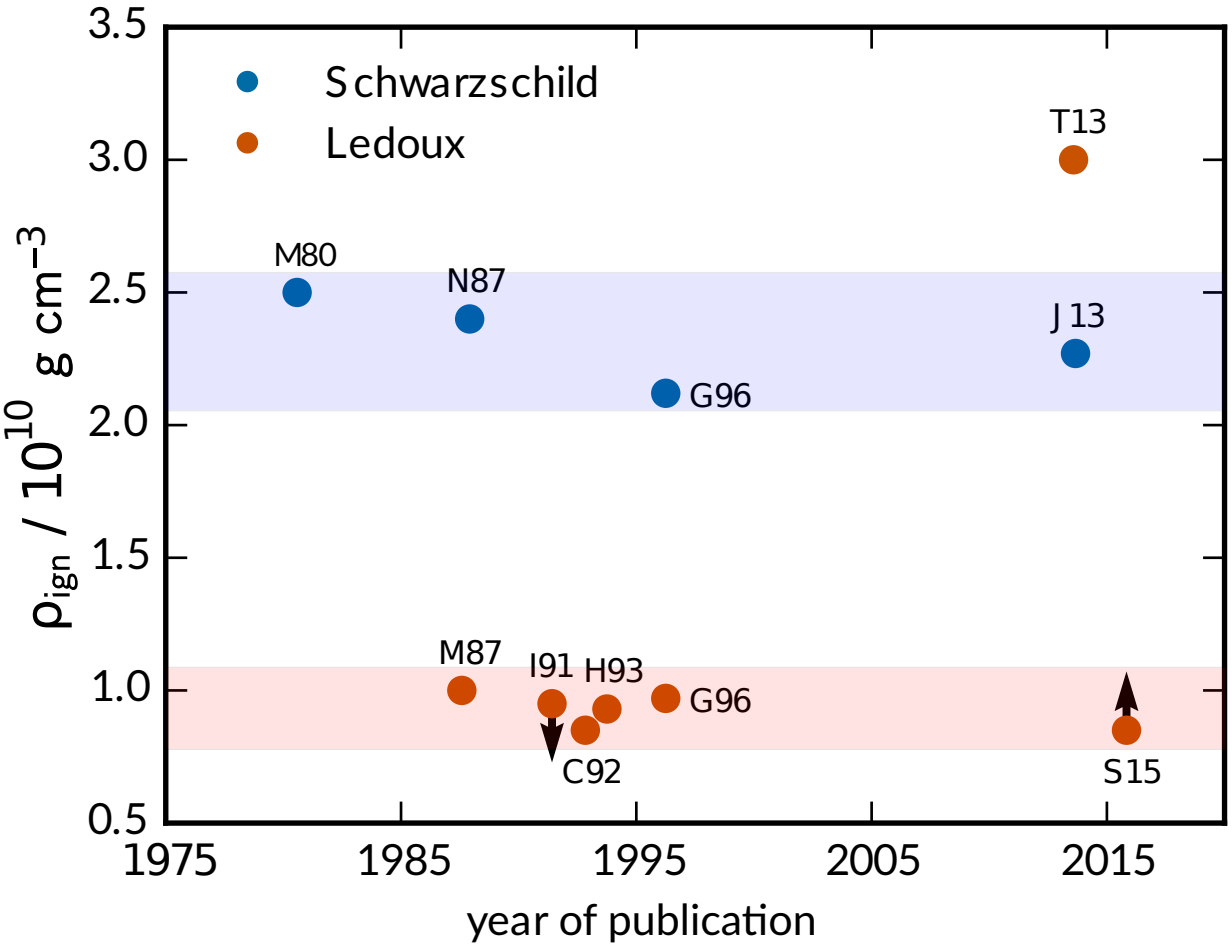

Figure 6.4: Ignition density of the oxygen deflagration in several published ECSN/AIC simulations. Upper and lower limits are shown with arrows and the convection criterion (Schwarzschild or Ledoux) is demarcated by glyph color. The references are as follows: Miyaji et al. (1980, M80), Miyaji & Nomoto (1987, M87), Nomoto (1987, N87), Isern et al. (1991, I91), Canal et al. (1992, C92), Hashimoto et al. (1993, H93), Gutierrez et al. (1996, G96), Takahashi et al. (2013, T13), Jones et al. (2013, J13), Schwab et al. (2015, S15). Modified from Samuel Jones.

seems to be rather well constrained, it has to be known very accurately in order to correctly predict the fate of the star. On the other hand, the uncertainties related to the post-ignition phase appear to be significantly higher. This has various reasons. First of all, the oxygen deflagration is a dynamical and multidimensional process that is very difficult to access in numerical simulations. As already pointed out, the first attempt to model the oxygen deflagration in 3D was performed by Jones et al. (2016). Interestingly, they concluded—contrary to the canonical picture—that an ONe core with a central density corresponding to Ledoux convection, does not collapse and explode in an ECSN but rather gets destroyed by the deflagration wave. On the other hand, a model with higher ignition densities, corresponding to Schwarzschild convection showed clear signs of collapsing to NS densities. If the transition between collapse and disruption would be between the two extreme cases of convection, it seems even more important to predict ϱ_{ign} as accurately as possible, as done in our studies in Section 6.3. On the other hand, it will be important to predict the density threshold between collapse and thermonuclear explosion, either by 3D simulations (that are still very expensive) or by (much cheaper) parametric flame models in 1D, relying on the turbulent flame velocities obtained by 3D simulations (see Section 6.4).

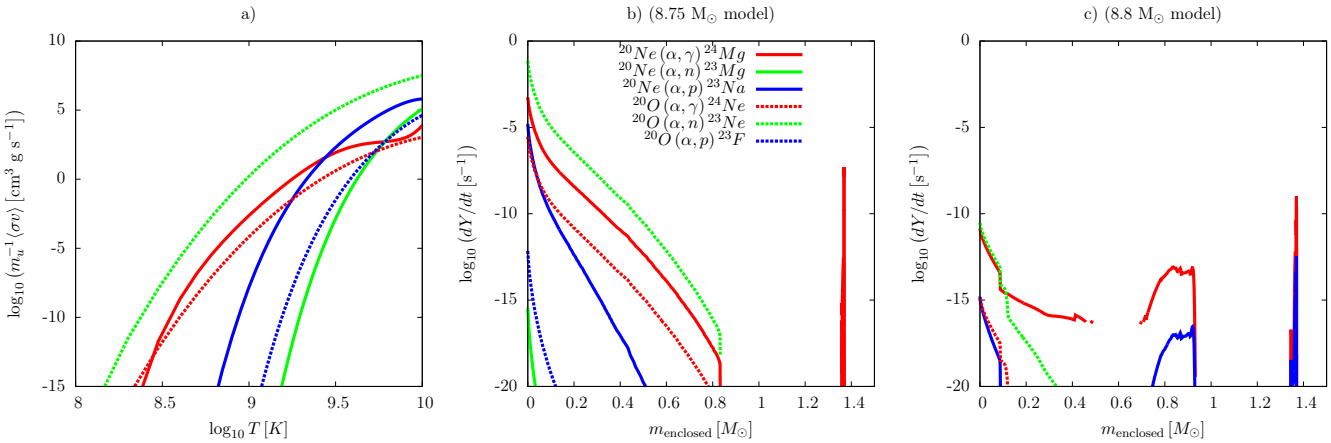

Figure 6.5: Panel a) shows $(\alpha, \{\gamma, \mathrm{n}, \mathrm{p}\})$-rates for ^{20}O and ^{20}Ne taken from the JINA Reaclib database (Cyburt et al., 2010). Panel b) and c) show the flux of the reactions displayed in panel a) for conditions taken from profiles of two different stellar evolution models Jones et al. (2013, as illustrated in Figure 6.1) prior to the neon burning phase. Panel b) corresponds to the 8.75 $M_\odot$ and panel c) to the 8.8 $M_\odot$ model.

6.2 Neon and Oxygen Burning at High Density

In this Section we propose modifications to the standard neon and oxygen burning in stars at high densities.[7] One reason why intermediate-mass stars between 7 and 11 $M_\odot$ are of particular interest compared to massive stars above $\approx 11\ M_\odot$ is, that nuclear reactions associated with specific burning processes, operate at significantly higher densities. It was shown in Jones et al. (2013), that for a range of initial progenitor masses from 8 to 9 $M_\odot$, the star will form a degenerate ONe core towards the end of its stellar life (see also left panel of Figure 6.1). Furthermore, it was found that in a narrow range between 8.7 and 8.8 $M_\odot$, Urca cooling occurs prior to the neon-burning phase by EC on odd-A sd-shell nuclei (^{23}Na, ^{25}Mg, ^{27}Al) above densities of 10^9 g/cm^{-3}. Afterwards, heating due to EC on even-A sd-shell nuclei (first ^{24}Mg) occurs once densities of 2×10^9 g/cm^{-3} are reached. Above 6×10^9 g/cm^{-3}, ECs on ^{20}Ne set in and produce considerable amounts of ^{20}O via the chain $^{20}\mathrm{Ne}(e^-, \nu_e)^{20}\mathrm{F}(e^-, \nu_e)^{20}\mathrm{O}$ (see Section 6.1). Hence, the stellar core consists mainly of ^{16}O and ^{20}Ne, ^{24}Ne and some fraction of ^{20}O (up to 4%, depending on the model). The situation is different compared to massive stars, where no EC-phase occurs before neon burning. As illustrated in the left panel of Figure 6.1, neon burning operates at a density between 10^8 and 10^9 g cm^{-3}, whereas the density is considerably lower in massive stars, at around 10^6 to 10^7 g cm^{-3}. As introduced in Chapter 5, the canonical values for the onset of neon and oxygen burning are $T = 1.5$ GK and $T = 2.0$ GK, respectively.

This raises the question, what impact the abundance of the double EC product ^{20}O has on the occurrence of neon as well as oxygen burning. Besides looking in detail at the nuclear reactions that are relevant for the two phases of nuclear burning, of course, also the environment in which they occur, plays a role. In Section 6.1, we discussed for example the evolution of ONe cores in cases where oxygen burning (and neon burning along with it) is ignited in a thermonuclear runaway already at the onset of gravitational collapse. In other cases, neon burning and later oxygen burning could occur after EC on ^{20}Ne have already produced significant amounts of ^{20}O, but still before the onset of gravitational collapse. In Jones et al. (2014), the authors studied SAGB stars with initial masses between 8.8 and 9.5 $M_\odot$. These stars ignite oxygen and neon-burning off-center, prior to collapse. In such an environment, it could also be interesting to investigate the key reactions during both burning stages in the presence of ^{20}O.

[7] The work presented here is based on Möller et al. (2014) and Möller et al. (to appear).

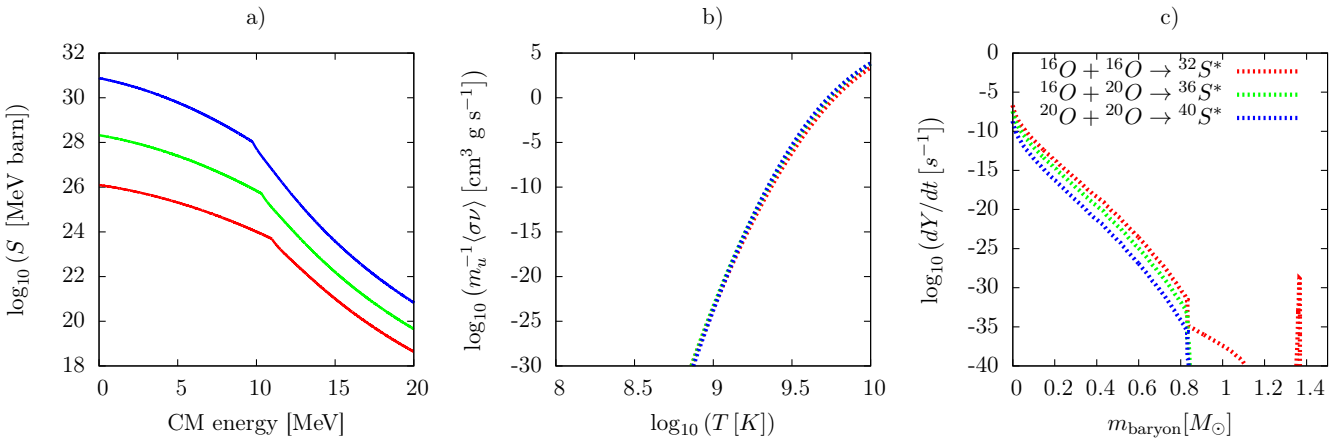

Figure 6.6: Panel a) shows S-factors of the different oxygen fusion channels as a function of the projectile center of mass energy and panel b) depicts the corresponding reaction rates. Panel c) shows the flux of each reaction for the same conditions as in panel b) of Figure 6.5. The S-factors are calculated based on Yakovlev et al. (2010).

In massive stars, where neon burning operates at densities around 10^6 to 10^7 g cm^{-3}, the key reactions are given by (Q value given in brackets):

$$^{20}\mathrm{Ne} + \gamma \rightarrow {}^{16}\mathrm{O} + \alpha \quad (Q = -4.730\ \mathrm{MeV}), \tag{6.16}$$

$$^{16}\mathrm{O} + \alpha \rightarrow {}^{20}\mathrm{Ne} + \gamma \quad (Q = 4.730\ \mathrm{MeV}), \tag{6.17}$$

$$^{20}\mathrm{Ne} + \alpha \rightarrow {}^{24}\mathrm{Mg} + \alpha \quad (Q = 9.316\ \mathrm{MeV}), \tag{6.18}$$

$$^{24}\mathrm{Mg} + \alpha \rightarrow {}^{28}\mathrm{Si} + \alpha \quad (Q = 9.984\ \mathrm{MeV}). \tag{6.19}$$

If there is now also ^{20}O abundant from previously occurring EC on ^{20}Ne, additional reaction channels need to be taken into account:

$$^{20}\mathrm{O} + \alpha \rightarrow {}^{24}\mathrm{Ne} + \gamma \quad (Q = 12.173\ \mathrm{MeV}), \tag{6.20}$$

$$^{20}\mathrm{O} + \alpha \rightarrow {}^{23}\mathrm{Ne} + \mathrm{n} \quad (Q = 3.304\ \mathrm{MeV}), \tag{6.21}$$

$$^{20}\mathrm{O} + \alpha \rightarrow {}^{23}\mathrm{F} + \mathrm{p} \quad (Q = -4.381\ \mathrm{MeV}). \tag{6.22}$$

In panel a) of Figure 6.5, we compare the rates of different reaction channels for the α-capture on ^{20}Ne and ^{20}O, respectively. The rates are taken from the JINA Reaclib database (Cyburt et al., 2010). As can be seen, the reaction $^{20}\mathrm{O}(\alpha, n)^{23}\mathrm{Ne}$ is by far dominating between 0.1 and 10 GK. Hence, we argue that the α-capture on ^{20}O can be a competitive process and should be considered in future calculations. This can be seen even better in panel b) and c), where we look at the reaction fluxes for conditions of the 8.75 M$_\odot$ and 8.8 M$_\odot$ model by Jones et al. (2013), at the onset of the neon burning phase. As defined in Equation (3.46), for a binary rate, the reaction flux is given by: $f_{\mathrm{AB}\rightarrow\mathrm{X}} = \varrho m_u^{-1} \langle\sigma\nu\rangle_{\mathrm{AB}\rightarrow\mathrm{X}} Y_\mathrm{A} Y_\mathrm{B}$, where the reaction rate $m_u^{-1} \langle\sigma\nu\rangle_{\mathrm{AB}\rightarrow\mathrm{X}}$ is evaluated at the corresponding temperature of the stellar model. Here, the abundances in the incoming channels are Y_A and Y_B. It is obvious that for the 8.75 M$_\odot$ model, where there is up to 4% of ^{20}O, the reaction $^{20}\mathrm{O}(\alpha, n)^{23}\mathrm{Ne}$ is dominant, also compared to the standard neon burning reaction $^{20}\mathrm{Ne}(\alpha, \gamma)^{24}\mathrm{Mg}$. In the case of the 8.8 M$_\odot$ model, where there is only up to 0.1% of ^{20}O, it is at least comparable to the $^{20}\mathrm{Ne}(\alpha, \gamma)^{24}\mathrm{Mg}$ channel in the center of the core.

Unfortunately, the reaction rate for the α-capture on ^{20}O has not been determined experimentally, yet. Hence, the rate provided by the JINA Reaclib has been determined theoretically by Hauser-Feshbach rates calculations with the NON-SMOKER code (Cyburt et al., 2010). This implies that the uncertainty of this rate could be rather large. For this reason, we will explore the impact of including and varying

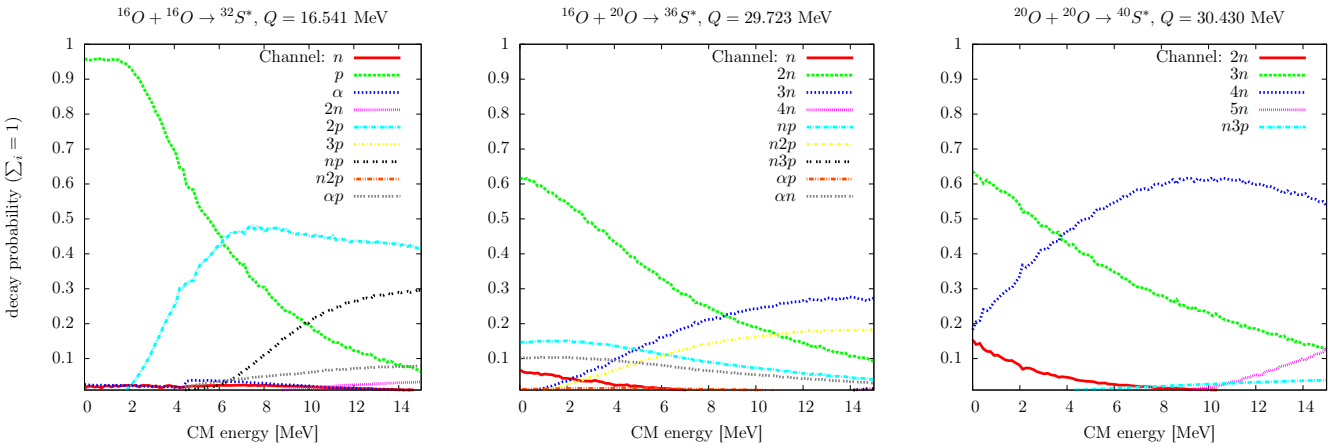

Figure 6.7: Calculated branching ratios for the deexcitation channels of the oxygen fusion compound-nucleus sulfur ^{32}S, ^{36}S and ^{40}S as a function of the center of mass energy of the projectiles. This means that the excitation energy is obtained by adding the Q-value to the center of mass energy. Only channels with significant contribution are displayed.

this reaction rate in the AIC models that we perform in Section 6.3.5 and study the impact on the thermonuclear runaway.

Once the star reaches temperatures over ≈ 2.0 GK, the fusion of oxygen will become important, as well. If there is still ^{20}O available during that phase, the fusion can now proceed via three channels (the first one being the standard fusion channel):

$$^{16}\mathrm{O} + {}^{16}\mathrm{O} \rightarrow {}^{32}\mathrm{S}^* \quad (Q = 16.5\ \mathrm{MeV}), \tag{6.23}$$

$$^{16}\mathrm{O} + {}^{20}\mathrm{O} \rightarrow {}^{36}\mathrm{S}^* \quad (Q = 29.7\ \mathrm{MeV}), \tag{6.24}$$

$$^{20}\mathrm{O} + {}^{20}\mathrm{O} \rightarrow {}^{40}\mathrm{S}^* \quad (Q = 30.4\ \mathrm{MeV}). \tag{6.25}$$

Due to the lack of experimental data for the fusion involving neutron-rich oxygen isotopes, we rely on a theoretical model by Yakovlev et al. (2010) for the calculation of the S-factors $S(E)$ together with branching ratios that were calculated according to Huther (2014). In this approach, the decay of the compound nucleus is described in the Hauser-Feshbach model, allowing for particle and multi-particle emission (if the excitation energy is high enough) within the framework of the MOD-SMOKER (Loens, 2011) and ABLA07 (Kelic et al., 2009) codes. The astrophysical rate is then obtained by numerical integration of the S-factor. Each individual temperature-dependent rate $m_u^{-1}\langle\sigma v\rangle$ is given by (same as Equation 3.43, except for the branching ratio $B(E)$ for each individual channel):

$$m_u^{-1}\langle\sigma v\rangle(T) = m_u^{-1}\left(\frac{8}{\pi m_{ij}}\right)^{1/2}(k_\mathrm{B}T)^{-3/2}\int_0^\infty B(E)S(E)\exp(-E/k_\mathrm{B}T)\exp(-2\pi\eta(E)). \tag{6.26}$$

In panels a) and b) of Figure 6.6, it is evident that, despite the fact that the S-factors vary by several orders of magnitude, the reaction rates for the three different oxygen fusion channels are very similar. This is the case because the differences in the individual S-factors are compensated by the different effective masses in η, which implies that the contribution of ^{20}O to the total fusion rate is relatively small. In panel c) of Figure 6.6, the reaction fluxes for the three oxygen fusion channels are displayed as a function of the enclosed mass of the same stellar model that was used in panel b) of Figure 6.5 (8.75 $\mathrm{M}_\odot$ model of Jones et al. (2013), prior to neon burning). We find that the contribution of the $^{16}\mathrm{O} + {}^{20}\mathrm{O}$-channel reaches up to 15%, while the $^{20}\mathrm{O} + {}^{20}\mathrm{O}$-channel is much less important and can be neglected. Additionally, the fusion involving ^{20}O has Q-values of 29.7 MeV and 30.4 MeV, respectively.

This does not only increase the rate of energy release during the fusion phase of oxygen by up 30%, but it also allows for more exotic decay channels including the emission of up to 5 neutrons.

Figure 6.7 depicts the branching ratios for the three oxygen fusion channels. On the left panel for ^{32}S, on the middle panel for ^{36}S and on the right panel for ^{40}S. While the regular oxygen fusion mainly releases single protons, for the two neutron-rich channels, the multi-neutron emission dominates. We speculate about the impact of the appearance of neutrons in the stellar plasma, as this could open up new reactions channels that so far have not been considered. Additionally, these reactions would serve as a strong neutron source, under conditions where there are not many neutrons available. In Section 6.3.5, we will include these additional oxygen fusion channels into AIC models of ONe cores, in order to study their impact on the ignition of oxygen burning in conditions where ^{20}O is abundant by several percent in mass fraction.

6.3 Pre-Ignition Phase towards Accretion-Induced Collapse

In this section, we will present stellar evolution models of the AIC of ONe WDs that were performed with MESA. We rely on the same procedure to generate the initial models as the AIC models, presented by Schwab et al. (2015). The authors studied the same scenario with MESA and incorporated the framework to evaluate weak reaction rates on-the-fly with a very high accuracy in MESA. It was previously pointed out, among others, by Jones et al. (2013) and Denissenkov et al. (2015), that the standard weak rate tabulations used in stellar astrophysics are insufficient to properly account for the effects of EC (heating and cooling) in degenerate conditions (for details see Section 4.4). Notice that the dense weak rate tabulation by Suzuki et al. (2016) has only become available very recently and has neither been employed by Schwab et al. (2015) or this study. In fact, the publication was particularly stimulated by the necessity of having a more accurate weak rate tabulation, especially in the context of degenerate ONe cores.

The main focus of the present study will be exploring uncertainties that have not been addressed before by Schwab et al. (2015) and to extent the weak rate formalism in MESA to Urca pairs. Hence, one should quickly summarize, which assumptions were already tested by Schwab et al. (2015) and which questions remain to be assessed. In Section 6.1, we presented results of the study by Schwab et al. (2015). The main conclusion was that—assuming Ledoux convection—the ONe core does not become convective due to EC on ^{24}Mg or ^{20}O, prior to the ignition of the oxygen deflagration. This leads to comparably low ignition densities around 8.5×10^9 g cm^{-3}, in accordance with previous studies, as displayed in Figure 6.4. Additionally, the authors gave arguments, based on the comparison of timescales, why semiconvection should not have enough time to develop in the core and did not include it in their study. Furthermore, they also studied the impact of $X\left(^{24}\mathrm{Mg}\right)$ and concluded that for all values compatible with current carbon burning rates, ^{24}Mg will not strongly affect the evolution of the core. In particular, ^{24}Mg does not trigger the oxygen deflagration itself (see Section 6.1). Also, the relevance of including the second forbidden ground state-ground state transition of $^{20}\mathrm{Ne} \rightarrow {}^{20}\mathrm{F}$ was investigated and the authors concluded that the inclusion will lead to an off-center ignition of the oxygen deflagration. Furthermore, the effect of various accretion rates $\dot{M}$ and different initial central temperatures was studied. It was found that the accretion rate is changing the ignition density of oxygen by up to 10%, while the impact of the initial temperature on the evolution of the ONe core is negligible. Finally, the inclusion of a larger reaction network was tested and it was concluded that there is no significant impact on the evolution.[8]

Using the findings of Schwab et al. (2015) as a basis, we will investigate several aspects in more detail that were only addressed briefly (i.e network size, second-forbidden transition, accretion rate). And in addition to that, we extended the study and the initial models to study phenomena that were left out previously (i.e. Urca processes, semiconvection, modified neon and oxygen burning reactions). They are presented in the following enumeration:

- **Weak Rates (Section 6.3.2)**: We will provide a pending validation of the on-the-fly weak rate calculation routine of MESA, comparing the rates to the recently published weak reaction rates by (Suzuki et al., 2016). Furthermore, we will extend the scheme to calculate EC and β^- decay rates for Urca processes involving odd-A sd-shell nuclei.[9]
- ^{20}**Ne-EC (Section 6.3.3)**: In the light of recent ongoing experimental and theoretical efforts to determine the second forbidden ground state-ground state transition of the EC on ^{20}Ne by Idini et al. (2014) and Kirsebom et al. (2017), we re-investigate this topic and study in detail how this transition affects the ignition density, as well as the ignition spot of the oxygen deflagration.

[8] This was however only mentioned in one sentence in the Appendix.

[9] To some extent, this was already done in a different context for CO WDs during the simmering phase (Martínez-Rodríguez et al., 2016). However, no rate comparison was performed.

- **Urca cooling (Section 6.3.4)**: What is the influence of having the Urca nuclei ^{23}Na and ^{25}Mg in the initial composition of the ONe core? Does Urca cooling play a role for the temporal evolution and if so, does it affect the ignition density of oxygen?
- **Nuclear reactions (Section 6.3.5)**: We will study the impact of the nuclear reactions on the evolution of ONe cores, as pointed out in Section 6.2. Furthermore, we investigate in more detail, the influence of using different reaction rate compilations (NACRE vs. JINA Reaclib), in connection with a larger nuclear reaction network.
- **Semiconvection (Section 6.3.6)**: How will the inclusion of semiconvection, based on the description of (Langer et al., 1983), in the stellar evolution models affect the evolution of degenerate ONe cores? Besides performing stellar evolution calculations, we will also make use of the instability growth analysis by Kato (1966), in order to discuss the possible appearance of semiconvection in the stellar core prior to the ignition of oxygen.
- **Thermonuclear Runaway (Section 6.3.7)**: We want to give a more concise estimation of the ignition density as a function of the accretion rate $\dot{M}$, assuming the Ledoux criterion for convection. The main purpose of this study will be to generate initial models for studying the oxygen deflagration wave with the CCSN code AGILE (see Section 6.4).

6.3.1 Stellar Evolution Code "MESA" and Accretion-induced Collapse Models

The AIC models of ONe cores presented in this section are calculated with the open-source stellar evolution code "Modules for Experiments in Stellar Astrophysics" (MESA, Paxton et al., 2011, 2013, 2015). Initially, the revision 7624 of MESA was used. Later, we moved to the more recent MESA revision 8118. Since the revision 7624, MESA supports the on-the-fly calculation of weak rates by numerically integrating the phase space integral (Schwab et al., 2015; Paxton et al., 2015). Some minor errors in the original implementation are corrected since revision 8118 (see Section 6.3.2).

In order to execute our calculation, initial ONe WD models have to be created. Then, these models can be used to accrete matter from an arbitrary external source. They were generated in a similar fashion to what is presented in Schwab et al. (2015). Initially, a pre-main sequence stellar profile is generated, with a total mass of 1.325 $M_\odot$ and roughly solar composition. Then, by disabling the occurrence of any nuclear reactions, the model contracts until a central density of 10^3 g cm^{-3} is reached, where it is manually stopped. Then MESA is set to relax the composition homogeneously to the desired initial composition of the ONe WD model. In our case, we adopted the composition from the fiducial model of Schwab et al. (2015), that most accurately reflects the expected composition after carbon burning (see also the discussion in Section 6.1). Hence, the composition is chosen to be $X\left(^{16}\mathrm{O}\right) = 0.5$, $X\left(^{20}\mathrm{Ne}\right) = 0.45$, $X\left(^{24}\mathrm{Mg}\right) = 0.05$. If other nuclear species, like $X\left(^{23}\mathrm{Na}\right)$ and $X\left(^{25}\mathrm{Mg}\right)$ are included (as is necessary for studying Urca cooling), the ratio of the main nuclear species is kept constant, while the additional nuclear species are added. During this relaxation step, nuclear reactions are disabled, as well. Once the core reaches a central density of 10^7 g cm^{-3}, it is set to accrete matter at a rate of $\dot{M} = 10^6\ M_\odot$ yr^{-1}, until a density of 10^9 g cm^{-3} is reached.[10] Now, the initial model represents a degenerate ONe core that can be used, by accreting mass, to study the AIC scenario. Of course, in the actual AIC simulations, all weak and thermonuclear reactions have to be considered and are consequently switched on.

Based on the initial models, we performed simulations with four different sets of resolution, called "default", "medium", "optimum" and "high". They are listed in Table 6.1.[11] One key advantage of MESA is, that it can use a very fine spatial zoning when it is required. In particular, it is possible to set a value

[10] In Schwab et al. (2015), the density limit was slightly higher, meaning that in this case, the first Urca phase would be missed entirely.

[11] Usually, we used the highest resolution that would allow the specific model to run in a reasonable time.

for the innermost zones of the stellar model as small as 10^{-13} $M_\odot$, a feature especially useful for studies where the evolution is driven by the central region of the star. In the inlist, this is controlled by the two parameters `max_center_cell_dq` and `center_avg_value_dq`. Furthermore, it is possible to limit the maximum timestep, based on maximum changes in certain quantities in the central zone. In the inlist, this is controlled by the parameters `delta_lgRho_cntr_hard_limit` and `delta_lgRho_cntr_limit` for the central density, and by `delta_lgT_cntr_hard_limit` and `delta_lgT_cntr_limit` for the central temperature. Additionally, the general spatial and temporal resolution can be set in the inlist by `mesh_delta_coeff` and `varcontrol_target`, respectively.

In the listing below, we show an exemplary inlist for our AIC MESA models. It only shows options that have an influence on the considered physics, while "cosmetic" options that control for example what is printed in the output files, are omitted in this example. Notice also, that the exact combination of options that is listed below, was not actually used in any model. Rather, the displayed inlist options should give an overview of which settings are necessary in order to obtain the same models, as in this study.

```
1       &star_job ! start of star_job namelist
2 !.....load the initial wd model (50% O, 45% Ne, 5% Mg).................
3       load_saved_model = .true.
4       saved_model_name = 'final_504505.mod'
5 !.....reset star age & model number...................................
6       set_initial_age = .true.
7       initial_age = 0 ! in years
8       set_initial_model_number = .true.
9       initial_model_number = 0
10 !.....use JINA REACLIB rates instead of NACRE.........................
11      set_rates_preference = .true.
12      new_rates_preference = 2
13 !.....use modified JINA REACLIB,IMPORTANT! clear MESA rates cache.....
14      jina_reaclib_filename = 'o20_fusion.jina'
15 !.....change reaction network compared to original model..............
16      change_net=.true.
17      new_net_name= 'wd_aic_big.net'
18 !.....cuts the envelope of the WD.....................................
19      set_tau_factor = .true.
20      set_to_this_tau_factor = 300
21 !.....uses the special description of weak rates.....................
22      use_special_weak_rates = .true.
23      special_weak_states_file = 'aic_ne20forb.states'
24      special_weak_transitions_file = 'aic_ne20forb.transitions'
25 !.....uses ion + electron coulomb corrections.........................
26      ion_coulomb_corrections = 'PCR2009'
27      electron_coulomb_corrections = 'Itoh2002'
28      / ! end of star_job namelist
29      &controls ! start of controls namelist
30 !.....important for C/O enhanced material.............................
31      use_Type2_opacities = .true.
32      Zbase = 0.02d0
33 !.....target value for relative variation in structure.................
34      varcontrol_target = 1e-3
35 !.....controls the number of grid points and max. zones................
36      mesh_delta_coeff = 1.0
37      max_allowed_nz = 100000
38 !.....limits on central variable changes..............................
39      delta_lgRho_cntr_hard_limit = 3e-3
40      delta_lgRho_cntr_limit = 1e-3
41      delta_lgT_cntr_hard_limit = 3e-3
42      delta_lgT_cntr_limit = 1e-3
43 !.....lower limit for the timestep.....................................
44      min_timestep_limit = 1e-5
45 !.....ledoux conv. + alpha value for semiconv.........................
46      use_Ledoux_criterion = .true.
47      alpha_semiconvection = 0d0
48 !.....suppress convection to occur.....................................
49      max_conv_vel_div_csound = 1d-99
50 !.....comp. of accretion material same as surface & accretion rate.....
51      accrete_same_as_surface = .true.
52      mass_change = 1d-6
53 !.....controls resolution in the center of the model...................
54      max_center_cell_dq = 1d-12
55      center_avg_value_dq = 1d-12
56      / ! end of controls namelist
```

Listing 6.1: Exemplary inlist of an AIC MESA model from the study in this section. All MESA inlist options are explained in detail in a documentation archive (MESA, 2017)

inlist parameter | model name	default	medium	optimum	high
varcontrol_target	$1 \cdot 10^{-3}$	$1 \cdot 10^{-3}$	$1 \cdot 10^{-3}$	$1 \cdot 10^{-4}$
mesh_delta_coeff	1.0	1.0	0.5	0.2
delta_lgRho_cntr_hard_limit	none	$5 \cdot 10^{-3}$	$3 \cdot 10^{-3}$	$3 \cdot 10^{-3}$
delta_lgRho_cntr_limit	$5 \cdot 10^{-2}$	$2 \cdot 10^{-3}$	$1 \cdot 10^{-3}$	$1 \cdot 10^{-3}$
delta_lgT_cntr_hard_limit	none	$5 \cdot 10^{-3}$	$3 \cdot 10^{-3}$	$3 \cdot 10^{-3}$
delta_lgT_cntr_limit	$1 \cdot 10^{-2}$	$2 \cdot 10^{-3}$	$1 \cdot 10^{-3}$	$1 \cdot 10^{-3}$
max_center_cell_dq	auto	$1 \cdot 10^{-11}$	$3 \cdot 10^{-13}$	$3 \cdot 10^{-13}$
center_avg_value_dq	auto	$1 \cdot 10^{-11}$	$3 \cdot 10^{-13}$	$3 \cdot 10^{-13}$

Table 6.1: Overview of the most important control parameters of the resolution of MESA models. In all above quantities, small values indicate a high resolution and vice versa. `varcontrol_target` controls the time resolution, `mesh_delta_coeff` denotes the spatial resolution, `delta_lgRho_cntr_hard_limit` and `delta_lgRho_cntr_limit` limit the central density changes of the model while `delta_lgT_cntr_hard_limit` and `delta_lgT_cntr_limit` do the same for the temperature. `max_center_cell_dq` and `center_avg_value_dq` determine the mass of the central zone. dq is given in $M_\odot$.

As pointed out in Section 6.3, the results of our models will be discussed in the upcoming sections, separately addressing the different uncertainties. The baseline for our MESA AIC models is a model that uses the same initial conditions and the same inlist as the fiducial model by Schwab et al. (2015), as illustrated in Figure 6.1. It is called `Res-1`. In Table 6.2, we present an overview of all our AIC models, that were computed over the course of this thesis, indicating the different input physics assumptions, together with the final outcome of each model in terms of the ignition density and the ignition spot of oxygen.

6.3.2 Determination of Weak Rates in "MESA"

By default, MESA considers weak rates in the usual way in stellar evolution calculations, relying on tabulations. The commonly used rate tabulations are provided by Fuller et al. (1980); Oda et al. (1994); Langanke & Martínez-Pinedo (2000), usually using the most recent rate, if more than one rate is available for the nucleus in question. Unfortunately, these tabulations use a relatively coarse grid in density and temperature (only one grid point per order of magnitude in density). This is especially problematic in degenerate conditions where the rate is virtually zero below the threshold density and very large above the threshold density. Hence, they are insufficient for the study of ONe cores, at least when an accurate determination of the deleptonization and the energy release from weak reactions is desired. For this reason, Schwab et al. (2015) implemented a routine in MESA to calculate weak rates on-the-fly. In this study, this effort was made in particular for the purpose of including the $0^+ \rightarrow 2^+$ transition of the ^{20}Ne EC, after it was pointed out by Martínez-Pinedo et al. (2014), that this transition could be relevant for conditions, present during the AIC of ONe WDs.

The above mentioned on-the-fly weak rate calculation is used, if the MESA inlist contains the option `use_special_weak_rates`. Then, the user has to provide both a list of nuclei with the considered nuclear levels, as well as a list of the considered EC and β decay transitions together with their $\log_{10}(ft)$ value. In the routine, the rate is then computed for each individual transition based on Equation (4.88) and the total rate, accounting for all considered transitions and accounting for the population probability of excited states, as in Equation (4.90). The same is done for the energy generation. Obviously, this is computationally more expensive than interpolating in a two-dimensional rate table[12], as the phase-space

[12] Weak rates are tabulated as a function of T and ϱY_e.

model	resolution (see Table 6.1)	^{20}Ne ($0^+ \rightarrow 2^+$)	rates	network	$X\left(^{23}\mathrm{Na}\right)$	$X\left(^{25}\mathrm{Mg}\right)$	convection type	$\dot{M}$ $\left(M_\odot \mathrm{yr}^{-1}\right)$	rho ig. $\log_{10}\left(\mathrm{g\,cm}^{-3}\right)$	ig. spot (km)
Res-1	default	no	NACRE	small	–	–	Ledoux ($\alpha_S = 0$)	10^{-6}	9.9365	center
Res-2	medium	no	NACRE	small	–	–	Ledoux ($\alpha_S = 0$)	10^{-6}	9.9382	center
Res-3	optimum	no	NACRE	small	–	–	Ledoux ($\alpha_S = 0$)	10^{-6}	9.9389	center
Res-4	high	no	NACRE	small	–	–	Ledoux ($\alpha_S = 0$)	10^{-6}	9.9387	center
Acc-1	optimum	no	NACRE	small	–	–	none	$1 \cdot 10^{-9}$	9.9750	center
Acc-2	optimum	no	NACRE	small	–	–	none	$3 \cdot 10^{-9}$	9.9698	center
Acc-3	optimum	no	NACRE	small	–	–	none	$1 \cdot 10^{-8}$	9.9630	center
Acc-4	optimum	no	NACRE	small	–	–	none	$3 \cdot 10^{-8}$	9.9546	center
Acc-5	optimum	no	NACRE	small	–	–	none	$1 \cdot 10^{-7}$	9.9467	center
Acc-6	optimum	no	NACRE	small	–	–	none	$3 \cdot 10^{-7}$	9.9424	center
Acc-7	optimum	no	NACRE	small	–	–	none	$1 \cdot 10^{-6}$	9.9390	center
Acc-8	optimum	no	NACRE	small	–	–	none	$3 \cdot 10^{-6}$	9.9368	center
Acc-9	optimum	no	NACRE	small	–	–	none	$1 \cdot 10^{-5}$	9.9343	center
Ne-1	optimum	Idini	NACRE	small	–	–	Ledoux ($\alpha_S = 0$)	10^{-6}	9.9064	48
Ne-2	optimum	Pinedo	NACRE	small	–	–	Ledoux ($\alpha_S = 0$)	10^{-6}	9.8978	53
Ne-3	optimum	"/10	NACRE	small	–	–	Ledoux ($\alpha_S = 0$)	10^{-6}	9.9265	12
Ne-4	optimum	"/10^2	NACRE	small	–	–	Ledoux ($\alpha_S = 0$)	10^{-6}	9.9108	center
Ne-5	optimum	"/10^3	NACRE	small	–	–	Ledoux ($\alpha_S = 0$)	10^{-6}	9.9192	center
Ne-6	optimum	"/10^4	NACRE	small	–	–	Ledoux ($\alpha_S = 0$)	10^{-6}	9.9333	center
Ne-7	optimum	"/10^5	NACRE	small	–	–	Ledoux ($\alpha_S = 0$)	10^{-6}	9.9382	center
Semi-1	medium	no	NACRE	small	–	–	Schwarzschild ($\alpha_S = 0$)	10^{-6}	9.9385	center
Semi-2	medium	no	NACRE	small	–	–	Ledoux ($\alpha_S = 10^{-3}$)	10^{-6}	9.9384	center
Semi-3	medium	no	NACRE	small	–	–	Ledoux ($\alpha_S = 10^{-2}$)	10^{-6}	9.9384	center
Semi-4	medium	no	NACRE	small	–	–	Ledoux ($\alpha_S = 10^{-1}$)	10^{-6}	9.9384	center
Semi-5	medium	no	NACRE	small	–	–	Ledoux ($\alpha_S = 1$)	10^{-6}	9.9384	center
Semi-6	medium	no	NACRE	small	–	–	Ledoux ($\alpha_S = 10$)	10^{-6}	9.9380	center
Net-1	medium	no	NACRE	big	–	–	Ledoux ($\alpha_S = 0$)	10^{-6}	9.9386	center
Net-2	medium	no	JINA	big	–	–	Ledoux ($\alpha_S = 0$)	10^{-6}	9.9382	center
Net-3	medium	no	JINA (Oe-3)	big	–	–	Ledoux ($\alpha_S = 0$)	10^{-6}	9.9382	center
Net-4	medium	no	JINA (Oe+3)	big	–	–	Ledoux ($\alpha_S = 0$)	10^{-6}	9.9384	center
Net-5	medium	no	JINA (Oe+6)	big	–	–	Ledoux ($\alpha_S = 0$)	10^{-6}	9.9384	center
Net-6	medium	no	JINA (Oe+9)	big	–	–	Ledoux ($\alpha_S = 0$)	10^{-6}	9.9382	center
Net-7	medium	no	JINA (fus. ex.)	big	–	–	Ledoux ($\alpha_S = 0$)	10^{-6}	9.9382	center
Net-8	medium	no	JINA (fus. all)	big	–	–	Ledoux ($\alpha_S = 0$)	10^{-6}	9.9388	center
Net-9	medium	no	JINA	small	–	–	Ledoux ($\alpha_S = 0$)	10^{-6}	9.9382	center
Net-10	medium	no	NACRE	small	–	–	Ledoux ($\alpha_S = 0$)	10^{-6}	9.9385	center
U23-1	medium	no	NACRE	small	$1 \cdot 10^{-5}$	–	none	10^{-6}	9.9388	center
U23-2	medium	no	NACRE	small	$5 \cdot 10^{-5}$	–	none	10^{-6}	9.9387	center
U23-3	medium	no	NACRE	small	$1 \cdot 10^{-4}$	–	none	10^{-6}	9.9386	center
U23-4	medium	no	NACRE	small	$5 \cdot 10^{-4}$	–	none	10^{-6}	9.9395	center
U23-5	medium	no	NACRE	small	$1 \cdot 10^{-3}$	–	none	10^{-6}	9.9403	center
U23-6	medium	no	NACRE	small	$5 \cdot 10^{-3}$	–	none	10^{-6}	9.9402	center
U23-7	medium	no	NACRE	small	$1 \cdot 10^{-2}$	–	none	10^{-6}	9.9397	center
U25-1	medium	no	NACRE	small	–	$1 \cdot 10^{-5}$	none	10^{-6}	9.9403	center
U25-2	medium	no	NACRE	small	–	$5 \cdot 10^{-5}$	none	10^{-6}	9.9455	center
U25-3	medium	no	NACRE	small	–	$1 \cdot 10^{-4}$	none	10^{-6}	9.9499	center
U25-4	medium	no	NACRE	small	–	$5 \cdot 10^{-4}$	none	10^{-6}	9.9644	center
U25-5	medium	no	NACRE	small	–	$1 \cdot 10^{-3}$	none	10^{-6}	9.9711	center
U25-6	medium	no	NACRE	small	–	$5 \cdot 10^{-3}$	none	10^{-6}	9.9829	center
U25-7	medium	no	NACRE	small	–	$1 \cdot 10^{-2}$	none	10^{-6}	9.9880	center
U2325-1	medium	no	NACRE	small	$1 \cdot 10^{-5}$	$1 \cdot 10^{-5}$	none	10^{-6}	9.9403	center
U2325-2	medium	no	NACRE	small	$5 \cdot 10^{-5}$	$5 \cdot 10^{-5}$	none	10^{-6}	9.9456	center
U2325-3	medium	no	NACRE	small	$1 \cdot 10^{-4}$	$1 \cdot 10^{-4}$	none	10^{-6}	9.9500	center
U2325-4	medium	no	NACRE	small	$5 \cdot 10^{-4}$	$5 \cdot 10^{-4}$	none	10^{-6}	9.9653	center
U2325-5	medium	no	NACRE	small	$1 \cdot 10^{-3}$	$1 \cdot 10^{-3}$	none	10^{-6}	9.9713	center
U2325-6	medium	no	NACRE	small	$5 \cdot 10^{-3}$	$5 \cdot 10^{-3}$	none	10^{-6}	9.9835	center
U2325-7	medium	no	NACRE	small	$1 \cdot 10^{-2}$	$1 \cdot 10^{-2}$	none	10^{-6}	???	???
U2325Ne-1	medium	Pinedo	NACRE	small	$1 \cdot 10^{-5}$	$1 \cdot 10^{-5}$	none	10^{-6}	9.8959	57
U2325Ne-2	medium	Pinedo	NACRE	small	$5 \cdot 10^{-5}$	$5 \cdot 10^{-5}$	none	10^{-6}	9.8973	56
U2325Ne-3	medium	Pinedo	NACRE	small	$1 \cdot 10^{-4}$	$1 \cdot 10^{-4}$	none	10^{-6}	9.8970	60
U2325Ne-4	medium	Pinedo	NACRE	small	$5 \cdot 10^{-4}$	$5 \cdot 10^{-4}$	none	10^{-6}	9.9214	57
U2325Ne-5	medium	Pinedo	NACRE	small	$1 \cdot 10^{-3}$	$1 \cdot 10^{-3}$	none	10^{-6}	9.9268	60
U2325Ne-6	medium	Pinedo	NACRE	small	$5 \cdot 10^{-3}$	$5 \cdot 10^{-3}$	none	10^{-6}	9.9460	49
U2325Ne-7	medium	Pinedo	NACRE	small	$1 \cdot 10^{-2}$	$1 \cdot 10^{-2}$	none	10^{-6}	???	???

Table 6.2: Overview of AIC models that were computed with MESA for the study in this thesis. The table depicts the model name along with the main physics assumptions (initial setup) and the outcome of the simulation. The resolution of the individual model is given as shown in Table 6.1. Furthermore, it is indicated if the $0^+ \rightarrow 2^+$ transition of the ^{20}Ne EC is included, which thermonuclear rates are used, which reaction network, which convection type, which accretion rate and which value of $X\left(^{23}\mathrm{Na}\right)$ and $X\left(^{25}\mathrm{Mg}\right)$ was assumed. The ignition density and ignition spot of oxygen burning are given, as well.

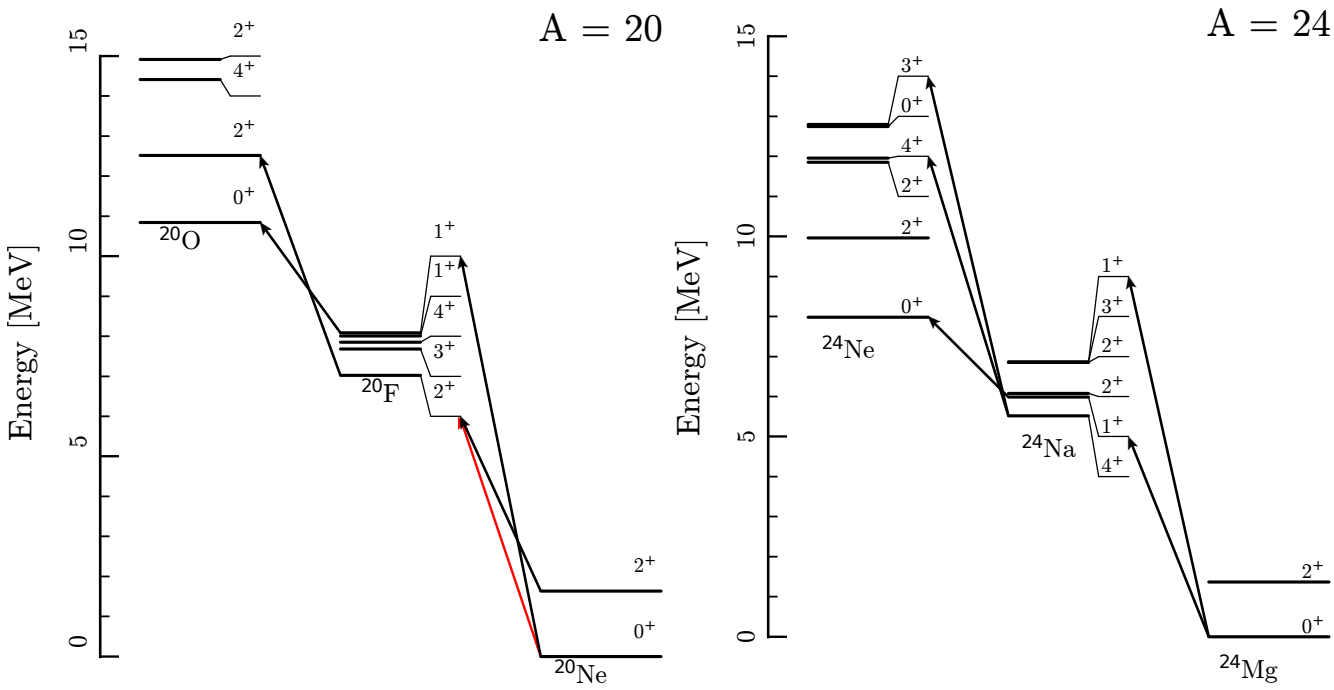

Figure 6.8: Level scheme of selected $A = 20$ and $A = 24$ nuclei with information about their quantum numbers (J^π) and excitation energies of the lowest excited states (E_{ex} in MeV). Adapted from Schwab et al. (2015). The transitions that were considered in said study are indicated by black arrows. The second forbidden ground state-ground state transition between ^{20}Ne and ^{20}F is indicated by a red arrow (see also Table 6.3).

integrals Φ (or Ψ) have to be solved numerically.[13] It should be mentioned that there were two minor errors in the original implementation of the on-the-fly weak rate routine in the MESA revision 7624, as described in Paxton et al. (2015) and Schwab et al. (2015). After they have been pointed out by us, they are corrected in MESA since revision 8118. Details can be found in the errata of the two aforementioned publications (Paxton et al., 2016; Schwab et al., 2016a).

In Schwab et al. (2015), only the EC and β^- decay for the chains $^{20}\mathrm{Ne}(e^-, \nu)^{20}\mathrm{F}(e^-, \nu)^{20}\mathrm{O}$ and $^{24}\mathrm{Mg}(e^-, \nu)^{24}\mathrm{Na}(e^-, \nu)^{24}\mathrm{Ne}$ were considered. The important transitions were selected according to Martínez-Pinedo et al. (2014). They are shown in Figure 6.8, that illustrates the level scheme for both EC chains. The transitions that have to be considered are indicated by arrows. As we also want to study the impact of EC on odd-A nuclei for the Urca process, we extended the scheme to the most abundant odd-A nuclei, being ^{23}Na and ^{25}Mg. In Table 6.3, we provide a list of all important transitions for the relevant EC and β decay nuclei in our study. The used $\log_{10}(ft)$ values are, if possible, experimental values. The relevant transitions for our study were selected manually, doing a similar analysis as in Martínez-Pinedo et al. (2014).

In order to make sure that the selected transitions are well describing the total rate for the conditions of our interest, we used the weak rates routine of MESA, together with the data provided in Table 6.3, to calculate EC and β^- decay rates. Then, we compare them to the previously published weak rate tabulations by Suzuki et al. (2016) that are provided on a dense grid. These rates rely on large-scale shell model calculations and, if possible, include experimentally measured transition strength. As of now, they can be considered to be the "gold standard" for weak rates involving sd-shell nuclei in astrophysics.[14] The results of this comparison are displayed in Figures 6.9 and 6.10. The different panels show the total

[13] Notice that several authors have provided analytical approximations of the phase space integral (see e.g. Martínez-Pinedo et al., 2014).

[14] Notice that their tables are limited to nuclei with mass number A = 20, 23, 24, 25, and 27.

$N_{EC,i}$	$N_{EC,f}$	$Q_{EC}/Q_{\beta-}$	E_i	J_i^π	E_f	J_f^π	$\log_{10}(ft)_{EC}$	$\log_{10}(ft)_{\beta-}$	remark
^{20}Ne	^{20}F	−7.536	0.000	0^+	0.000	2^+	9.801	10.500	u.l.+forb.
		+7.025	0.000	0^+	1.057	1^+	4.380	4.857	exp.
			1.634	2^+	0.000	2^+	4.970	4.970	exp.
^{20}F	^{20}O	−4.326	0.000	2^+	1.674	2^+	5.429	5.429	th.
		+3.815	1.057	1^+	0.000	0^+	4.211	3.734	exp.
^{23}Na	^{23}Ne	−4.886	0.000	$3/2^+$	0.000	$5/2^+$	5.093	5.269	exp.
		+4.375	0.440	$5/2^+$	0.000	$5/2^+$	5.381	5.381	exp.
^{23}Ne	^{23}F	−8.981	0.000	$5/2^+$	0.000	$5/2^+$	5.717	5.717	exp.
		+8.470							
^{24}Mg	^{24}Na	−6.026	0.000	0^+	0.472	1^+	4.815	5.292	exp.
		+5.515	0.000	0^+	1.347	1^+	3.772	4.249	exp.
^{24}Na	^{24}Ne	−2.978	0.000	4^+	3.972	4^+	6.209	6.209	th.
		+2.467	0.000	4^+	4.817	3^+	4.423	4.314	th.+lvl.
			0.472	1^+	0.000	0^+	4.829	4.352	exp.
^{25}Mg	^{25}Na	−4.346	0.000	$5/2^+$	0.000	$5/2^+$	5.251	5.251	exp.
		+3.835	0.000	$5/2^+$	0.090	$3/2^+$	5.427	5.251	as above
			0.975	$3/2^+$	0.000	$5/2^+$	4.867	5.043	exp.
			1.612	$7/2^+$	0.000	$5/2^+$	5.155	5.030	exp.
^{25}Na	^{25}Ne	−7.811	0.089	$1/2^+$	0.000	$3/2^+$	4.707	4.406	exp.
		+7.300	1.069	$1/2^+$	0.000	$1/2^+$	4.702	4.702	exp.

Table 6.3: EC and β^- decay transitions considered for the MESA on-the-fly weak rate determination. The table displays the considered mother and daughter nuclei, together with their ground state-ground state Q value, the excitation energy $E_{i/f}$, the total spin $J_{i/f}$, the parity $\pi_{i/f}$ and the $\log_{10}(ft)$ value. The experimental $\log_{10}(ft)$ values (indicated by "exp.") are taken from the ENSDF database (ENSDF, 2017). The theoretical $\log_{10}(ft)$ values (indicated by "th." or "th.+lvl." if also the excitation energies were calculated) are from Martínez-Pinedo et al. (2014). The same authors also provided an estimate for the second forbidden $0^+ \rightarrow 2^+$ transition for the EC on ^{20}Ne, based on the experimental upper limit (indicated by "u.l.+forb."). For the $5/2^+ \rightarrow 3/2^+$ EC transition of ^{25}Mg, no $\log_{10}(ft)$ value is known and we simply assumed that the strength is comparable to the closest transition between the same nuclei (indicated by "as above").

EC and β^- decay rates for all nuclei considered in our study (as listed in Table 6.3) for electron densities between $\log_{10}\left(\varrho Y_e/\mathrm{g\ cm^{-3}}\right) = 8.5$ and 10, for selected temperatures between $\log_{10}(T/K) = 7.4$ and 9.4. We also made sure, that both rates use the same screening corrections.

In general, we find an excellent agreement between the rates calculated by MESA, based on our set of transitions and $\log_{10}(ft)$ values, and the rates by Suzuki et al. (2016). Notice that this comparison was not possible for the first study by Schwab et al. (2015), as the rates on a dense grid were not yet available at this time. In this light, this is an important validation of the results presented in Schwab et al. (2015), that relied on the same method to calculate the weak rates on-the-fly. As can be seen in the four upper panels of Figure 6.9, the agreement is nearly perfect for the chain of nuclei ^{20}Ne $\leftrightarrow$ ^{20}F $\leftrightarrow$ ^{20}O. For the chain ^{24}Mg $\leftrightarrow$ ^{24}Na $\leftrightarrow$ ^{24}Ne, that is displayed in the lower panel of the same figure, the agreement is excellent only for the EC direction. In the β^- decay direction, from ^{24}Na to ^{24}Mg, there seems to be a transition missing in our description, that plays a role for β^- decay at low temperatures (i.e. $\log_{10}(T/K) \lesssim 8.2$) and densities below 10^9 g cm^{-3}. From the analysis in Martínez-Pinedo et al. (2014), it is possible to conclude, that this has to be the second forbidden ($4^+ \rightarrow 2^+$) transition from the ^{24}Na ground state. The transition matrix element has been determined experimentally and hence, this transition can be easily included. According to the ENSDF database (ENSDF, 2017), the $\log_{10}(ft)$

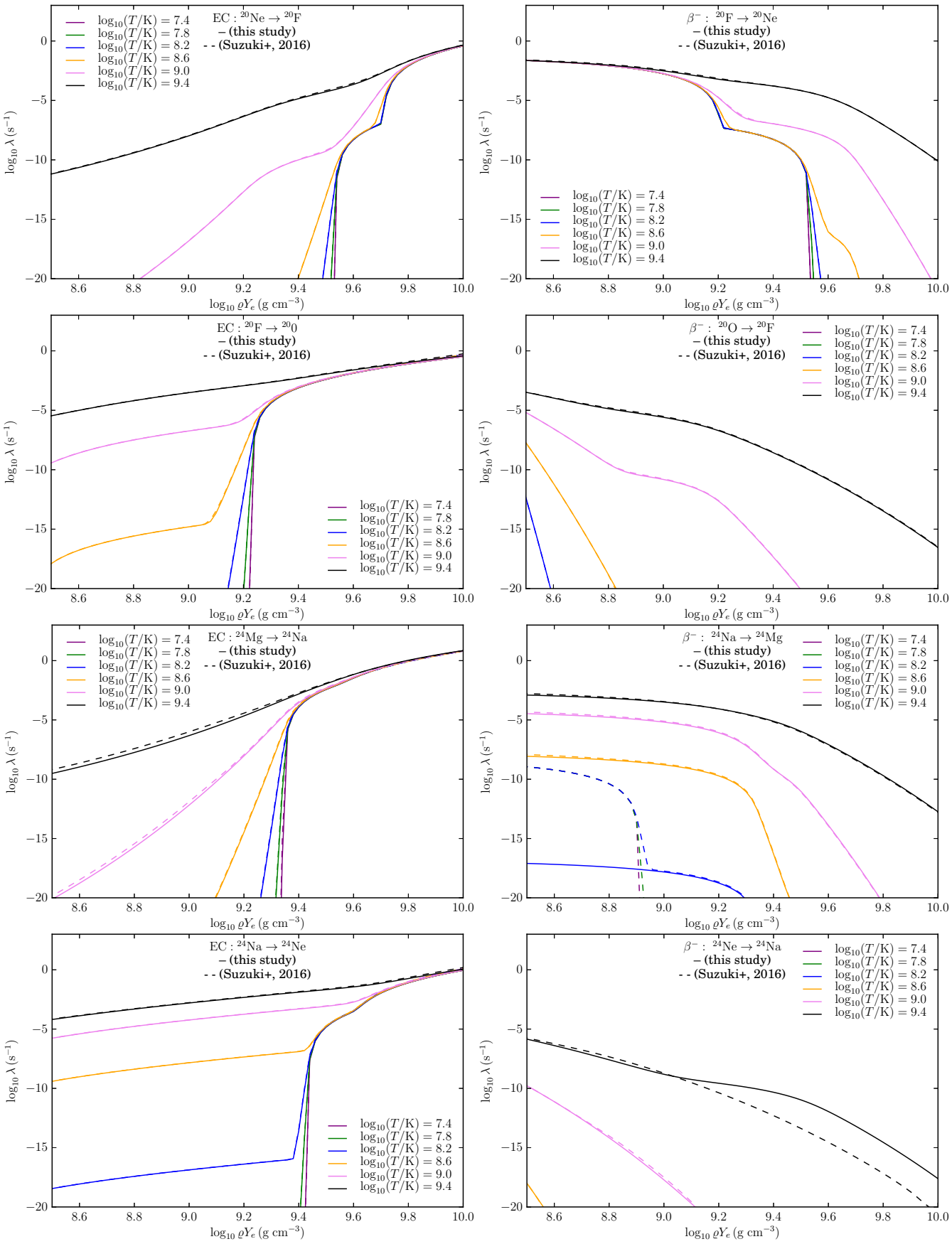

Figure 6.9: Comparison of even-A sd-shell EC and β^- decay rates used in MESA on the basis of the transitions in Table 6.3. The rate λ is plotted for selected temperatures as a function of ϱY_e. Our rates are calculated by the on-the-fly routine of MESA. The rates of the dense tabulation by Suzuki et al. (2016) are taken as reference.

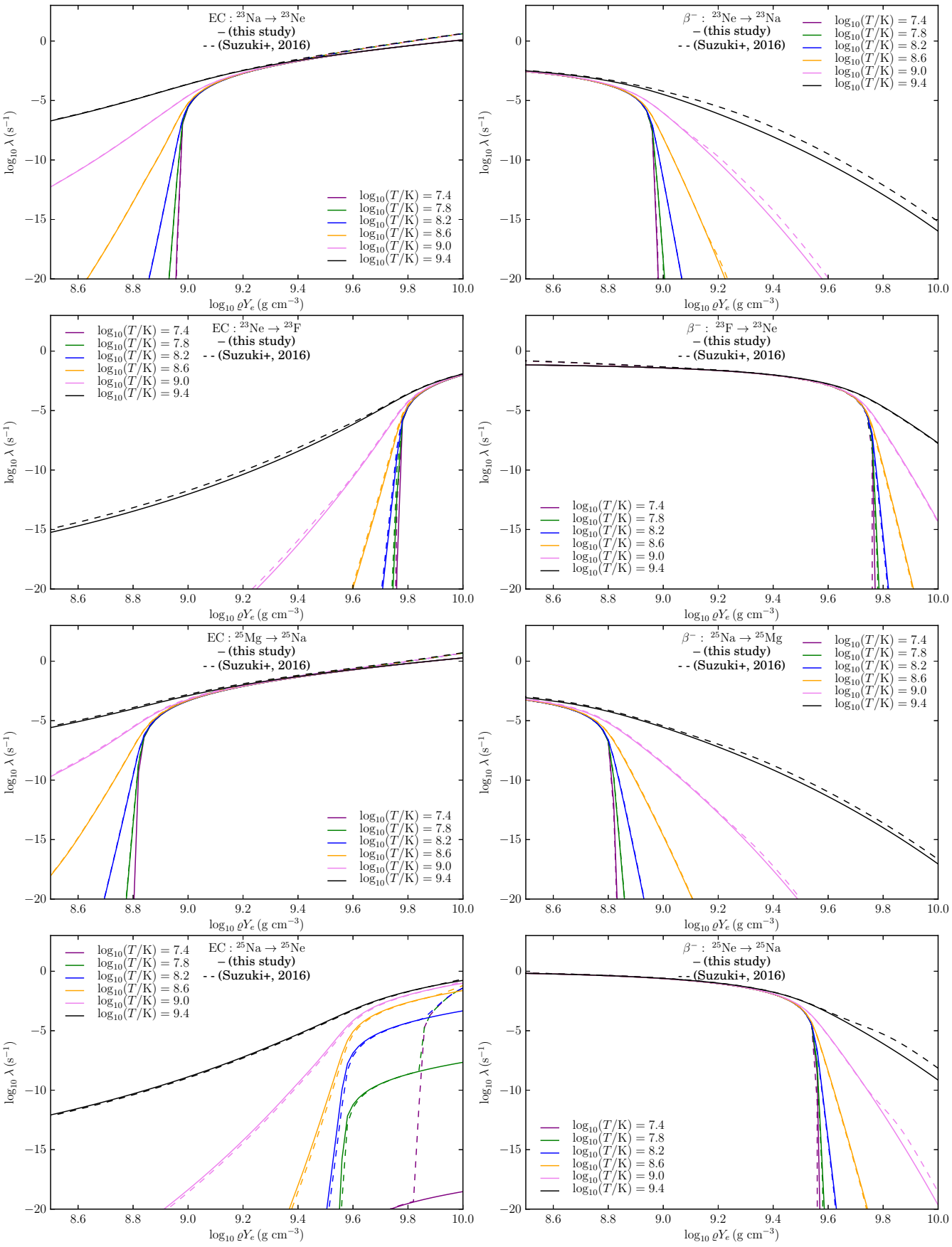

Figure 6.10: Comparison of odd-A sd-shell EC and β^- decay rates used in MESA on the basis of the transitions in Table 6.3. The rate λ is plotted for selected temperatures as a function of ϱY_e. Our rates are calculated by the on-the-fly routine of MESA. The rates of the dense tabulation by Suzuki et al. (2016) are taken as reference.

value in the β^- direction is given by 11.355. It future studies, it will be straight forward to include this transition. As it is going to matter only in the β^--decay direction, we will not expect it to alter our results.

Surprisingly, in the β^- decay direction from ^{24}Ne to ^{24}Na, the situation is reverse. In this case, it seems that the β^- decay rate from the tabulation of Suzuki et al. (2016) is missing a relevant transition at high densities. As they included all experimentally known transitions, we can only speculate, that they did not include the $(4^+ \rightarrow 3^+)$ transition, that we computed based on the theoretically calculated levels as well as transitions strength given by Martínez-Pinedo et al. (2014). Also in this case, this discrepancy is not expected have an impact on the upcoming findings in this chapter. More importantly, for the EC direction from ^{24}Na to ^{24}Ne, the rate is reproduced perfectly by our approach.

The comparison of the relevant weak rates for odd-A nuclei is presented in Figure 6.10. We find that, in general, the on-the-fly rate calculation of MESA reproduces very well the dense tabulations of Suzuki et al. (2016). As these nuclei are responsible for the Urca process, both the EC and the β^- direction are important. As will be shown in Section 6.3.4, in our simulations, the relevant Urca processes occur at electron densities between $\log_{10}\left(\varrho Y_e/\mathrm{g\ cm^{-3}}\right) = 8.7$ and 9.7 and at a temperature of $\log_{10}(T/K) \approx 8.2$ (corresponding to the blue lines in Figure 6.10). At those conditions, the limited set of transitions that we use can nearly perfectly reproduce the required β^- decay rates. Nevertheless, it seems to be the case that the MESA approach, using the limited set of transitions as listed in Table 6.3, is missing a lot of the total β^- decay rate at high temperature and density. This is however not surprising. At those conditions, a lot of β^-decay transitions from excited states of the mother nucleus have to be considered and due to the lack of experimental data, these are not included in our tabulation. Also, as these conditions do not occur in our simulations, we do not have to be worried about that regime. Hence, even if the transitions would be obtained from shell-model calculations, their inclusion will only slow down the calculation, without affecting the outcome. In general, for these conditions, tabulated rates should be used.

This leads us to the conclusion, that (assuming a careful analysis of the relevant nuclear states and transitions has been made) it is sufficient to include only a few transitions into the approach of MESA in order to obtain a very accurate weak rate. Of course, it can still be argued that it would always be preferable to use rates that are tabulated on a dense grid and include all experimentally available information (as is the case in Suzuki et al. (2016)). But this is not entirely true. Even on a dense grid, the interpolation errors can be rather large for low temperatures and around $\varrho_{\mathrm{threshold}}$. Maybe even more important is the fact that a tabulation is much less flexible compared to an on-the-fly computation when it comes to changing input physics, like adding or removing single transitions or changing the description of screening. Of course, it is still much faster to interpolate in a 2D table than to numerically determine the phase space integral. Hence, it should be decided (e.g. in MESA), based on the exact requirements of the astrophysical problem, how the weak reaction rates should be determined.

6.3.3 Neon-20 Second-Forbidden Transition

It was demonstrated by Schwab et al. (2015), that the inclusion of the second forbidden ground state-ground state transition $(0^+ \rightarrow 2^+)$ between ^{20}Ne and ^{20}F can have a significant impact on the evolution of degenerate ONe cores, as in this case the oxygen deflagration will be ignited off-center. As listed and explained in Table 6.3, they relied on the matrix element that was derived in Martínez-Pinedo et al. (2014), based on the experimental upper limit by Tilley et al. (1998).

Nevertheless, we will re-investigate this topic for two particular reasons. First of all, this topic was not discussed in great detail in Schwab et al. (2015) and especially the off-center ignition of the oxygen flame is a very interesting feature that should be explored in more depth. For the carbon deflagration of WDs, it was found that the exact ignition spot of the deflagration can have a significant impact on its propagation (see e.g. Fink et al., 2014). Knowing that the oxygen deflagration is a very similar scenario, the outcome

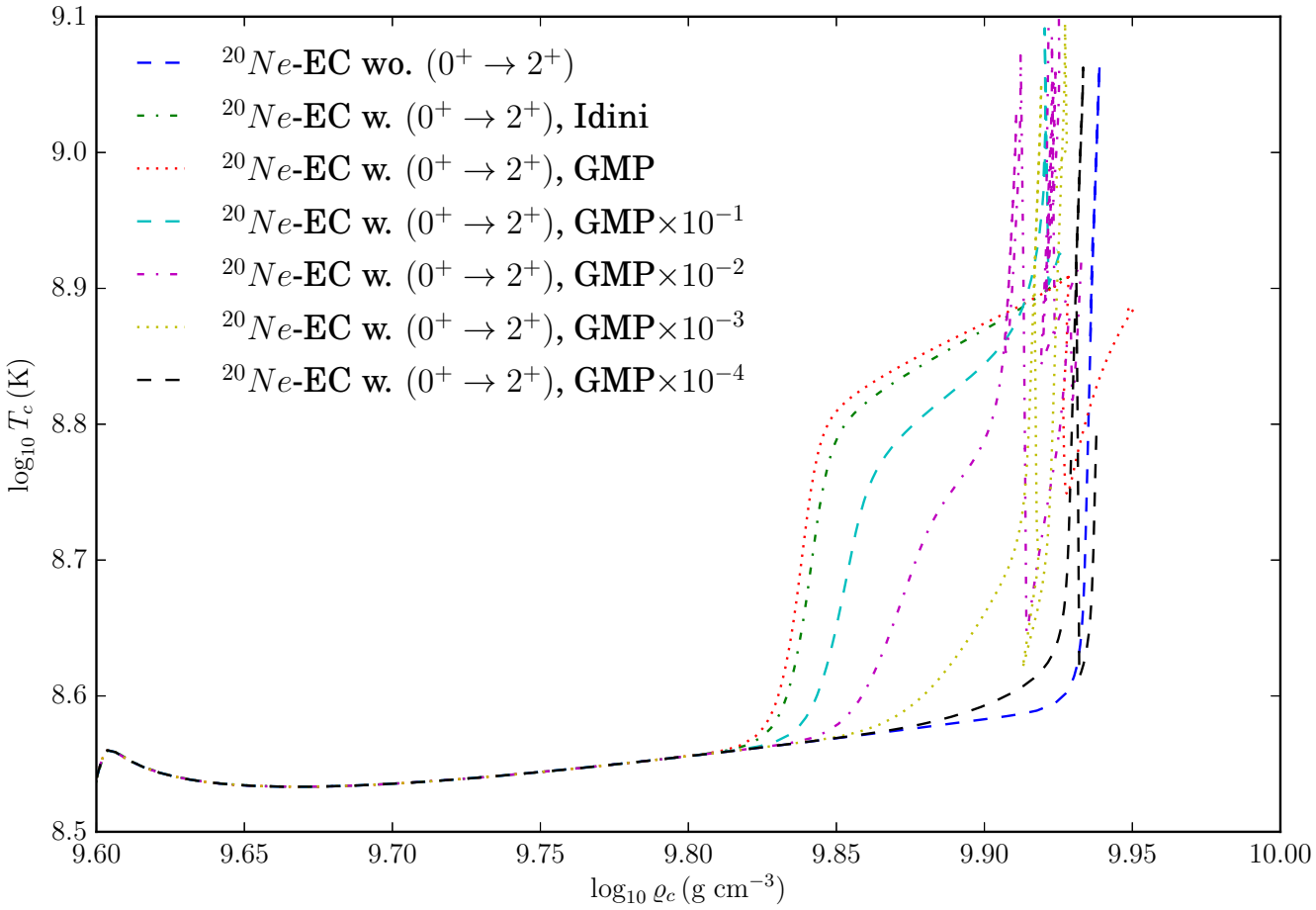

Figure 6.11: The $T_c - \varrho_c$-diagram shows the time evolution of the MESA AIC models `Ne-1` to `Ne-7` and `Res-3` which serves as reference (see Table 6.2). In this series of models, the impact of the inclusion of the second forbidden ground state-ground state transition between ^{20}Ne and ^{20}F is studied. The $\log_{10}(ft)$ value is either not considered at all, taken from Martínez-Pinedo et al. (2014) or based on Idini et al. (2014), as indicated by the label. Additional models were calculated where the $\log_{10}(ft)$ value based on the experimental upper limit was increased by a constant factor. Notice that an increase in the $\log_{10}(ft)$ value leads to a reduction of the rate.

of such an event—collapse or explosion—might be sensitive to the ignition spot, as well. In Jones et al. (2016), it was announced that such a study would be on their agenda. Secondly, the recent publications, dealing with this topic, have stimulated both, an experimental as well as a theoretical determination of the matrix element corresponding to the second forbidden transition (Idini et al., 2014; Kirsebom et al., 2017). While the measurement is still being done, we obtained a theoretically determined value for the transition matrix element (Idini, 2016).

In this Section, we will present the results of the series of models `Ne-1` to `Ne-7`, as listed in Table 6.2. They will explore the impact of including the $0^+ \rightarrow 2^+$ transition. In model `Ne-2`, the second-forbidden transition $\log_{10}(ft)$ value is chosen to be at the experimental upper limit, as provided in Table 6.3 and used by Schwab et al. (2015). The model `Ne-1` relies on the $\log_{10}(ft)$ values given by Idini (2016), which are 10.3 in EC direction and 10.34 in the β^- direction. As the $\log_{10}(ft)$ provided by Martínez-Pinedo et al. (2014) is an upper limit, we perform five additional simulations where we reduce the matrix element repeatedly by a factor of 10. This implies that the $\log_{10}(ft)$ value is increased by 1 for each reduction. As a result, the models `Ne-3` - `Ne-7` correspond to $\log_{10}(ft)$ values of 10.8, 11.8, 12.8, 13.8 and 14.8, respectively.

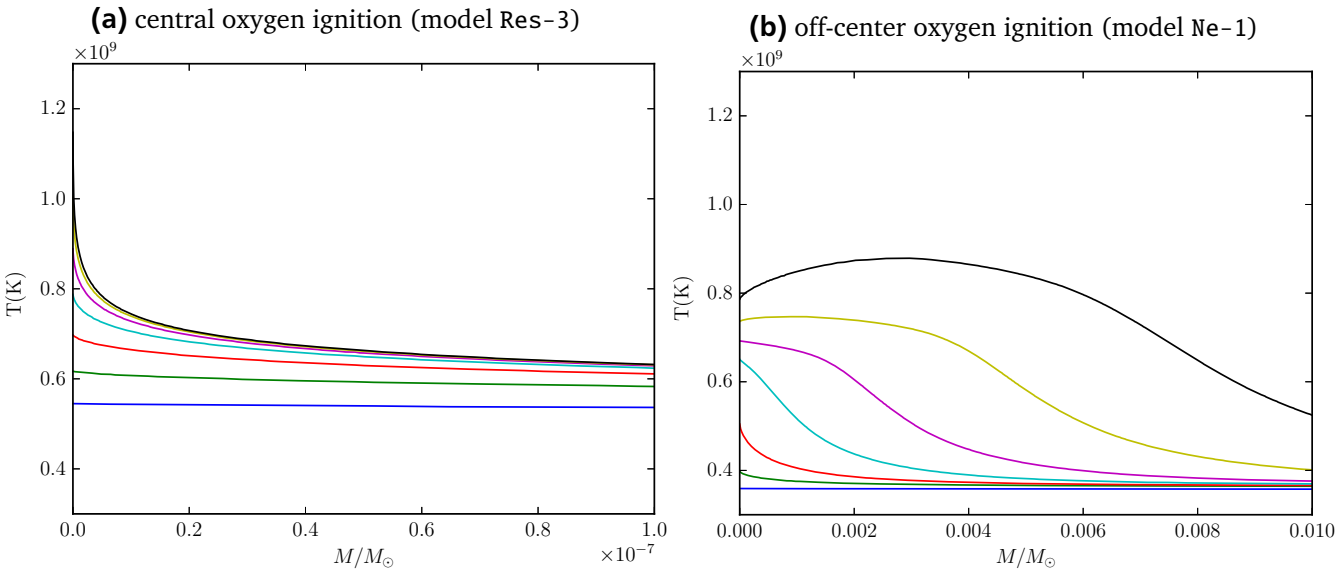

Figure 6.12: Comparison of AIC models with central and off-center oxygen flame ignition. Both panels depict the temperature evolution for a consecutive series of stellar profiles (as a function of $M/M_{\odot}$). The left panel corresponds to model `Res-3` where the $0^+ \rightarrow 2^+$ transition for the ^{20}Ne EC is not included. In this case, the time between onset of ^{20}Ne EC and oxygen ignition is $\approx$ few days and occurs sharply confined in the central zone. The right panel corresponds to model `Ne-1` where the $0^+ \rightarrow 2^+$ transition for the ^{20}Ne EC is included. In this case, the time between onset of ^{20}Ne EC and oxygen ignition is $\approx$ few years and occurs at a mass coordinate of $\approx 0.003\ M_{\odot}$.

The results of those set of models are presented in Figure 6.11. This $T_c - \varrho_c$-diagrams shows the time evolution of the MESA AIC models `Ne-1` to `Ne-7` and `Res-3` which serves as reference. The main effect the inclusion of the $0^+ \rightarrow 2^+$ transition has on the evolution of the model is that EC on ^{20}Ne set in significantly earlier. This effect is most pronounced for model `Ne-1`, where the $\log_{10}(ft)$ value has the lowest value compatible with experiment. Consequently, the effect becomes increasingly smaller, the more this transition gets suppressed, as can be seen by looking at the models `Ne-3` - `Ne-7`. The reason why EC on ^{20}Ne, including the second forbidden transition, set in at lower densities, originates in its lower Q value. In the reference model `Res-1` without this particular transition, the first ^{20}Ne EC transition that is allowed to occur is the allowed $0^+ \rightarrow 1^+$ ground state-excited state transition, as listed in Table 6.3. And because the 1^+ state of ^{20}F has an excitation energy of 1.057 MeV, the electron has to overcome a Q value of -8.593 MeV, corresponding to a threshold density of $\log_{10}\left(\varrho/\mathrm{g\ cm^{-3}}\right) \approx 9.95$. The ground-state ground-state transition on the other hand has a significantly lower Q value of -7.536 MeV, meaning that it sets in earlier at $\log_{10}\left(\varrho/\mathrm{g\ cm^{-3}}\right) \approx 9.8$.

As the $0^+ \rightarrow 2^+$ transition is forbidden, is has a much smaller matrix element compared to allowed transitions. As discussed in Section 4.3.3, a second-forbidden transition is typically suppressed by a factor of 10^6. Because of this, even once E_F is significantly larger than the Q value, the EC rate does not become larger than $\lambda_{EC} \approx 10^{-8}\ s^{-1}$, as can be seen in the top left panel of Figure 6.9. This also explains, why the initial increase of the central temperature of the ONe core due to the $0^+ \rightarrow 2^+$ transition is insufficient to ignite oxygen by itself. Only once the allowed $0^+ \rightarrow 1^+$ transition becomes enabled, the temperature is lifted beyond the critical value for oxygen ignition.

As pointed out by Schwab et al. (2015), the inclusion of the second-forbidden ^{20}Ne EC transition leads to an off-center ignition of the core. In Figure 6.13, we show Kippenhahn diagrams of the MESA models `Ne-1` to `Ne-5` and `Res-6`. Hence, from the left top panel to the bottom right panel, the influence of the second-forbidden transition is continuously reduced. If we look at the two top panels, depicting the models `Ne-1` and `Ne-2`, we see that they have a very similar temperature evolution and in both

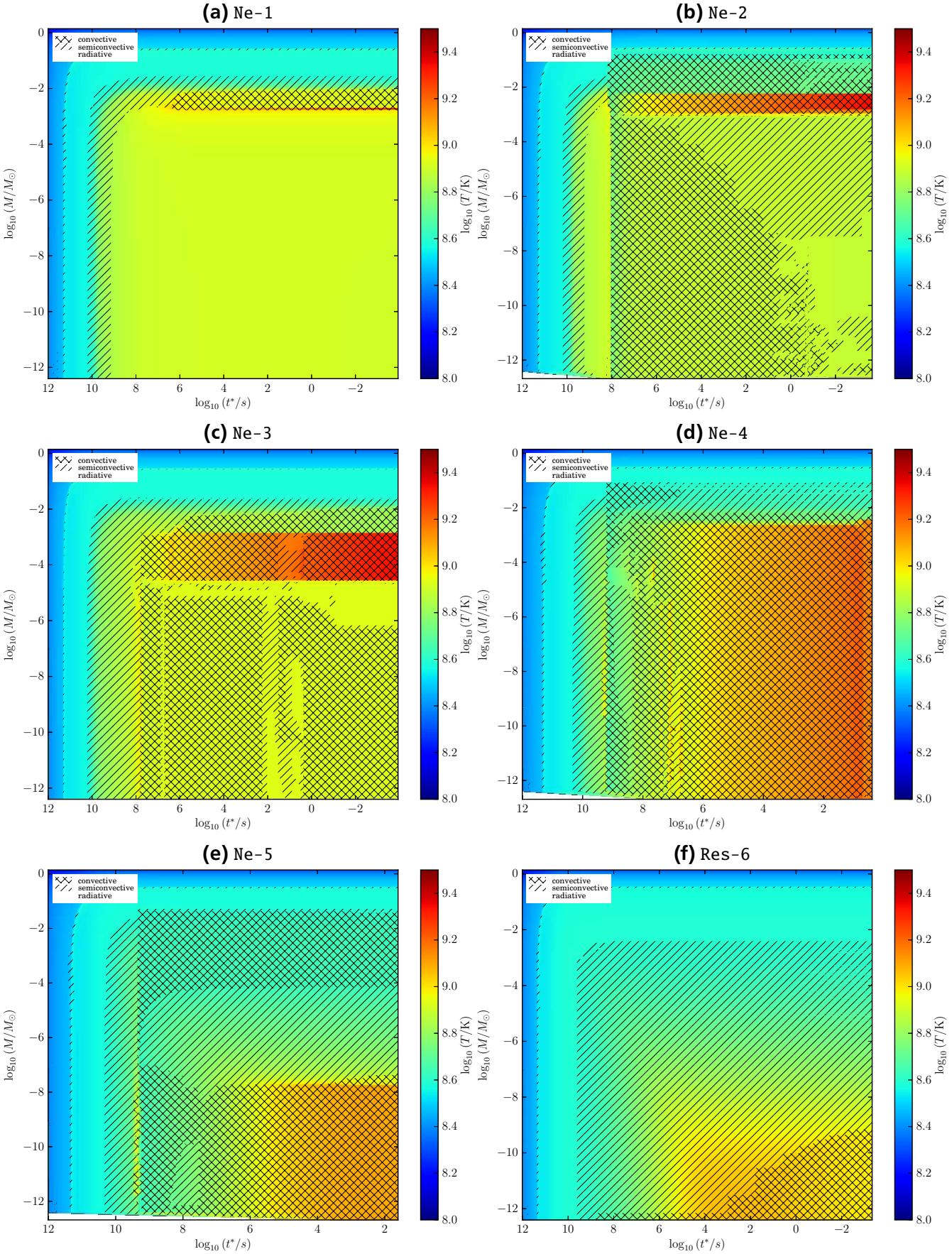

Figure 6.13: Kippenhahn diagrams of MESA AIC runs `Ne-1` to `Ne-5` and `Res-6`, as listed in Table 6.2. Shown is the temperature (T/K, color coded) as a function of enclosed mass ($M/M_\odot$) and time until oxygen ignition (t^*/s). Convective and semiconvective regions are indicated by crosses and dashes, respectively.

cases, it is clearly visible that oxygen is ignited off center at a mass coordinate of roughly $3 \times 10^{-3}\ M_\odot$, corresponding to a radius of ≈ 50 km. With increasingly weaker $0^+ \rightarrow 2^+$ transition, the models `Ne3` to `Ne5` asymptotically approach the behavior of the fiducial model `Res-3`, in which case oxygen is ignited in the center (see middle and bottom panels of Figure 6.13).

The reason why EC on ^{20}Ne, including the second-forbidden transition, lead to an off-center ignition, can be understood better by looking at stellar profiles. In Figure 6.12, we compare various temperature profiles of two characteristic models of accreting ONe cores. The left panel corresponds to model `Res-3` where the $0^+ \rightarrow 2^+$ transition for the ^{20}Ne EC is not included, while the right panel corresponds to model `Ne-1` where said transition is included. As discussed before, in model `Res-3`, EC on ^{20}Ne set in late (i.e. high density) via the strong allowed $0^+ \rightarrow 1^+$ transition that has a very low $\log_{10}(ft)$ value of 4.380. As illustrated in Figure 6.12, the heat released by this reaction causes the core to exceed oxygen burning temperatures on a very short timescale of days, meaning that there is not enough time for the EC heat to be transported away from the center of the core.

In contrast to this, the initial heating in model `Ne-1` originates from the much weaker $0^+ \rightarrow 2^+$ forbidden transition, that originally sets in in the center, as well. But because it acts on a much longer timescale (years), the core has enough time to react to the excess heat and despite its high degeneracy, will eventually expand. This behavior is displayed in the right panel of Figure 6.12. After the center of the core has expanded, it shifts the zone with the maximum temperature to a mass coordinate of ≈ 50 km. As soon as the allowed transition becomes relevant, the EC heat release will ignite the oxygen deflagration as well, but this time slightly off-center.

6.3.4 Abundance of Urca Nuclei and Cooling

As described in Section 6.3.2, we extend the list of levels and transitions for the MESA on-the-fly weak rate determination routine to include the two odd-A chains $^{23}\text{Na} \leftrightarrow {}^{23}\text{Ne} \leftrightarrow {}^{23}\text{F}$ and $^{25}\text{Mg} \leftrightarrow {}^{25}\text{Na} \leftrightarrow {}^{25}\text{Ne}$. This allows us to explore the impact of the post-carbon burning Urca nuclei ^{23}Na and ^{25}Mg (that can be abundant up to a few percent) on the evolution of the ONe core before the deflagration sets in. In Schwab et al. (2015), where Urca processes were not considered, it was concluded that AIC models that start at different initial temperatures (Figure 11 in Schwab et al., 2015), follow a very similar evolution and ignite oxygen at roughly the same density. The reason for this behavior originates mainly in the first EC heating episode at $\log_{10}\left(\varrho/\mathrm{g\ cm^{-3}}\right) \approx 9.6$, due to ^{24}Mg that erases the "temperature history" of the core. Similarly, a naive expectation would be that Urca processes, as they do not affect the deleptonization but only the temporal evolution, will also not have a big impact on the ignition density, at least if they occur before the EC phase involving ^{20}Mg. If they however occur close enough to the critical density for EC on ^{20}Ne, the cooling might increase $\varrho_{\mathrm{thresh}}$ by removing electrons from the tail of the distribution.

In this section, we will present the results of four series of models that all study the influence of Urca cooling on the evolution of ONe cores. They are: `U23`, `U25`, `U2325` and `U2325Ne`, as listed in Table 6.2. In all of those four model series, we set all convective velocities to zero (this is done by setting the option `max_conv_vel_div_csound` to zero). It has the "cosmetic" effect, that the thermonuclear runaway can be followed to higher temperatures, as MESA is prevented from using convection in the core, already during the onset of the oxygen deflagration. On such short timescales, the standard description of convection in stellar evolution via mixing-length theory (as described in Section 2.3.2) will yield wrong results. Of course, it was made sure that using this inlist option does have no impact on the evolution before. Otherwise, all inlist options are identical to the default model `Res-2`. In order to study the impact of Urca cooling, the Urca nuclei and carbon-burning products ^{23}Na and ^{25}Mg need to be abundant in the initial models. The exact abundances of those two nuclei may be looked up in Table 6.2. Furthermore, the model series `U2325Ne` also includes the second-forbidden transition of ^{20}Ne.

(a) MESA AIC runs `U23-1` to `U23-7` (see Table 6.2)

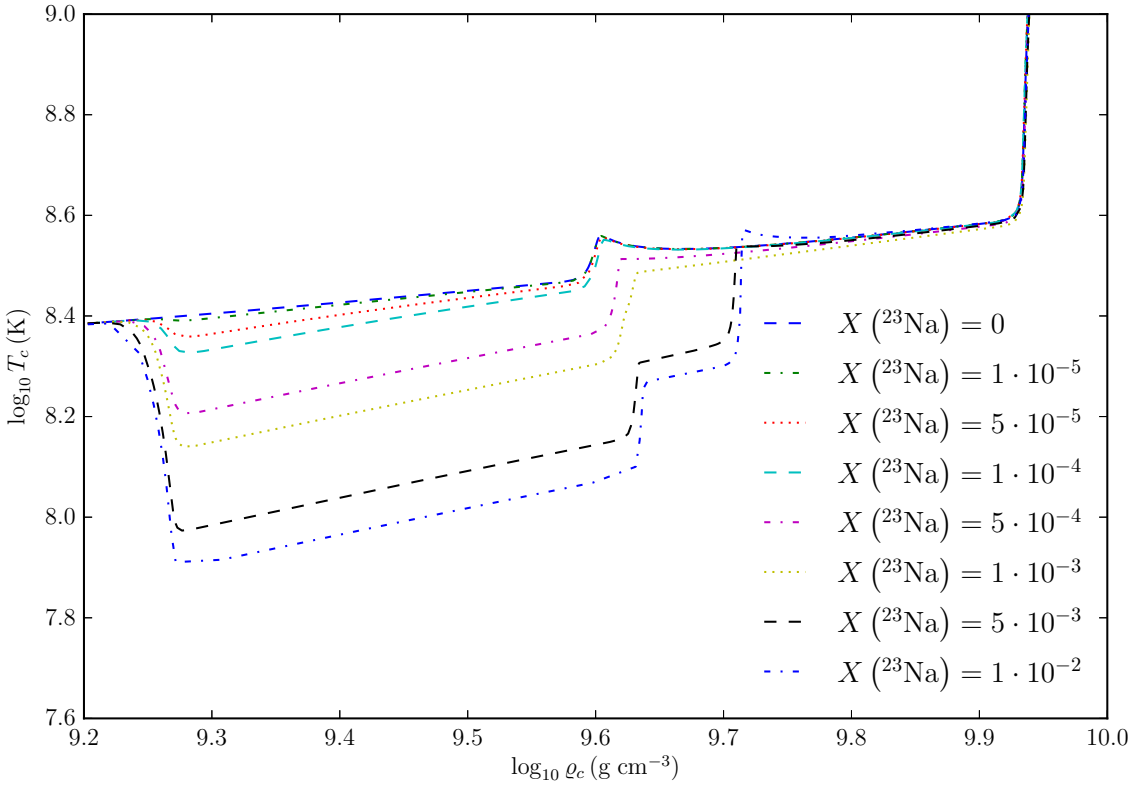

(b) MESA AIC runs `U25-1` to `U25-7` (see Table 6.2)

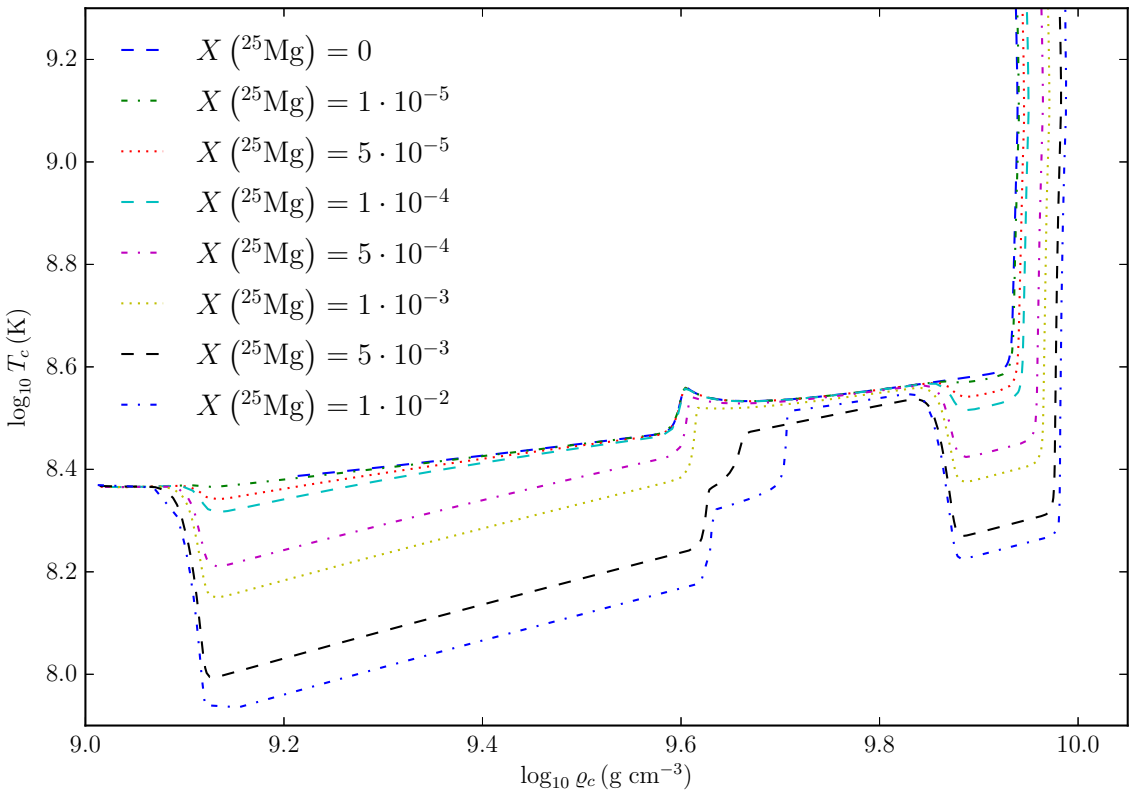

Figure 6.14: The two $T_c - \varrho_c$-diagrams depict the time evolution of the MESA AIC models as indicated by the panel caption. In the upper panel and the lower panel, the impact of the initial value of $X\left(^{23}\mathrm{Na}\right)$ and $X\left(^{25}\mathrm{Mg}\right)$ are studied, respectively.

(a) MESA AIC runs `U2325-1` to `U2325-7` (see Table 6.2)

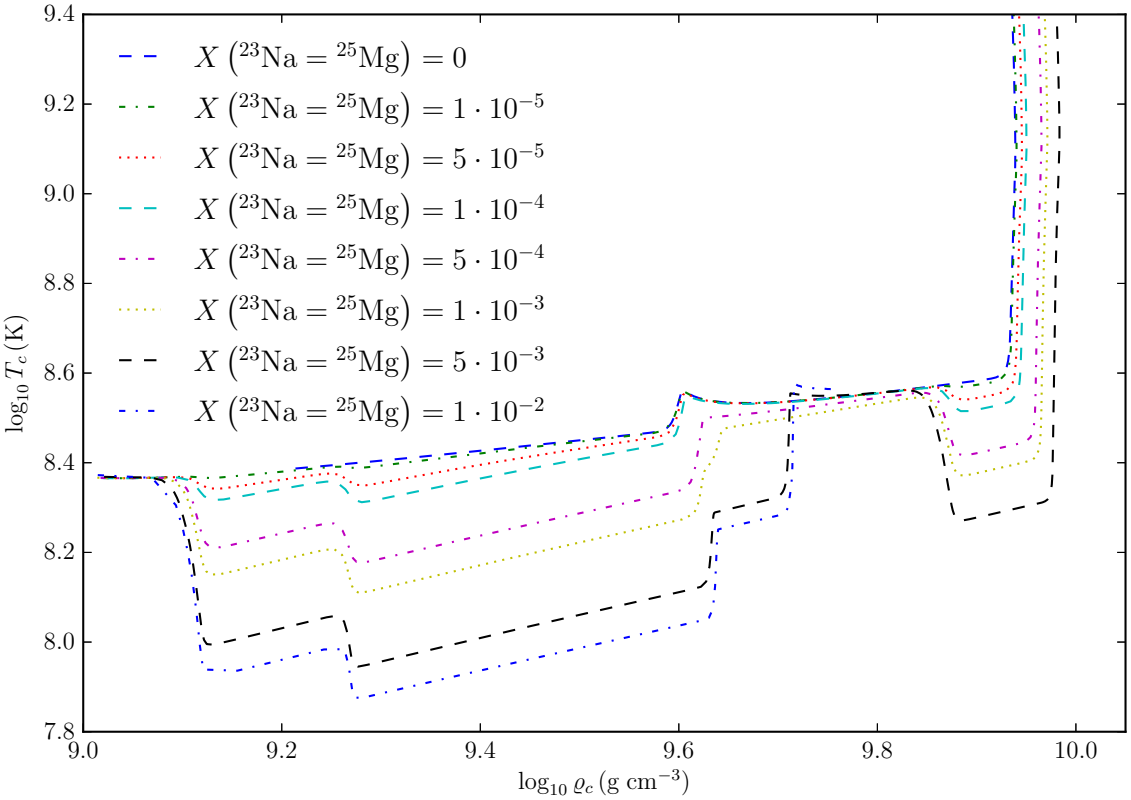

(b) MESA AIC runs `U2325Ne-1` to `U2325Ne-7` (see Table 6.2)

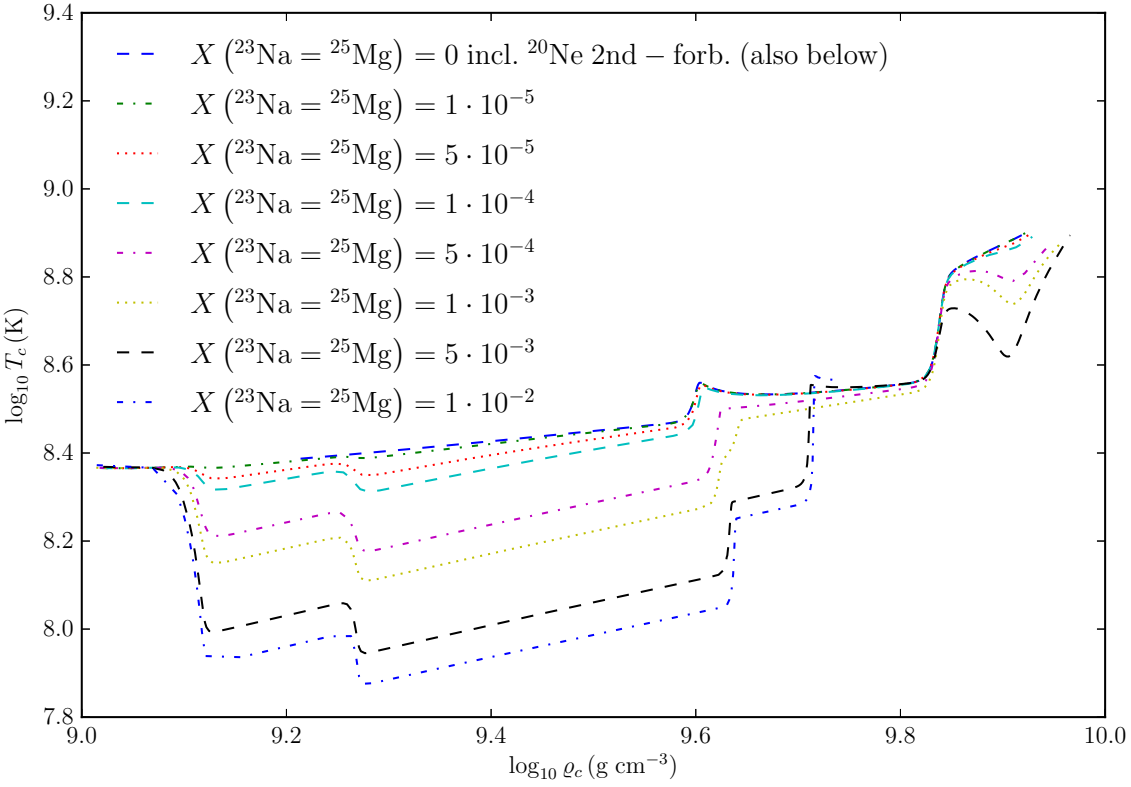

Figure 6.15: The two $T_c - \varrho_c$-diagrams depict the time evolution of the MESA AIC models as indicated by the panel caption. In the upper panel and the lower panel, the impact of the initial value of $X\left(^{23}\mathrm{Na}\right)$ and $X\left(^{25}\mathrm{Mg}\right)$ are studied. The lower panel also includes the second forbidden $0^+ \rightarrow 2^+$ transition of the ^{20}Ne EC.

In the U23 series, we varied the mass fraction of ^{23}Na between $X\left(^{23}\mathrm{Na}\right) = 0$ and $X\left(^{23}\mathrm{Na}\right) = 0.01$. The results of those runs are displayed in the upper panel of Figure 6.14. In this $T_c - \varrho_c$-diagram, the time evolution of said models is illustrated until the ignition of oxygen. It is apparent that, starting from the same initial temperature, Urca cooling due to the pair ^{23}Na $\leftrightarrow$ ^{23}Ne leads to a strong cooling effect that is roughly proportional to the abundance of ^{23}Na. It sets in at a density of $\log_{10}\left(\varrho/\mathrm{g\ cm^{-3}}\right) \approx 9.25$, corresponding to a ground state-ground state Q value of -4.886 MeV. For the model with $X\left(^{23}\mathrm{Na}\right) = 0.01$, the ONe core receives a significant amount of cooling and T_c is reduced by a factor of 3 from initially $\log_{10}(T/\mathrm{K}) = 8.4$ to 7.9. Nevertheless, similar to what has been found by Schwab et al. (2015) regarding the initial temperature dependence, the EC phase on ^{24}Mg deletes the temporal history of the ONe core. Afterwards, exceeding a density of $\log_{10}\left(\varrho/\mathrm{g\ cm^{-3}}\right) \approx 9.7$, the evolution of all models is very similar again and consequently, the ignition of oxygen occurs basically at the same density. Hence, we can conclude that the abundance of ^{23}Na has no influence on the ignition density of the deflagration.

In complete analogy, in the U25 series, we varied the mass fraction of ^{25}Mg between $X\left(^{25}\mathrm{Mg}\right) = 0$ and $X\left(^{25}\mathrm{Mg}\right) = 0.01$. The results of those runs are displayed in the lower panel of Figure 6.14. Due to the low Q value of -4.346 MeV for the EC on ^{25}Mg, the first Urca cooling effect sets in very early around $\log_{10}\left(\varrho/\mathrm{g\ cm^{-3}}\right) \approx 9.1$ and the cooling effect has a similar magnitude as the one of ^{23}Na. Afterwards, the evolution proceeds unaffected by weak reactions, until the EC phase on ^{24}Mg sets in and rises the temperature again. As discussed before, EC on ^{24}Mg release sufficient heat to erase the temporal history of the ONe core and the central temperature of all runs has consequently very similar values. Then the accretion onto the ONe core proceeds until a density of around $\log_{10}\left(\varrho/\mathrm{g\ cm^{-3}}\right) = 9.9$ is reached. At this point, another Urca cooling phase sets in, before the ignition of oxygen occurs. This time, the secondary Urca pair ^{25}Na $\leftrightarrow$ ^{25}Ne is responsible for the cooling. ^{25}Na, that is initially not abundant, has been produced by EC on ^{25}Mg, as soon as the continuously increasing electron density blocks the β^- decay back to ^{25}Mg (see middle right panel of Figure 6.10). Similar to ^{25}Mg $\leftrightarrow$ ^{25}Na, ^{25}Na $\leftrightarrow$ ^{25}Ne is an Urca pair, as well. This is because the Q value between ^{25}Ne and ^{25}F is already 13 MeV and hence once the EC on ^{25}Na is enabled ($Q_{\mathrm{gs}\rightarrow}\mathrm{gs} = -7.811$ MeV), the nucleus can only decay back via β^- decay. As this cooling sets in so briefly before the onset of EC on ^{20}Ne, the threshold density of this EC is affected, as well. In Section 6.1, we concluded that for low temperature conditions, the EC rate is mainly determined by the Q value of the dominating transition. But there is still a small temperature dependence of the actual threshold density for EC. This is related to the fact that the high-energy tail of the electron Fermi distribution function is smaller for low temperatures. Hence, also the ignition of oxygen is delayed to higher densities. Within the range of $X\left(^{25}\mathrm{Mg}\right)$ explored in our models, the ignition density varies between 9.94 and 9.98, i.e. by roughly 10%.

In the model series U2325, we explored the impact of including both Urca nuclei ^{23}Na and ^{25}Mg with equal fractions, ranging from $X\left(^{23}\mathrm{Na} = {}^{25}\mathrm{Mg}\right) = 0 - 0.01$. The results of this series of models are presented in the upper panel of Figure 6.15. In general, similar conclusions can be drawn, as for the series U23 and U25. The initial cooling history, this time caused by the Urca pairs ^{23}Na $\leftrightarrow$ ^{23}Ne and ^{25}Mg $\leftrightarrow$ ^{25}Na, is mostly deleted by the EC on ^{24}Mg. Afterwards, the evolution of the model series U25 and U2325 is nearly identical and the ignition density is varied only by the different abundance of ^{25}Na, which is limited by the initial value of $X\left(^{25}\mathrm{Mg}\right)$. As a result, we find the same dependency of the ignition density on $X\left(^{25}\mathrm{Mg}\right)$. The exact values are listed in Table 6.2. In order to illustrate the cooling effect due to the presence of Urca nuclei for the whole ONe core, we present their evolution also in a series of Kippenhahn diagrams in Figure 6.16, depicting the models U2325-1 to U2325-6. It is apparent that the Urca processes do not only affect the center of the core, but the whole core is cooled down—the stronger, the more abundant the Urca nuclei are. Summarizing the findings, based on the series of models U23, U25 and U2325, we can conclude that Urca processes prior to the onset of EC on ^{20}Ne (in particular involving the pair ^{25}Na $\leftrightarrow$ ^{25}Ne) do not only have an impact on the temporal evolution of the ONe core, but they also affect the ignition density of oxygen by up to 10%.

Notice that these findings are in disagreement with the conclusions in Gutiérrez et al. (2005), where the effects of the Urca pairs ^{23}Na-^{23}Ne and ^{25}Mg-^{25}Na were studied, as well. This has two reasons. The first reason is, that in this study, the EC and β decay rates of Oda et al. (1994) were used. As shown by Jones et al. (2013) and Denissenkov et al. (2015), these rates are missing the cooling effect of the Urca nuclei to a great extent. The second and even more important reason is that they did not include the secondary Urca pair ^{25}Na-^{25}Ne, that according to our study is the main reason why the ignition density of oxygen depends on $X\left(^{25}\mathrm{Mg}\right)$.

The last models that were simulated as part of the exploration of Urca processes in the AIC scenario, is the series `U2325Ne`. In these models, the abundance of ^{23}Na and ^{25}Mg are varied between $X\left(^{23}\mathrm{Na} = {}^{25}\mathrm{Mg}\right) = 0 - 0.01$, as in series `U2325`. At the same time, the ^{20}Ne second-forbidden transition was included, as described in Section 6.3.3. The results of this simulation are depicted in the lower panel of figure 6.15. The $T_c - \varrho_c$-diagram illustrates that—not surprisingly—the evolution of all models are identical to the model series `U2325`, until at a density of roughly $\log_{10}\left(\varrho/\mathrm{g\ cm^{-3}}\right) = 9.85$, the second forbidden $0^+ \rightarrow 2^+$ transition of the ^{20}Ne EC starts to become relevant and heats up the core, similar to the findings in Section 6.3.3. But due to the initial abundance of the ^{25}Mg, there is also some amount of ^{25}Na available. And as discussed before, the Urca pair $^{25}\mathrm{Na} \longleftrightarrow {}^{25}\mathrm{Ne}$, has a Q value of -7.811 MeV, corresponding to a threshold density of $\log_{10}\left(\varrho/\mathrm{g\ cm^{-3}}\right) = 9.9$. Consequently, especially for models with $X\left(^{25}\mathrm{Mg}\right) \gtrsim 5 \times 10^{-4}$, the Urca cooling can temporarily counter the heating due to EC on ^{20}Ne, at this moment purely driven by the forbidden transition. Of course, due to the continuous accretion, the much stronger EC on ^{20}Ne via the $(0^+ \rightarrow 1^+)$ transition sets in eventually and overwhelms the Urca cooling effect in all cases and increases the temperature to a point where oxygen gets ignited. Similar to the model series `Ne`, the much earlier onset of EC and heating via the second-forbidden transition, leads to an off center ignition of the deflagration wave. However, the radius of the off-center ignition appears not to be very sensitive to the abundance of ^{25}Mg, and lies between 49 and 60 km off-center for all models.

6.3.5 Network Size and Considered Nuclear Reactions

In Schwab et al. (2015), it was commented in a single sentence that using a larger reaction network compared to the fiducial model, does not significantly affect the outcome of the AIC of the ONe WD. As the core has already burned carbon but is too cold for the subsequent neon and oxygen burning stages, it is quite clear that thermonuclear reactions have no impact on the evolution of the core before the onset of oxygen burning, during the thermonuclear runaway. When the runaway proceeds in the core, due to EC on ^{20}Ne, the temperature is lifted from initially ≈ 0.4 GK (not considering Urca nuclei), first to temperatures, where neon burning sets in around 1.5 GK. But as this runaway proceeds so fast, oxygen burning is directly initiated along with it at slightly higher temperatures of appropriately 2 GK. Hence, even though strictly speaking, both neon and oxygen get ignited, the results of this runway is nevertheless called oxygen deflagration, as the fusion of oxygen liberates far more energy that neon burning, which proceeds mainly via α-capture (see 6.2).

In any case, while including a larger reaction network was reported to not play a role, in this section, it is our aim to clarify further uncertainties regarding the nuclear physics input. In Section 6.2, we discussed in great detail how neon and oxygen burning will be affected in a high-density situation, where, as in our models, most importantly ^{20}O becomes abundant due to double EC on ^{20}Ne via the chain $^{20}\mathrm{Ne} \rightarrow {}^{20}\mathrm{F} \rightarrow {}^{20}\mathrm{O}$. Based on typical abundances in SAGB models, we concluded that especially neon burning might proceed significantly more rapid than without ^{20}O. Hence, one part of this study will be to include those modified sets of reactions into the AIC models on ONe cores. Furthermore, we will test if the choice of reaction rate compilation plays a role. By default, MESA relies on the NACRE reaction database (Angulo et al., 1999), but it is also possible to change to the JINA Reaclib database (Cyburt et al., 2010) by using the following two inlist options: `set_rates_preference=.true.` and `new_rates_preference=2`.

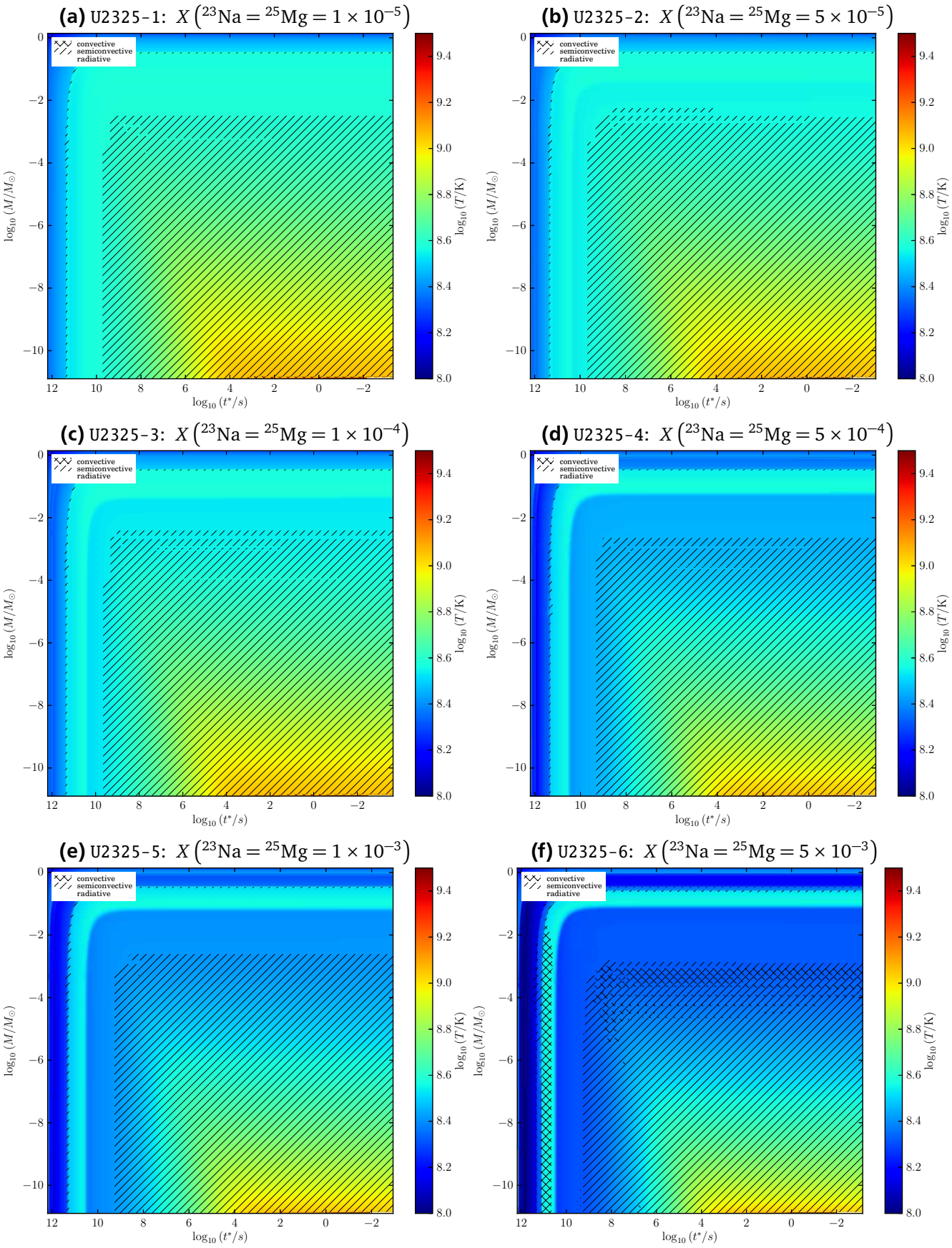

Figure 6.16: Kippenhahn diagrams of MESA AIC runs U2325-1 to U2325-6, as listed in Table 6.2. Shown is the temperature (T/K, color coded) as a function of enclosed mass ($M/M_\odot$) and time until oxygen ignition (t^*/s). Convective and semiconvective regions are indicated by crosses and dashes, respectively.

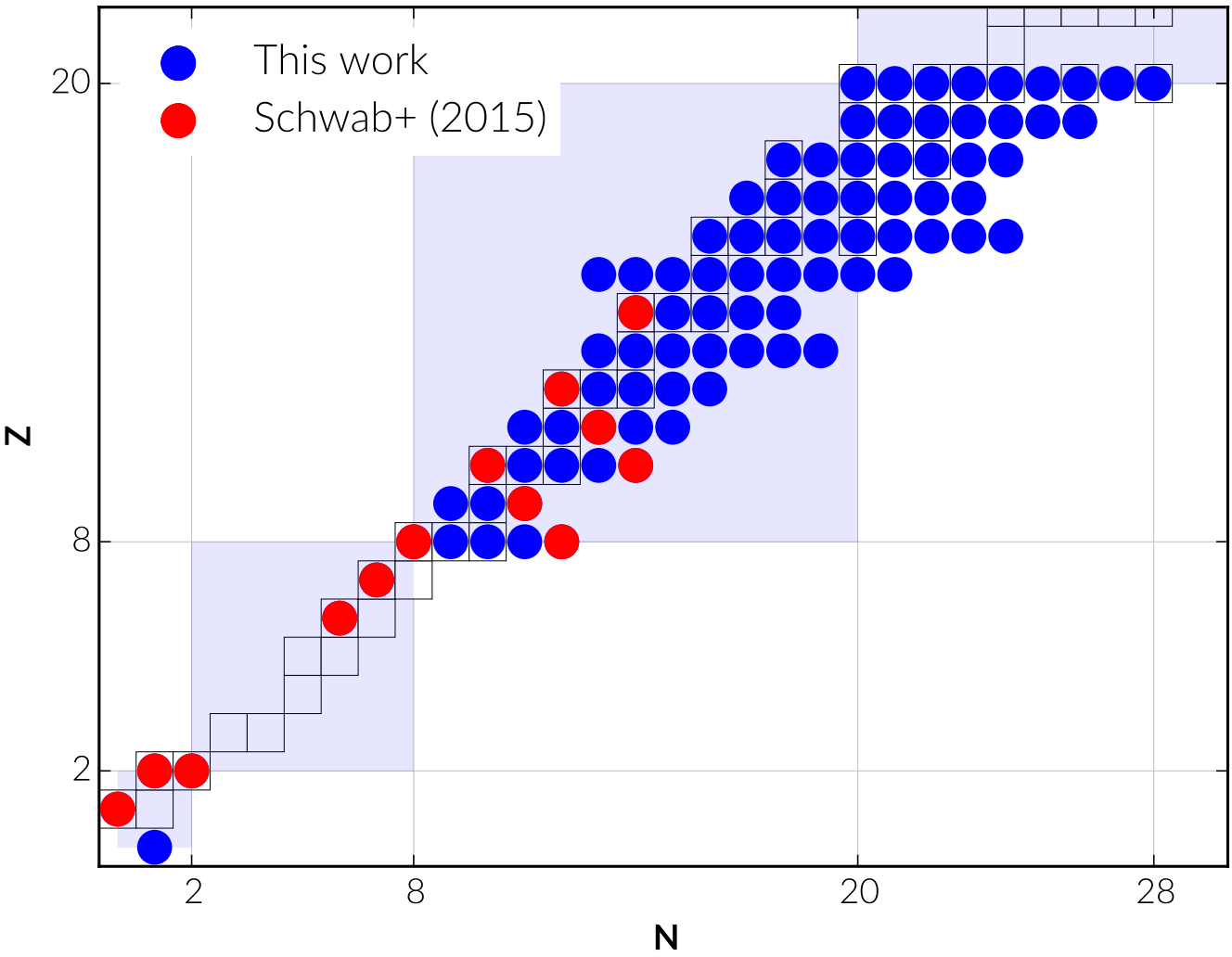

Figure 6.17: Nuclear reaction network used for modeling the AIC of ONe cores with MESA, part of a study regarding nuclear input for neon and oxygen burning. On the nuclear chart, the red dots indicate the nuclear species considered by Schwab et al. (2015) compared to the work in this thesis (nuclei indicated with blue dots). Notice that in the Appendix of Schwab et al. (2015), there is also a model used with a larger reaction network. Closed shells are indicated by blue shaded areas.

For the purpose of this study, the model series `Net` was created. Most of the models that are part of this series, use an extended network compared to the fiducial models in our study and also compared to the default model in Schwab et al. (2015). The two different network sizes, named "small" and "big" are illustrated in Figure 6.17. In total, the ten models of series `Net` probe different aspects of the possible uncertainties related to neon and oxygen burning reaction rates. The detailed setup can be found in Table 6.2. In model `Net-1`, NACRE is used along with a "big" network, while in model `Net-2`, JINA Reaclib is used along with a "big" network. In models `Net-3` to `Net-6`, the experimentally unknown reaction rate of $^{20}\mathrm{O}(\alpha,\gamma)^{24}\mathrm{Ne}$ is varied, as indicated by the labels in Figure 6.18. In models `Net-7` and `Net-8`, the additional oxygen fusion channels are included, as discussed in Section 6.2. In the latter case, also the regular fusion channel is replaced by the theoretically determined reaction rate. In model `Net-9`, JINA is used along with the "small" network and in model `Net-10`, NACRE is used with a small network, manually including the $^{20}\mathrm{O}(\alpha,\gamma)^{24}\mathrm{Ne}$ reaction rate.

The results of this study are presented in Figure 6.18. The left panel shows a $\log T_c$ - $\log \varrho_c$ -diagram of all models from the `Net` series along with the reference run `Res-2`. As one can easily see, the evolution of all models seems to be nearly completely unaffected by the different assumptions that were made about

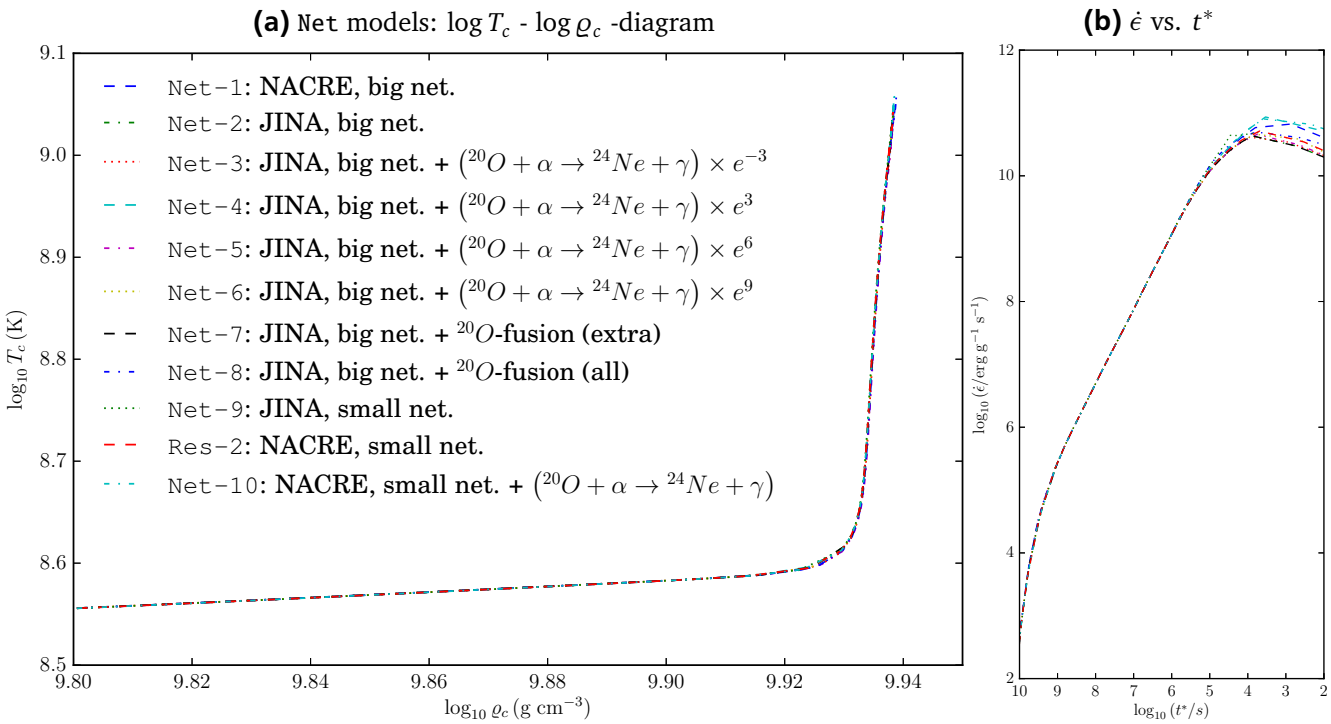

Figure 6.18: AIC of ONe core, log T_c - log ϱ_c -diagram and energy generation in `Net`-series models. The left panel illustrates the time evolution of the `Net`-series models. The right panel illustrates the energy generation ($\dot{\epsilon}$/erg g^{-1}s^{-1}) as a function of the time until oxygen ignition t^*. Details about the different models can be found in Table 6.2.

the nuclear input. Hence, we can confirm the conclusion from Schwab et al. (2015), that at least for the pre-ignition phase that captures the thermonuclear runaway, details of the thermonuclear reactions do not play a role. The right panel of Figure 6.18 displays the energy generation ($\dot{\epsilon}$/erg g^{-1}s^{-1}) rate of all nuclear reactions as a function of the time t^* until oxygen is ignited (in this case determined by a threshold temperature of 1.5 GK). It is visible, that the first differences in the energy production only start to appear very shortly before oxygen is ignited ($t^* \approx 10^4$ s) and even afterwards, the differences in $\dot{\epsilon}$ are not much larger than a factor of five. This observation supports the fact that the evolution of the ONe core is entirely unaffected by the differences of the models in the `Net` series.

On the other hand, this does not mean that the exact way the oxygen deflagration proceeds is unaffected by these uncertainties. Ultimately, the velocity of a deflagration is also determined by the magnitude and the rate at which energy is liberated by the flame (of course, many other aspects play a role as well). It could be interesting to investigate this in the future.

6.3.6 Semiconvection

In Section 2.3.2, the different types of convective regimes were introduced. It was pointed out that a semiconvective regime is characterized by a medium that is unstably stratified in temperature (i.e. Schwarzschild unstable), but becomes stable to convection in the presence of a mean molecular weight gradient (i.e. Ledoux stable). In the seminal work by Kato (1966), it was derived that such a type of stratification can never be entirely stable in the presence of a heat diffusivity different from zero. The perturbation of a fluid element in a semiconvective regime would result in an oscillatory behavior, whose amplitude grows continuously, due to the slight temperature change of the perturbed mass element caused by heat diffusion. In Kato (1966) this behavior is called overstable convection. In Section

2.3.2, using the terminology from Kippenhahn & Weigert (1990), this instability was called vibrational instability in contrast to the "regular" dynamical instability.

In Section 6.1, it was also pointed out that if the growth timescale of such oscillations in a semiconvective regime is short, the composition gradient will quickly be erased and the region becomes convective. On the other hand, if these oscillations grow very slowly, nearly no mixing will take place. These circumstances would have the same outcomes as assuming either the strict Schwarzschild or strict Ledoux criteria for convection, respectively. In the initial work on the final evolution of degenerate ONe cores (evolving toward ECSN) by Miyaji et al. (1980), ignoring the stabilizing mean molecular weight gradient, convection is developing in the core prior to the ignition of the oxygen deflagration, triggered by energy production due to ECs on ^{24}Mg and ^{20}Ne. Mochkovitch (1984), and subsequently Miyaji & Nomoto (1987), showed that if one considers the stabilizing effect of the stratification in mean molecular weight produced by the ECs alongside the steep temperature gradient (i.e. Ledoux criterion), the core will be stable to convection. The impact of the choice of convection criterion on the ignition density of the oxygen deflagration has since been described in several works. As already mentioned, Figure 6.4 shows the ignition densities found in various simulations from the literature. With the exception of Takahashi et al. (2013), all studies adopting the Ledoux criterion for convection find ignition densities below 10^{10} g cm^{-3}. The key difference is that Takahashi et al. (2013) also included an approximation for semiconvective mixing processes. If, as for example in Miyaji et al. (1980), the Schwarzschild criterion for convection is assumed, this results in a convective core that delays the ignition of oxygen to a density around $\approx 2 \times 10^{10}$ g cm^{-3}. As pointed out by Jones et al. (2016), performing 3D hydrodynamical simulations of the oxygen deflagration, ignition densities around 2×10^{10} g cm^{-3} result in a core collapse, while densities around 10^{10} g cm^{-3} result in a thermonuclear explosion.

Treatment of Convection in AIC Models

In this Section, we will explore the sensitivity of the AIC models to the treatment of convection (considering in particular semiconvection). The MESA runs conducted for this purpose are collated in model series `Semi`. In MESA, semiconvection is treated as a time-dependent diffusive mixing process (see Paxton et al., 2013, Chapter 4), following the description of Langer et al. (1983). It is given by Equation (2.122) and contains a dimensionless efficiency parameter α_S. Typical values of α_S range between 10^{-3} and 1 in the literature. By default, all of our models assume the Ledoux criterion for convection and $\alpha_S = 0$. As indicated by Table 6.2, the series `Semi` uses the "medium" resolution settings, thus the reference run for this series is `Res-2`. In model `Semi-1`, the Schwarzschild criterion for convection is used instead of Ledoux. In the models `Semi-2` - `Semi-6`, we employ the Ledoux criterion for convection at the same time using different values for α_S different from zero, ranging somewhere in between the canonical values found in the literature from $\alpha_S = 10^{-3}$ to 10.

The results of this series of models are displayed in Figure 6.19, a $\log T_c$ - $\log \varrho_c$ -diagram illustrating the evolution of the model series `Semi`. For reference, we also ran one model assuming the Schwarzschild criterion for convection, because based on the previous discussion, we would expect Schwarzschild convection to denote the limiting case of very efficient energy transport in the semiconvective regime. In this case, the evolution is significantly altered, because EC on ^{24}Mg trigger core convection. This is also illustrated in the top left panel of Figure 6.20 that shows a Kippenhahn diagram of model `Semi-1`. It is visible that approximately 10^{11} s before the ignition of oxygen, the core becomes convective. Because of the efficient heat transport, the whole inner part of the core has basically the same temperature and oxygen is ignited simultaneously. Surprisingly, different from what has been found by previous publications, the ignition density is much lower than 2×10^{10} g cm^{-3}, as visible in Figure 6.19. Additionally, the core appears to expand again after oxygen has been ignited. But it is questionable, whether this phase can be captured properly by MESA.

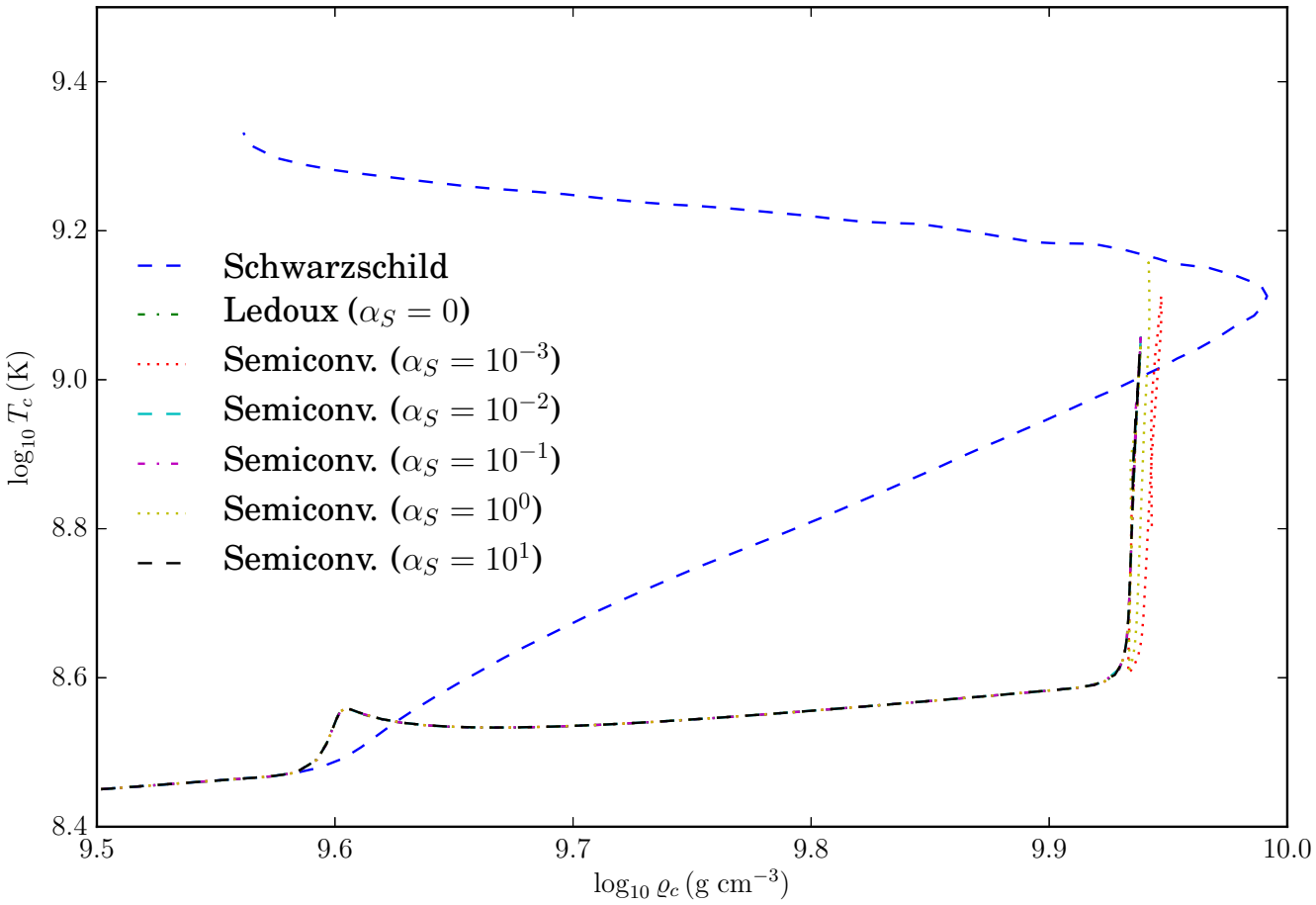

Figure 6.19: AIC of ONe core, $\log T_c$ - $\log \varrho_c$ -diagram, sensitivity to the treatment of convection.

Regarding the models including semiconvection, it is clearly visible that even for very efficient semiconvection ($\alpha_S = 10$), the corresponding model evolves identical to the case of $\alpha_S = 0$. Hence, we can confirm the timescale arguments (i.e. not enough time for overstable convection to develop) made in Schwab et al. (2015), meaning that semiconvection, at least in the usual diffusive approximation, has no impact on the evolution of degenerate ONe cores. While the evolution of the different models in the $\log T_c$ - $\log \varrho_c$ -diagram seems to be nearly identical, some differences become visible when looking at panels b) to f) of Figure 6.19. For some values of α_S different from zero (panels b) and e), the core appears to enable convection around 10^9 s prior to the oxygen ignition. But in both cases, this convection is restricted to the innermost few kilometers of the core, whereas in the Schwarzschild case, nearly the whole core becomes convective (notice the logarithmic mass scale in Figure 6.19). Even though it is unclear why there seems to be no clear trend of the occurrence of this limited convective behavior with varying α_S, in none of the cases, the spatially very limited convection zone in the code has any influence on the evolution of the different models. For this reason, they lie on top of each other in the $\log T_c$ - $\log \varrho_c$ -diagram in Figure 6.19. As a concluding remark, it is clear that a further exploration of the uncertainties related to the possible occurrence of overstable convection prior to the ignition of oxygen has to go beyond the standard assumption where this complicated process is approximated by diffusion.

Kato's Linear Stability Analysis

In this section, we want to make use of the technique from Kato (1966) called linear stability analysis. This analysis allows us to determine an approximate growth rate of the oscillatory or overstable convec-

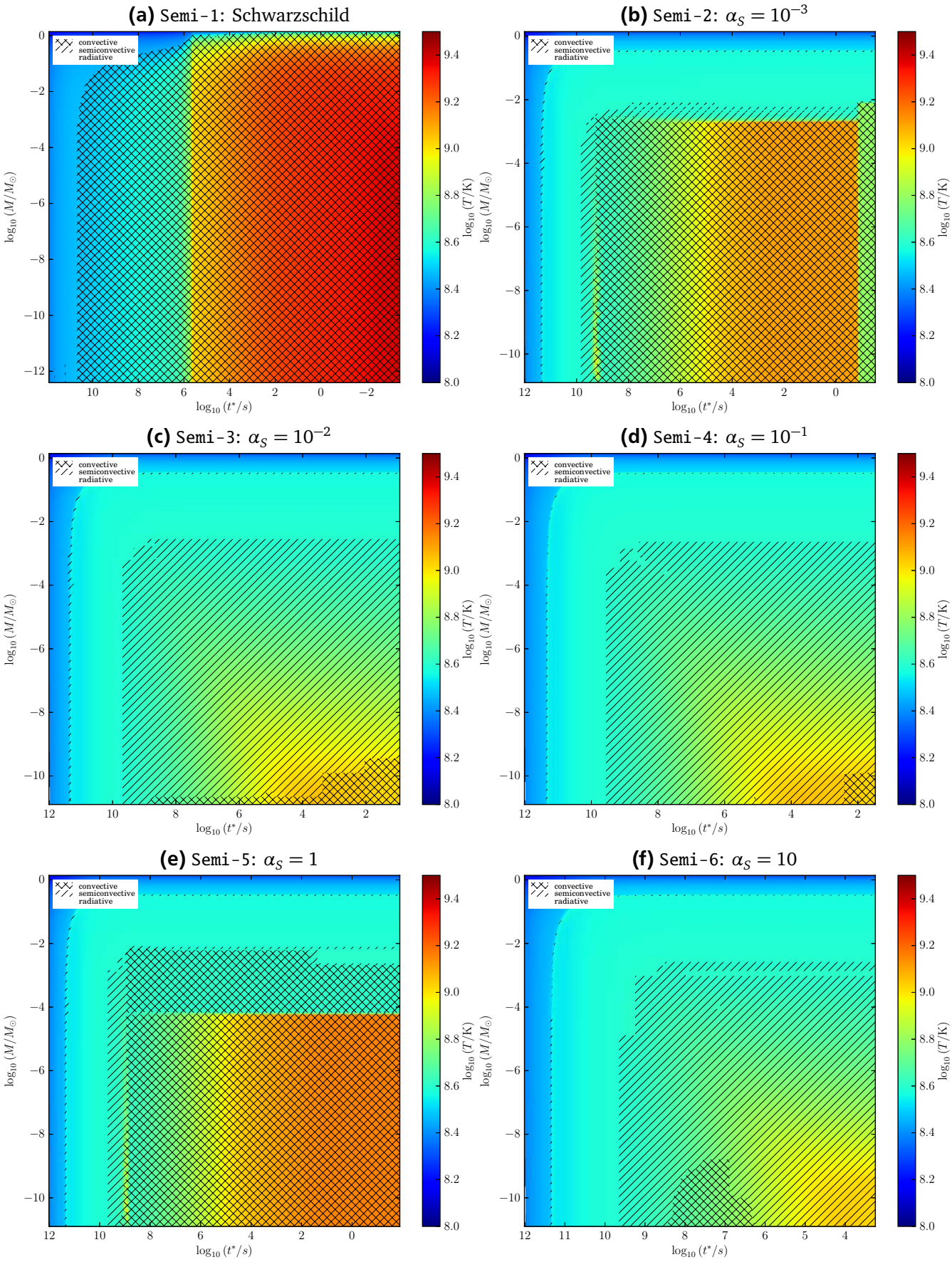

Figure 6.20: Kippenhahn diagrams of MESA AIC runs `Semi-1` to `Semi-6`, as listed in Table 6.2. Shown is the temperature (T/K, color coded) as a function of enclosed mass ($M/M_\odot$) and time until oxygen ignition (t^*/s). Convective and semiconvective regions are indicated by crosses and dashes, respectively.

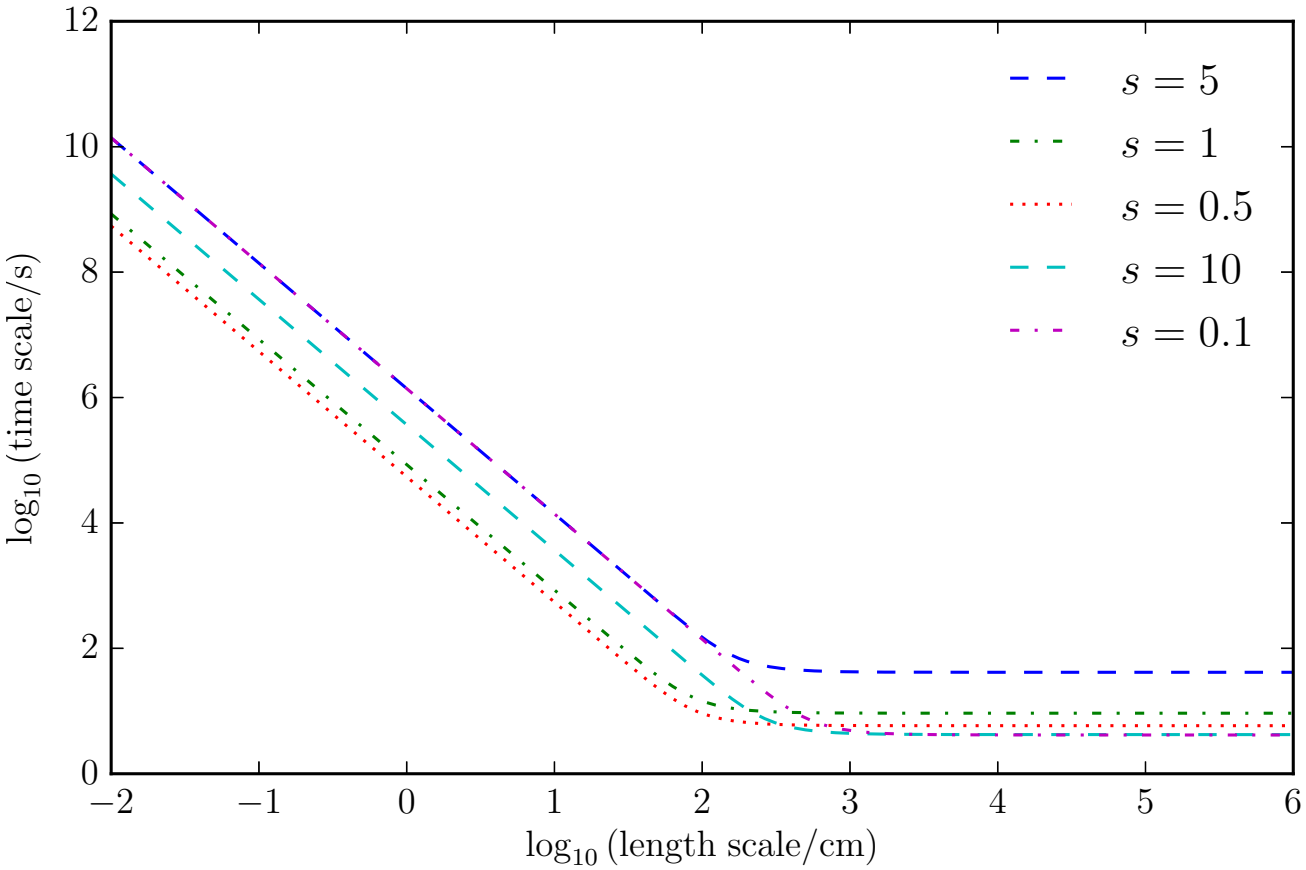

Figure 6.21: Growth time scale (in seconds) of overstable convection in an ONe core during EC on ^{20}Ne as a function of length scale (in centimeter), following the linear stability analysis of Kato (1966).

tion as it is speculated to occur in degenerate ONe cores due to EC on ^{24}Mg and ^{20}Ne. While the details of this analysis are discussed at length in Kato (1966), we will only sketch it here briefly. Kato assumed that the form of the fluid disturbances is given by:

$$\exp\left[nt + i\left(k_x x + k_y y + k_z z\right)\right], \tag{6.27}$$

where k_x, k_y and k_z are the components of the wavenumber in the direction of the three spatial dimensions x,y and z. t denotes the time. Then, the growth timescale τ of the oscillatory convection is given by the reciprocal of the real part of n:

$$\tau \approx \frac{1}{\mathrm{Re}(n)} = \frac{\varrho_0 c_P}{\eta k_z^2}. \tag{6.28}$$

The radiative conductivity K is defined as in Equation (2.79):

$$K = \frac{4acT^3}{3\kappa\varrho_0}. \tag{6.29}$$

ϱ_0 is the density of the stratification, c_P the specific heat at constant pressure and κ the total effective opacity. Then η is defined as the dimensionless growth rate or frequency

$$\eta = \frac{n}{Kk_z^2}\varrho_0 c_P. \tag{6.30}$$

It can be found by solving the following equation:

$$\eta^3 + \left(1+s^2\right)\eta^2 + \frac{s^2}{1+s^2}\left(\bar{W}-\bar{R}\right)\eta + s^2\bar{W} = 0. \tag{6.31}$$

The quantity s is defined by

$$s = \frac{\left(k_x + k_y\right)^{1/2}}{k_z}. \tag{6.32}$$

A priory, all values of s (i.e combinations of wave amplitudes) can in principle occur, but it is the combination of k's, which causes the amplitude of the oscillatory convection to grow the fastest, that will prevail and in which one is ultimately interested. In Kato (1966, Figure 2) the fastest growth was obtained for roughly $s = 1$. Now, it is convenient to write $\bar{W}$ and $\bar{R}$ (Equation 21 Kato, 1966) in terms of variables that can easily be obtained from the output of a typical stellar evolution code. Consequently, they are given by:

$$\bar{W} = \frac{\varrho_0}{P}\left(\frac{c_P}{K}\right)^2 \nabla_\mu k_z^{-4}, \tag{6.33}$$

and

$$\bar{R} = \frac{\delta}{\varphi} P \varrho_0 \left(\frac{c_P}{K H_P}\right)^2 (\nabla - \nabla_{ad})\, k_z^{-4}, \tag{6.34}$$

where H_P is the so called pressure scale height:

$$H_P = -\frac{dr}{d\ln P} \tag{6.35}$$

and the other symbols have their usual meanings. Repeating what we introduced in Chapter 2, the other quantities are given by:

$$\nabla_\mu = \frac{\partial \ln \mu}{\partial \ln P}; \quad \delta = -\left(\frac{\partial \ln \varrho}{\partial \ln T}\right)_{p,\mu}; \quad \varphi = -\left(\frac{\partial \ln \varrho}{\partial \ln \mu}\right)_{p,T}; \quad \nabla = \frac{\partial \ln T}{\partial \ln P}; \quad \nabla_{\rm ad} = -\left(\frac{\partial \ln T}{\partial \ln P}\right)_S. \tag{6.36}$$

The component of the wavenumber in the z direction k_z can be varied, solving Equation (6.31) for each value in order to get a timescale by using Equation (6.28). Notice again that only the wavenumber that yields the shortest growth timescale of the oscillatory convection is of interest here. The length scale of the oscillation mode is then given by $2\pi k_z^{-1}$. The growth time scale of semiconvection in the ONe core during the ^{20}Ne EC phase is plotted in Figure 6.21 as a function of length scale for a range of values of s (defined in Equation (6.32)). On length scales larger than a few meters, the overstable convection grows on the same time scale for any length scale. For length scales smaller than about one meter, the time scale increases as a power law with the length scale, following $\tau \propto l^{-4}$. The lines in Figure 6.21 are the result of applying Kato's analysis (Equations (6.28) and (6.31) - (6.34)) to a region of a stellar model in which ^{20}Ne has been activated, about 2 years prior to the thermonuclear runaway. The model that served as a basis for this analysis was the high-resolution model `Res-4`. According to the AIC calculations, the semiconvective region is a sphere of roughly 60 km in radius, at the center of the star. This should allow for the growth of the overstable convection at all of the length scales shown in Figure 6.21. Based on this analysis, one would expect the overstable convection to grow on a timescale of around $10-100$ s.

Unfortunately, it is not clear what the exact outcome of such convection would be and over which radii it would extent in the star. Also because the answer that we obtain from Kato's analysis is quite different from the findings in Section 6.3.6, a more conclusive answer can probably be only obtained by performing 3D hydrodynamic simulations of such a stratification. A readily available computer code that could be suitable for this task, is the low mach number hydrodynamic code MAESTRO (2017).

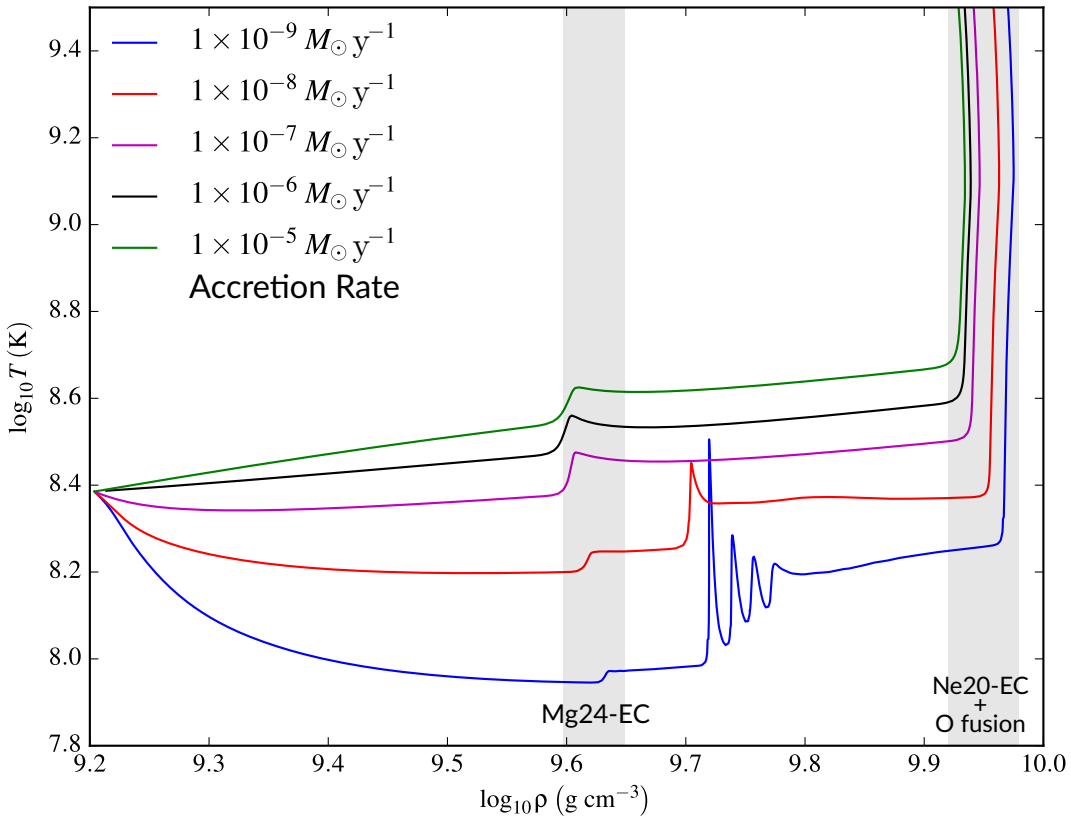

Figure 6.22: AIC of ONe core, $\log T_c$ - $\log \varrho_c$ -diagram that illustrates the dependency of accretion rate $\dot{M}$. The constant accretion rate is varied among the set of models between 10^{-9} and $10^{-5}\ M_\odot\ \mathrm{yr}^{-1}$. The occurrence of ECs on ^{24}Mg and ^{20}Ne are marked by gray shaded areas. EC on ^{20}Ne rises the temperature above the threshold for oxygen fusion which initiates the thermonuclear runaway.

6.3.7 Thermonuclear Runaway

Schwab et al. (2015) studied how the accretion rate $\dot{M}$ affects the evolution of the ONe core. Remember that in those, as well as in our simulations, the accretion rate is a free parameter which can be varied within some reasonable limits, inferred for example from detailed studies of the late time SAGB star evolution. In this Section, we will follow along the same lines and construct several models with different accretion rates, ranging from $\dot{M} = 10^{-9}\ M_\odot \mathrm{yr}^{-1}$ to $\dot{M} = 10^{-5}\ M_\odot \mathrm{yr}^{-1}$. In the model series `Acc`, we vary the accretion rate while leaving all other input settings identical to the fiducial high-resolution model `Res-4`. Additionally, we suppress the occurrence of convection during the onset of the deflagration as described in Section 6.3.4. Before, convection is absent from the ONe anyway, because the Ledoux criterion for convection is applied. It is not the goal of this study to show that the accretion rate influences the ignition density of oxygen, as this was already done by Schwab et al. (2015). Rather, we would like to generate models with a very high central resolution, in order to use them in studies that explore the oxygen deflagration, as we will do in Section 6.4. In this sense, the variation of the accretion rate simply provides a “natural” way of obtaining models with different ignition densities.

The results of this survey are presented in Figure 6.22. Not surprisingly, we find that lower accretion rates lead to higher ignition densities and vice versa. The reason was already explained in Section 6.3.4 in the context of Urca cooling. When the temperature is lower because the accretion rate is also small, then the threshold density for EC on ^{20}Ne is delayed to higher temperatures. Consequently, also the ignition of oxygen occurs at larger densities. More importantly, by choosing the highest resolution possible, we wanted to explore how well MESA is able to resolve the AIC model in the very center of the core, where the thermonuclear runaway occurs. Figure 6.23 shows temperature profiles of the innermost

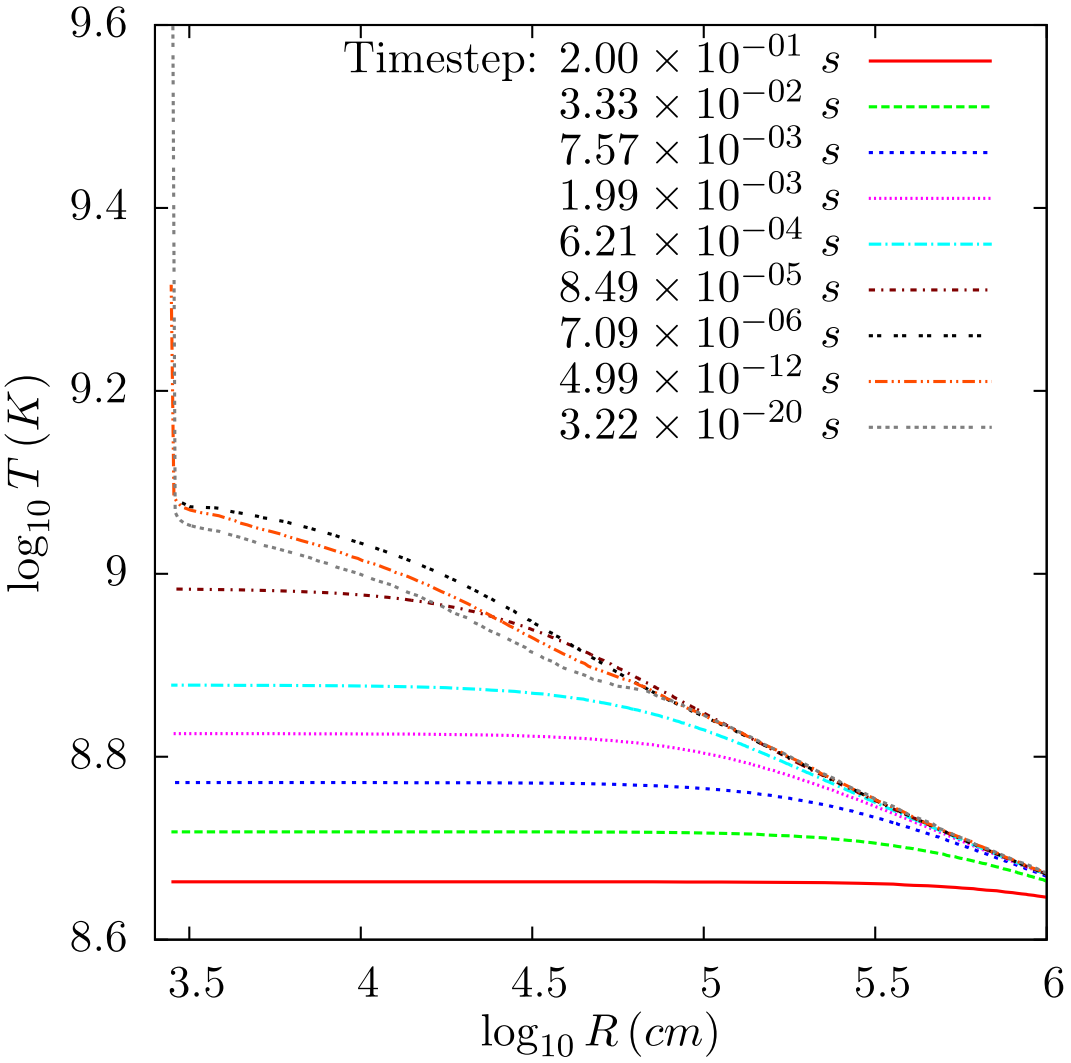

Figure 6.23: Radial temperature profiles of ONe core AIC model with an accretion rate of 10^{-6} $M_\odot$ yr^{-1} and suppressed convection. Shown are selected profiles during the last phase of evolution until the thermonuclear runaway ensues. They are labeled according to the current timestep in the computation which is equal to the nuclear burning timescale during that phase.

part of the ONe core of the high-resolution model with an accretion rate of $\dot{M} = 10^{-6}$ $M_\odot$ yr^{-1} (model `Acc-7`). Notice that the profiles are chosen to be consecutive in time and they are labeled according to the current timestep in MESA. The main conclusion from Figure 6.23 is that MESA is capable to resolve the thermonuclear runaway, both in time and in spatial coordinates, assuming that no convection occurs. In the corresponding model, the mass of the central zone is only 10^{-13} $M_\odot$ and it only extends to a radius of 25 meters. Nevertheless, in the absence of convection, the runaway will occur only in a single zone (here the central one) and the calculation only stops once the central zone is burned into NSE. From this moment on, the evolution of the system is determined by the oxygen deflagration that cannot be modeled by a stellar evolution code. The main reason is that even in the laminar flame case, the width of the flame is extremely narrow, on the order of centimeters, and can hence impossibly be resolved by MESA.

The main purpose of this study was to create a set of "realistic" ONe core models with different ignition densities that can later be explored in detail, with regard to the question of what the critical density between collapse and thermonuclear explosion is. In Section 6.4, we will present preliminary results of such simulation with the CCSN code AGILE-IDSA.

6.4 Simulation of the Oxygen Deflagration in 1D

In this section, it is our goal to simulate the oxygen deflagration that is occurring in mass-accreting ONe cores, triggered by EC on ^{20}Ne. For this purpose, we want to utilize a hydrodynamic code that is able to describe the possible gravitational collapse of the star and the subsequent CCSN explosion. Our code of choice for this study is the implicit shock-capturing spherically-symmetric general-relativistic hydrodynamic code AGILE-IDSA (Liebendörfer et al., 2002). In Möller (2013), we confirmed that ONe(Mg) core progenitors explode in one-dimensional neutrino-driven supernova models, with the help of AGILE-IDSA. In this study, we used the canonical 8.8 $M_\odot$ ONe(Mg) core progenitor by Nomoto. In Section 6.4.1, we will present those findings briefly as they serve as a proof of concept for the study of the oxygen deflagration. The initial ONe core model for our study will come, as pointed out before, from the high-resolution AIC models done with MESA that were presented in Section 6.3.7.

In the light of the first multidimensional hydrodynamic simulations of the oxygen deflagration by Jones et al. (2016), we want to point out that our complementary approach of studying the deflagration in a 1D CCSN code, will hopefully give valuable input to the significantly more expensive 3D simulations. For example many models with different ignition densities can be studied at the same time. This could be a valuable addition to the simulations by Jones et al. (2016) that showed that the critical ignition density that marks the difference between collapse and thermonuclear explosion, lies inside the physically reasonable values for the ignition density, meaning that the outcome is not certain. A study like Jones et al. (2016) is of course able to treat the deflagration wave in a much more realistic approach and should be considered as the "gold standard" in terms of turbulent flame physics, as it uses a very sophisticated method to calculate the turbulent flame velocities. Nevertheless, it lacks other important input physics, as this study was performed with a numerical code whose main purpose is to simulate a the deflagration wave in WDs very accurately. For example, it is not suited to simulate even the collapse phase of a stellar core. The explosion of a CCSN proceeds always as a shock. This feature requires the use of specialized shock-capturing hydrodynamics. Furthermore, also an EoS for matter around nuclear densities and a description of neutrino-matter interaction are required in order to describe CCSNe. On the other hand, a CCSN code lacks the description of (subsonic) deflagration physics.[15]

Of course, there have been also several studies in the past that studied the oxygen deflagration in 1D, relying on a parametric description of the flame (see e.g. Nomoto & Kondo, 1991; Isern et al., 1991; Takahashi et al., 2013), but none of them simulated the full collapse of the star to NS densities, in case it exploded as ECSN.

Weak reactions are not only important prior to the ignition of the flame but also afterwards. Once the material behind the flame has been burned into NSE, the EC rates on the now prevalent iron-group nuclei are significantly higher compared to *sd*-shell nuclei and will start to deleptonize the core on very short timescales on the order of a second. In a CCSN simulation, this phenomenon occurs as well. However, in this case, it is sufficient to use the tabulation by Juodagalvis et al. (2010) that only considers EC processes. This simplification is acceptable for the study of CCSNe (i.e. always assuming that the collapse occurs), because the collapse proceeds sufficiently fast to not make the (reverse) β^- rates relevant. However, in the close case of a potentially collapsing ONe core, the whole deflagration phase lasts around $2-3$ seconds and in that period of time, β equilibrium can be easily reached. This equilibrium can obviously only be described if also β^- decays are considered. Consequently, the usual tabulation of Juodagalvis et al. (2010) cannot be used.

For the numerical models in this section, the CCSN code AGILE-IDSA (Liebendörfer et al., 2009) is used. The basis for the AGILE-IDSA is the hydrodynamics code AGILE (Liebendörfer et al., 2001, 2002), an implicit code for spherically-symmetric general-relativistic hydrodynamics in comoving coordinates including an adaptive grid. The purpose of the adaptive grid is to reduce the number of required radial

[15] In fact heat transport by radiation and electrons is usually neglected entirely.

zones for the same average level of precision. This means that resolution is shuffled dynamically to zones with steep gradients of relevant physical quantities. In order to use the hydrodynamic code in CCSN simulations, it is combined with an algorithm that solves the neutrino transport problem. The IDSA is an approximate radiation transport scheme that is available open-source (IDSA, 2017). In the IDSA, the neutrino distribution function is decomposed into a trapped and a free-streaming component based on the local mean-free path, so that adequate approximations can be used in both regimes. In regions where neutrinos have a short mean free path (i.e. high matter densities) they are considered to be trapped. Then the diffusion limit is applied. In the optically thin regime, ray tracing is used to describe the propagation of the neutrinos. Since its development the IDSA scheme was used in several published supernova simulations. Notable results could be achieved for example by Suwa et al. (2010, 2013) that performed two-dimensional simulations and successfully obtained explosions. In the IDSA that we use, EC and PC on nucleons and reverse reactions and isoenergetic scattering on nucleons are considered.

Before we discuss the modeling of the oxygen deflagration with AGILE-IDSA, we will exemplify the capabilities of the code by simulating the canonical ONeMg-core ECSN progenitor of Nomoto in Section 6.4.1. Then, in Section 6.4.2, we will introduce the advanced setup that considers all the necessary physics that have to be included for the modeling of the oxygen deflagration.

6.4.1 Simulating Electron-Capture Supernovae with "AGILE-IDSA"

Low-mass stars between 8 and 10 $M_\odot$ are of special importance for the understanding of CCSNe as they explode in spherically symmetric models. The reasons for this originates mainly in the special stellar evolution of the SAGB stars (see Section 5.4.2). The most relevant CCSN progenitor in the low-mass range of stars is the 8.8 $M_\odot$ ONe(Mg) progenitor by Nomoto (1987). As recent simulations show, the star explodes in spherically symmetric models, applying a sophisticated Boltzmann neutrino-transport scheme, including a large variety of charged-current and neutral-current weak interactions for all three neutrino flavors. In this context it is worth mentioning the recent studies done by Kitaura et al. (2006); Janka et al. (2008) and Fischer et al. (2010). The latter used Nomoto's ONe(Mg) star to simulate collapse, bounce, explosion and the neutrino-driven wind phase at once, using the AGILE-BOLTZTRAN code. In (Möller, 2013), we use for the first time the 8.8 $M_\odot$ ONe(Mg) core progenitor by Nomoto to perform simulations with AGILE-IDSA.

For the study of ECSNe, additional physics have to be included compared to the simulation of a FeCCSNe, where the whole collapsing core is already consisting of iron-group nuclei. By default, the AGILE-IDSA code uses the Lattimer-Swesty EoS (high-density high-temperature nuclear EoS that implicitly assumes NSE) in form of a table. But as the ONe core progenitor is not yet fully in iron-group NSE, we have to additionally implement a low-density EoS, where we choose the Helmholtz EoS. It is used for temperatures below 0.5 MeV and nuclear burning is treated in an effective way by instantaneous shell burning. In the progenitor model of Nomoto, the innermost part of the core is in NSE while the out parts are mostly oxygen and neon. Of course, the oxygen deflagration would occur in this progenitor, as well and burn the rest of the core into NSE during the collapse. But in ECSNe studies, this flame is usually not considered. Rather, the burning front "propagates" purely by compressional heating. Because the width of the flame is in the centimeter regime (Timmes & Woosley, 1992), it cannot be resolved in any case. Therefore in 1D, such a flame has to be described in a parametric way, as we will do in Section 6.4.2. But for the simulation that we present here, i.e. a standard ECSN, this is not of any concern.

Even though we assume that the flame propagates by compression, we still have to account for the energy generation during the collapse, when oxygen and neon are transformed into iron-group nuclei, thereby releasing ≈ 1 MeV/nucleon. Conveniently, the Lattimer-Swesty EoS already assumes NSE. In this case, the equilibrium state is readily computed by the Lattimer-Swesty EoS which approximates the

composition in NSE by calculating average mass and charge of a single species of heavy nuclei. This means that once NSE temperatures are reached about 1 MeV of binding energy per baryon are released into the system and increase the temperature. By computing the new temperature for the new value of the internal energy, this will always result in an increase in temperature between 0.3 and 1.2 MeV. This idea of instantaneously burning the initial progenitor composition into NSE ("flash") is described by Rampp & Janka (2002). For this approach we choose the same temperature criterion as for the transition between both EoSs of 0.5 MeV. If we look at the onset temperatures for the relevant nuclear burning reactions (see e.g. Arnett, 1996, p. 163), this seems to be a good approximation. Thus at 0.5 MeV, baryonic matter would consist mostly of iron-group nuclei and indeed for these conditions the Lattimer-Swesty EoS computes the mass of the average heavy nucleus to be between 55 and 56. This shows that the burning scheme computes at least the correct release of binding energy inside a mass shell, while of course the dynamics of the flame are not reproduced correctly.

Simulation of Nomoto's canonical ECSN

Notice that the progenitor that Nomoto's progenitor that we use in our ECSN simulation, is already evolved a little bit towards the core collapse compared to the last stage of stellar evolution. Hence there is already a certain mass fraction of nuclei burned into NSE which we assumed to be iron. Apart from that the core consists mostly of neon, oxygen and magnesium. Further outside the core, there is also carbon from shell burning. Above 1.37 $M_\odot$ the progenitor is enclosed by a hydrogen envelope ($X_{\mathrm{He}} = 0.15$, $X_{\mathrm{H}} = 0.85$). However it is not possible to consider the whole hydrogen-rich envelope (2.6 $M_\odot$ masses including the core) in the CCSN simulation, as the densities go down to 10^{-8} g cm^{-3}. A detailed study of Nomoto's 8.8 $M_\odot$ progenitor and how the hydrogen envelope is attached to the core, can be found in Janka et al. (2008). By comparing the progenitor profiles of the 8.8 $M_\odot$ progenitor in comparison with the ones of more massive stars, we can already understand why it is more difficult for the heavier stars to explode in spherically-symmetric models whereas the 8.8 $M_\odot$ progenitor is expected to do so for the simulation with AGILE-IDSA. The density profile of the 8.8 $M_\odot$ progenitor is much steeper than the one of the iron-core stars. Exactly this feature makes it easier for the shock wave to propagate away from the central regions of the star once the density drops by many orders of magnitude (see Figure 5.6).

In agreement with previous studies, we obtained a successful explosion for the 8.8 $M_\odot$ ONe(Mg) core progenitor. In Möller (2013), we compared our results in detail with a simulation performed with the AGILE-BOLTZTRAN code. This numerical model is based on the same hydrodynamics code AGILE, but is relying on spectral three-flavor Boltzmann neutrino transport. In general we find good agreement. However, we find shorter a explosion timescale and also a substantially lower explosion energy of only 10^{48} erg. The results of our simulation are displayed in Figure 6.24. Even though this specific plot and also the specific simulation were performed specifically for this section, a nearly identical simulation was presented in far more detail in Möller (2013). Here, it is simply important to point out that, ignoring the oxygen deflagration, it is possible to obtain a self-consistent explosion of collapsing ONe cores with AGILE-IDSA, despite having to use a lot of simplifications like 1D hydrodynamics and an approximate neutrino transport scheme. As one can expect from a progenitor without an extended envelope, the explosion is rather prompt. In Figure 6.24, one can see that the shock travels through the star in about 0.1 s, measured after the core bounce that creates the detonation. Afterwards, the evolution of the displayed mass shells occurs, as expected and ultimately some of the outer layers will be accelerated to infinity and compose the ejecta of the ECSN. The light blue line in the same figure illustrates the position of the PNS surface (density threshold of 10^{13} g cm^{-3}). One can see that after 500 ms, the surface of the PNS has already contracted to approximately 30 kilometers.

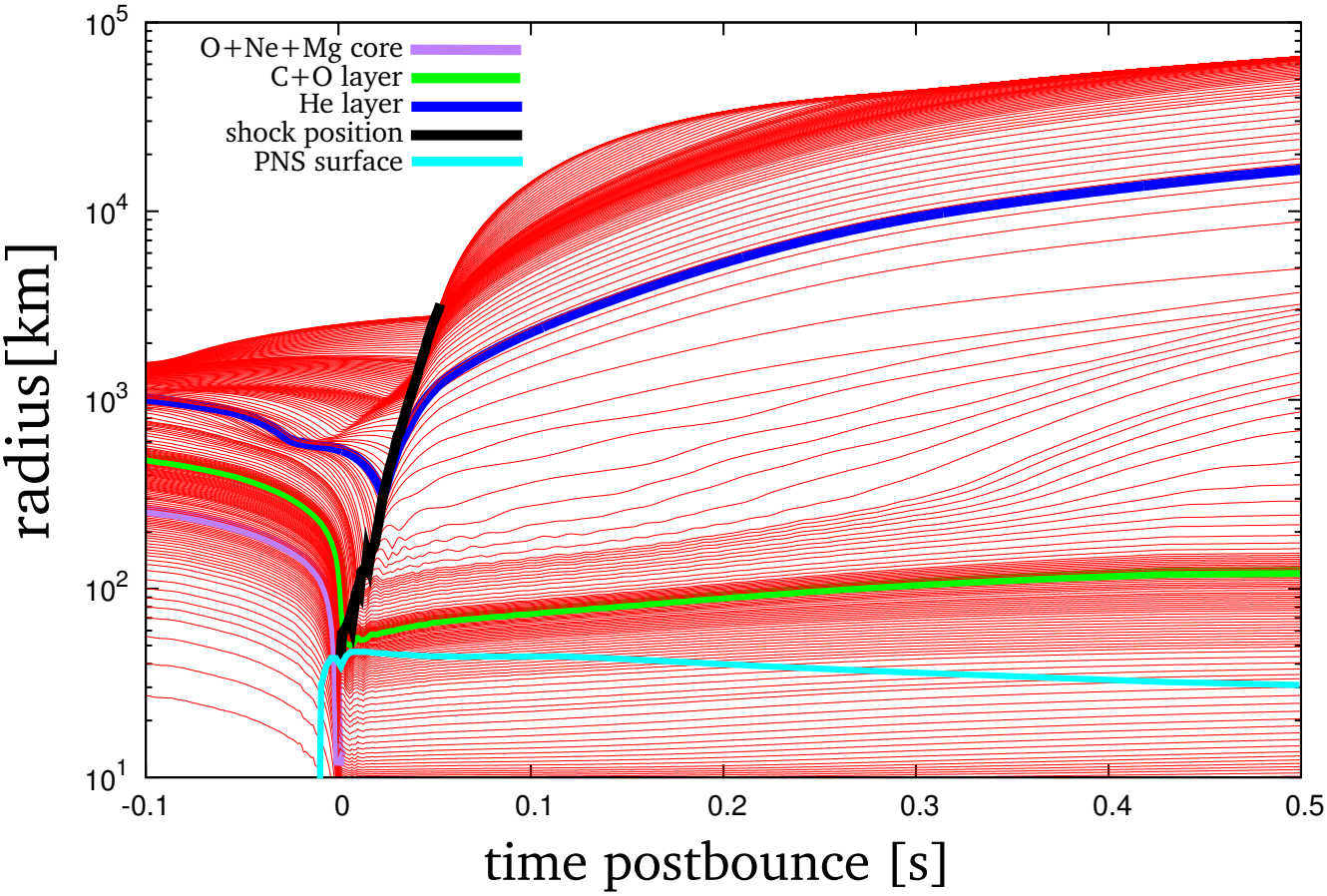

Figure 6.24: Outcome of the ECSN simulation with AGILE-IDSA, using the canonical 8.8 $M_\odot$ ONe(Mg) progenitor from Nomoto (1984). This figure illustrates the evolution of the ECSN, showing the simulated mass shells (red lines) as a function of radius (r/km) and the time post-bounce (t/s). Additionally, the surface of the ONe(Mg) core is indicated by a purple line, the CO layer by a green line, the He layer by a dark blue line, the shock position by a black line and the PNS surface by a light blue line.

6.4.2 Advanced Setup for Oxygen Deflagration

As already mentioned, the ECSN simulation in Section 6.4.1 demonstrates that with the "standard" CCSN setup plus the inclusion of a low-density EoS and "flashing" the composition into NSE due to compressional heating, it is possible to simulate ECSNe with AGILE-IDSA. It should be pointed out again, that in none of the standard simulations, the oxygen deflagration is considered and one focuses either on the ECSN supernova simulation or one simulates the oxygen deflagration separately. Studying both aspects of the same astrophysical scenario at the same time, is a novel approach, that we will follow here. In the following paragraphs, we will briefly summarize the additional ingredients that are necessary to study the oxygen deflagration with the help of AGILE-IDSA.

Initial model

For the initial model, we have to rely on a SAGB star or accreting ONe WD model that has been evolved exactly until the ignition of oxygen in the core. For this reason Nomoto's progenitor is not suitable as it is already evolved too far and the center of the core consists of NSE material in the region of iron. On the other hand, the stellar evolution models in Jones et al. (2013) are still not evolved sufficiently far to collapse. However, it might be also possible to use them for a similar study. In this study, we will rely on the AIC models that we generated in Section 6.3.7 specifically for this purpose. They are the well suited

for our survey, as they are evolved to the exact right moment of the ignition of oxygen with a very high spatial resolution.

Flame model

In the next step, we need to construct a parametric flame model that calculates the position of the deflagration based on flame velocities from microscopic calculations. As a consequence of the thermonuclear runaway, a subsonic laminar deflagration wave will form where the flame propagation is initially driven by thermal conduction. However, a (laminar) subsonic burning front is prone to hydrodynamic instabilities that can result in the production of turbulence. Generally speaking, the turbulent combustion front has a much larger surface area compared to the laminar case and accelerates the propagation of the flame. In this paragraph, we will describe how the model of the flame as such can be implemented into AGILE-IDSA, marking the most important addition to the code. In multi-dimensional simulations of astrophysical deflagrations, multiple methods exist to determine the burning front of the flame. One is the so called level-set method by Reinecke et al. (1999), wile another common approach is the artificially broadened flame (see e.g. Khokhlov, 1995).

In our code, we will implement the flame in a similar way to the level-set method. This means that we track the current position of the flame which of course, given the fact that the resolution of the hydrocode is limited, will be positioned somewhere in-between the limits of a mass-shell. As the flame speed in our parametrization will depend only on local conditions, we now have to determine average quantities for the intershell region, based on the lower and upper boundary. Then in every timestep, the flame is advances forward, accordingly.

Laminar Flame Velocities

Initially, the flame will be laminar, mostly because the laminar flame velocity is very fast for degenerate conditions. Assuming that the flame propagates as a deflagration, given the high densities, the oxygen deflagration in the ONe core has an extremely small flame width in the sub-centimeter regime (Timmes & Woosley, 1992). Obviously such a resolution cannot be achieved in any simulation that covers the whole star. In a microscopic simulation of the laminar flame regime, the flame would have to be resolved entirely, strongly limiting the computational domain. In Timmes & Woosley (1992), laminar flame speeds of the oxygen deflagration, driven by heat conduction across the flame front by mainly electrons, were calculated. The authors obtained a rather accurate fit formula, stemming from said simulation in 1D. The flame speeds based on this formula are illustrated in figure 6.25. The fit formula is given by:

$$v_{\mathrm{cond}} = 5.18 \left(\frac{\varrho}{6 \times 10^9 \ \mathrm{g\ cm^{-3}}} \right)^{1.06} \left(\frac{X\left(^{16}\mathrm{O}\right)}{0.6} \right)^{0.688} \ \mathrm{km\ s^{-1}}. \tag{6.37}$$

As can be seen, the flame speed is mainly dependent on the amount of oxygen $X\left(^{16}\mathrm{O}\right)$ in front of the flame and on the ambient density ϱ. Typical velocities range between 50 and 100 km s^{-1}.

Turbulent Flame Velocities

Eventually, the oxygen flame will enter into the turbulent flame regime, at least according to the observation of Jones et al. (2016). As soon as the flame enters into the turbulent regime, the situation gets more complicated, as turbulent eddies increase the flame surface and consequently the propagation velocity is increased significantly, as well. In the past, many authors used very simplistic approaches to estimate the turbulent flame velocity, also due to the lack of more realistic calculations. But due to the 3D simulations of Jones et al. (2016) that simulated the deflagration of oxygen in 3D, "microscopic" flame velocities of the turbulent regime are available, as well. In said simulations, the turbulent flame speed is calculated based a localized subgrid scale model for hydrodynamical simulations (Schmidt et al.,

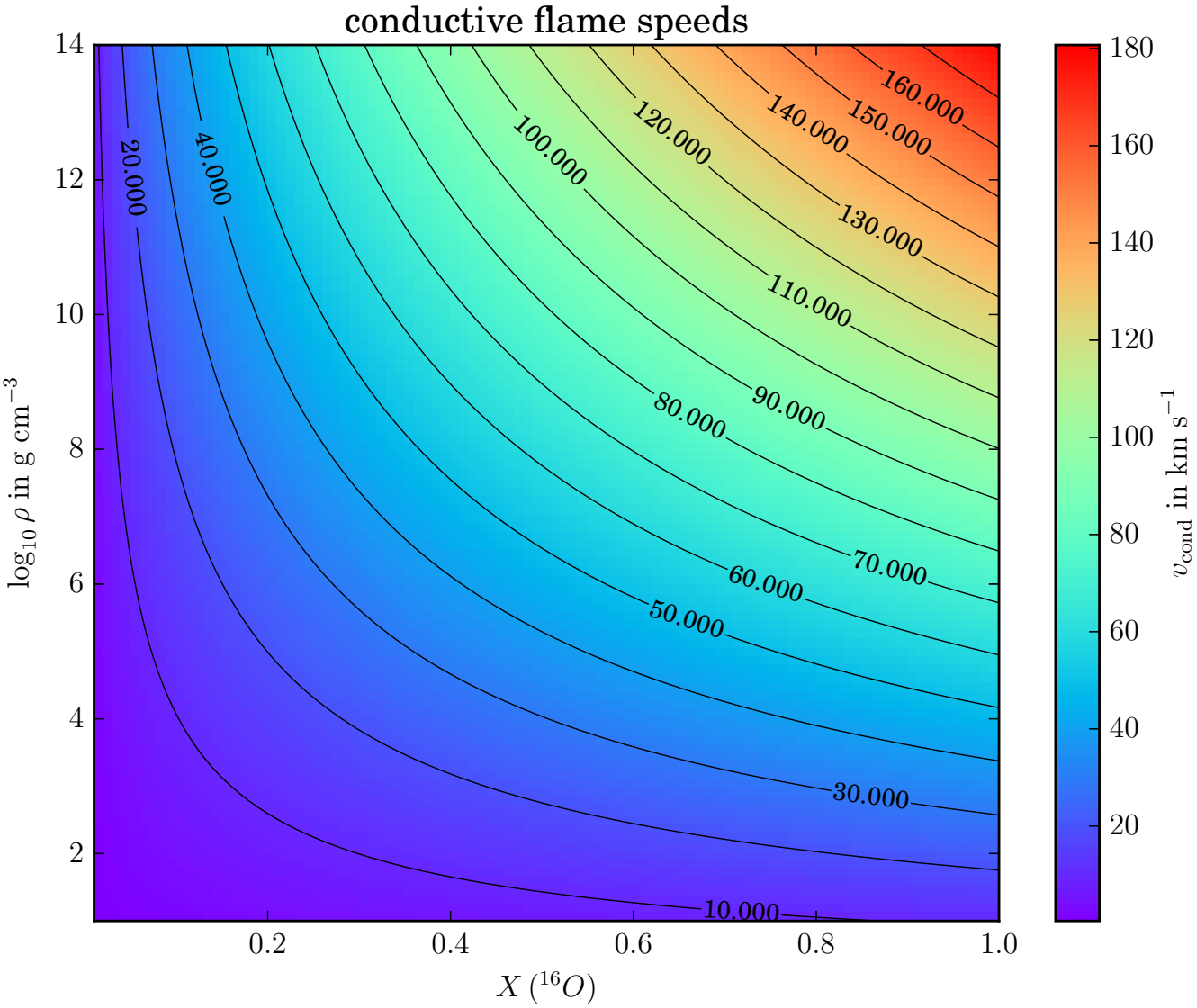

Figure 6.25: Conductive (laminar) flame speeds for the oxygen deflagration, using the fit formula of Timmes & Woosley (1992). The figure illustrates the conductive flame speed $\left(v_{\mathrm{cond}}/\mathrm{km\ s^{-1}}\right)$ as a function of $X\left(^{16}O\right)$ and $\varrho/\mathrm{g\ cm^{-3}}$.

2006a,b), using the LEAFS code (Reinecke et al., 2002; Röpke & Hillebrandt, 2005). The subgrid model is used to calculate the kinetic energy of the fluid on length scales which are smaller than the resolution of the model. Consequently, the subgrid model determines the turbulent flame speed and feeds it back into the simulation. Even though in this study, only 6 models were calculated, it should be possible to extract some kind of formula for the turbulent flame speeds depending on local conditions like density and radius of the flame, which will allow us to use them in our 1D simulations. This approach is to be considered more realistic than the other approaches that only guess the flame speed in the turbulent regime with crude approximations (see also the next paragraph).

In general, we would suggest to compare all the different turbulent flame descriptions that are used in the different previous studies and compare them to the “realistic” determination in (Jones et al., 2016). Independent from the viability of the different methods, we hence propose several different flame parametrization that can be studied in 1D. This also allows us to compare our outcomes more closely to what other people have obtained before. Note also that the exact time of the transition from the laminar to the turbulent flame is not clear. The flame becomes turbulent as soon as the turbulent

flame speed becomes larger than the laminar flame speed. The moment of this transition is called t_{trans}. Then the flame velocity v_{flame} is given by:

$$v_{\mathrm{flame}} = \max\left(v_{\mathrm{cond}}, v_{\mathrm{turb}}\right). \tag{6.38}$$

Additionally, it should be noted, that the flame velocity of course refers to the comoving fluid frame. Hence, in a code like AGILE-IDSA, where the independent variable is the mass, the flame velocity has to be transformed into a propagation in mass by integration over the passed volume of the flame. Also, in a 1D code, this velocity will be the same in all directions, even in the turbulent flame regime. Hence, even though it is possible to account for the turbulent flame by using the radially averaged flame velocities, the deviations from spherical symmetry that arise in the turbulent flame regime, as found by Jones et al. (2016), cannot be accounted for with our approach.

Proposed Flame Parametrizations:

- Laminar only, based on microscopic flame velocities from Timmes & Woosley (1992).
- Laminar based on Timmes & Woosley (1992) until $t_{\mathrm{trans}} \approx 0.5$ seconds (based on t_{trans} from Jones et al., 2016) and then turbulent based on Isern et al. (1991), that use the formula from Woosley (1986) for estimating the turbulent flame speed.
- Laminar based on Timmes & Woosley (1992) until $t_{\mathrm{trans}} \approx 0.5$ seconds (based on t_{trans} from Jones et al., 2016) and then turbulent according to Nomoto & Kondo (1991). For details see time-dependent mixing length theory, as introduced by Unno (1967).
- Laminar based on Timmes & Woosley (1992) and average turbulent flame speeds of Jones et al. (2016). Transition according to Equation (6.38).
- Applying a simple parametrization, using $v_{\mathrm{flame}} = A \times c_s$ where A is a constant in the range of $A = 0.005 - 0.015$ (see e.g. Thielemann et al., 2004).
- Flame velocity only based on Isern et al. (1991), for comparison with their simulation.
- Flame velocity only based on Nomoto & Kondo (1991), for comparison with their simulation.

Implementation of "Burning" into NSE

In the standard description that was used to simulate ECSNe with AGILE (see Section 6.4.1), the burning of oxygen fuel into NSE was purely driven by the collapse-induced compression. This is obviously not an appropriate method to describe the flame. But that is what will happen in any CCSN code, given that not the whole core is already made of iron-group nuclei. In the "realistic" oxygen deflagration case, the situation is more complicated. Here, the energy released by the flame has to be determined by assuming that the whole composition will be burned into NSE while ϱ and Y_e are kept constant. This will result in a new temperature T and internal energy e_{int} that have to be solved iteratively until the e_{tot} is exactly the same as before (as this is a conserved quantity), yielding a unique new temperature and composition of the burned material behind the flame. Obviously, this approach works perfectly fine, as long as the new temperature is sufficiently high ($T \gtrsim 5$ GK). As soon as is gets lower than the threshold temperature that allows us to assume NSE, the outcome will be more complicated, as the deflagration will not burn the whole material into NSE. The exact energy release in such a case cannot be determined with our simple approach. As we will see in Section 6.4.3, this problem occurs only at a very late stage of the deflagration, when the flame has burned already through $\approx 90\%$ of the fuel in the core. The NSE abundances are computed with an NSE solver that takes into account the screening corrections of the ion chemical potential in a dense plasma, as described in Section 3.2.4.

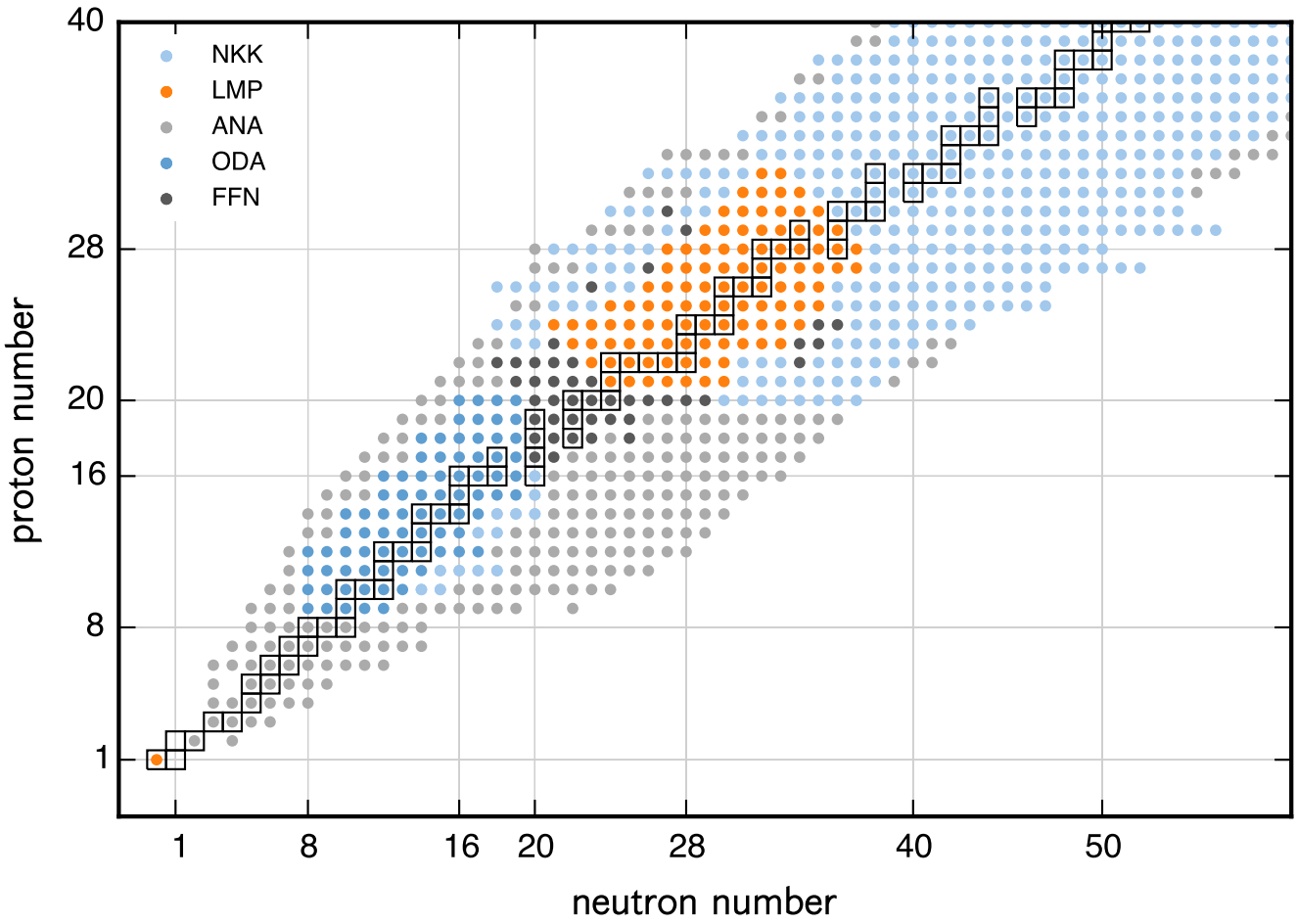

Figure 6.26: Nuclei for which EC and β^- decay rates are considered on the NSE ashes during the oxygen deflagration. Figure from Jones et al. (2016). The rates (reaction rate and energy generation) are folded with NSE abundances to obtain dY_e/dt and $\dot{\epsilon}_{\mathrm{weak}}$. The labels indicate the source of the rate: Nabi & Klapdor-Kleingrothaus (2004, NKK), Fuller et al. (1985, FFN), Langanke & Martínez-Pinedo (2000, LMP), Oda et al. (1994, ODA). ANA corresponds to weak rates calculated by Jones et al. (2016) using an analytical formula similar to Arcones et al. (2010) and Sullivan et al. (2016).

Deleptonization of Ashes

A very crucial point of the oxygen deflagration is the consideration of the deleptonization of the NSE ashes. For this reason EC- and β^--decay rates for neutron-rich iron-group nuclei have to be considered, including Coulomb corrections. In such conditions, EC rates on iron-group nuclei are very high and hence the Fe core deleptonizes very quickly. By this process, even more than before by EC on *sd*-shell nuclei, the dominating pressure support is removed, which supports the star against its own gravity.

As mentioned before, the deleptonization has to be properly described in this close case when the outcome of the simulation depends critically on small details. Different from CCSNe, where the collapse is certain to occur and EC processes only slightly affect the collapse timescale (Sullivan et al., 2016), for ECSNe, we also have to consider β^- decay rates besides EC on all nuclei that are abundant in NSE, to correctly predict the energy loss and the deleptonization. As of now, the standard set of weak rates for the collapse phase of CCSNe is provided by Juodagalvis et al. (2010), but because their only include EC and not β^- decay, they cannot be used for our simulation.

For this reason, we rely on a tabulated compilation of EC and β^- decay rates that was used by Jones et al. (2016) for their 3D oxygen-deflagration simulations. The considered nuclei and the original source of the weak reaction rates are are presented in Figure 6.26. As one can see, the tabulation contains weak

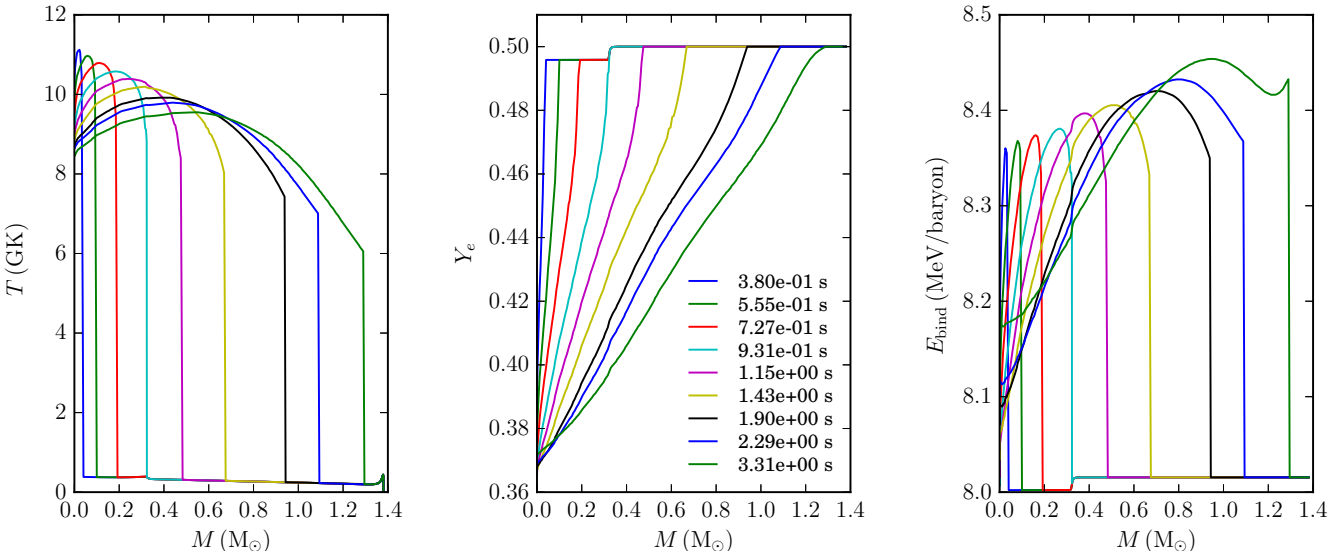

Figure 6.27: Outcome of the oxygen deflagration simulated with AGILE-IDSA, using an initial model from the MESA AIC study. The three panels shows stellar profiles (at different times, $t = 0$ corresponds to the ignition time) of the oxygen deflagration as a function of enclosed baryon mass ($M/M_\odot$). The left panel shows the temperature (T/K), the middle panel shows the electron fraction (Y_e) and the right panel shows the average binding energy per nucleon ($E_{\rm bind}$/MeV). In this model, laminar flame velocities were used according to Timmes & Woosley (1992) and turbulent flame velocities are chosen to be $0.05 \times c_s$, as done in Thielemann et al. (2004).

rates over a large region in the nuclear chart. But this is necessary for a correct determination of the deleptonization of the oxygen-burning ashes.

Additionally, if we would only consider weak rates involving the NSE material behind the flame, a huge simplification can be made. As introduced in Section 4.4.4, the weak reaction rates can be folded with the NSE abundances (yielding dY_e/dt) as obtained from the NSE solver and tabulated in a 3D table as a function of ϱ, T and Y_e. In this way, one table will contain the value of dY_e/dt and one table will contain the energy loss $\dot{\epsilon}_{weak}$ from nuclear neutrino losses and they can be easily used in our simulation.

Collapse Phase

Another aspect that has to be considered in case the collapse ultimately wins over the energy released by deflagration, is the transition to a high-density EoS. In our canonical ECSN simulation, we simply switched from the Helmholtz EoS to the Lattimer-Swesty EoS in the moment where the compression caused the ignition of oxygen. This was a simple and valid way of avoiding any problems when switching from one EoS to another (i.e. from a low- to a high-density EoS). However, for the current setup, this is not possible. The deflagration is now described independently and the transition from one EoS to another occurs based on a density criterion (e.g. 10^{11} g cm^{-3}). Unfortunately, the transition turns out not to be very smooth, suggesting that is might be better to interpolate between both EoSs for a certain transition region (see also Section 6.4.3).

6.4.3 Preliminary Results

In this Section, we present preliminary results of the oxygen deflagration simulated with AGILE-IDSA. In the particular model that we will present here, we employ the laminar flame velocities according to Timmes & Woosley (1992) and the turbulent flame velocities are chosen to be $0.05 \times c_s$, as suggested in Thielemann et al. (2004). For every timestep, the maximum of both velocities is chosen and

used to determine the propagation of the flame. Of course, it would be more sophisticated to use the radially-averaged turbulent flame velocities of the simulation by Jones et al. (2016), but this is not yet implemented into our model and has to be tested in the future. Furthermore, we include plasma neutrino losses according to Itoh et al. (1996), despite the fact that they should not be very important for a simulation that covers only few seconds. In case of a complete gravitational collapse, they furthermore have to be disabled at some point, as neutrinos can no longer be assumed to be free streaming. The deleptonization and the energy generation in the NSE ashes are calculated based on the tables of Jones et al. (2016). The initial AIC MESA model for this study is model `Acc-7`, which has an ignition density of $\log_{10}\left(\varrho/\mathrm{g\ cm^{-3}}\right) = 9.9390$.

The results of this preliminary exploration are displayed in Figure 6.27. The main purpose of the presented model, as of now, is not to give a conclusive answer whether the core will collapse or not, but first of all show that our implementation of the flame works as intended. Hence, this preliminary model is supposed to show that both, the burning and the deleptonization are implemented correctly. The left panel of Figure 6.27 shows the temperature (T/K), the middle panel shows the electron fraction (Y_e) and the right panel shows the average binding energy per nucleon ($E_{\mathrm{bind}}/\mathrm{MeV}$) for a series of profiles that illustrate how the flame is propagating through the star. Within our parametrization of the flame, the same needs roughly 3 seconds to pass through 90% of the ONe core (in terms of mass). At this point, the simulation that is illustrated in Figure 6.27, had to be stopped. The reason is exactly that the flame is not sufficiently energetic anymore to burn the material into NSE and in this case, the determination of the energy release by the flame be very difficult. Based on the observed deleptonization (from $Y_e \approx 0.5$ to 0.37) and the shift of the NSE to more neutron-rich material (observed by the decrease in $E_{\mathrm{bind}}/\mathrm{MeV}$ from ≈ 8.35 to ≈ 8.1), we can conclude that the flame model as such is behaving as desired.

While we achieved the goal to implement the deflagration into AGILE-IDSA, as of now, we are not yet able to simulate collapsing models of the star. The main reason for this is that the transition from the low-density to the high-density EoS introduces too many discrepancies in certain physical quantities (especially the total energy). Because of this, the code has problems with convergence and the numerical simulation crashes. In order to do this properly, it will be necessary to generate a smooth transition from one EoS to the other, as discussed in the previous Section. Hence, it should be stressed again that the primary goal of the study presented here, was to show that our novel approach to model the combined scenario of the oxygen deflagration and ECSNe in a CCSN code works. Consequently, further studies can build upon this framework in order to have the possibility of consistently simulating the oxygen deflagration in 1D.

7 Summary and Conclusions

Since the seminal work of Miyaji et al. (1980), it has been proposed that SAGB stars ($8 \lesssim M/M_\odot \lesssim 10$) host electron-degenerate ONe cores towards the end on their life, that—triggered by EC on mainly ^{20}Ne—collapse and explode in ECSNe. The simultaneous ignition of the oxygen deflagration has been considered as a possible reason that prevents the gravitational collapse and leads to a thermonuclear explosion of the star. This scenario would be similar to the carbon deflagration in CO WDs, responsible for Type 1A supernovae.

The primary goal of the studies in this thesis was to investigate the evolution of ONe WDs that are undergoing mass-accretion in the AIC scenario. It was pointed out by many authors that the fate of these objects depends critically on the density at which the oxygen in core gets ignited. Most recently, this was confirmed by the first 3D simulations of the oxygen deflagration in ONe cores by Jones et al. (2016). For this reason, the main part of our investigations was devoted to the exact determination of the ignition density, accounting for all effects that have an influence on it, and if possible quantifying the related uncertainties. They concern the treatment of convection, the determination of weak reaction rates, the accretion rate and the initial abundances, especially regarding ^{24}Mg and the Urca nuclei ^{23}Na and ^{25}Mg.

For this reason, we performed simulations of the AIC scenario, making use of the stellar evolution code MESA. To some extend, our work can be regarded as a follow-up of the excellent study by Schwab et al. (2015). In order to determine the EC and β^- decay rates, we made use of the recently implemented capability of MESA to evaluate weak reaction rates on-the-fly with very high accuracy, only requiring matrix elements and excitation energies of all contributing transitions, either known experimentally or originating from shell-model calculations. Because in the meantime, high-resolution weak rate tabulations for the relevant set of nuclei were made available by Suzuki et al. (2016), we compared the rates, as determined by MESA, with the aforementioned study and confirm the viability of the on-the-fly determination of weak rates in MESA. Furthermore, we extend it to the Urca nuclei ^{23}Na and ^{25}Mg.

By including the secondary carbon-burning products ^{23}Na and ^{25}Mg in the initial ONe-WD models, new insights were obtained into the Urca cooling phase. The MESA models of accreting ONe cores show, that especially the abundance of ^{25}Mg and the related Urca cooling can affect ϱ_{ign} by 10 %, resulting in densities between $8.7-9.7\times10^9$ g cm^{-3}. In particular, we find that the secondary Urca pair ^{25}Na $\longleftrightarrow$ ^{25}Ne has the biggest impact on the ignition density. This is to be seen in contrast to the findings in Gutiérrez et al. (2005) that found no significant influence. However, this study only considered the primary Urca pair ^{25}Mg $\longleftrightarrow$ ^{25}Na and had to rely on a coarse weak rate tabulation by Oda et al. (1994) which was shown to miss many features of Urca cooling (see e.g. the studies by Jones et al. (2013) and Denissenkov et al. (2015)).

There has been a consensus in the community that the EC processes do not trigger convection in the ONe core if the Ledoux criterion for convection is applied. While this is certainly supported by many arguments (see e.g. Schwab et al., 2015), it should be mentioned that the phenomenon of overstable convection, as it can appear in a stratification that is unstable by means of the temperature gradient but stabilized by a gradient in mean molecular weight, is poorly understood. Our investigations of this question are two-fold. On the one hand we show that, treating overstable convection, as implemented into MESA based on Langer et al. (1983), as a diffusive process, does not affect the evolution of the ONe core. On the other hand, the author that originally introduced the concept of overstable convection (Kato, 1966), provided a simple formalism to study the possible growth of instabilities in such a stratification. Applying Kato's analysis to the ^{20}Ne-EC phase of ONe cores, suggests that instabilities could

develop on a small timescale of around $10-100$ s. This would give enough time for such hydrodynamical instabilities to grow, as the time between the possible onset of overstable convection in the core, due to EC on ^{20}Ne, and collapse is around 100 years.

Furthermore, modifications to the standard set of nuclear reactions at high densities, responsible for neon and oxygen burning, were proposed and investigated. Previously, reaction channels that become possible due to the presence of ^{20}O, formed by double-EC on ^{20}Ne, have not been considered. Neon burning is modified by the reaction $^{20}\mathrm{O}(\alpha,\gamma)^{24}\mathrm{Ne}$ and oxygen burning can additionally proceed by the fusion involving neutron-rich oxygen isotopes: $^{20}\mathrm{O}+{}^{16/20}\mathrm{O}\rightarrow{}^{36/40}\mathrm{S}^{*}$. As in neither cases, experimental data is available, we study the sensitivity of our AIC models to the corresponding reaction rates, simultaneously including a larger reaction network. However, we find that the modified set of reactions during neon and oxygen burning, has no impact on the evolution of the ONe core, at least if the burning is initiated by a thermonuclear runaway.

Further investigations were dedicated to exploring the origin and the consequences of an off-center ignition of the flame, due to EC processes. It was found by Schwab et al. (2015) that including the experimentally unknown second-forbidden ground state-ground state EC transition from ^{20}Ne to ^{20}F into the AIC simulations, can results in such a behavior. For this reason, we simulated similar conditions and confirm the previously reported off-center ignition (≈ 50 km) of the oxygen deflagration. In addition to that, we reveal the origin of this behavior, concluding that in this case, EC heating on ^{20}Ne acts on much longer timescales ($\approx$ years) because the forbidden transition has a significantly lower Q value and gets activated in the ONe core much earlier during the evolution. This gives the core (albeit being highly degenerate) sufficient time to expand and shifts the ignition away from the center.

Another purpose of this study was to generate initial models of ONe cores that ignite oxygen in the center and can then be used to study questions related to the deflagration wave in hydrodynamic simulations. As the oxygen deflagration is potentially followed by an ECSN, we proposed to approach this question by combining the 1D shock-capturing core-collapse-supernova code AGILE-IDSA with a level-set-based flame description, using laminar and turbulent flame velocities based on microscopic calculations. Additionally, all relevant weak processes on the oxygen-burning ashes were considered, in order to correctly predict the deleptonization and energy generation. Using spatially high-resolution ONe core models that develop a thermonuclear runaway in the center, we show preliminary results of the oxygen deflagration, simulated with AGILE-IDSA. We further demonstrate the capability of AGILE-IDSA to perform self-consistent ECSN simulations with the canonical progenitor model of Nomoto (1984), based on the work in Möller (2013). We want to point out that this approach can efficiently complement expensive 3D simulations, by performing parameter studies, allowing for a better exploration of this subject in the future.

Recommendations for Future Work

- We found that the presence of ^{20}O has no impact on the ignition density of the oxygen deflagration, if it occurs in a thermonuclear runaway. The situation might be different when neon and oxygen burning occur prior to the gravitational collapse in stars. Hence, it might be interesting to study the modified neon and oxygen burning—as proposed by us—for example in the context of "failed massive stars" (Jones et al., 2014). In those stars, which are located in-between SAGB stars and massive stars, neon and oxygen are ignited off-center at high densities and burn inward as a flame.
- Even though we studied the occurrence of overstable convection in detail, it turned out to be difficult to give a conclusive answer, at least with both studies that were presented in this thesis. A very interesting and promising approach will be to study a stratification corresponding to the conditions during the EC phase in ONe cores as a separate problem in a 3D low Mach-number hydrodynamical code (e.g. MAESTRO, 2017). Then, it is possible to determine from first principles whether, how and on which timescales overstable convection can occur under such conditions.

- It will be also interesting to study ONe WD models with MESA where a small amount of ^{12}C remains in the core due to incomplete carbon burning. In previous studies by Gutiérrez et al. (2005) (motivated by Dominguez et al. (1993)), it was observed in numerical simulations, that even a small mass fraction of carbon $X\left(^{12}\mathrm{C}\right) \approx 0.01$ in the ONe core could lead to a premature detonation of the core at very low densities of $\approx 10^9$ g cm^{-3}. It would be insightful to find out if those results can be reproduced with MESA.
- We showed that the direct weak rate determination in MESA is a very accurate method to obtain EC and β^- decay rates for low-temperature and high-density conditions, as they appear in ONe cores. However, this approach is usually not feasible (and not necessary) at high temperatures, where many transitions contribute to the total transition strength of the weak process. In principle, it should be possible to use analytic expressions for the determination of the phase space integral, as for example derived by Martínez-Pinedo et al. (2014), to provide a robust and fast approximation of weak rates for both low and high temperature conditions. They could be further improved by combining them with a coarse interpolation table that stores the residual deviation of the analytic formula to the actual rate (similar to tabulating effective $\log_{10}(ft)$ values). Obviously, the interpolation would be only good as long as the residual deviation is not too large.
- The customary approach to determine the energy generation by the oxygen deflagration wave fails, as soon as the flame does not burn the composition into NSE anymore. Even though we have shown that this will only be a problem once the flame has burned already through roughly 90% of the star, this is a problem that should be addressed in the future. It should be possible to determine the exact energy generation and final abundance of the oxygen deflagration ashes by doing microscopic calculations of the flame front, similar to what has been done by Timmes & Woosley (1992).
- Closely related to the previous remark, it might be worth to repeat the calculations of Timmes & Woosley (1992), in order to re-investigate the laminar propagation of the oxygen deflagration in degenerate conditions, using up-to-date reaction rates and also the latest post-carbon burning abundances. And furthermore to study the impact of the abundance of ^{20}O in the fuel on the conductive flame speed, taking into account the modified set of neon and oxygen burning reactions that was pointed out by us.
- It was noted by Jones et al. (2016) that in the future, more 3D hydrodynamical simulations of the oxygen deflagration should be performed. In this way, not only a larger variety of ignition densities can be probed, but also the impact of an off-center ignition and the exact geometry of the ignition spots (see also Fink et al., 2014) can be studied. It should be stressed that, because 3D simulations are still very expensive, our approach to study the flame in 1D, using realistic turbulent flame speeds from 3D simulations, can provide valuable input to narrow down the range of conditions that have to be studied in 3D.
- Of course, the results presented in Section 6.4 regarding the simulation of the oxygen deflagration in a CCSN code are preliminary and we have just started to explore this approach in detail. In the future, many interesting questions can be addressed. This includes aspects like the turbulent flame parametrization, the off-center ignition and of course also different ignition densities.

List of Tables

List of Figures

Bibliography

Abbott, B. P., Abbott, R., Abbott, T. D., Abernathy, M. R., Acernese, F., Ackley, K., Adams, C., Adams, T., Addesso, P., Adhikari, R. X. et al., *GW151226: Observation of Gravitational Waves from a 22-Solar-Mass Binary Black Hole Coalescence*, Physical Review Letters **116** (2016a) 24, 241103.

Abbott, B. P., Abbott, R., Abbott, T. D., Abernathy, M. R., Acernese, F., Ackley, K., Adams, C., Adams, T., Addesso, P., Adhikari, R. X. et al., *Observation of Gravitational Waves from a Binary Black Hole Merger*, Physical Review Letters **116** (2016b) 6, 061102.

Aglietta, M., Badino, G., Bologna, G., Castagnoli, C., Castellina, A., Dadykin, V. L., Fulgione, W., Galeotti, P., Kalchukov, F. F., Khalchukov, F. F. et al., *On the event observed in the Mont Blanc Underground Neutrino Observatory during the occurrence of supernova 1987a.*, EPL (Europhysics Letters) **3** (1987), 1315.

Angulo, C., Arnould, M., Rayet, M., Descouvemont, P., Baye, D., Leclercq-Willain, C., Coc, A., Barhoumi, S., Aguer, P., Rolfs, C. et al., *A compilation of charged-particle induced thermonuclear reaction rates*, Nuclear Physics A **656** (1999), 3.

Arcones, A., Martínez-Pinedo, G., Roberts, L. F. & Woosley, S. E., *Electron fraction constraints based on nuclear statistical equilibrium with beta equilibrium*, A&A **522** (2010), A25.

Arnett, D. (1996), *Supernovae and Nucleosynthesis: An Investigation of the History of Matter from the Big Bang to the Present*.

Arnould, M., Goriely, S. & Takahashi, K., *The r-process of stellar nucleosynthesis: Astrophysics and nuclear physics achievements and mysteries*, Phys. Rep. **450** (2007), 97.

Asplund, M., Grevesse, N., Sauval, A. J. & Scott, P., *The Chemical Composition of the Sun*, ARA&A **47** (2009), 481.

Baade, W. & Zwicky, F., *Remarks on Super-Novae and Cosmic Rays*, Physical Review **46** (1934), 76.

Bethe, H. A., *Energy Production in Stars*, Physical Review **55** (1939), 434.

Bethe, H. A., *Supernova mechanisms*, Reviews of Modern Physics **62** (1990), 801.

Bethe, H. A. & Bacher, R. F., *Nuclear Physics A. Stationary States of Nuclei*, Reviews of Modern Physics **8** (1936), 82.

Bethe, H. A. & Critchfield, C. L., *The Formation of Deuterons by Proton Combination*, Physical Review **54** (1938), 248.

Bethe, H. A. & Wilson, J. R., *Revival of a stalled supernova shock by neutrino heating*, ApJ **295** (1985), 14.

Bionta, R. M., Blewitt, G., Bratton, C. B., Casper, D. & Ciocio, A., *Observation of a neutrino burst in coincidence with supernova 1987A in the Large Magellanic Cloud*, Physical Review Letters **58** (1987), 1494.

Blaum, K., *High-accuracy mass spectrometry with stored ions*, Phys. Rep. **425** (2006), 1.

Böhm-Vitense, E., *Über die Wasserstoffkonvektionszone in Sternen verschiedener Effektivtemperaturen und Leuchtkräfte. Mit 5 Textabbildungen*, ZAp **46** (1958), 108.

Bravo, E. & García-Senz, D., *Coulomb corrections to the equation of state of nuclear statistical equilibrium matter: implications for SNIa nucleosynthesis and the accretion-induced collapse of white dwarfs*, MNRAS **307** (1999), 984.

Buchler, J. R. & Yueh, W. R., *Compton scattering opacities in a partially degenerate electron plasma at high temperatures*, ApJ **210** (1976), 440.

Burbidge, E. M., Burbidge, G. R., Fowler, W. A. & Hoyle, F., *Synthesis of the Elements in Stars*, Reviews of Modern Physics **29** (1957), 547.

Burrows, A., Hayes, J. & Fryxell, B. A., *On the Nature of Core-Collapse Supernova Explosions*, ApJ **450** (1995), 830.

Burrows, A., Livne, E., Dessart, L., Ott, C. D. & Murphy, J., *A New Mechanism for Core-Collapse Supernova Explosions*, ApJ **640** (2006), 878.

Busso, M., Gallino, R. & Wasserburg, G. J., *Nucleosynthesis in Asymptotic Giant Branch Stars: Relevance for Galactic Enrichment and Solar System Formation*, ARA&A **37** (1999), 239.

Cameron, A. G. W., *Nuclear Reactions in Stars and Nucleogenesis*, PASP **69** (1957), 201.

Canal, R., Isern, J. & Labay, J., *The quasi-static evolution of ONeMg cores - Explosive ignition densities and the collapse/explosion alternative*, ApJ **398** (1992), L49.

Canal, R. & Schatzman, E., *Non explosive collapse of white dwarfs*, A&A **46** (1976), 229.

Caughlan, G. R. & Fowler, W. A., *Thermonuclear Reaction Rates V*, Atomic Data and Nuclear Data Tables **40** (1988), 283.

Caughlan, G. R., Fowler, W. A., Harris, M. J. & Zimmerman, B. A., *Tables of Thermonuclear Reaction Rates for Low-Mass Nuclei ($1 \leq Z \leq 14$)*, Atomic Data and Nuclear Data Tables **32** (1985), 197.

Caurier, E., Langanke, K., Martínez-Pinedo, G. & Nowacki, F., *Shell-model calculations of stellar weak interaction rates. I. Gamow-Teller distributions and spectra of nuclei in the mass range A=45-65*, Nuclear Physics A **653** (1999), 439.

Chabrier, G. & Potekhin, A. Y., *Equation of state of fully ionized electron-ion plasmas*, Phys. Rev. E **58** (1998), 4941.

Chabrier, G., Potekhin, A. Y. & Yakovlev, D. G., *Cooling Neutron Stars with Accreted Envelopes*, ApJ **477** (1997), L99.

Chandrasekhar, S., *The Maximum Mass of Ideal White Dwarfs*, ApJ **74** (1931), 81.

Chandrasekhar, S. (1939), *An introduction to the study of stellar structure*.

Christenson, J. H., Cronin, J. W., Fitch, V. L. & Turlay, R., *Evidence for the 2π Decay of the K20 Meson*, Physical Review Letters **13** (1964), 138.

Clayton, D. D. (1983), *Principles of stellar evolution and nucleosynthesis*.

Clifford, F. E. & Tayler, R. J., *The equilibrium distribution of nuclides in matter at high temperatures.*, MmRAS **69** (1965), 21.

Colgate, S. A. & White, R. H., *The Hydrodynamic Behavior of Supernovae Explosions*, ApJ **143** (1966), 626.

Collins, G. W., II, Claspy, W. P. & Martin, J. C., *A Reinterpretation of Historical References to the Supernova of A.D. 1054*, PASP **111** (1999), 871.

Cowan, J. J., Thielemann, F.-K. & Truran, J. W. (manuscript in preparation), *Nuclear Evolution of the Universe*.

Cyburt, R. H., Amthor, A. M., Ferguson, R., Meisel, Z., Smith, K., Warren, S., Heger, A., Hoffman, R. D., Rauscher, T., Sakharuk, A. et al., *The JINA REACLIB Database: Its Recent Updates and Impact on Type-I X-ray Bursts*, ApJS **189** (2010), 240.

Denissenkov, P. A., Truran, J. W., Herwig, F., Jones, S., Paxton, B., Nomoto, K., Suzuki, T. & Toki, H., *Hybrid C-O-Ne white dwarfs as progenitors of Type Ia supernovae: dependence on Urca process and mixing assumptions*, MNRAS **447** (2015), 2696.

Dessart, L., Burrows, A., Ott, C. D., Livne, E., Yoon, S.-C. & Langer, N., *Multidimensional Simulations of the Accretion-induced Collapse of White Dwarfs to Neutron Stars*, ApJ **644** (2006), 1063.

Doherty, C. L., Gil-Pons, P., Lau, H. H. B., Lattanzio, J. C. & Siess, L., *Super and massive AGB stars - II. Nucleosynthesis and yields - $Z = 0.02$, 0.008 and 0.004*, MNRAS **437** (2014a), 195.

Doherty, C. L., Gil-Pons, P., Lau, H. H. B., Lattanzio, J. C., Siess, L. & Campbell, S. W., *Super and massive AGB stars - III. Nucleosynthesis in metal-poor and very metal-poor stars - $Z = 0.001$ and 0.0001*, MNRAS **441** (2014b), 582.

Doherty, C. L., Gil-Pons, P., Siess, L., Lattanzio, J. C. & Lau, H. H. B., *Super- and massive AGB stars - IV. Final fates - initial-to-final mass relation*, MNRAS **446** (2015), 2599.

Doherty, C. L., Siess, L., Lattanzio, J. C. & Gil-Pons, P., *Super asymptotic giant branch stars. I - Evolution code comparison*, MNRAS **401** (2010), 1453.

Dominguez, I., Tornambe, A. & Isern, J., *On the Formation of O-Ne White Dwarfs in Metal-rich Close Binary Systems*, ApJ **419** (1993), 268.

Eddington, A. S. (1926), *The Internal Constitution of the Stars*.

Eldridge, J. J. & Tout, C. A., *The progenitors of core-collapse supernovae*, MNRAS **353** (2004), 87.

ENSDF (2017), *Data extracted using the NNDC On-Line Data Service from the ENSDF database*, `http://www.nndc.bnl.gov/ensdf/`, accessed 17/01/2017.

Ertl, T., Janka, H.-T., Woosley, S. E., Sukhbold, T. & Ugliano, M., *A Two-parameter Criterion for Classifying the Explodability of Massive Stars by the Neutrino-driven Mechanism*, ApJ **818** (2016), 124.

Farmer, R., Fields, C. E. & Timmes, F. X., *On Carbon Burning in Super Asymptotic Giant Branch Stars*, ApJ **807** (2015), 184.

Feenberg, E. & Trigg, G., *The Interpretation of Comparative Half-Lives in the Fermi Theory of Beta-Decay*, Reviews of Modern Physics **22** (1950), 399.

Fetter, A. L. & Walecka, J. D. (1971), *Quantum theory of many-particle systems*.

Fink, M., Kromer, M., Seitenzahl, I. R., Ciaraldi-Schoolmann, F., Röpke, F. K., Sim, S. A., Pakmor, R., Ruiter, A. J. & Hillebrandt, W., *Three-dimensional pure deflagration models with nucleosynthesis and synthetic observables for Type Ia supernovae*, MNRAS **438** (2014), 1762.

Fischer, T., Sagert, I., Pagliara, G., Hempel, M., Schaffner-Bielich, J., Rauscher, T., Thielemann, F.-K., Käppeli, R., Martínez-Pinedo, G. & Liebendörfer, M., *Core-collapse Supernova Explosions Triggered by a Quark-Hadron Phase Transition During the Early Post-bounce Phase*, ApJS **194** (2011), 39.

Fischer, T., Whitehouse, S. C., Mezzacappa, A., Thielemann, F.-K. & Liebendörfer, M., *Protoneutron star evolution and the neutrino-driven wind in general relativistic neutrino radiation hydrodynamics simulations*, A&A **517** (2010), A80.

Fowler, W. A., Caughlan, G. R. & Zimmerman, B. A., *Thermonuclear Reaction Rates*, ARA&A **5** (1967), 525.

Fowler, W. A., Caughlan, G. R. & Zimmerman, B. A., *Thermonuclear Reaction Rates, II*, ARA&A **13** (1975), 69.

Fowler, W. A. & Hoyle, F., *Neutrino Processes and Pair Formation in Massive Stars and Supernovae.*, ApJS **9** (1964), 201.

Freiburghaus, C., Rosswog, S. & Thielemann, F.-K., *R-Process in Neutron Star Mergers*, ApJ **525** (1999), L121.

Fröhlich, C., Martínez-Pinedo, G., Liebendörfer, M., Thielemann, F.-K., Bravo, E., Hix, W. R., Langanke, K. & Zinner, N. T., *Neutrino-Induced Nucleosynthesis of A>64 Nuclei: The νp Process*, Physical Review Letters **96** (2006) 14, 142502.

Fryer, C., Benz, W., Herant, M. & Colgate, S. A., *What Can the Accretion-induced Collapse of White Dwarfs Really Explain?*, ApJ **516** (1999), 892.

Fuller, G. M., Fowler, W. A. & Newman, M. J., *Stellar weak-interaction rates for sd-shell nuclei. I - Nuclear matrix element systematics with application to Al-26 and selected nuclei of importance to the supernova problem*, ApJS **42** (1980), 447.

Fuller, G. M., Fowler, W. A. & Newman, M. J., *Stellar weak interaction rates for intermediate-mass nuclei. II - A = 21 to A = 60*, ApJ **252** (1982a), 715.

Fuller, G. M., Fowler, W. A. & Newman, M. J., *Stellar weak interaction rates for intermediate mass nuclei. III - Rate tables for the free nucleons and nuclei with A = 21 to A = 60*, ApJS **48** (1982b), 279.

Fuller, G. M., Fowler, W. A. & Newman, M. J., *Stellar weak interaction rates for intermediate-mass nuclei. IV - Interpolation procedures for rapidly varying lepton capture rates using effective log (ft)-values*, ApJ **293** (1985), 1.

Gallino, R., Arlandini, C., Busso, M., Lugaro, M., Travaglio, C., Straniero, O., Chieffi, A. & Limongi, M., *Evolution and Nucleosynthesis in Low-Mass Asymptotic Giant Branch Stars. II. Neutron Capture and the S-Process*, ApJ **497** (1998), 388.

Garcia-Berro, E. & Iben, I., *On the formation and evolution of super-asymptotic giant branch stars with cores processed by carbon burning. 1: SPICA to Antares*, ApJ **434** (1994), 306.

García-Berro, E., Ritossa, C. & Iben, I., Jr., *On the Evolution of Stars that Form Electron-Degenerate Cores Processed by Carbon Burning. III. The Inward Propagation of a Carbon-Burning Flame and Other Properties of a 9 M_{solar} Model Star*, ApJ **485** (1997), 765.

Gizon, L. & Birch, A. C., *Local Helioseismology*, Living Reviews in Solar Physics **2** (2005), 6.

Greiner, W. & Maruhn, J. A. (1996), *Nuclear models: with 50 figures and 39 worked examples and problems* (Springer, Berlin).

Greiner, W. & Müller, B. (2009), *Gauge Theory of Weak Interactions*.

Gutiérrez, J., Canal, R. & García-Berro, E., *The gravitational collapse of ONe electron-degenerate cores and white dwarfs: The role of ^{24}Mg and ^{12}C revisited*, A&A **435** (2005), 231.

Gutierrez, J., Garcia-Berro, E., Iben, I., Jr., Isern, J., Labay, J. & Canal, R., *The Final Evolution of ONeMg Electron-Degenerate Cores*, ApJ **459** (1996), 701.

Hanke, F., Marek, A., Müller, B. & Janka, H.-T., *Is Strong SASI Activity the Key to Successful Neutrino-driven Supernova Explosions?*, ApJ **755** (2012), 138.

Hansen, C. J., Primas, F., Hartman, H., Kratz, K.-L., Wanajo, S., Leibundgut, B., Farouqi, K., Hallmann, O., Christlieb, N. & Nilsson, H., *Silver and palladium help unveil the nature of a second r-process*, A&A **545** (2012), A31.

Harris, M. J., Fowler, W. A., Caughlan, G. R. & Zimmerman, B. A., *Thermonuclear reaction rates. III*, ARA&A **21** (1983), 165.

Hashimoto, M., Iwamoto, K. & Nomoto, K., *Type II supernovae from 8-10 solar mass asymptotic giant branch stars*, ApJ **414** (1993), L105.

Haxton, W. C., Hamish Robertson, R. G. & Serenelli, A. M., *Solar Neutrinos: Status and Prospects*, ARA&A **51** (2013), 21.

Heisenberg, W., *Über den Bau der Atomkerne. I*, Zeitschrift für Physik **77** (1932), 1.

Helmholtz-EoS (2017), *Timmes EoS and Helmholtz EoS*, `http://cococubed.asu.edu/code_pages/eos.shtml`, accessed: 21/01/2017.

Hempel, M. & Schaffner-Bielich, J., *A statistical model for a complete supernova equation of state*, Nuclear Physics A **837** (2010), 210.

Henyey, L. G., Forbes, J. E. & Gould, N. L., *A New Method of Automatic Computation of Stellar Evolution.*, ApJ **139** (1964), 306.

Herwig, F., *Evolution of Asymptotic Giant Branch Stars*, ARA&A **43** (2005), 435.

Hillebrandt, W. & Niemeyer, J. C., *Type IA Supernova Explosion Models*, ARA&A **38** (2000), 191.

Hillebrandt, W., Nomoto, K. & Wolff, R. G., *Supernova explosions of massive stars - The mass range 8 to 10 solar masses*, A&A **133** (1984), 175.

Hirata, K., Kajita, T., Koshiba, M., Nakahata, M. & Oyama, Y., *Observation of a neutrino burst from the supernova SN1987A*, Physical Review Letters **58** (1987), 1490.

Hofmeister, E., Kippenhahn, R. & Weigert, A., *Sternentwicklung I. Ein Programm zur Lösung der zeitabhängigen Aufbaugleichungen. Mit 3 Textabbildungen*, ZAp **59** (1964), 215.

Hüdepohl, L., Müller, B., Janka, H.-T., Marek, A. & Raffelt, G. G., *Neutrino Signal of Electron-Capture Supernovae from Core Collapse to Cooling*, Physical Review Letters **104** (2010) 25, 251101.

Huther, L. (2014), *Nucleosynthesis in neutrino-driven winds*, Ph.D. thesis, Darmstadt, Techn. Univ., Diss., 2013.

Iben, I., Jr. & Ehrman, J. R., *The Internal Structure of Middle Main-Sequence Stars.*, ApJ **135** (1962), 770.

Iben, I., Jr. & Renzini, A., *Asymptotic giant branch evolution and beyond*, ARA&A **21** (1983), 271.

Iben, I., Jr., Ritossa, C. & García-Berro, E., *On the Evolution of Stars that Form Electron-degenerate Cores Processed by Carbon Burning. IV. Outward Mixing During the Second Dredge-up Phase and Other Properties of a 10.5 M_{solar} Model Star*, ApJ **489** (1997), 772.

Ichimaru, S., *Nuclear fusion in dense plasmas*, Reviews of Modern Physics **65** (1993), 255.

Idini, A. (2016), *Matrix element of the* $0^+ \rightarrow 2^+$ *transition from* ^{20}Ne *to* ^{20}F, private communication.

Idini, A., Brown, A., Langanke, K. & Martínez-Pinedo, G. (2014), *Electron capture processes in intermediate mass stars*, in *XIII Nuclei in the Cosmos (NIC XIII)*, p. 2.

IDSA (2017), *Agile-IDSA*, `http://www.physik.unibas.ch/~liebend/download/index.html`, accessed: 01/02/2017.

Iliadis, C. (2007), *Nuclear Physics of Stars* (Wiley-VCH Verlag).

Isern, J., Canal, R. & Labay, J., *The outcome of explosive ignition of ONeMg cores - Supernovae, neutron stars, or 'iron' white dwarfs?*, ApJ **372** (1991), L83.

Itoh, N., Hayashi, H., Nishikawa, A. & Kohyama, Y., *Neutrino Energy Loss in Stellar Interiors. VII. Pair, Photo-, Plasma, Bremsstrahlung, and Recombination Neutrino Processes*, ApJS **102** (1996), 411.

Itoh, N., Kuwashima, F., Ichihashi, K. & Mutoh, H., *The Rosseland mean free-free Gaunt factor of the dense high-temperature stellar plasma*, ApJ **382** (1991), 636.

Itoh, N., Tomizawa, N., Tamamura, M., Wanajo, S. & Nozawa, S., *Screening Corrections to the Electron Capture Rates in Dense Stars by the Relativistically Degenerate Electron Liquid*, ApJ **579** (2002), 380.

Janka, H.-T., *Conditions for shock revival by neutrino heating in core-collapse supernovae*, A&A **368** (2001), 527.

Janka, H.-T., *Explosion Mechanisms of Core-Collapse Supernovae*, Annual Review of Nuclear and Particle Science **62** (2012), 407.

Janka, H.-T., Langanke, K., Marek, A., Martínez-Pinedo, G. & Müller, B., *Theory of core-collapse supernovae*, Phys. Rep. **442** (2007), 38.

Janka, H.-T., Melson, T. & Summa, A., *Physics of Core-Collapse Supernovae in Three Dimensions: A Sneak Preview*, Annual Review of Nuclear and Particle Science **66** (2016), 341.

Janka, H.-T., Müller, B., Kitaura, F. S. & Buras, R., *Dynamics of shock propagation and nucleosynthesis conditions in O-Ne-Mg core supernovae*, A&A **485** (2008), 199.

Jennings, Z. G., Williams, B. F., Murphy, J. W., Dalcanton, J. J., Gilbert, K. M., Dolphin, A. E., Fouesneau, M. & Weisz, D. R., *Supernova Remnant Progenitor Masses in M31*, ApJ **761** (2012), 26.

Jones, S., Hirschi, R. & Nomoto, K., *The Final Fate of Stars that Ignite Neon and Oxygen Off-center: Electron Capture or Iron Core-collapse Supernova?*, ApJ **797** (2014), 83.

Jones, S., Hirschi, R., Nomoto, K., Fischer, T., Timmes, F. X., Herwig, F., Paxton, B., Toki, H., Suzuki, T., Martínez-Pinedo, G. et al., *Advanced Burning Stages and Fate of 8-10 $M_\odot$ Stars*, ApJ **772** (2013), 150.

Jones, S., Röpke, F. K., Pakmor, R., Seitenzahl, I. R., Ohlmann, S. T. & Edelmann, P. V. F., *Do electron-capture supernovae make neutron stars? First multidimensional hydrodynamic simulations of the oxygen deflagration*, A&A **593** (2016), A72.

Juodagalvis, A., Langanke, K., Hix, W. R., Martínez-Pinedo, G. & Sampaio, J. M., *Improved estimate of electron capture rates on nuclei during stellar core collapse*, Nuclear Physics A **848** (2010), 454.

Just, O., Bauswein, A., Pulpillo, R. A., Goriely, S. & Janka, H.-T., *Comprehensive nucleosynthesis analysis for ejecta of compact binary mergers*, MNRAS **448** (2015), 541.

Käppeler, F., Gallino, R., Bisterzo, S. & Aoki, W., *The s process: Nuclear physics, stellar models, and observations*, Reviews of Modern Physics **83** (2011), 157.

Karakas, A. I., *Updated stellar yields from asymptotic giant branch models*, MNRAS **403** (2010), 1413.

Kato, S., *Overstable Convection in a Medium Stratified in Mean Molecular Weight*, PASJ **18** (1966), 374.

Kelic, A., Valentina Ricciardi, M. & Schmidt, K.-H., *ABLA07 - towards a complete description of the decay channels of a nuclear system from spontaneous fission to multifragmentation*, ArXiv e-prints (2009).

Khokhlov, A. M., *Propagation of Turbulent Flames in Supernovae*, ApJ **449** (1995), 695.

Kippenhahn, R. & Weigert, A. (1990), *Stellar Structure and Evolution*.

Kippenhahn, R., Weigert, A. & Weiss, A. (2012), *Stellar Structure and Evolution*.

Kirsebom, O. S., Cederkäll, J., Jenkins, D. G., Joshi, P., Julin, R., Kankainen, A., Kibédi, T., Tengblad, O. & Trzaska, W. H. (2017), *Towards an experimental determination of the transition strength between the ground states of ^{20}F and ^{20}Ne*.

Kitaura, F. S., Janka, H.-T. & Hillebrandt, W., *Explosions of O-Ne-Mg cores, the Crab supernova, and subluminous type II-P supernovae*, A&A **450** (2006), 345.

Knigge, C., Coe, M. J. & Podsiadlowski, P., *Two populations of X-ray pulsars produced by two types of supernova*, Nature **479** (2011), 372.

Lam, Y. H., Martínez-Pinedo, G., Langanke, K., Jones, S., Hirschi, R., Zegers, R. G. T. & Brown, B. A. (2014), *Electron Capture and Beta-Decay Rates for the Collapse of O+Ne+Mg Cores*, in *European Physical Journal Web of Conferences*, volume 66 of *European Physical Journal Web of Conferences*, p. 07011.

Landau, L. D., *On the theory of stars*, Phys. Z. Sowjetunion **1** (1932), 285.

Langanke, K. & Martínez-Pinedo, G., *Shell-model calculations of stellar weak interaction rates: II. Weak rates for nuclei in the mass range $A = 45 - 65$ in supernovae environments*, Nuclear Physics A **673** (2000), 481.

Langer, N., Fricke, K. J. & Sugimoto, D., *Semiconvective diffusion and energy transport*, A&A **126** (1983), 207.

Lattimer, J. M., *The Nuclear Equation of State and Neutron Star Masses*, Annual Review of Nuclear and Particle Science **62** (2012), 485.

Lattimer, J. M., Pethick, C. J., Ravenhall, D. G. & Lamb, D. Q., *Physical properties of hot, dense matter: The general case*, Nuclear Physics A **432** (1985), 646.

Lattimer, J. M. & Swesty, F. D., *A generalized equation of state for hot, dense matter*, Nuclear Physics A **535** (1991) 2, 331 , ISSN 0375-9474.

LeBlanc, J. M. & Wilson, J. R., *A Numerical Example of the Collapse of a Rotating Magnetized Star*, ApJ **161** (1970), 541.

Liebendörfer, M., Mezzacappa, A. & Thielemann, F.-K., *Conservative general relativistic radiation hydrodynamics in spherical symmetry and comoving coordinates*, Phys. Rev. D **63** (2001) 10, 104003.

Liebendörfer, M., Rosswog, S. & Thielemann, F.-K., *An Adaptive Grid, Implicit Code for Spherically Symmetric, General Relativistic Hydrodynamics in Comoving Coordinates*, ApJS **141** (2002), 229.

Liebendörfer, M., Whitehouse, S. C. & Fischer, T., *The Isotropic Diffusion Source Approximation for Supernova Neutrino Transport*, ApJ **698** (2009), 1174.

Loens, H. P. (2011), *Microscopic radiative strength functions and fission barriers for r-process nucleosynthesis*, Ph.D. thesis, Darmstadt, Techn. Univ., Diss., 2011.

LS-EoS (2017), *Lattimer-Swesty-EoS*, `http://www.astro.sunysb.edu/dswesty/lseos.html`, accessed: 01/02/2017.

Lugaro, M., Doherty, C. L., Karakas, A. I., Maddison, S. T., Liffman, K., García-Hernández, D. A., Siess, L. & Lattanzio, J. C., *Short-lived radioactivity in the early solar system: The Super-AGB star hypothesis*, Meteoritics and Planetary Science **47** (2012), 1998.

MAESTRO (2017), *MAESTRO: Low Mach Number Astrophysics Code*, `https://ccse.lbl.gov/Research/MAESTRO/index.html`, accessed 27/01/2017.

Martínez-Pinedo, G., Lam, Y. H., Langanke, K., Zegers, R. G. T. & Sullivan, C., *Astrophysical weak-interaction rates for selected A =20 and A =24 nuclei*, Phys. Rev. C **89** (2014) 4, 045806.

Martínez-Rodríguez, H., Piro, A. L., Schwab, J. & Badenes, C., *Neutronization During Carbon Simmering In Type Ia Supernova Progenitors*, ApJ **825** (2016), 57.

Mayle, R. & Wilson, J. R., *Supernovae from collapse of oxygen-magnesium-neon cores*, ApJ **334** (1988), 909.

MESA (2017), *MESA documentation archive*, `http://mesa.sourceforge.net/docs.html`, accessed 17/01/2017.

Miyaji, S. & Nomoto, K., *On the collapse of 8-10 solar mass stars due to electron capture*, ApJ **318** (1987), 307.

Miyaji, S., Nomoto, K., Yokoi, K. & Sugimoto, D., *Supernova Triggered by Electron Captures*, PASJ **32** (1980), 303.

Mochkovitch, R. (1984), *Final Evolution of 8-10 $M_\odot$ Stars*, in *NATO Advanced Science Institutes (ASI) Series C*, edited by D. Bancel & M. Signore, volume 134 of *NATO Advanced Science Institutes (ASI) Series C*, p. 125.

Möller, H. (2013), *Electron Capture Supernovae*, Master's thesis, Technische Universität Darmstadt, Germany.

Möller, H., Jones, S., Fischer, T. & Martínez-Pinedo, G. (2014), *Impact of Nuclear Reactions at High Densities on the Fate of Intermediate-Mass Stars*, in *XIII Nuclei in the Cosmos (NIC XIII)*, p. 125.

Möller, H., Jones, S., Fischer, T. & Martínez-Pinedo, G., *Role of nuclear reactions on evolution of intermediate-mass stars*, Journal of Physics Conference Series (to appear).

Müller, B., *The Status of Multi-Dimensional Core-Collapse Supernova Models*, PASA **33** (2016), e048.

Nabi, J.-U. & Klapdor-Kleingrothaus, H. V., *Microscopic calculations of stellar weak interaction rates and energy losses for fp- and fpg-shell nuclei*, Atomic Data and Nuclear Data Tables **88** (2004), 237.

Ning, H., Qian, Y.-Z. & Meyer, B. S., *r-Process Nucleosynthesis in Shocked Surface Layers of O-Ne-Mg Cores*, ApJ **667** (2007), L159.

Nishimura, N., Fischer, T., Thielemann, F.-K., Fröhlich, C., Hempel, M., Käppeli, R., Martínez-Pinedo, G., Rauscher, T., Sagert, I. & Winteler, C., *Nucleosynthesis in Core-collapse Supernova Explosions Triggered by a Quark-Hadron Phase Transition*, ApJ **758** (2012), 9.

Nomoto, K. (1981), *Supernova explosions in degenerate stars - Detonation, deflagration, and electron capture*, in *Fundamental Problems in the Theory of Stellar Evolution*, edited by D. Sugimoto, D. Q. Lamb & D. N. Schramm, volume 93 of *IAU Symposium*, pp. 295–314.

Nomoto, K., *Evolution of 8-10 solar mass stars toward electron capture supernovae. I - Formation of electron-degenerate O + NE + MG cores*, ApJ **277** (1984), 791.

Nomoto, K., *Evolution of 8-10 solar mass stars toward electron capture supernovae. II - Collapse of an O + NE + MG core*, ApJ **322** (1987), 206.

Nomoto, K. & Kondo, Y., *Conditions for accretion-induced collapse of white dwarfs*, ApJ **367** (1991), L19.

Nomoto, K., Sugimoto, D., Sparks, W. M., Fesen, R. A., Gull, T. R. & Miyaji, S., *The Crab Nebula's progenitor*, Nature **299** (1982), 803.

Nordhaus, J., Burrows, A., Almgren, A. & Bell, J., *Dimension as a Key to the Neutrino Mechanism of Core-collapse Supernova Explosions*, ApJ **720** (2010), 694.

Oda, T., Hino, M., Muto, K., Takahara, M. & Sato, K., *Rate Tables for the Weak Processes of sd-Shell Nuclei in Stellar Matter*, Atomic Data and Nuclear Data Tables **56** (1994), 231.

Oertel, M., Hempel, M., Klähn, T. & Typel, S., *Equations of state for supernovae and compact stars*, ArXiv e-prints (2016).

Ogata, S. & Ichimaru, S., *Critical examination of N dependence in the Monte Carlo calculations for a classical one-component plasma*, Phys. Rev. A **36** (1987), 5451.

Osterfeld, F., *Nuclear spin and isospin excitations*, Reviews of Modern Physics **64** (1992), 491.

Ott, C. D., *TOPICAL REVIEW: The gravitational-wave signature of core-collapse supernovae*, Classical and Quantum Gravity **26** (2009) 6, 063001.

Patrignani, C., *Review of Particle Physics*, Chin. Phys. **C40** (2016) 10, 100001.

Paxton, B., Bildsten, L., Dotter, A., Herwig, F., Lesaffre, P. & Timmes, F., *Modules for Experiments in Stellar Astrophysics (MESA)*, ApJS **192** (2011), 3.

Paxton, B., Cantiello, M., Arras, P., Bildsten, L., Brown, E. F., Dotter, A., Mankovich, C., Montgomery, M. H., Stello, D., Timmes, F. X. et al., *Modules for Experiments in Stellar Astrophysics (MESA): Planets, Oscillations, Rotation, and Massive Stars*, ApJS **208** (2013), 4.

Paxton, B., Marchant, P., Schwab, J., Bauer, E. B., Bildsten, L., Cantiello, M., Dessart, L., Farmer, R., Hu, H., Langer, N. et al., *Modules for Experiments in Stellar Astrophysics (MESA): Binaries, Pulsations, and Explosions*, ApJS **220** (2015), 15.

Paxton, B., Marchant, P., Schwab, J., Bauer, E. B., Bildsten, L., Cantiello, M., Dessart, L., Farmer, R., Hu, H., Langer, N. et al., *Erratum: Modules for Experiments in Stellar Astrophysics (MESA): Binaries, Pulsations, and Explosions*, ApJS **223** (2016), 18.

Pearson, J. M., Goriely, S. & Chamel, N., *Microscopic mass models for astrophysics*, International Journal of Mass Spectrometry **349** (2013), 57.

Poelarends, A. J. T., Herwig, F., Langer, N. & Heger, A., *The Supernova Channel of Super-AGB Stars*, ApJ **675** (2008), 614-625.

Potekhin, A. Y. & Chabrier, G., *Equation of state of fully ionized electron-ion plasmas. II. Extension to relativistic densities and to the solid phase*, Phys. Rev. E **62** (2000), 8554.

Potekhin, A. Y., Chabrier, G. & Rogers, F. J., *Equation of state of classical Coulomb plasma mixtures*, Phys. Rev. E **79** (2009) 1, 016411.

Rampp, M. & Janka, H.-T., *Radiation hydrodynamics with neutrinos. Variable Eddington factor method for core-collapse supernova simulations*, A&A **396** (2002), 361.

Rauscher, T. & Thielemann, F.-K., *Astrophysical Reaction Rates From Statistical Model Calculations*, Atomic Data and Nuclear Data Tables **75** (2000), 1.

Ravenhall, D. G., Pethick, C. J. & Wilson, J. R., *Structure of Matter below Nuclear Saturation Density*, Physical Review Letters **50** (1983), 2066.

Reinecke, M., Hillebrandt, W. & Niemeyer, J. C., *Three-dimensional simulations of type Ia supernovae*, A&A **391** (2002), 1167.

Reinecke, M., Hillebrandt, W., Niemeyer, J. C., Klein, R. & Gröbl, A., *A new model for deflagration fronts in reactive fluids*, A&A **347** (1999), 724.

Ritossa, C., Garcia-Berro, E. & Iben, I., Jr., *On the Evolution of Stars That Form Electron-degenerate Cores Processed by Carbon Burning. II. Isotope Abundances and Thermal Pulses in a 10 M_{sun} Model with an ONe Core and Applications to Long-Period Variables, Classical Novae, and Accretion-induced Collapse*, ApJ **460** (1996), 489.

Ritossa, C., García-Berro, E. & Iben, I., Jr., *On the Evolution of Stars that Form Electron-degenerate Cores Processed by Carbon Burning. V. Shell Convection Sustained by Helium Burning, Transient Neon Burning, Dredge-out, Urca Cooling, and Other Properties of an 11 M_{solar} Population I Model Star*, ApJ **515** (1999), 381.

Röpke, F. K. & Hillebrandt, W., *Full-star type Ia supernova explosion models*, A&A **431** (2005), 635.

Sagert, I., Fischer, T., Hempel, M., Pagliara, G., Schaffner-Bielich, J., Mezzacappa, A., Thielemann, F.-K. & Liebendörfer, M., *Signals of the QCD Phase Transition in Core-Collapse Supernovae*, Physical Review Letters **102** (2009) 8, 081101.

Saio, H. & Nomoto, K., *Evolution of a merging pair of C + O white dwarfs to form a single neutron star*, A&A **150** (1985), L21.

Salpeter, E. E., *The Luminosity Function and Stellar Evolution.*, ApJ **121** (1955), 161.

Schatz, H., Bildsten, L., Cumming, A. & Wiescher, M., *The Rapid Proton Process Ashes from Stable Nuclear Burning on an Accreting Neutron Star*, ApJ **524** (1999), 1014.

Schmidt, W., Niemeyer, J. C. & Hillebrandt, W., *A localised subgrid scale model for fluid dynamical simulations in astrophysics. I. Theory and numerical tests*, A&A **450** (2006a), 265.

Schmidt, W., Niemeyer, J. C., Hillebrandt, W. & Röpke, F. K., *A localised subgrid scale model for fluid dynamical simulations in astrophysics. II. Application to type Ia supernovae*, A&A **450** (2006b), 283.

Schwab, J., Podsiadlowski, P. & Rappaport, S., *Further Evidence for the Bimodal Distribution of Neutron-star Masses*, ApJ **719** (2010), 722.

Schwab, J., Quataert, E. & Bildsten, L., *Thermal runaway during the evolution of ONeMg cores towards accretion-induced collapse*, MNRAS **453** (2015), 1910.

Schwab, J., Quataert, E. & Bildsten, L., *Erratum: Thermal runaway during the evolution of ONeMg cores towards accretion-induced collapse*, MNRAS **458** (2016a), 3613.

Schwab, J., Quataert, E. & Kasen, D., *The evolution and fate of super-Chandrasekhar mass white dwarf merger remnants*, MNRAS **463** (2016b), 3461.

Seitenzahl, I. R., Townsley, D. M., Peng, F. & Truran, J. W., *Nuclear statistical equilibrium for Type Ia supernova simulations*, Atomic Data and Nuclear Data Tables **95** (2009), 96.

Shen, H., Toki, H., Oyamatsu, K. & Sumiyoshi, K., *Relativistic equation of state of nuclear matter for supernova and neutron star*, Nuclear Physics A **637** (1998), 435.

Siess, L. (2006a), *Evolution of massive AGB stars*, in *EAS Publications Series*, edited by T. Montmerle & C. Kahane, volume 19 of *EAS Publications Series*, pp. 103–124.

Siess, L., *Evolution of massive AGB stars. I. Carbon burning phase*, A&A **448** (2006b), 717.

Siess, L., *Evolution of massive AGB stars. II. model properties at non-solar metallicity and the fate of Super-AGB stars*, A&A **476** (2007), 893.

Siess, L., *Evolution of massive AGB stars. III. the thermally pulsing super-AGB phase*, A&A **512** (2010), A10.

Slattery, W. L., Doolen, G. D. & Dewitt, H. E., *N-dependence in the classical one-component plasma Monte Carlo calculations*, Phys. Rev. A **26** (1982), 2255.

Sullivan, C., O'Connor, E., Zegers, R. G. T., Grubb, T. & Austin, S. M., *The Sensitivity of Core-collapse Supernovae to Nuclear Electron Capture*, ApJ **816** (2016), 44.

Suwa, Y., Kotake, K., Takiwaki, T., Whitehouse, S. C., Liebendörfer, M. & Sato, K., *Explosion Geometry of a Rotating 13$M_\odot$ Star Driven by the SASI-Aided Neutrino-Heating Supernova Mechanism*, PASJ **62** (2010), L49.

Suwa, Y., Takiwaki, T., Kotake, K., Fischer, T., Liebendörfer, M. & Sato, K., *On the Importance of the Equation of State for the Neutrino-driven Supernova Explosion Mechanism*, ApJ **764** (2013), 99.

Suzuki, T., Toki, H. & Nomoto, K., *Electron-capture and β-decay Rates for sd-Shell Nuclei in Stellar Environments Relevant to High-density O-Ne-Mg Cores*, ApJ **817** (2016), 163.

Takahara, M., Hino, M., Oda, T., Muto, K., Wolters, A. A., Glaudemans, P. W. M. & Sato, K., *Microscopic calculation of the rates of electron captures which induce the collapse of O+Ne+Mg cores*, Nuclear Physics A **504** (1989), 167.

Takahashi, K., Yoshida, T. & Umeda, H., *Evolution of Progenitors for Electron Capture Supernovae*, ApJ **771** (2013), 28.

Thielemann, F.-K., Brachwitz, F., Höflich, P., Martinez-Pinedo, G. & Nomoto, K., *The physics of type Ia supernovae*, New A Rev. **48** (2004), 605.

Thielemann, F.-K., Nomoto, K. & Hashimoto, M.-A., *Core-Collapse Supernovae and Their Ejecta*, ApJ **460** (1996), 408.

Tilley, D. R., Cheves, C. M., Kelley, J. H., Raman, S. & Weller, H. R., *Energy levels of light nuclei, A = 20*, Nuclear Physics A **636** (1998), 249.

Timmes, F. X., *Integration of Nuclear Reaction Networks for Stellar Hydrodynamics*, ApJS **124** (1999), 241.

Timmes, F. X. & Arnett, D., *The Accuracy, Consistency, and Speed of Five Equations of State for Stellar Hydrodynamics*, ApJS **125** (1999), 277.

Timmes, F. X. & Swesty, F. D., *The Accuracy, Consistency, and Speed of an Electron-Positron Equation of State Based on Table Interpolation of the Helmholtz Free Energy*, ApJS **126** (2000), 501.

Timmes, F. X. & Woosley, S. E., *The conductive propagation of nuclear flames. I - Degenerate C + O and O + NE + MG white dwarfs*, ApJ **396** (1992), 649.

Toki, H., Suzuki, T., Nomoto, K., Jones, S. & Hirschi, R., *Detailed β-transition rates for URCA nuclear pairs in 8-10 solar-mass stars*, Phys. Rev. C **88** (2013) 1, 015806.

Towner, I. S. & Hardy, J. C. (1995), *Currents and Their Couplings in the Weak Sector of the Standard Model* (World Scientific Publishing Co), pp. 183–249.

Tsuruta, S. & Cameron, A. G. W., *URCA Shells in Dense Stellar Interiors*, Ap&SS **7** (1970), 374.

Unno, W., *Stellar Radial Pulsation Coupled with the Convection*, PASJ **19** (1967), 140.

Wanajo, S., Janka, H.-T. & Müller, B., *Electron-capture Supernovae as The Origin of Elements Beyond Iron*, ApJ **726** (2011), L15.

Wanajo, S., Nomoto, K., Janka, H.-T., Kitaura, F. S. & Müller, B., *Nucleosynthesis in Electron Capture Supernovae of Asymptotic Giant Branch Stars*, ApJ **695** (2009), 208.

Wanajo, S., Tamamura, M., Itoh, N., Nomoto, K., Ishimaru, Y., Beers, T. C. & Nozawa, S., *The r-Process in Supernova Explosions from the Collapse of O-Ne-Mg Cores*, ApJ **593** (2003), 968.

Wang, M., Audi, G., A. H., W., F. G., K., MacCormick, M., Xu, X. & Pfeiffer, B., *The Ame2012 atomic mass evaluation*, Chinese Physics C **36** (2012), 003.

Weiss, A., Hillebrandt, W., Thomas, H.-C. & Ritter, H. (2004), *Cox and Giuli's Principles of Stellar Structure*.

Wheeler, J. C., Cowan, J. J. & Hillebrandt, W., *The r-Process in Collapsing O/Ne/Mg Cores*, ApJ **493** (1998), L101.

Wikipedia (2016), *Evolution of a 5 $M_\odot$ star — Wikipedia, The Free Encyclopedia*, `https://upload.wikimedia.org/wikipedia/commons/3/3b/Evolutionary_track_5m.svg`, accessed 18/12/2016.

Winkler, P. F., Gupta, G. & Long, K. S., *The SN 1006 Remnant: Optical Proper Motions, Deep Imaging, Distance, and Brightness at Maximum*, ApJ **585** (2003), 324.

Winteler, C., Käppeli, R., Perego, A., Arcones, A., Vasset, N., Nishimura, N., Liebendörfer, M. & Thielemann, F.-K., *Magnetorotationally Driven Supernovae as the Origin of Early Galaxy r-process Elements?*, ApJ **750** (2012), L22.

Wong, S. S. M. (1998), *Introductory Nuclear Physics, 2nd Edition*.

Woosley, S. E. (1986), *Nucleosynthesis and Stellar Evolution*, in *Saas-Fee Advanced Course 16: Nucleosynthesis and Chemical Evolution*, edited by J. Audouze, C. Chiosi & S. E. Woosley, p. 1.

Woosley, S. E. & Heger, A., *The Remarkable Deaths of 9-11 Solar Mass Stars*, ApJ **810** (2015), 34.

Woosley, S. E., Heger, A. & Weaver, T. A., *The evolution and explosion of massive stars*, Reviews of Modern Physics **74** (2002), 1015.

Woosley, S. E. & Weaver, T. A., *The physics of supernova explosions*, ARA&A **24** (1986), 205.

Woosley, S. E. & Weaver, T. A., *The Evolution and Explosion of Massive Stars. II. Explosive Hydrodynamics and Nucleosynthesis*, ApJS **101** (1995), 181.

Woosley, S. E., Wilson, J. R., Mathews, G. J., Hoffman, R. D. & Meyer, B. S., *The r-process and neutrino-heated supernova ejecta*, ApJ **433** (1994), 229.

Wu, C. S., Ambler, E., Hayward, R. W., Hoppes, D. D. & Hudson, R. P., *Experimental Test of Parity Conservation in Beta Decay*, Physical Review **105** (1957), 1413.

Xu, Y., Goriely, S., Jorissen, A., Chen, G. L. & Arnould, M., *Databases and tools for nuclear astrophysics applications. BRUSsels Nuclear LIBrary (BRUSLIB), Nuclear Astrophysics Compilation of REactions II (NACRE II) and Nuclear NETwork GENerator (NETGEN)*, A&A **549** (2013), A106.

Yakovlev, D. G., Beard, M., Gasques, L. R. & Wiescher, M., *Simple analytic model for astrophysical S factors*, Phys. Rev. C **82** (2010) 4, 044609.

Yakovlev, D. G. & Shalybkov, D. A., *Degenerate Cores of White Dwarfs and Envelopes of Neutron Stars - Thermodynamics and Plasma Screening in Thermonuclear Reactions*, Astrophysics and Space Physics Reviews **7** (1989), 311.

Yakovlev, D. G. & Urpin, V. A., *Thermal and Electrical Conductivity in White Dwarfs and Neutron Stars*, Soviet Ast. **24** (1980), 303.

Yoon, S.-C., Langer, N. & Norman, C., *Single star progenitors of long gamma-ray bursts. I. Model grids and redshift dependent GRB rate*, A&A **460** (2006), 199.

Zhao, F.-Y., Strom, R. G. & Jiang, S.-Y., *The Guest Star of AD185 must have been a Supernova*, Chinese J. Astron. Astrophys. **6** (2006), 635.

Zwicky, F., *On Collapsed Neutron Stars.*, ApJ **88** (1938), 522.

Acknowledgments

Foremost, I would like to express my sincere gratitude to my doctoral advisor Gabriel Martínez-Pinedo for giving me the opportunity and the necessary support to work on my PhD project in his group at TU Darmstadt and GSI. You have been especially helpful in challenging and sharpening my understanding of physics since I first attended your astrophysics lecture as a student. I am also extremely grateful to you for giving me the freedom to work on a science topic that I really enjoyed. Furthermore, you have been very supportive in attending schools, workshops and conferences around the world. Muchas gracias por todo!

I would also like to offer my special thanks to my doctoral advisor Karlheinz Langanke for supporting me as a PhD student and for giving me invaluable advise from the standpoint of an experienced researcher.

Special thanks goes to Tobias Fischer who not only supervised me during my master's thesis but also ignited my motivation to pursue a PhD in physics. It has always been a pleasure to work with you.

I owe my deepest gratitude to Samuel Jones. Not only do I share a lot of memorable moments with you, especially from Hirschegg, Victoria, Kyoto and Tokyo, but also the mutual interest in a fascinating science topic. Our frequent and intensive exchange of ideas had an immense impact on the work that is presented in my PhD thesis.

I am in debt to Ken´ichi Nomoto for his hospitality during my two visits at Kavli IMPU in Tokyo and for a lot of stimulating and fruitful discussions that sharpened my understanding of astrophysics.

I would like to express my gratitude to Fritz Röpke and his group in Heidelberg for the hospitality during many visits at HITS.

Special thanks are offered to my host Falk Herwig and my graduate school HGS-HIRe for giving me the possibility to stay as a visiting research student at the University of Victoria within the HGS-HIRe Abroad program.

Furthermore, I would also like to thank Friedel Thielemann for giving me the opportunity to attend the "brainstorming an fun" meetings in Basel on two occasions and for his helpful advise during his summer visits in Darmstadt.

My greatest appreciation goes to my current and former group members from the nuclear astrophysics group at TU Darmstadt and GSI for five very pleasant years with a lot of unforgettable memories. Shout-out to Joel de Jesús Mendoza-Temis for being a funny and loveable person and for sharing a lot of good memories, Tobias Fischer for starting the kart racing tradition, to Yi-Hua Lam for his honesty, Tomás Raúl Rodríguez Frutos for being el capítan, Qi-Jun Zhi for his sense of humor, Lutz Huther for relaxing walks to the supermarket, Meng-Ru Wu for being a great mentor, Alexander Arzhanov for unforgettable cycling adventures, André Sieverding for many helpful discussions about physics, Andrea Idini for his enthusiasm for Italian cuisine, David Volk for becoming a good friend, Stephen Frieß for being a unique person, Samuel Andrea Giuliani for his humble character and bringing sunshine into our office, Tomislav Marketin for his admirable sarcasm, Masahiko Katsuma for his hospitality, Max Enders for sharing the passion of football and especially to Andreas Lohs for becoming a good friend and for leading the Soccernova team at the GSI football cup.

I will also keep especially positive memories of the ECT* Doctoral Training Program in spring 2013 in Trento before the start of my PhD where I had the privilege to meet a lot of interesting people and also learned a lot about nuclear astrophysics.

Regarding the results presented in Section 6.3, I would like to thank Josiah Schwab for making the initial white dwarf models available and all people that contributed to make the open-source stellar evolution code MESA available to the community.

Many thanks to Gabriel Martínez-Pinedo, Samuel Jones, Andreas Lohs, Sven Möller and Bernadette Wezorke for proofreading parts of my thesis.

Des Weiteren möchte ich natürlich auch in ganz besonderem Maße meinen Eltern Elke und Jürgen, meinen Großeltern Magda und Ernst, meiner Tante Heike als auch meinem Bruder Sven für ihre Unterstützung und ihr Verständnis in allen Lebenslagen danken.

Ich möchte auch meinem Physiklehrer Klaus Becker danken, dem es mit seinem Unterricht gelungen ist, sowohl meinen Verstand als auch meine Faulheit herauszufordern. Ohne Sie hätte ich wohlmöglich nie mit dem Studium der Physik begonnen.

Zu guter Letzt möchte ich natürlich auch meiner besseren Hälfte und Seelenfreundin Bernadette danken. Ohne deine moralische und alltägliche Unterstützung, für deren Anerkennung mir keine angemessenen Worte einfallen, wäre die Vollendung dieser Arbeit gewiss nicht möglich gewesen.

Lebenslauf

Persönliche Daten

Geburtsdatum	10 Juli, 1988
Geburtsort	Wiesbaden
Nationalität	Deutsch

Erfahrung

2016–2017	Wissenschaftlicher Mitarbeiter am GSI Helmholtzzentrum für Schwerionenforschung GmbH
2015–2016	Wissenschaftlicher Mitarbeiter an der TU Darmstadt im Rahmen des ”Nuclear Astrophysics Virtual Institute (NAVI)”
2013–2015	Wissenschaftlicher Mitarbeiter an der TU Darmstadt im Rahmen des SFB 634 ”Kernstruktur, nukleare Astrophysik und fundamentale Experimente bei kleinen Impulsüberträgen am supraleitenden Darmstädter Elektronenbeschleuniger S-DALINAC”
2013–2017	Doktorand im HGS-HIRe Graduiertenkolleg

Bildung

2010–2013	**M.Sc. in Physik, TU Darmstadt, Darmstadt, Deutschland** ”Electron-Capture Supernovae”
2007–2010	**B.Sc. in Physik, TU Darmstadt, Darmstadt, Deutschland** ”Verbesserung der Energieauflösung von HPGe-Detektoren”
1998–2007	**Max-Planck-Schule, Rüsselsheim, Deutschland** Erlangung der allgemeinen Hochschulreife
1995–1998	**Georg-Mangold-Schule, Bischofsheim, Deutschland** Grundschule, 2. - 4. Klasse
1994–1995	**Theodor-Heuss-Schule, Bischofsheim, Deutschland** Grundschule, 1. Klasse

Erklärung zur Dissertation

Hiermit versichere ich, die vorliegende Dissertation ohne Hilfe Dritter nur mit den angegebenen Quellen und Hilfsmitteln angefertigt zu haben. Alle Stellen, die aus Quellen entnommen wurden, sind als solche kenntlich gemacht. Diese Arbeit hat in gleicher oder ähnlicher Form noch keiner Prüfungsbehörde vorgelegen. Eine Promotion wurde bisher noch nicht versucht.

Darmstadt, den 13. November 2017

(Heiko Möller)